

The Pierre Auger Observatory Upgrade

“AugerPrime”

Preliminary Design Report



The Pierre Auger Collaboration
April, 2015



Observatorio Pierre Auger,
Av. San Martín Norte 304,
5613 Malargüe, Argentina

The Pierre Auger Collaboration, April 2015

A. Aab⁴¹, P. Abreu⁶⁵, M. Aglietta⁵², E.J. Ahn⁸², I. Al Samarai²⁸, I.F.M. Albuquerque¹⁶, I. Allekotte¹, P. Allison⁸⁷, A. Almela^{11,8}, J. Alvarez Castillo⁵⁸, J. Alvarez-Muñiz⁷⁵, R. Alves Batista⁴⁰, M. Ambrosio⁴³, A. Aminaei⁵⁹, L. Anchordoqui⁸¹, S. Andringa⁶⁵, C. Aramo⁴³, F. Arqueros⁷², N. Arsene⁶⁸, H. Asorey^{1,24}, P. Assis⁶⁵, J. Aublin³⁰, M. Ave¹, M. Avenier³¹, G. Avila¹⁰, N. Awal⁸⁵, A.M. Badescu⁶⁹, K.B. Barber¹², J. Bäuml³⁵, C. Baus³⁵, J.J. Beatty⁸⁷, K.H. Becker³⁴, J.A. Bellido¹², C. Berat³¹, M.E. Bertaina⁵², X. Bertou¹, P.L. Biermann³⁸, P. Billoir³⁰, S.G. Blaess¹², A. Blanco⁶⁵, M. Blanco³⁰, J. Blazek²⁶, C. Bleve⁴⁷, H. Blümer^{35,36}, M. Boháčová²⁶, D. Boncioli⁵¹, C. Bonifazi²², N. Borodai⁶³, J. Brack⁷⁹, I. Brancus⁶⁶, A. Bridgeman³⁶, P. Brogueira⁶⁵, W.C. Brown⁸⁰, P. Buchholz⁴¹, A. Bueno⁷⁴, S. Buitink⁵⁹, M. Buscemi⁴³, K.S. Caballero-Mora⁵⁶, B. Caccianiga⁴², L. Caccianiga³⁰, M. Candusso⁴⁴, L. Caramete⁶⁷, R. Caruso⁴⁵, A. Castellina⁵², G. Cataldi⁴⁷, L. Cazon⁶⁵, R. Cester⁴⁶, A.G. Chavez⁵⁷, A. Chiavassa⁵², J.A. Chinellato¹⁷, J. Chudoba²⁶, M. Cilmo⁴³, R.W. Clay¹², G. Cocciole⁴⁷, R. Colalillo⁴³, A. Coleman⁸⁸, L. Collica⁴², M.R. Coluccia⁴⁷, R. Conceição⁶⁵, F. Contreras⁹, M.J. Cooper¹², A. Cordier²⁹, S. Coutu⁸⁸, C.E. Covault⁷⁷, J. Cronin⁸⁹, R. Dallier^{33,32}, B. Daniel¹⁷, S. Dasso^{5,3}, K. Daumiller³⁶, B.R. Dawson¹², R.M. de Almeida²³, S.J. de Jong^{59,61}, G. De Mauro⁵⁹, J.R.T. de Mello Neto²², I. De Miti⁴⁷, J. de Oliveira²³, V. de Souza¹⁵, L. del Peral⁷³, O. Deligny²⁸, H. Dembinski³⁶, N. Dhital⁸⁴, C. Di Giulio⁴⁴, A. Di Matteo⁴⁸, J.C. Diaz⁸⁴, M.L. Díaz Castro¹⁷, F. Diogo⁶⁵, C. Dobrigkeit¹⁷, W. Docters⁶⁰, J.C. D'Olivo⁵⁸, A. Dorofeev⁷⁹, Q. Dorosti Hasankiadeh³⁶, M.T. Dova⁴, J. Ebr²⁶, R. Engel³⁶, M. Erdmann³⁹, M. Erfani⁴¹, C.O. Escobar^{82,17}, J. Espadanal⁶⁵, A. Etchegoyen^{8,11}, H. Falcke^{59,62,61}, K. Fang⁸⁹, G. Farrar⁸⁵, A.C. Fauth¹⁷, N. Fazzini⁸², A.P. Ferguson⁷⁷, M. Fernandes²², B. Fick⁸⁴, J.M. Figueira⁸, A. Filevich⁸, A. Filipčič^{70,71}, B.D. Fox⁹⁰, O. Fratu⁶⁹, M.M. Freire⁶, B. Fuchs³⁵, T. Fujii⁸⁹, B. García⁷, D. Garcia-Pinto⁷², F. Gate³³, H. Gemmeke³⁷, A. Gherghel-Lascu⁶⁶, P.L. Ghia³⁰, U. Giaccari²², M. Giannarchi⁴², M. Giller⁶⁴, D. Glas⁶⁴, C. Glaser³⁹, H. Glass⁸², G. Golup¹, M. Gómez Berisso¹, P.F. Gómez Vitale¹⁰, N. González⁸, B. Gookin⁷⁹, J. Gordon⁸⁷, A. Gorgi⁵², P. Gorham⁹⁰, P. Gouffon¹⁶, N. Griffith⁸⁷, A.F. Grillo⁵¹, T.D. Grubb¹², F. Guarino⁴³, G.P. Guedes¹⁸, M.R. Hampel⁸, P. Hansen⁴, D. Harari¹, T.A. Harrison¹², S. Hartmann³⁹, J.L. Harton⁷⁹, A. Haungs³⁶, T. Hebbeker³⁹, D. Heck³⁶, P. Heimann⁴¹, N. Hemery³⁶, A.E. Herve³⁶, G.C. Hill¹², C. Hojvat⁸², N. Hollon⁸⁹, E. Holt³⁶, P. Homola³⁴, J.R. Hörandel^{59,61}, P. Horvath²⁷, M. Hrabovsky^{27,26}, D. Huber³⁵, T. Huege³⁶, A. Insolia⁴⁵, P.G. Isar⁶⁷, I. Jandt³⁴, S. Jansen^{59,61}, C. Jarne⁴, J.A. Johnsen⁷⁸, M. Josebachuili⁸, A. Kääpä³⁴, O. Kambeitz³⁵, K.H. Kampert³⁴, P. Kasper⁸², I. Katkov³⁵, B. Kégl²⁹, B. Keilhauer³⁶, A. Keivani⁸⁸, E. Kemp¹⁷, R.M. Kieckhafer⁸⁴, H.O. Klages³⁶, M. Kleifges³⁷, J. Kleinfeller⁹, R. Krause³⁹, N. Krohm³⁴, O. Krömer³⁷, D. Kuempel³⁹, G. Kukuc Mezek⁷¹, N. Kunka³⁷, D. LaHurd⁷⁷, L. Latronico⁵², R. Lauer⁹², M. Lauscher³⁹, P. Lautridou³³, S. Le Coz³¹, D. Lebrun³¹, P. Lebrun⁸², M.A. Leogui de Oliveira²¹, A. Letessier-Selvon³⁰, I. Lhenry-Yvon²⁸, K. Link³⁵, L. Lopes⁶⁵, R. López⁵³, A. López Casado⁷⁵, K. Louedec³¹, L. Lu^{34,9999}, A. Lucero⁸, M. Malacari¹², S. Maldera⁵², M. Mallamaci⁴², J. Maller³³, D. Mandat²⁶, P. Mantsch⁸², A.G. Mariazzi⁴, V. Marin³³, I.C. Maris⁷⁴, G. Marsella⁴⁷, D. Martello⁴⁷, L. Martin^{33,32}, H. Martinez⁵⁴, O. Martínez Bravo⁵³, D. Martraire²⁸, J.J. Masías Meza³, H.J. Mathes³⁶, S. Mathys³⁴, J. Matthews⁸³, J.A.J. Matthews⁹², G. Matthiae⁴⁴, D. Maurizio¹³, E. Mayotte⁷⁸, P.O. Mazur⁸², C. Medina⁷⁸, G. Medina-Tanco⁵⁸, R. Meissner³⁹, V.B.B. Mello²², D. Melo⁸, A. Menshikov³⁷, S. Messina⁶⁰, R. Meyhandan⁹⁰, M.I. Micheletti⁶, L. Middendorf³⁹, I.A. Minaya⁷², L. Miramonti⁴², B. Mitrica⁶⁶, L. Molina-Bueno⁷⁴, S. Mollerach¹, F. Montanet³¹, C. Morello⁵², M. Mostafá⁸⁸, C.A. Moura²¹, M.A. Muller^{17,20}, G. Müller³⁹, S. Müller³⁶, R. Mussa⁴⁶, G. Navarra^{52 ‡}, S. Navas⁷⁴, P. Necesal²⁶, L. Nellen⁵⁸, A. Nelles^{59,61}, J. Neuser³⁴, P.H. Nguyen¹², M. Niculescu-Oglizanu⁶⁶, M. Niechciol⁴¹, L. Niemietz³⁴, T. Niggemann³⁹, D. Nitz⁸⁴, D. Nosek²⁵, V. Novotny²⁵, L. Nožka²⁷, L. Ochilo⁴¹, F. Oikonomou⁸⁸, A. Olinto⁸⁹, N. Pacheco⁷³, D. Pakk Selmi-Dei¹⁷, M. Palatka²⁶, J. Pallotta², P. Papenbreer³⁴, G. Parente⁷⁵,

A. Parra⁵³, T. Paul^{81,86}, M. Pech²⁶, J. Pěkala⁶³, R. Pelayo⁵⁵, I.M. Pepe¹⁹, L. Perrone⁴⁷, E. Petermann⁹¹, C. Peters³⁹, S. Petrera^{48,49}, Y. Petrov⁷⁹, J. Phuntsok⁸⁸, R. Piegaia³, T. Pierog³⁶, P. Pieroni³, M. Pimenta⁶⁵, V. Pirronello⁴⁵, M. Platino⁸, M. Plum³⁹, A. Porcelli³⁶, C. Porowski⁶³, R.R. Prado¹⁵, P. Privitera⁸⁹, M. Prouza²⁶, V. Purrello¹, E.J. Quel², S. Querchfeld³⁴, S. Quinn⁷⁷, J. Rautenberg³⁴, O. Ravel³³, D. Ravignani⁸, D. Reinert³⁹, B. Revenu³³, J. Ridky²⁶, S. Riggi⁴⁵, M. Risso⁴¹, P. Ristori², V. Rizi⁴⁸, W. Rodrigues de Carvalho⁷⁵, G. Rodriguez Fernandez⁴⁴, J. Rodriguez Rojo⁹, M.D. Rodríguez-Frías⁷³, D. Rogozin³⁶, J. Rosado⁷², M. Roth³⁶, E. Roulet¹, A.C. Rovero⁵, S.J. Saffi¹², A. Saftoiu⁶⁶, F. Salamida²⁸, H. Salazar⁵³, A. Saleh⁷¹, F. Salesa Greus⁸⁸, G. Salina⁴⁴, F. Sánchez⁸, P. Sanchez-Lucas⁷⁴, E. Santos¹⁷, E.M. Santos¹⁶, F. Sarazin⁷⁸, B. Sarkar³⁴, R. Sarmento⁶⁵, R. Sato⁹, C. Scarso⁹, M. Schauer³⁴, V. Scherini⁴⁷, H. Schieler³⁶, D. Schmidt³⁶, O. Scholten⁶⁰^a, H. Schoorlemmer⁹⁰, P. Schovánek²⁶, F.G. Schröder³⁶, A. Schulz³⁶, J. Schulz⁵⁹, J. Schumacher³⁹, S.J. Sciutto⁴, A. Segreto⁵⁰, M. Settimo³⁰, A. Shadkam⁸³, R.C. Shellard¹³, I. Sidelnik¹, G. Sigl⁴⁰, O. Sima⁶⁸, A. Śmiałkowski⁶⁴, R. Šmídá³⁶, G.R. Snow⁹¹, P. Sommers⁸⁸, J. Sorokin¹², R. Squartini⁹, Y.N. Srivastava⁸⁶, D. Stanca⁶⁶, S. Stanič⁷¹, J. Stapleton⁸⁷, J. Stasielak⁶³, M. Stephan³⁹, A. Stutz³¹, F. Suarez^{8,11}, T. Suomijärvi²⁸, A.D. Supanitsky⁵, M.S. Sutherland⁸⁷, J. Swain⁸⁶, Z. Szadkowski⁶⁴, O.A. Taborda¹, A. Tapia⁸, A. Tepe⁴¹, V.M. Theodoro¹⁷, C. Timmermans^{61,59}, C.J. Todero Peixoto¹⁴, G. Toma⁶⁶, L. Tomankova³⁶, B. Tomé⁶⁵, A. Tonachini⁴⁶, G. Torralba Elipe⁷⁵, D. Torres Machado²², P. Travnick²⁶, M. Trini⁷¹, R. Ulrich³⁶, M. Unger⁸⁵, M. Urban³⁹, J.F. Valdés Galicia⁵⁸, I. Valiño⁷⁵, L. Valore⁴³, G. van Aar⁵⁹, P. van Bodegom¹², A.M. van den Berg⁶⁰, S. van Velzen⁵⁹, A. van Vliet⁴⁰, E. Varela⁵³, B. Vargas Cárdenas⁵⁸, G. Varner⁹⁰, R. Vasquez²², J.R. Vázquez⁷², R.A. Vázquez⁷⁵, D. Veverič³⁶, V. Verzi⁴⁴, J. Vicha²⁶, M. Videla⁸, L. Villaseñor⁵⁷, B. Vlcek⁷³, S. Vorobiov⁷¹, H. Wahlberg⁴, O. Wainberg^{8,11}, D. Walz³⁹, A.A. Watson⁹⁹⁹⁹, M. Weber³⁷, K. Weidenhaupt³⁹, A. Weindl³⁶, F. Werner³⁵, A. Widom⁸⁶, L. Wiencke⁷⁸, H. Wilczyński⁶³, T. Winchen³⁴, D. Wittkowski³⁴, B. Wundheiler⁸, S. Wykes⁵⁹, L. Yang⁷¹, T. Yapici⁸⁴, A. Yushkov⁴¹, E. Zas⁷⁵, D. Zavrtanik^{71,70}, M. Zavrtanik^{70,71}, A. Zepeda⁵⁴, Y. Zhu³⁷, B. Zimmermann³⁷, M. Ziolkowski⁴¹, Z. Zong²⁸, F. Zuccarello⁴⁵

¹ Centro Atómico Bariloche and Instituto Balseiro (CNEA-UNCuyo-CONICET), San Carlos de Bariloche, Argentina

² Centro de Investigaciones en Láseres y Aplicaciones, CITEDEF and CONICET, Argentina

³ Departamento de Física, FCEyN, Universidad de Buenos Aires and CONICET, Argentina

⁴ IFLP, Universidad Nacional de La Plata and CONICET, La Plata, Argentina

⁵ Instituto de Astronomía y Física del Espacio (IAFE, CONICET-UBA), Buenos Aires, Argentina

⁶ Instituto de Física de Rosario (IFIR) - CONICET/U.N.R. and Facultad de Ciencias Bioquímicas y Farmacéuticas U.N.R., Rosario, Argentina

⁷ Instituto de Tecnologías en Detección y Astropartículas (CNEA, CONICET, UNSAM), and Universidad Tecnológica Nacional - Facultad Regional Mendoza (CONICET/CNEA), Mendoza, Argentina

⁸ Instituto de Tecnologías en Detección y Astropartículas (CNEA, CONICET, UNSAM), Buenos Aires, Argentina

⁹ Observatorio Pierre Auger, Malargüe, Argentina

¹⁰ Observatorio Pierre Auger and Comisión Nacional de Energía Atómica, Malargüe, Argentina

¹¹ Universidad Tecnológica Nacional - Facultad Regional Buenos Aires, Buenos Aires, Argentina

¹² University of Adelaide, Adelaide, S.A., Australia

¹³ Centro Brasileiro de Pesquisas Fisicas, Rio de Janeiro, RJ, Brazil

- ¹⁴ Universidade de São Paulo, Escola de Engenharia de Lorena, Lorena, SP, Brazil
¹⁵ Universidade de São Paulo, Instituto de Física de São Carlos, São Carlos, SP, Brazil
¹⁶ Universidade de São Paulo, Instituto de Física, São Paulo, SP, Brazil
¹⁷ Universidade Estadual de Campinas, IFGW, Campinas, SP, Brazil
¹⁸ Universidade Estadual de Feira de Santana, Brazil
¹⁹ Universidade Federal da Bahia, Salvador, BA, Brazil
²⁰ Universidade Federal de Pelotas, Pelotas, RS, Brazil
²¹ Universidade Federal do ABC, Santo André, SP, Brazil
²² Universidade Federal do Rio de Janeiro, Instituto de Física, Rio de Janeiro, RJ, Brazil
²³ Universidade Federal Fluminense, EEIMVR, Volta Redonda, RJ, Brazil
²⁴ Universidad Industrial de Santander, Bucaramanga, Colombia
²⁵ Charles University, Faculty of Mathematics and Physics, Institute of Particle and Nuclear Physics, Prague, Czech Republic
²⁶ Institute of Physics of the Academy of Sciences of the Czech Republic, Prague, Czech Republic
²⁷ Palacky University, RCPTM, Olomouc, Czech Republic
²⁸ Institut de Physique Nucléaire d'Orsay (IPNO), Université Paris 11, CNRS-IN2P3, Orsay, France
²⁹ Laboratoire de l'Accélérateur Linéaire (LAL), Université Paris 11, CNRS-IN2P3, France
³⁰ Laboratoire de Physique Nucléaire et de Hautes Energies (LPNHE), Universités Paris 6 et Paris 7, CNRS-IN2P3, Paris, France
³¹ Laboratoire de Physique Subatomique et de Cosmologie (LPSC), Université Grenoble-Alpes, CNRS/IN2P3, France
³² Station de Radioastronomie de Nançay, Observatoire de Paris, CNRS/INSU, France
³³ SUBATECH, École des Mines de Nantes, CNRS-IN2P3, Université de Nantes, France
³⁴ Bergische Universität Wuppertal, Department of Physics, Wuppertal, Germany
³⁵ Karlsruhe Institute of Technology - Campus South - Institut für Experimentelle Kernphysik (IEKP), Karlsruhe, Germany
³⁶ Karlsruhe Institute of Technology - Campus North - Institut für Kernphysik, Karlsruhe, Germany
³⁷ Karlsruhe Institute of Technology - Campus North - Institut für Prozessdatenverarbeitung und Elektronik, Karlsruhe, Germany
³⁸ Max-Planck-Institut für Radioastronomie, Bonn, Germany
³⁹ RWTH Aachen University, III. Physikalisches Institut A, Aachen, Germany
⁴⁰ Universität Hamburg, Hamburg, Germany
⁴¹ Universität Siegen, Siegen, Germany
⁴² Università di Milano and Sezione INFN, Milan, Italy
⁴³ Università di Napoli "Federico II" and Sezione INFN, Napoli, Italy
⁴⁴ Università di Roma II "Tor Vergata" and Sezione INFN, Roma, Italy
⁴⁵ Università di Catania and Sezione INFN, Catania, Italy
⁴⁶ Università di Torino and Sezione INFN, Torino, Italy
⁴⁷ Dipartimento di Matematica e Fisica "E. De Giorgi" dell'Università del Salento and Sezione INFN, Lecce, Italy
⁴⁸ Dipartimento di Scienze Fisiche e Chimiche dell'Università dell'Aquila and INFN, Italy
⁴⁹ Gran Sasso Science Institute (INFN), L'Aquila, Italy
⁵⁰ Istituto di Astrofisica Spaziale e Fisica Cosmica di Palermo (INAF), Palermo, Italy
⁵¹ INFN, Laboratori Nazionali del Gran Sasso, Assergi (L'Aquila), Italy

- ⁵² Osservatorio Astrofisico di Torino (INAF), Università di Torino and Sezione INFN, Torino, Italy
- ⁵³ Benemérita Universidad Autónoma de Puebla, Puebla, México
- ⁵⁴ Centro de Investigación y de Estudios Avanzados del IPN (CINVESTAV), México, México
- ⁵⁵ Unidad Profesional Interdisciplinaria en Ingeniería y Tecnologías Avanzadas del Instituto Politécnico Nacional (UPIITA-IPN), México, D.F., México
- ⁵⁶ Universidad Autónoma de Chiapas, Tuxtla Gutiérrez, Chiapas, México
- ⁵⁷ Universidad Michoacana de San Nicolás de Hidalgo, Morelia, Michoacán, México
- ⁵⁸ Universidad Nacional Autónoma de México, México, D.F., México
- ⁵⁹ IMAPP, Radboud University Nijmegen, Netherlands
- ⁶⁰ KVI - Center for Advanced Radiation Technology, University of Groningen, Netherlands
- ⁶¹ Nikhef, Science Park, Amsterdam, Netherlands
- ⁶² ASTRON, Dwingeloo, Netherlands
- ⁶³ Institute of Nuclear Physics PAN, Krakow, Poland
- ⁶⁴ University of Łódź, Łódź, Poland
- ⁶⁵ Laboratório de Instrumentação e Física Experimental de Partículas - LIP and Instituto Superior Técnico - IST, Universidade de Lisboa - UL, Portugal
- ⁶⁶ 'Horia Hulubei' National Institute for Physics and Nuclear Engineering, Bucharest- Magurele, Romania
- ⁶⁷ Institute of Space Sciences, Bucharest, Romania
- ⁶⁸ University of Bucharest, Physics Department, Romania
- ⁶⁹ University Politehnica of Bucharest, Romania
- ⁷⁰ Experimental Particle Physics Department, J. Stefan Institute, Ljubljana, Slovenia
- ⁷¹ Laboratory for Astroparticle Physics, University of Nova Gorica, Slovenia
- ⁷² Universidad Complutense de Madrid, Madrid, Spain
- ⁷³ Universidad de Alcalá, Alcalá de Henares, Madrid, Spain
- ⁷⁴ Universidad de Granada and C.A.F.P.E., Granada, Spain
- ⁷⁵ Universidad de Santiago de Compostela, Spain
- ⁷⁷ Case Western Reserve University, Cleveland, OH, USA
- ⁷⁸ Colorado School of Mines, Golden, CO, USA
- ⁷⁹ Colorado State University, Fort Collins, CO, USA
- ⁸⁰ Colorado State University, Pueblo, CO, USA
- ⁸¹ Department of Physics and Astronomy, Lehman College, City University of New York, NY, USA
- ⁸² Fermilab, Batavia, IL, USA
- ⁸³ Louisiana State University, Baton Rouge, LA, USA
- ⁸⁴ Michigan Technological University, Houghton, MI, USA
- ⁸⁵ New York University, New York, NY, USA
- ⁸⁶ Northeastern University, Boston, MA, USA
- ⁸⁷ Ohio State University, Columbus, OH, USA
- ⁸⁸ Pennsylvania State University, University Park, PA, USA
- ⁸⁹ University of Chicago, Enrico Fermi Institute, Chicago, IL, USA
- ⁹⁰ University of Hawaii, Honolulu, HI, USA
- ⁹¹ University of Nebraska, Lincoln, NE, USA
- ⁹² University of New Mexico, Albuquerque, NM, USA

(‡) Deceased

(a) Also at Vrije Universiteit Brussels, Belgium

Foreword

The Pierre Auger Observatory has begun a major Upgrade of its already impressive capabilities, with an emphasis on improved mass composition determination using the surface detectors of the Observatory. Known as AugerPrime, the upgrade will include new 4 m^2 plastic scintillator detectors on top of all 1660 water-Cherenkov detectors, updated and more flexible surface detector electronics, a large array of buried muon detectors, and an extended duty cycle for operations of the fluorescence detectors.

This Preliminary Design Report was produced by the Collaboration in April 2015 as an internal document and information for funding agencies. It outlines the scientific and technical case for AugerPrime¹. We now release it to the public via the arXiv server. We invite you to review the large number of fundamental results already achieved by the Observatory and our plans for the future.

The Pierre Auger Collaboration

¹As a result of continuing R&D, slight changes have been implemented in the baseline design since this Report was written. These changes will be documented in a forthcoming Technical Design Report.

Executive Summary

Present Results from the Pierre Auger Observatory

Measurements of the Auger Observatory have dramatically advanced our understanding of ultra-high energy cosmic rays. The suppression of the flux around 5×10^{19} eV is now confirmed without any doubt. Strong limits have been placed on the photon and neutrino components of the flux indicating that “top-down” source processes, such as the decay of super-heavy particles, cannot account for a significant part of the observed particle flux. A large-scale dipole anisotropy of $\sim 7\%$ amplitude has been found for energies above 8×10^{18} eV. In addition there is also an indication of the presence of a large scale anisotropy below the ankle. Particularly exciting is the observed behavior of the depth of shower maximum with energy, which changes in an unexpected, non-trivial way. Around 3×10^{18} eV it shows a distinct change of slope with energy, and the shower-to-shower variance decreases. Interpreted with the leading LHC-tuned shower models, this implies a gradual shift to a heavier composition. A number of fundamentally different astrophysical model scenarios have been developed to describe this evolution. The high degree of isotropy observed in numerous tests of the small-scale angular distribution of UHECR above 4×10^{19} eV is remarkable, challenging original expectations that assumed only a few cosmic ray sources with a light composition at the highest energies. Interestingly, the largest departures from isotropy are observed for cosmic rays with $E > 5.8 \times 10^{19}$ eV in $\sim 20^\circ$ sky-windows. Due to a duty cycle of $\sim 15\%$ of the fluorescence telescopes, the data on the depth of shower maximum extend only up to the flux suppression region, i.e. 4×10^{19} eV. Obtaining more information on the composition of cosmic rays at higher energies will provide crucial means to discriminate between the model classes and to understand the origin of the observed flux suppression. Care must be taken, since precision Auger measurements of shower properties, strongly constrained by the hybrid data, have revealed inconsistencies within present shower models, opening the possibility that the unexpected behavior is due to new hadronic interaction physics at energy scales beyond the reach of the LHC.

Motivation for the upgrade

It is planned to operate the Pierre Auger Observatory until the end of 2024. The motivation of the upgrade is to provide additional measurements to allow us to address the following important questions:

- Elucidate the mass composition and the origin of the flux suppression at the highest energies, i.e. the differentiation between the energy loss effects due to propagation, and the maximum energy of particles injected by astrophysical sources.

- Search for a flux contribution of protons up to the highest energies. We aim to reach a sensitivity to a contribution as small as 10% in the flux suppression region. The measurement of the fraction of protons is the decisive ingredient for estimating the physics potential of existing and future cosmic ray, neutrino, and gamma-ray detectors; thus prospects for proton astronomy with future detectors will be clarified. Moreover, the flux of secondary gamma-rays and neutrinos due to proton energy loss processes will be predicted.
- Study extensive air showers and hadronic multiparticle production. This will include the exploration of fundamental particle physics at energies beyond those accessible at man-made accelerators, and the derivation of constraints on new physics phenomena, such as Lorentz invariance violation or extra dimensions.

With operation planned until 2024, event statistics will more than double compared with the existing Auger data set, with the critical added advantage that every event will now have mass information. Obtaining additional composition-sensitive information will not only help to better reconstruct the properties of the primary particles at the highest energies, but also improve the measurements in the important energy range just above the ankle. Furthermore, measurements with the new detectors will help to reduce systematic uncertainties related to modeling hadronic showers and to limitations of reconstruction algorithms. This improved knowledge of air shower physics will likely then also allow a re-analysis of existing data - for improved energy assignments, for mass composition studies, and for photon and neutrino searches.

The Auger upgrade promises high-quality future data, and real scope for new physics uses of existing events. Furthermore, the addition of scintillator detectors across the entire Observatory will also make possible direct comparisons of Auger measurements with those of the surface detectors of the Telescope Array experiment. This will strengthen the already productive cooperation between the two collaborations, which has an aim of understanding the highest energy cosmic ray flux across the entire sky.

The configuration of the Auger upgrade

The proposed Auger upgrade consists of the following components:

- A complementary measurement of the shower particles will be provided by a plastic scintillator plane above the existing Water-Cherenkov Detectors (WCD). This allows the sampling of the shower particles with two detectors having different responses to muons and electromagnetic particles. The design of the Surface Scintillator Detectors (SSD) is simple, reliable and they can be easily deployed over the full 3000 km² area of the Surface Detector.
- The surface detector stations will be upgraded with new electronics that will process both WCD and SSD signals. Use of the new electronics also aims to increase the data quality (with faster sampling of ADC traces, better timing accuracy, increased dynamic range), to enhance the local trigger and processing capabilities (with a more powerful local station processor and FPGA) and to improve calibration and monitoring capabilities of the surface detector stations. The surface detector electronics upgrade (SDEU) can be easily deployed, and will have only minimal impact on the continuous data taking of the Surface Detector.

- An Underground Muon Detector (UMD) is required in the existing SD infill area of 23.5 km^2 . The UMD will provide important direct measurements of the shower muon content and its time structure, while serving as verification and fine-tuning of the methods used to extract muon information with the SSD and WCD measurements. The performance and characteristics of the AMIGA underground muon detectors, now being deployed, match these requirements, and thus the completed AMIGA array will serve as the UMD.
- In parallel with the Surface Detector upgrade, the operation mode of the Fluorescence Detector (FD) will be changed to extend measurements into periods with higher night sky background. This will allow an increase of about 50% in the current duty cycle of the FD.

The Auger upgrade will not affect the continuous data taking and maintenance of the existing detectors. The current communication system and solar power system for the Surface Detector will remain unchanged. Only minor software changes are required for the central data acquisition system (CDAS) and for the monitoring system.

Organization, cost, and schedule

The Auger Project Management Plan [1] has provided the basis for the detailed organization and management of both the construction and the operation of the Auger Observatory. It has been updated to describe the organizational and management features of the upgrade. In particular, the MOUs with each institution participating in the Auger upgrade will include the commitment of institutional collaborators to the upgrade effort, their deliverables, and delivery schedule.

The Pierre Auger Project has a Quality Assurance Plan [2] to ensure the performance and reliability of the Observatory systems. This plan will be followed to accommodate the specific quality assurance/quality control requirements of the upgrade. The risk management structure will include processes for risk management planning, identification, analysis, monitoring and control.

The cost and schedule estimates for the Auger upgrade are based on the upgrade work breakdown structure (WBS). The total cost with contingency, including infrastructure costs, is currently estimated to be US\$ 15.2 M. The total cost with contingency, but without infrastructure costs (the so-called European accounting) is estimated to be US\$ 12.7 M. AMIGA muon counters will be used for the UMD and the estimated cost for the completion of the AMIGA counters is US\$ 1.6 M without infrastructure costs. The overall increase in operating costs as a result of the upgrade is expected to be less than five percent.

The components of the baseline design have been tested for their suitability for the upgrade. Some specific R&D is still in progress to optimize the quality/cost ratio, in particular for the scintillator detectors and the underground muon detectors. The production of the detectors and electronics boards will be done in parallel at three or four production sites. The final validation of the SSD and SDEU designs will be undertaken in an Engineering Array of 10 detector stations at the end of 2015. The production and deployment of the SSD, the SDEU and the UMD will be done in parallel and will extend over the period 2016-18. The production schedule is mainly driven by the funding profiles in the countries of the collaboration, not by the production or deployment rates.

Contents

1	Introduction	1
2	Scientific Achievements and Goals	3
2.1	Scientific results from the Pierre Auger Observatory	3
2.2	Open questions and goals of upgrading the Observatory	10
2.3	Importance of determining the muonic shower component	16
3	Expected Physics Performance	27
3.1	Introduction	27
3.2	Water Cherenkov Detector global performance parameters	28
3.3	Scintillator Detector performance considerations	31
3.4	Underground Muon Detector performance considerations	35
3.5	Primary Particle Identification with Surface Detector	36
3.6	Fluorescence Detector performance parameters	42
3.7	Benefits of hybrid (multi-detector) measurements	43
3.8	Application to physics goals	44
4	The Surface Detector	53
4.1	The Water Cherenkov Detector	53
4.2	The Scintillator Detector	57
4.3	Surface Detector Electronics	69
4.4	Surface Detector expected performance	75
5	The Underground Muon Detector	81
5.1	Introduction and design objectives	81
5.2	Detector design	81
5.3	Implementation	82
6	Extending the Duty Cycle of Fluorescence Detector Observations	83
6.1	Laboratory test measurements	83
6.2	Test measurement with an FD telescope	84
6.3	Air showers measured during high night sky background	85
6.4	Increase of the duty cycle	87
7	Communication System and Data Acquisition	89
7.1	Communications System	89
7.2	Central Data Acquisition System (CDAS)	94

7.3	Monitoring	95
8	Data Processing and Offline	97
8.1	Physics modules	97
8.2	Data access	99
8.3	Configuration	100
8.4	Utilities, testing and quality control, and build system	100
8.5	Production	101
9	Reception Tests, Deployment and Maintenance	103
9.1	Reception and testing of Scintillator Detectors	103
9.2	Deployment of Scintillator Detectors	104
9.3	Reception and testing of Surface Detector Electronics kits	106
9.4	Deployment of new SDE kits and small PMTs	107
9.5	Reception and testing of Underground Muon Detectors	107
9.6	Deployment of Underground Muon Detectors	108
9.7	Maintenance of Surface Detector System	109
9.8	Maintenance of Underground Muon Detectors	109
9.9	Maintenance of the Upgraded FD	110
10	Upgrade Organization and Management	111
10.1	Introduction	111
10.2	Organization	111
10.3	Management Structure	112
10.4	Upgrade Management	115
10.5	Quality Management	115
10.6	Risk Management	116
11	Cost, Schedule, and Funding	119
11.1	Introduction	119
11.2	Cost estimation	119
11.3	Upgrade Construction Funding	120
11.4	Schedule	120
11.5	Operating Funds	121
12	Outreach and Education	123
13	Acknowledgements	125
A	Work Breakdown Structure (WBS) and Schedule	127
A.1	WBS	127
A.2	Schedule	128
B	The Current Pierre Auger Observatory	131
B.1	Introduction	131
B.2	The Surface Detector	134
B.3	The Fluorescence Detector	138
B.4	Communications System and CDAS	143

B.5	Data processing and <u>Offline</u> Software	148
B.6	Event Reconstruction and Aperture	149
B.7	Enhancements	156
B.8	Performance of the Observatory	161
B.9	Maintenance	166

Chapter 1

Introduction

The Pierre Auger Observatory, located on a vast, high plain near Malargüe in western Argentina, is the world's largest cosmic ray observatory. The objectives of the Observatory are to probe the origin and characteristics of cosmic rays above 10^{17} eV and to study the interactions of them, the most energetic particles observed in nature, with the Earth's atmosphere.

Figure 1.1 shows an overview of the Observatory. It features an array of 1660 water-Cherenkov particle detector stations spread over 3000 km^2 over-looked by 24 air fluorescence telescopes. In addition, three high elevation fluorescence telescopes overlook a 23.5 km^2 , 61 detector array with spacing of 750 m (the Infill).

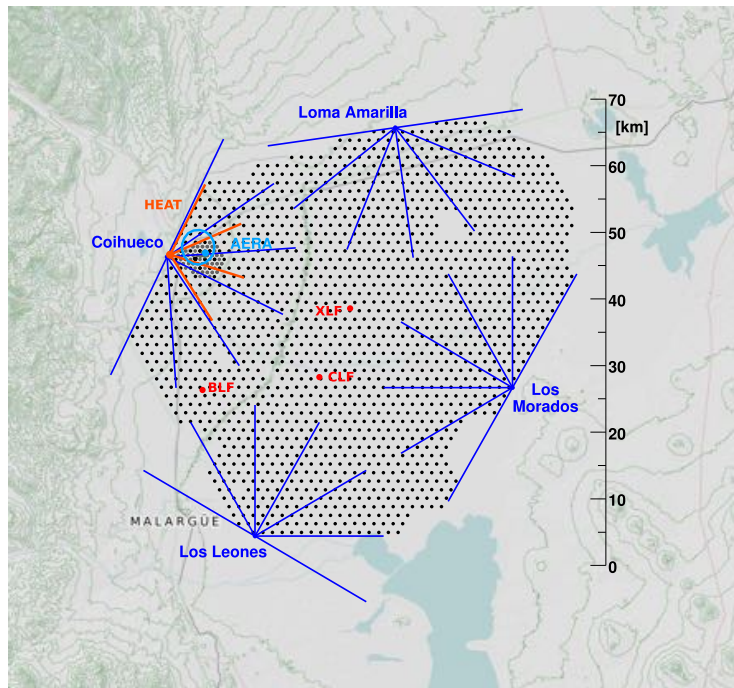


Figure 1.1: The Auger Observatory layout. Each dot corresponds to one of the 1660 surface detector stations. The four fluorescence detector sites are shown, each with the field of view of its six telescopes. The Coihueco site hosts three extra high elevation (HEAT) telescopes. Laser (CLF, XLF) and weather balloon launching (BLF) facilities are also shown. The 750 m array and the AERA radio array are located a few kilometers from Coihueco.

The genesis of the Observatory was a vision of Jim Cronin and Alan Watson in 1991 to build an experiment with sufficient size and precision to answer many of the long-standing questions in this field. A collaboration was built which now amounts to over 500 scientists from 16 countries. Construction of the Observatory began in 2002 after a period of prototyping and a successful engineering array. Construction was completed in 2008, and the integrated exposure of the observatory now exceeds $40,000 \text{ km}^2 \text{ sr yr}$ at energies above $3 \times 10^{18} \text{ eV}$. A thorough description of the Observatory is provided in Appendix B. This description also includes recent enhancements, including high elevation fluorescence telescopes (HEAT), the AMIGA underground muon detectors, and detectors for radio (AERA) and microwave emissions from air showers.

The rich science outcomes from the Auger Observatory up to the present time are described in Chapter 2. This proposal to upgrade the Auger Observatory follows from a decade of discovery and a recognition that shower-by-shower measurements of cosmic ray mass-related properties are essential to further advance the field. The proposed solution is to infer the muon component of the air showers by installing a complementary scintillator detector on top of every water-Cherenkov detector across the array, coupled with upgraded station electronics with enhanced capabilities.

The goals of the upgrade are described below in Chapter 2, before the physics performance of the proposed solution is detailed in Chapter 3. The following chapters describe the design of the new scintillator detectors and electronics, and the underground muon array that will be used to verify the performance of the scintillator and water-Cherenkov detector combination. A description of plans to extend the duty cycle of the fluorescence detector system follows. The impact of the upgrade on key systems of the Observatory, including communications, data acquisition and data processing is described. Finally, we outline plans for deployment and maintenance of the upgrade, and the structures in place to manage its funding and organization.

Chapter 2

Scientific Achievements and Goals

2.1 Scientific results from the Pierre Auger Observatory

The data taken with the Pierre Auger Observatory have led to a number of major breakthroughs in the field of ultra-high energy cosmic rays (UHECRs). Firstly, a suppression of the cosmic ray flux at energies above 4×10^{19} eV has been established unambiguously [3–5]. Secondly, due to the Auger limits on photon [6–9] and neutrino [10–13] fluxes at ultra-high energy, it is now clear that unusual “top-down” source processes such as the decay of super-heavy particles cannot account for a significant part of the observed particle flux. Thirdly, a large-scale $\sim 7\%$ dipole anisotropy is found at energies exceeding the ankle, $E > 8 \times 10^{18}$ eV [14]. At lower energy, however, where the transition from galactic to extragalactic cosmic rays is expected, the dipolar anisotropy of the particle arrival directions is quite small [15–17], which in combination with the light composition at this energy challenges models in which cosmic rays are of Galactic origin up to the ankle. Furthermore, there were indications of an anisotropic distribution of the arrival directions of particles with energies greater than 5.5×10^{19} eV [18–20] but, at the time being, the sensitivity of the Auger Observatory does not allow source correlations to be established [21]. The fourth discovery is that of an unexpected evolution of the mass composition of cosmic rays in the energy range from 10^{18} to $10^{19.5}$ eV. Interpreting the observed longitudinal shower profiles [22] with LHC-tuned interaction models, we can conclude that there is a large fraction of protons present at 10^{18} eV, changing to a heavier composition, possibly dominated by elements of the CNO group, at $10^{19.5}$ eV [23]. In addition, it has been demonstrated that the Auger data can be used for particle physics studies. Examples are the measurement of the proton-air and corresponding proton-proton cross sections at 57 TeV c.m.s. energy [24] and the finding that current air shower simulations fail to describe the relationship between the longitudinal shower profile and the lateral particle densities at ground level [25, 26]. In the following we will briefly review these key observations.

2.1.1 All-particle flux

The all-particle spectrum of the Auger Observatory [27] is shown in Fig. 2.1, and compared with two model calculations. The energy spectrum was obtained by combining the individual energy spectra derived from the array with 1500 m spacing, the smaller array of 750 m station separation, and the hybrid data set. Showers with zenith angles up to 60°

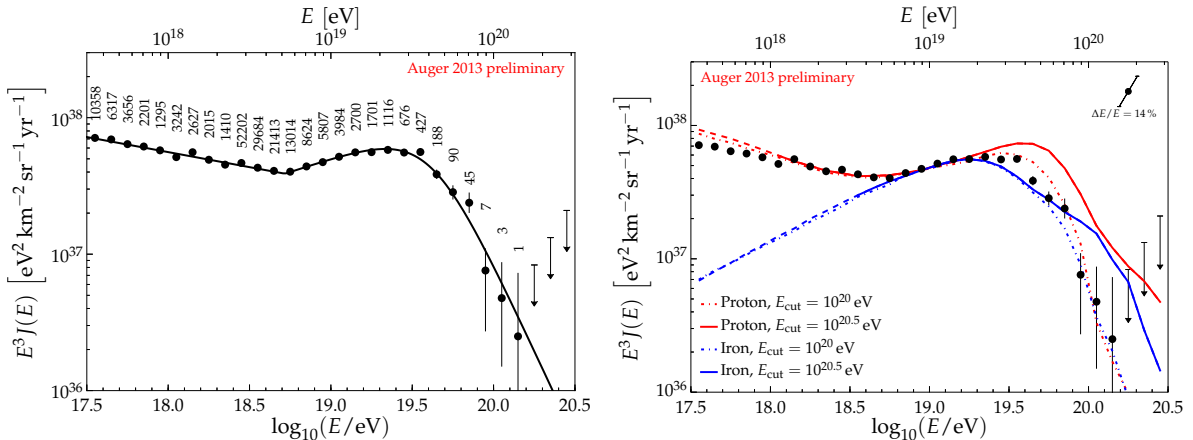


Figure 2.1: All-particle flux measured with the Auger Observatory [27]. Left panel: The Auger data are shown with an empirical fit. In addition the number of events is given for each energy bin. Right panel: The energy spectrum is compared to predictions for the idealized scenario of homogeneously distributed sources injecting either only proton or iron primaries, see text. The model lines have been calculated using CRPropa [28,29] and validated with SimProp [30].

as well as inclined showers ($\theta > 60^\circ$) have been used from the 1500 m array. The statistics at high energy are dominated by the surface detector array, having reached, after quality cuts, an exposure of about $32,000 \text{ km}^2 \text{ sr yr}$ by the end of 2012. The suppression of the flux at high energy is established beyond any doubt. Compared to a power-law extrapolation, the energy at which the flux has dropped to 50% of the value of the extrapolation is $E_{50\%} \approx 10^{19.6} \text{ eV} \approx 4 \times 10^{19} \text{ eV}$. There are 4 events above 10^{20} eV in this spectrum. The low-energy part of the spectrum is driven by data of the later-built 750 m array with an exposure of $80 \text{ km}^2 \text{ sr yr}$ [31]. The energy scale of the spectrum has an overall systematic uncertainty of 14% [32].

For orientation, the data are compared to two model scenarios, namely continuously distributed sources that inject either only proton or iron primaries. The sources are assumed to produce particles with the energy spectrum $dN/dE \propto E^{-\beta}$ and the cosmological evolution of the source luminosity is parameterized as $(1+z)^m$. The model spectra are assumed to be exponentially suppressed with the scale parameter E_{cut} . The proton (iron) lines correspond to $m = 5$ ($m = 0$) and $\beta = 2.35$ ($\beta = 2.3$). In the case of proton primaries, a significantly better description of the data is obtained by choosing $E_{\text{cut}} = 10^{20} \text{ eV}$ rather than a higher value as typically done in literature (see, for example, [33–37]).

The recent, independent measurement of the energy spectrum using inclined showers ($\theta > 60^\circ$) [5] confirms the flux measured with showers up to a zenith angle of 60° . Within the systematic uncertainties, the data of the Auger Observatory are compatible with the measurements of the Telescope Array (TA) [38,39] and HiRes [40]. While the energy of the ankle are within 10% in the TA and Auger data sets, the suppression of the flux is shifted by $\sim 70\%$ to higher energies in the TA spectrum, see Fig. 2.2. Work is in progress to determine to what degree, if any, the observed difference of the spectra measured in the northern and southern hemispheres might be a real astrophysical effect.

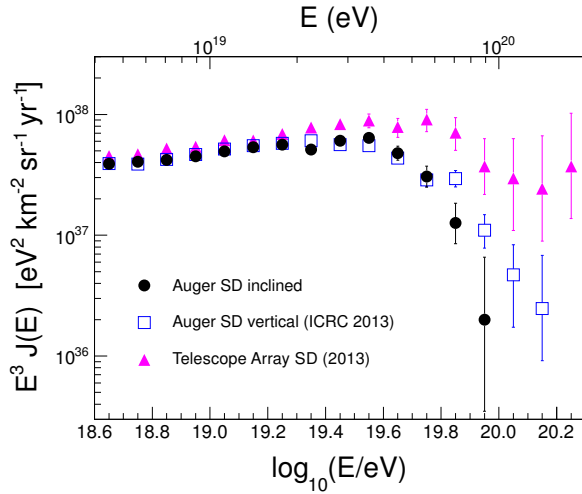


Figure 2.2: Comparison of the two flux measurements of the Auger Collaboration [5, 27] with that of Telescope Array [38]. The differences of the spectra at the highest energies are intriguing but still within the systematic uncertainties of the measurements.

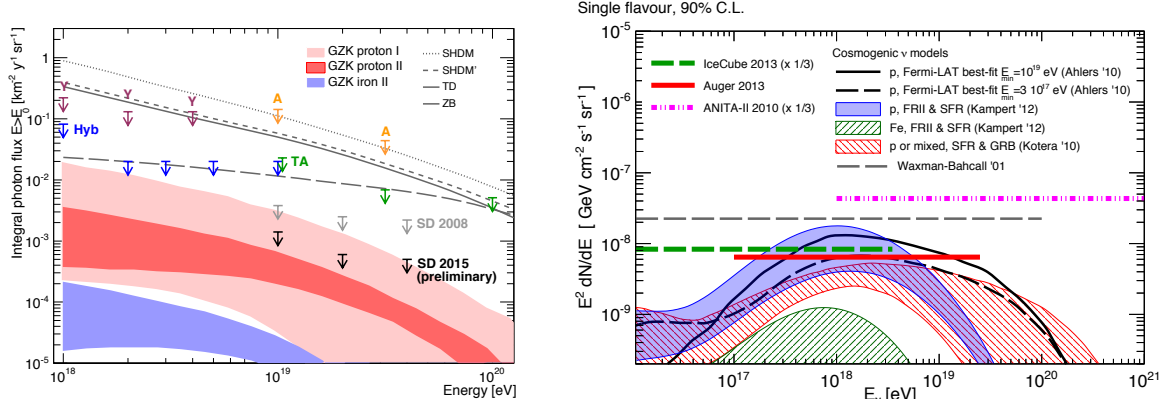


Figure 2.3: Limits on the flux of photons (left) [6–9] and neutrinos (right) [41] obtained from the Pierre Auger Observatory. The data are shown together with the current limits from other experiments [42–48] and some examples of predicted fluxes, see text.

2.1.2 Photon and neutrino limits

The latest limits on the fluxes of photons [6–9] and neutrinos [10, 11, 13, 41] obtained with the Pierre Auger Observatory are shown in Fig. 2.3. Model scenarios for sources of UHE-CRs, in which the observed particles are produced by the decay of other particles (top-down models), lead to large secondary fluxes of photons and neutrinos [49]. In contrast, models in which the production of photons and neutrinos originates from secondaries generated by the propagation in the cosmic background (GZK effect) lead to much lower fluxes. Some representative examples of predicted secondary fluxes of such models are shown in Fig. 2.3 (photons: GZK [50–52], top-down (TD), Z-burst, and super-heavy dark matter (SHDM) [53], SHDM' [54]; neutrinos: TD [55], Z-burst [56]). The neutrino flux limit of the Auger Observatory is now lower than the Waxman-Bahcall flux [57, 58].

The current flux limits rule out, or strongly disfavor, that top-down models can account

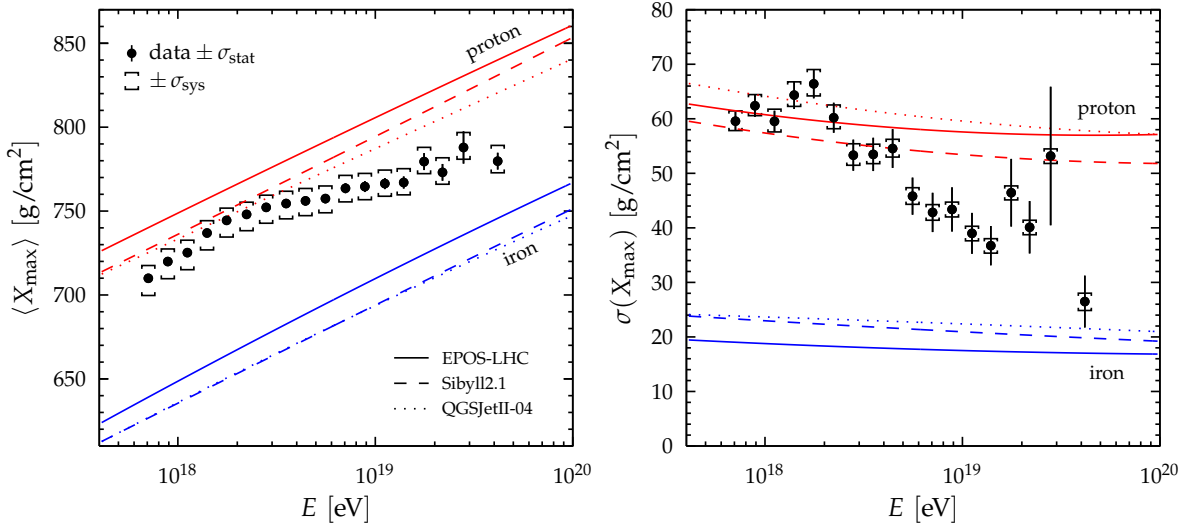


Figure 2.4: Depth of shower maximum, X_{\max} , as measured with the Pierre Auger Observatory [22]. The left panel shows the mean X_{\max} , and the dispersion is given in the right panel after correcting for the reconstruction resolution. The data are compared to model predictions for proton and iron primaries [73–76].

for a significant part of the observed UHECR flux. The bounds are reliable as the photon flux limits in Fig. 2.3 depend only on the simulation of electromagnetic showers and, hence, are very robust against assumptions about hadronic interactions at very high energy [59].

In addition, the flux limits already probe the predicted secondary fluxes for models in which the suppression of the cosmic ray flux is assumed to originate entirely from the GZK energy loss process for a proton dominated flux [50–53].

The photon flux limits have further far-reaching consequences by providing important constraints on theories of quantum gravity involving Lorentz invariance violation (LIV), see, for example, [60–63]. Further, identifying a single photon shower at ultra-high energy would imply very strong limits on another set of parameters of LIV theories [64–66]. Similarly, observing cosmogenic neutrinos would allow placing constraints on LIV in the neutrino sector [67].

2.1.3 Depth of shower maximum

The Pierre Auger Collaboration has addressed the challenge of determining the composition of UHECRs by measuring the depth of shower maximum X_{\max} [22, 23], the muon production depth [68], and rise-time asymmetry of the shower disk at ground level [69]. Out of these observables, the X_{\max} measurement using fluorescence telescopes is currently the one with the smallest systematic uncertainties and the most direct link to the mass distribution of the primary particles [70–72]. The mean depth of shower maximum and the fluctuations measured by the shower-to-shower variation of X_{\max} , which are a superposition of fluctuations of showers of a given primary and differences due to different primary particles, are shown in Fig. 2.4 together with model predictions for proton and iron primaries. The data of the fluorescence telescopes cover energies up to the suppression range with good statistics. The last data point represents all events with $E > 3 \times 10^{19}$ eV.

The comparison of X_{\max} and $\sigma(X_{\max})$ with models, of which EPOS-LHC [77] and QGSJetII-04 [78] have already been tuned to describe the new LHC data [79], shows that the composition appears to be predominantly light from 10^{18} eV up to about 3×10^{18} eV. Above this energy the elongation rate changes, indicating a transition to heavier elements. This interpretation as a change of composition is supported by the change of the variance of X_{\max} in the same energy region. The trend in composition is also confirmed by the other aforementioned composition-sensitive measurements [68, 69]. If interpreted with current interaction models, the size of the fluctuations relative to the mean X_{\max} implies a very small variance in the masses of the primary particles contributing at a given energy [72]. Alternatively, these observations could be interpreted as an unexpected change of the properties of hadronic interactions, most likely involving new particle physics, see [80–82].

A comparison of the Auger data on X_{\max} with that from HiRes [83] and TA [84] is not straightforward as the latter two data sets are not corrected for detector acceptance effects. A joint working group of the Auger and TA collaborations is investigating to what degree the two data sets are compatible [85]. In a recent study published by this working group, the mean X_{\max} of the Auger and TA data has been found to be in good agreement within current statistical and systematic errors [86].

2.1.4 Arrival direction distribution

The arrival direction distribution is one of the key observables to search for the transition from galactic to extragalactic cosmic rays, and for sources or source regions of UHECRs.

Combining the data set of showers with zenith angles up to 60° , which is typically used for anisotropy studies, with that of inclined showers ($60^\circ < \theta < 80^\circ$), a large-scale dipolar anisotropy was found for showers with $E > 8 \times 10^{18}$ eV [14]. An amplitude of the first harmonic in right ascension of $r_{1\alpha} = (4.4 \pm 1.0) \times 10^{-2}$ was measured, having a chance probability of $P(\geq r_{1\alpha}) = 6.4 \times 10^{-5}$. Under the assumption that the only significant contribution to the anisotropy is from the dipolar component, this observation would correspond to a dipole of amplitude $d = 0.073 \pm 0.015$ pointing to $(\alpha, \delta) = (95^\circ \pm 13^\circ, -39^\circ \pm 13^\circ)$. The origin of this anisotropy is subject to ongoing discussions. It could arise, for example, from an inhomogeneity of the distribution of nearby sources, see [87].

The full-acceptance threshold of the 1500 m-array, having the highest exposure of all detectors of the Auger Observatory, is in the energy range of the ankle. Therefore, to search for anisotropies in the energy range of the transition from Galactic to extragalactic cosmic rays, it is crucial to combine this data set with that of the 750 m array [88]. Both the Rayleigh [89] and differential East-West [90] methods have been applied to the Auger data [15]. Updated results for the measured amplitude of the dipole (as well as the corresponding upper limit) and its phase angle are shown in Fig. 2.5 as a function of energy. The phase angle exhibits a smooth change with energy. It points near the Galactic center below 10^{18} eV, suggesting an origin in a galactic component. The phase angle points in the opposite direction at higher energy, possibly manifesting a signature of the inhomogeneous distribution of nearby extragalactic matter. Given that the phase angle is statistically more sensitive than the dipole amplitude [89], a prescribed test to determine the statistical significance of the observed transition in the phase is being performed, and will run until mid-2015.

Up to now it has not been possible to establish small-angle correlations of the arrival direction distribution of Auger data with possible sources or source regions beyond any doubt [21], even though there were some intriguing indications [18–20]. Here we only

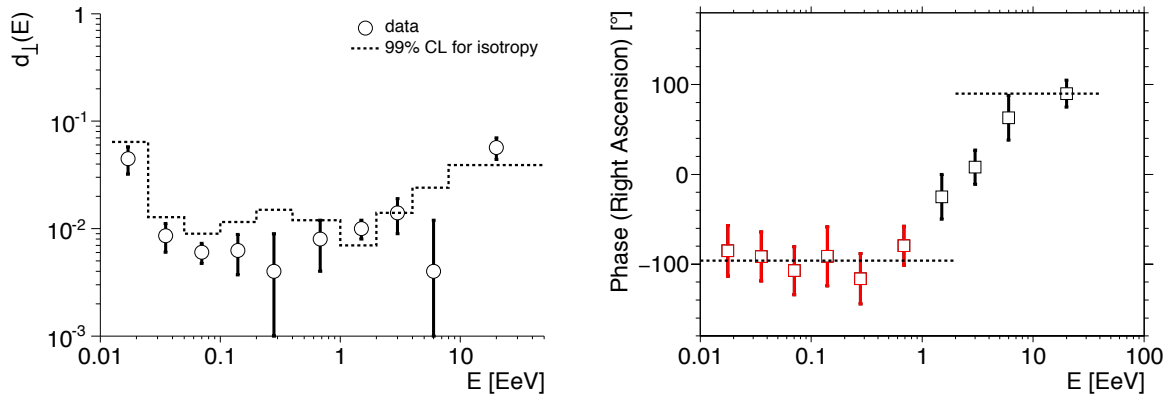


Figure 2.5: Large scale anisotropy search. Left: 99% limits on the dipole anisotropy in the equatorial plane for the collected statistics until end of 2014 (dashed line) and values of the dipole amplitude d_{\perp} . Right: estimated phase angles. The red points of the equatorial phase are from the analysis of the 750 m array. The data shown is an update of the analyses [15, 88], to be published at ICRC 2015.

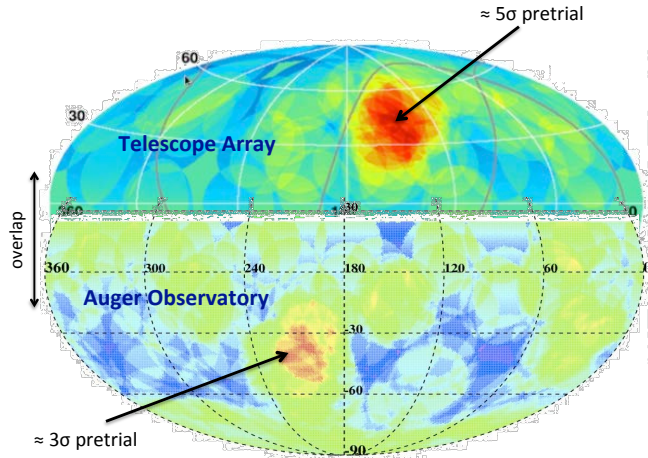


Figure 2.6: Regions of over-density observed after $\sim 20^\circ$ -smearing of the arrival directions of particles with $E > 5.5 \times 10^{19}$ eV. The results from the northern hemisphere are from the TA Collaboration [91].

want to mention the 15° region of over-density observed around the direction of Centaurus A [21]. Although not being a statistically significant excess beyond 3σ , it is interesting to note that the TA Collaboration has recently reported a “hot spot” of similar intermediate angular scale [91], see Fig. 2.6.

2.1.5 Air shower and hadronic interaction physics

The depth of shower maximum is directly related to the depth of the first interaction of the cosmic ray in the atmosphere [92]. Based on this correlation, the proton-air cross section has been measured at 57 TeV c.m.s. energy using hybrid data of the Auger Observatory [24]. Applying the Glauber approximation [93] this cross section can be converted to an equivalent (inelastic) proton-proton cross section, see Fig. 2.7. The cross section is found to be consistent with model extrapolations that describe the LHC data, which were becoming available

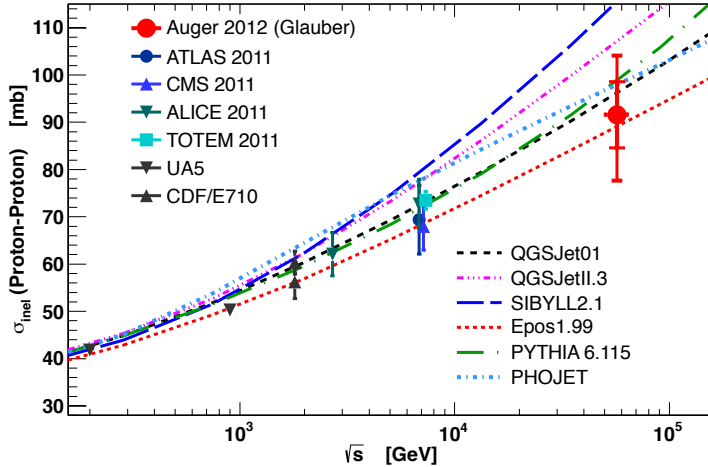


Figure 2.7: Proton-proton cross section derived from the proton-air cross section measured with the Pierre Auger Observatory [24]. The Auger result is shown together with collider measurements and model extrapolations.

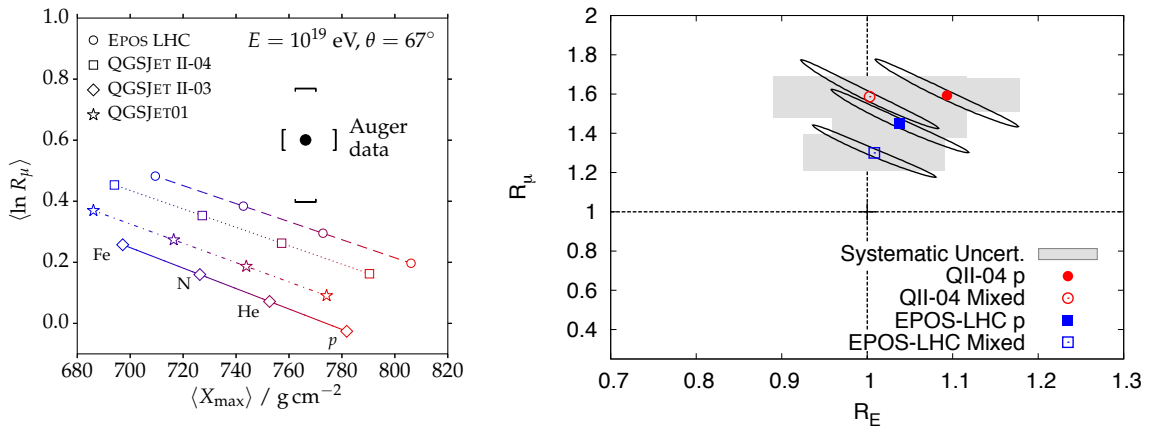


Figure 2.8: Left: Mean number of muons R_μ relative to that of proton reference showers, and depth of shower maximum at 10^{19} eV. The Auger data point [26], where the muon number is derived from inclined showers, is compared with predictions obtained from different interaction models. Right: Muon discrepancy [25] observed in showers of 10^{19} eV. Shown are the phenomenological scaling factors R_E and R_μ for the primary energy and the hadronic (primarily muonic) component of the shower that would be needed to bring a model calculation into agreement with Auger data, see text.

at the same time as the Auger measurement was published. An unexpected, rapid increase of the cross section directly above the LHC energy is not evident.

The muonic component of air showers is sensitive to hadronic particle interactions at all stages in the air shower cascade, and to many properties of hadronic interactions such as the multiplicity, elasticity, fraction of neutral secondary pions, and the baryon-to-pion ratio [71, 94]. Currently the number of muons can only be measured indirectly [95] except at very large lateral distances [68, 96] and in very inclined showers [26, 97], where muons dominate the shower signal at ground level, and for which the electromagnetic component due to muon decay and interaction is understood [98].

Despite these limitations, it was possible to show that current hadronic interaction models do not provide a good description of the number of muons produced in air showers [25, 26]. This is illustrated in Fig. 2.8 (left) where the observed muon number, given relative to proton reference showers, is compared with predictions of commonly used hadronic interaction models. Even though some of these models have been re-tuned recently to provide an improved description of LHC data and fixed-target measurements, none of the models can reproduce the muon number. This conclusion still holds even if different primary mass compositions, as indicated by X_{\max} in the plot, are considered.

Similar results are found in an independent analysis of showers of $\theta < 60^\circ$ measured with the surface array in coincidence with fluorescence light observation, see Fig. 2.8 (right). There the scaling factors needed to obtain a good description of Auger showers of 10^{19} eV are given for air shower simulations made with the models QGSJet II-04 [75] and EPOS-LHC [73, 74], both already tuned to LHC data. Matching the measured longitudinal shower profile with a simulated profile of the same energy, the muon signal has been derived by comparing the surface detector signals of the measured and simulated showers [25].

An observable sensitive to composition and hadronic interactions is the distribution of the production depths of muons [96]. Hadronic interaction models can be tested by comparing the mass estimates derived from the longitudinal shower profiles with that derived from the muon production profiles [68].

Finally it should be mentioned that, although not directly comparable due to the different types of surface detectors, the discrepancy between the fluorescence and surface detector signals of $\sim 27\%$ reported by the TA Collaboration [99] is qualitatively in agreement with the Auger data [100].

2.2 Open questions and goals of upgrading the Observatory

The data of the Pierre Auger Observatory are often considered as providing strong support for classic models of UHECR sources (e.g. [35, 101–104]). In these models it is typically assumed that particle acceleration takes place at sites distributed in a similar way to the matter distribution in the Universe and the effect of energy loss processes [105, 106] (either pion-photoproduction or photo-disintegration) causes the observed flux suppression at energies above 5×10^{19} eV, and some anisotropy of the arrival direction distribution. It is common to these models that particles are injected at extra-galactic sources with an energy spectrum following a power-law $E^{-\beta}$ with $\beta \geq 2$ and a maximum energy exceeding 10^{20} eV. The main differences of the models are related to the assumptions on the index of the power-law and the mass composition at the sources. While almost all models attribute the suppression of the energy spectrum to propagation effects, different interpretations of the origin of the ankle [35, 101–104, 107–109] are considered.

2.2.1 Possible data interpretations and astrophysical scenarios

In the face of these usual assumptions, the measurements of the Pierre Auger Observatory have led to a number of puzzling observations that indicate a much more complex astrophysical scenario, with a phenomenology that is far from being understood. In the following we will discuss some aspects of possible interpretations to illustrate the wealth of information we have collected, but also to point out the lack of some key measurements.

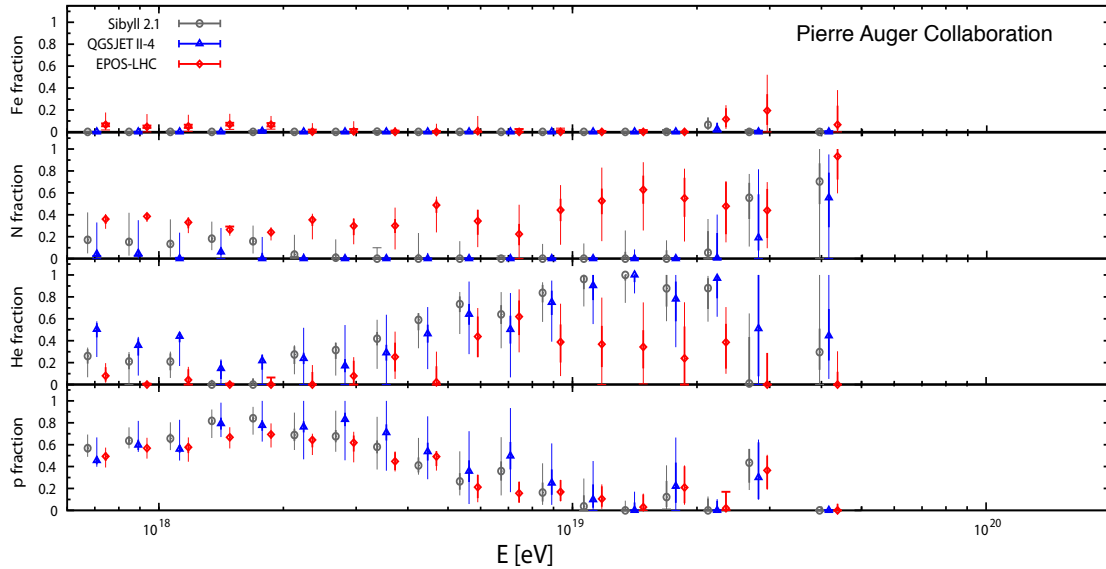


Figure 2.9: Estimate of the composition of ultra-high energy cosmic rays at the top of the atmosphere [23]. The X_{\max} distributions measured with the Auger Observatory have been fitted by a superposition of four mass groups accounting for detector resolution and acceptance effects. The error bars show the combined statistical and systematic uncertainties of the mass estimates, except those related to the choice of the hadronic interaction models.

The X_{\max} distributions measured with the fluorescence telescopes for different energy intervals [22] can be used to estimate the UHECR composition at Earth. This composition will depend on the number of mass groups considered and the hadronic interaction models employed in the simulations. The result of such analysis, fitting four mass groups to the measured X_{\max} distributions [23], is shown in Fig. 2.9. The interaction models EPOS-LHC [73, 74], QGSJet II.04 [75] and Sibyll 2.1 [76] have been used for data interpretation to get some understanding of the systematic uncertainties related to the modeling of hadronic interactions.

One striking result is the presence of a large fraction of protons in the energy range of the ankle. At the same time, according to the Auger data, the anisotropy of the arrival directions of these protons cannot be larger than a few percent. This is in contradiction to the expectations for light particles produced in continuously distributed Galactic sources, given the current knowledge of propagation in the Galactic magnetic field [110, 111]. Thus the protons at energies as low as 10^{18} eV are most likely of extragalactic origin, or one has to accept rather extreme assumptions about the Galactic magnetic field.

Another surprising observation is the disappearance of the proton component just below 10^{19} eV and, at the same time, the appearance of a helium component. There are indications that a similar transition from helium to the nitrogen mass group could take place at higher energy, but the statistics of the data of the fluorescence telescopes are not high enough to be conclusive. Furthermore there is a large correlation between the fractions of the different mass groups. We will not attempt here to speculate on the origin of these transitions and only point out that we do not have enough composition-sensitive data to derive the composition at energies higher than a few times 10^{19} eV, even if we understood hadronic interactions at these energies perfectly.

Finally we want to mention that there are indications for a possible re-appearance of a proton component at high energy that could be related to the possible anisotropy on the 15 degrees scale. With respect to the model scenarios we will discuss below, confirming the existence of a proton population at the highest energies would indicate another class of sources, possibly distributed over cosmological distances. These protons are expected to be correlated in arrival direction with their sources and could open a window to particle astronomy.

A number of authors have used our data on the all-particle spectrum and X_{\max} to develop generic scenarios of UHECR models. We will discuss some of these scenarios here to demonstrate fundamentally different interpretations of the Auger data (see also the recent articles [112–114]). All the models we consider here are, of course, very much simplified representations of the complex physics of UHECR sources and propagation. For example, the inhomogeneous distribution of the sources and the detailed magnetic structure of the Universe is not accounted for, and all sources are assumed to inject similar particle spectra (i.e. mass composition and energy distribution).

Maximum-rigidity scenario If one assumes that the sources accelerate particles to maximum energies proportional to their charge (i.e. to the same maximum rigidity), one obtains a model in which the proton component around $10^{18.5}$ eV is naturally related to similar components of heavier elements, each shifted in energy by the charge number Z . The upper end of the all-particle spectrum would then be dominated by heavy elements of the iron group. The observed suppression of the flux at the highest energies would then be caused by the cutoff of the source spectrum rather than energy loss processes (photo-disintegration) during propagation. In Ref. [107, 115] the mass composition needed to describe both the flux and X_{\max} data of the Auger Observatory is assumed similar to that of Galactic cosmic rays with fluxes having the same spectral index in energy per nucleon, but with a strong enhancement of heavy elements. One key feature of this scenario is that the protons in the energy range of the ankle are injected by the same extragalactic sources that produce the flux at the highest energies.

Photo-disintegration scenario If one assumes that the sources accelerate nuclei to a maximum energy above the energy threshold for photo-disintegration on CMB photons, the light elements could then be fragments of heavier nuclei that disintegrated during propagation. In this scenario (see e.g. [37, 116]) the suppression of the all-particle flux originates mainly from energy loss processes (photo-disintegration of nuclei). Lighter elements appear at energies shifted by the ratio of the daughter to parent mass numbers. Again the protons at the ankle energy are naturally linked to the particles at the highest energy of the spectrum, and are of extragalactic origin. The heaviest elements need to be in the mass range between nitrogen and silicon to describe the Auger data, and it is assumed that almost no light elements are accelerated in the sources.

Neither the maximum-rigidity scenario nor the photo-disintegration scenario provide an explanation of the ankle. An extra component, possibly of galactic origin, is required to generate the ankle in these models.

Proton-dominance model [35, 117] This well-known model, also often referred to as the dip model, provides a natural explanation of the ankle as the imprint of e^+e^- pair production. In

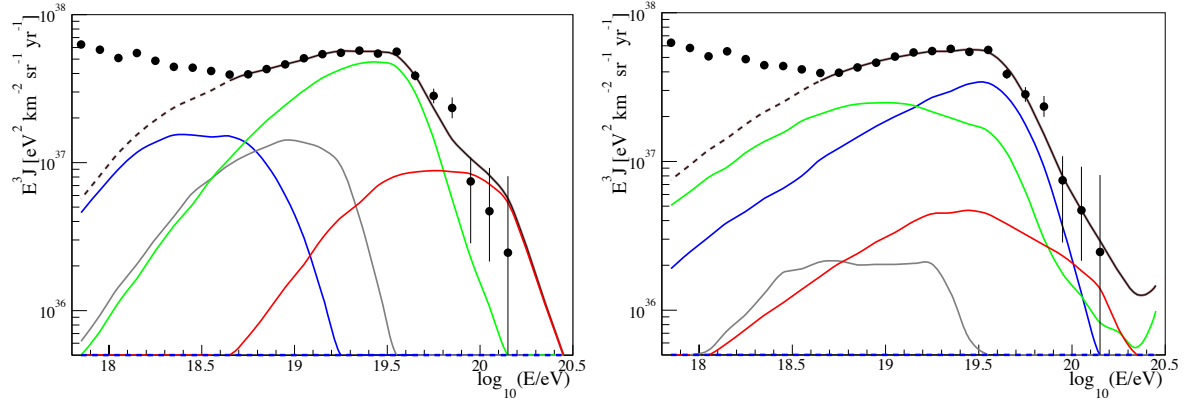


Figure 2.10: Examples of fluxes of different mass groups for describing the Auger spectrum and composition data. Shown are the fluxes of different mass groups that are approximations of one maximum-rigidity scenario (left panel) and one photo-disintegration scenario (right panel). The colors for the different mass groups are protons – blue, helium – gray, nitrogen – green, and iron – red. The model calculations were done with SimProp [30], very similar results are obtained with CRPropa [29].

this model the all-particle flux consists mainly of extragalactic protons at all energies higher than 10^{18} eV. The suppression of the spectrum at the highest energies is attributed solely to pion-photoproduction. Fig. 2.1 (right) shows the best fit of this model to the Auger flux data; it shows that a maximum injection energy much higher than 10^{20} eV is only marginally compatible with the Auger data within the systematic uncertainties. A source cutoff energy just below 10^{20} eV would improve the description of the spectrum data. Such a low source cutoff energy would also imply that part of the observed suppression of the all-particle flux would be related to the details of the upper end of source spectra. And, of course, new particle physics would be needed to describe the X_{\max} data with a proton-dominated flux.

Representative examples of descriptions of the latest Auger flux data within the maximum-rigidity and photo-disintegration models are shown in Fig. 2.10. A numerical fit was made to optimize the description of the all-particle flux and the X_{\max} distributions in the different energy intervals. For sake of simplicity we have assumed homogeneously distributed sources injecting identical power-law spectra of energy-independent mass composition. The index of the injection power law, the maximum energy of the particles injected by the sources, and the source composition were free parameters. Even after accounting for the systematic uncertainties, it is difficult to obtain a satisfactory description of the flux and composition data of the Auger Observatory with these approximations. The best description is obtained for a hard source spectrum $dN/dE \sim E^{-1}$ and a low cutoff energy of $E_{\text{cut}} \sim 10^{18.7}$ eV for protons at the source. The cutoff energies of the other primaries are taken to scale in proportion to their charge. This parameter set corresponds to a good approximation to a “maximum-rigidity scenario.” A somewhat better description of the Auger data, in particular the X_{\max} fluctuations at high energy, can be obtained if an additional light component is assumed to appear in a limited energy range.

The quality of data description is shown in Fig. 2.11 as function of the two-dimensional parameter space of the injection index and maximum proton energy. There is a wide range

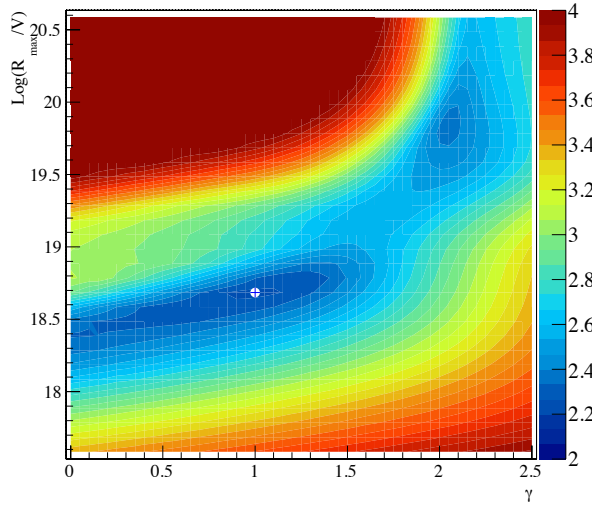


Figure 2.11: Two-dimensional projection of the parameter space illustrating the goodness of data description. The colors denote $\log_{10}(D_{\min})$, where D_{\min} is the minimum log-likelihood and is approximately χ^2 distributed with the number of degrees of freedom 124. The $\log_{10}(D_{\min})$ for a four-component source composition is shown as function of the injection index γ and the maximum rigidity R_{\max} above which an exponential suppression of the source flux is assumed.

of possible parameter combinations, and given the simplifications of the source model, one should not over-interpret the numerical values of the parameters, nor the actual values of the minimum. It is interesting to note that there is a second local minimum, although disfavored in this simple model scenario, which corresponds to an injection index compatible with $dN/dE \sim E^{-2}$, i.e. Fermi acceleration. The second minimum is an example of the “photo-disintegration scenario.”

It should be noted that both the maximum-rigidity and the photo-dissociation scenarios require a composition of the particles injected by the sources that is heavier than the composition of Galactic cosmic rays. While the fraction of heavy elements in the source flux has to be enhanced by a factor of a few in the case of the maximum-rigidity model [104, 115], essentially only nuclei of the nitrogen or silicon groups have to be injected by the sources to describe the Auger data within a photo-disintegration scenario [37, 116]. In other words, the Auger data require a very unusual metallicity of the sources, or a change of the properties of hadronic interactions at the highest energies [118].

We have presented here very different scenarios for interpreting the Auger data. Of course, a steady transition between these models, as well as a superposition of them, is possible. For example, by adjusting the maximum injection energy of the sources, the importance of energy losses during propagation relative to that of the rigidity-dependent cutoff of the source spectra can be changed. In general, it is possible that both the maximum-rigidity effect and the energy loss processes are important for shaping the flux, composition, and arrival direction distribution observed at Earth.

There are many other scenarios which we will not discuss here. These include, for example, models that place transient sources in the Galaxy [119], scenarios in which Galactic and extragalactic neutron stars are the sources [109, 120], or Cen-A [121] (scaling of the max-

imum energy of individual elements proportional to Z), and models of vacuum Cherenkov radiation that lead to a flux scaling which is proportional to the particle velocity and, hence, mass number A [64].

We conclude from these considerations that the origin of the flux suppression observed in the all-particle spectrum is not understood. Furthermore, anisotropy and composition data are compatible with the hypothesis of an additional proton component appearing at very high energy ($E > 4 \times 10^{19}$ eV), but mainly due to the lack of composition data no conclusion can be drawn.

However, it should not be forgotten that the interpretation of the Auger data in terms of composition does rely on the accuracy of modeling air showers and, in particular, hadronic multiparticle production. Therefore all these possible astrophysical interpretations have to be considered in the context of our current understanding of hadronic interactions. It is not excluded that changes of hadronic interaction models within the limitations given by accelerator data can lead to a different interpretation of our composition-sensitive measurements [82, 94, 122]. In addition, it is possible that the overall features of hadronic interactions are significantly different at energies, and in phase space regions, not accessible to current colliders. Such a deviation could be related to new particle physics or just an unreliable extrapolation of existing data.

2.2.2 Goals of the detector upgrade

It is planned to operate the Pierre Auger Observatory until end of 2024. This will triple the statistics of the data set presented in this proposal which contains all data until the end of 2012. However, increasing the statistics of the measured showers will not be sufficient to answer the key questions outlined in the previous section. Therefore, we aim at an upgrade of the Pierre Auger Observatory to ensure that the data collected after 2017 will provide additional information to allow us to address the following questions.

1. The primary objective of the upgrade of the Auger Observatory is to elucidate the mass composition and the origin of the flux suppression at the highest energies, i.e. the differentiation between the energy loss effects due to propagation and the maximum energy of particles injected by astrophysical sources. This is a natural evolution and major step forward from the original objective of the Pierre Auger Observatory, which was motivated primarily by the question of the existence of a GZK-like flux suppression. Understanding the origin of the flux suppression will provide fundamental constraints on the astrophysical sources and will allow much more reliable estimates of neutrino and gamma-ray fluxes at ultra-high energy for which we will continue to search.
2. The search for a flux contribution of protons up to the highest energies will be the second key science objective. We aim to reach a sensitivity to a contribution as small as 10% in the flux suppression region. The measurement of the fraction of protons is the decisive ingredient for estimating the physics potential of existing and future cosmic ray, neutrino, and gamma-ray detectors; prospects for proton astronomy with future detectors will be clarified. Moreover, the flux of secondary gamma-rays and neutrinos due to proton energy loss processes will be predicted.

3. Determining the mass composition of ultra-high energy cosmic rays is closely related to, and crucially depends on, understanding extensive air showers and hadronic interactions. When estimating the number of muons in air showers from Auger data, a discrepancy between the observed and expected muon numbers is found. Therefore, the third key science objective will be the study of extensive air showers and hadronic multiparticle production. This will include the exploration of fundamental particle physics at energies beyond those accessible at man-made accelerators, and the derivation of constraints on new physics phenomena, such as Lorentz invariance violation or extra dimensions [64, 123, 124].

To accomplish these science objectives it will be of central importance to improve the composition sensitivity of the Auger Observatory and to extend it into the energy region of the flux suppression. The most promising way to obtain further composition-sensitive information is the discrimination between the electromagnetic and muonic components of the shower with ground-array measurements.

It is clear that obtaining additional composition-sensitive information will not only help to better reconstruct the properties of the primary particles at the highest energies. Also, measurements in the important energy range just above the ankle will greatly profit from the additional observables. Furthermore, it is expected that the additional composition-sensitive information will help to reduce systematic uncertainties related to modeling hadronic showers and to limitations of reconstruction algorithms.

2.3 Importance of determining the muonic shower component

Optical observations of X_{\max} can presently be performed only with a duty cycle of about 15%. Therefore, the largest boost in performance towards the aforementioned science goals is expected from an improved composition sensitivity of the surface detector array with its 100% duty cycle. Such an improvement can be reached by measuring, in addition to the total particle signal, the decomposition between electromagnetic and muonic components at ground level.

Currently, information on the muonic component of the bulk of air showers is obtained by employing indirect methods which lack the desired precision, and moreover require validation through direct observation. Muons lead to characteristic peaks in the time trace of the water-Cherenkov surface detectors [95], and their number can be estimated for example by subtracting the signal of the electromagnetic shower component obtained from shower universality considerations [125–127] (see also below). Only for sufficiently inclined showers, or at large lateral distance from the shower core, can the muon component be measured directly [26, 68, 96]. A shower-by-shower measurement of the muon component would allow us to

- extend the composition measurement into the flux suppression region to eventually distinguish different model scenarios for understanding the origin of the flux suppression.
- estimate the primary mass and charge on a shower-by-shower basis. This would enable us to select light elements and perform composition-enhanced anisotropy studies. Moreover, back-tracking of particles through the Galactic magnetic field can also be done for particles of different charges in directions of low integrated field strength.

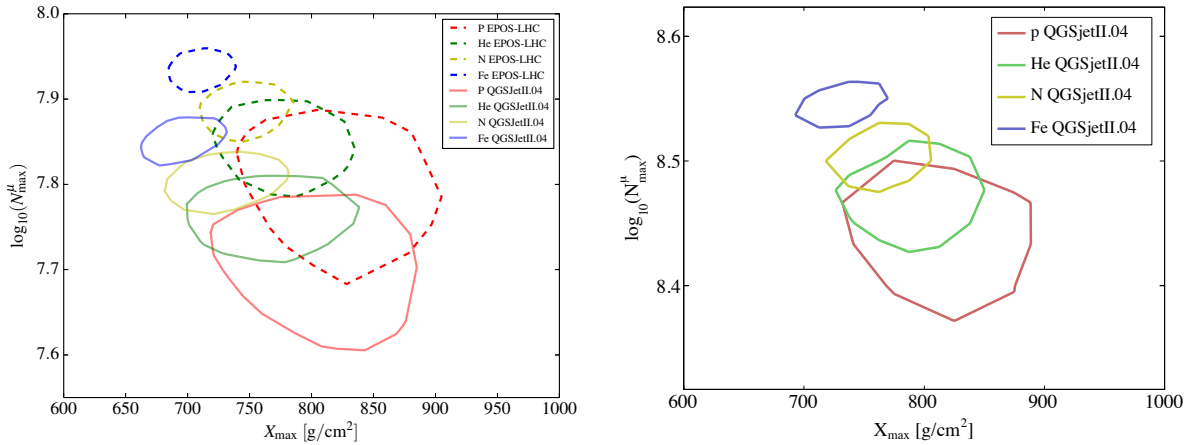


Figure 2.12: The 1σ contour of the number of muons at maximum of the muon shower development, $\log_{10} N_{\max}^\mu$, vs the depth of shower maximum, X_{\max} , for fixed energies, $E = 10^{19}$ eV (left) and $E = 5 \times 10^{19}$ eV (right), and fixed zenith angle, $\theta = 38^\circ$.

- study hadronic interactions at high energy, understand the observed muon discrepancy, and discriminate between different exotic interaction model scenarios. Furthermore, we could study systematic uncertainties by performing measurements with different observables and derive consistency checks on models.
- improve the current photon and neutrino sensitivity not only by collecting more statistics, but also by having a much improved discrimination power.
- understand better, and reduce the systematic uncertainties of, many different measurements including the all-particle flux and the cosmic ray composition measurement.

The key question is whether we can use additional information on the separation between the electromagnetic and muonic shower components for improving the estimate of the mass of the primary particles.

The simulated number of muons at maximum of the muon shower development, $\log_{10} N_{\max}^\mu$, versus the shower maximum X_{\max} at 10^{19} eV (5×10^{19} eV) and 38° of zenith angle, as well as the marginal distributions are displayed in Figs. 2.12 and 2.13.

The difference in $\log_{10} N_{\max}^\mu$ and X_{\max} for the two most recent incarnations of LHC tuned models (EPOS-LHC and QGSJetII.04) are of the order of $\Delta \log_{10} N_{\max}^\mu \approx 0.1$ and $\Delta X_{\max} \approx 15 \text{ g/cm}^2$ independent of the primary. Within the frame of a single model, a clear separation of light and heavy primaries seems possible. Even intermediate primaries like nitrogen can be separated from protons and helium if the recorded statistics permit. Overall, the expectations from air shower simulations strongly indicate the feasibility of composition determination at the highest energies. It can be expected that, if the detector resolution is smaller or of the order of the shower fluctuations, the primary mass can be inferred on an event-by-event basis.

The fact that the average properties of the cascade can, to a large extent, be described in terms of energy and shower age only is called *shower universality*, see [128] and Refs. therein. To first approximation there is no direct dependence on the primary mass nor zenith angle. This is a very remarkable result. Despite the vast number of interactions in an air shower, its overall shape as well as the time profiles of particles reaching ground can be described very well with very few measurable quantities. In the literature it has been described for the

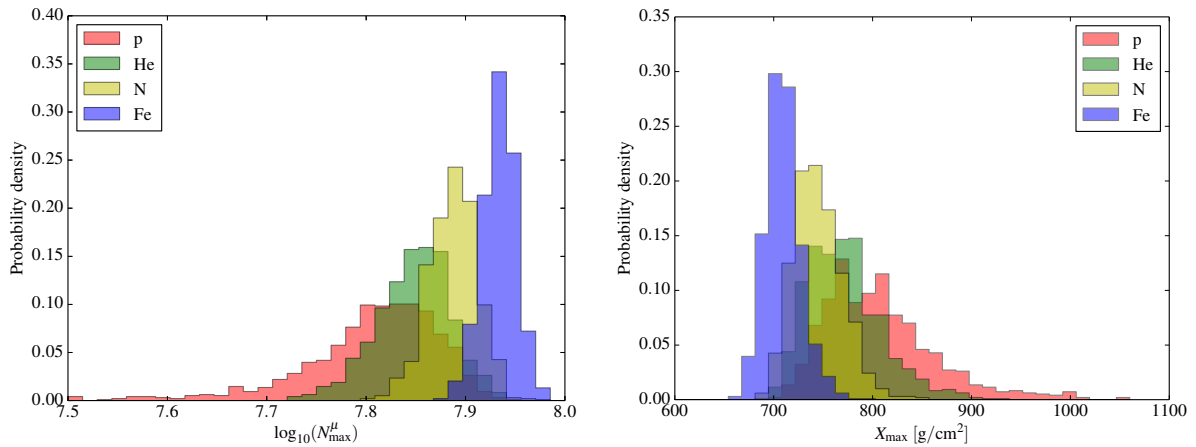


Figure 2.13: Number of muons at maximum of the muon shower development, $\log_{10} N_{\max}^{\mu}$ (left) and depth of shower maximum, X_{\max} , for fixed energy, $E = 10^{19}$ eV, and fixed zenith angle $\theta = 38^\circ$ (EPOS-LHC is the generator for hadronic interactions).

electromagnetic component of showers [126, 128–131]. The concept can also be extended to hadronic showers by introducing one additional parameter, the muon scale N_{μ} [125, 127, 132]. The result is a model that describes showers initiated by protons, nuclei up to iron as well as photon showers using only three parameters: E , X_{\max} and N_{μ} . Based on the signal and timing information in individual SD stations we have encouraging results on event-by-event determination of the primary mass exploiting shower universality features to decompose the relative abundances of shower components, e.g. the muon content. Nevertheless, these results are based on Monte Carlo parameterizations only, which eventuate in large systematic uncertainties and call for a significant step forward in a direct measurement of individual components of air-shower events.

In the following we will show some examples to demonstrate the improved physics power of an enhanced surface detector array.

2.3.1 Mass composition and anisotropy

We can already use parameterizations based on shower universality [127, 132] to analyze our data at high energy. A fit of parameterized shower components to the time traces of the water-Cherenkov detector signals of a high-energy shower yields estimates of the depth of shower maximum, and either an unbiased energy estimator or the muon number, without referring to any data from the fluorescence telescopes (see Chap. 3). This approach can extend our measurements of X_{\max} to energies higher than the fluorescence detector. However, due to the lack of direct muon information, the method currently relies heavily on shower simulations and is characterized by systematic uncertainties that are difficult to estimate. In addition, the large correlation between the SD-based estimates for the shower energy and muon number limits the composition sensitivity. It is clear, however, that improvements in the systematic uncertainties and potential model sensitivity – as addressed by this upgrade proposal – are needed to obtain reliable estimates of the primary mass composition.

Applying cuts on the estimated depth of shower maximum (and muon number or other composition sensitive parameters if available) one can pre-select shower candidates of light and heavy primary particles and perform composition-improved anisotropy studies.

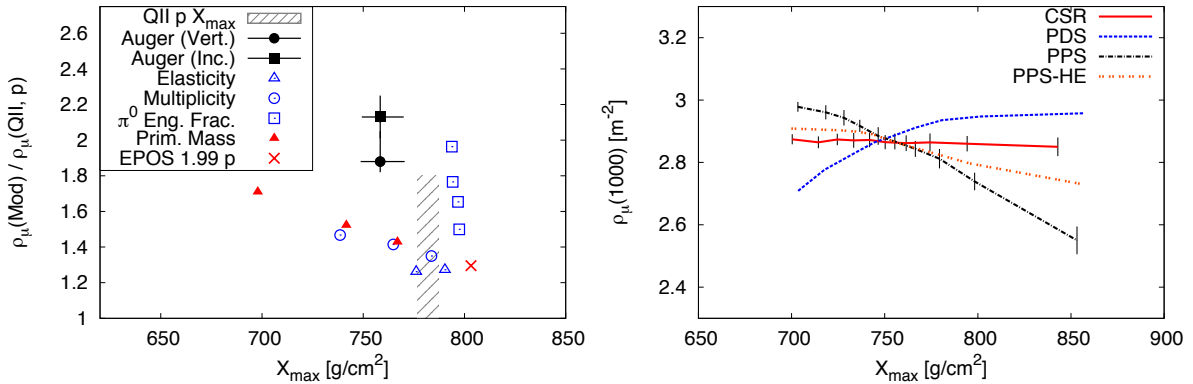


Figure 2.14: Discrimination power of the event-by-event correlation between the muonic signal at ground and the depth of shower maximum X_{\max} [82]. Left panel: Relative number of muons at 1000 m from the shower core and X_{\max} for EPOS 1.99 and QGSJET II.04 and modified versions of it (see text). The Auger data are also shown as derived from showers of 10^{19} eV with zenith angles smaller (larger) than 60° . Right panel: Mean shower-by-shower correlation of the number of muons and X_{\max} for different exotic interaction model scenarios. The scenarios are CSR – chiral symmetry restoration, PPS – pion production suppression, PDS – pion decay suppression, and PPS-HE – pion production suppression at high energy [122].

2.3.2 Physics of air showers and hadronic interactions

Having direct muon information will also greatly enhance our capabilities of studying hadronic interactions. In particular the shower-by-shower correlation of the depth of shower maximum with the number of muons at ground level has proven to be a very powerful observable to distinguish different conventional or exotic interaction scenarios [82]. This can be understood by realizing that the depth of shower maximum is mainly determined by the secondary particles of high energy produced in the first few interactions of the cascade. In contrast, muons are produced only if pions decay, which is only the case at low energy. A simulation study for different modifications of hadronic interaction models is shown in Fig. 2.14.

Already the comparison of the mean depth of shower maximum with the mean muon number provides strong constraints on the interaction model. The simulations also demonstrate how different scenarios of modified hadronic interactions can be distinguished if the event-by-event correlation of N_μ and X_{\max} can be measured. For details see [82, 122].

2.3.3 Upper limits on photon and neutrino fluxes

In case no positive photon or neutrino signal is found, the limits will improve relative to the current values for several reasons:

- The statistics of the events available for determining the limits will triple relative to the data collected by the end of 2012.
- In 2013 two new trigger algorithms (ToTd and MoPS) have been added to the local station software of the water-Cherenkov stations to lower the trigger threshold, in particular for signals dominated by the electromagnetic component. As a result, there will be more stations contributing to the typical shower footprint, improving the reconstruction and, for example, photon/hadron separation at low energies in particular. New

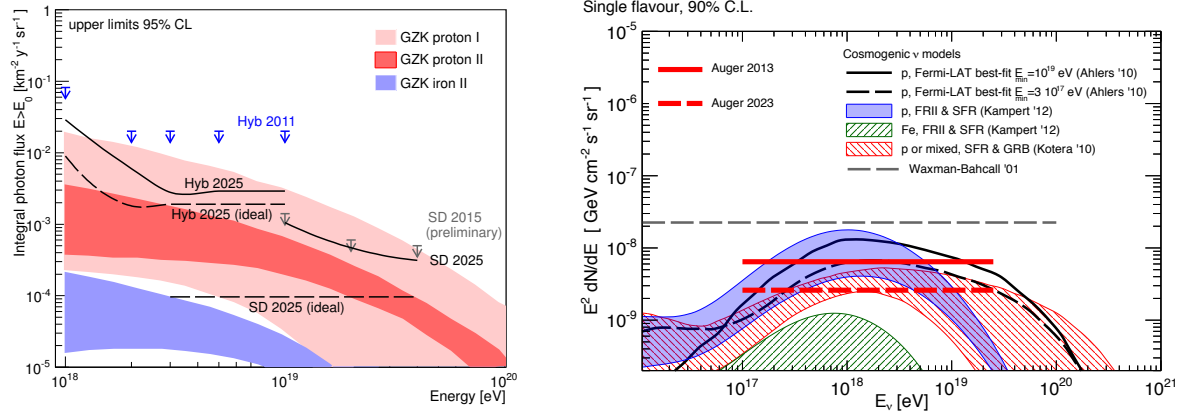


Figure 2.15: Expected sensitivity on the flux of photons and neutrinos. In addition to the conservative estimates based on the increase of statistics, also the projected photon sensitivity for the ideal case of being able to reject any hadronic background due to the upgraded surface detector array is shown.

station electronics, as foreseen for the upgrade (see Sec. 4.3), will allow us to improve the triggering algorithms further.

- At the present time, the photon limits are no longer background free. Improved muon discrimination will help to reduce the background due to hadronic events in our photon candidate sample, or to identify photons and neutrinos.

The analyses of the impact of the improved triggering algorithms and composition sensitivity are still underway. Therefore, we show in Fig. 2.15 (dashed lines) the maximum reach allowed by exposure until 2024. In case of the photon studies a selection efficiency of 50% (due to the a-priori cut) is assumed. Also, the hypothesis that a perfect background rejection after the detector is upgraded and that the new triggers are fully exploited is taken. These lines have to be interpreted as a boundary of what we can do in an optimistic case. The improvement compared to the simple extension of the current data analysis (solid line) until 2024 is significant. The extension of the energy range for current limits below 10 EeV is due to the new triggers. The predicted hybrid limits include the exposure gained with the extended duty cycle. The limits are compared to theoretical predictions (photons: GZK fluxes proton I [53], proton & iron II [133]; neutrinos: AGN [134], Waxman-Bahcall flux [57, 58], cosmogenic neutrino fluxes [50, 51, 133]).

By 2024 we expect to lower our photon limits to reach the band of even conservative predictions for GZK photons – or discover ultra-high energy photons. It is expected that the limits will improve further, mainly at the low-energy end, due to optimized trigger algorithms. If we were able to reject our current photon candidates due to improved analysis algorithms these limits could be much stronger.

2.3.4 Methods for determining the muonic shower component

There are different methods of measuring the density of muons as function of the lateral distance. The most direct method, of using detectors sufficiently shielded to absorb the electromagnetic shower component by, for example, burying them under a layer of soil, is

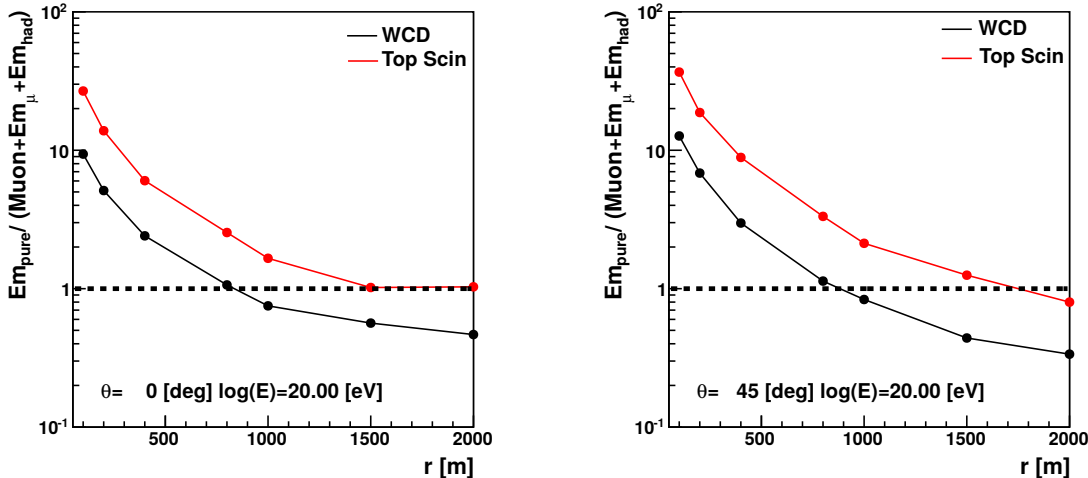


Figure 2.16: Ratios of different contributions to the integrated signal detected for air showers of 10^{20} eV at two zenith angles. Shown is the ratio between the electromagnetic component (without the part related to muon decay or low-energy hadronic interactions) and the muonic part. The electromagnetic particles from muon decay are included in the muonic contribution. The different terms are explained in the text. The curve labeled “WCD” corresponds to the water-Cherenkov detectors of the Auger array, while the red one “Top Scin” corresponds to a thin scintillator.

not feasible for the 1660 surface detectors of the Auger Observatory. Therefore, we have chosen to add another particle detector to each water-Cherenkov detector of the surface array taking advantage of the fact that the two detectors have a different response to the electromagnetic and muonic shower components. Comparing the signal traces of the two detectors allows us to derive the contributions due to electromagnetic and muonic particles and thus to reconstruct the number of muons.

A thin scintillation detector, which is mounted above and triggered by the larger water-Cherenkov detector below it, provides a robust and well-understood way of particle detection that is sufficiently complementary to obtain a good measurement of the density of muons. This can be understood by comparing the signal contributions for different shower components as shown in Fig. 2.16. Over a wide range in lateral distance, the ratio between the integrated signal of electromagnetic particles (photons and electrons) and that of muons is more than a factor two higher in a scintillation detector without any shielding than in a water-Cherenkov detector.

Matrix inversion approach

The matrix formalism developed in [135] for a layered surface detector can be adapted for the reconstruction of the muonic signal contribution and, hence, the number of muons detected in a single upgraded detector station. The motivation for this formalism is to relate intrinsic shower parameters at ground level, such as energy or particle fluxes, to the detector signals via a matrix whose coefficients depend only on the shower geometry but very little on the shower primary mass or on the interaction model used to describe it.

For the combination of the SSD and the Auger WCD we can relate the signal in MIP measured with the SSD and the signal in VEM measured by the WCD to the electromagnetic

energy flux \mathcal{F}_{em} and the muonic flux \mathcal{F}_μ at ground, both expressed in VEM/m², by

$$\begin{pmatrix} S_{\text{SSD}} \\ S_{\text{WCD}} \end{pmatrix} = \begin{pmatrix} \lambda \mathcal{A}_{\text{SSD}} & \mathcal{A}_{\text{SSD}} \\ \beta \mathcal{A}_{\text{WCD}} & \mathcal{A}_{\text{WCD}} \end{pmatrix} \begin{pmatrix} \mathcal{F}_{\text{em}} \\ \mathcal{F}_\mu \end{pmatrix}. \quad (2.1)$$

where \mathcal{A}_{SSD} (respectively \mathcal{A}_{WCD}) are the horizontal area of the SSD (respectively WCD), β represents the projection factor of the WCD surface perpendicularly to the electromagnetic flux ($\beta = 1$ at vertical incidence)¹, and λ is the average energy (in units of MIP/VEM/cos θ) deposited in the scintillator per VEM of electromagnetic flux. The parameter λ depends on the electron to photon ratio and on the energy distribution of the electromagnetic particles in the shower. Note that because the average energy deposition of the muons is proportional to their path length which increases with zenith angle it compensates the decrease of perpendicular surface (this is also true for electrons above one MIP/cos θ in the scintillators). With those definitions and expressing the fluxes in VEM/m², S_{SSD} will be expressed in MIP and S_{WCD} in VEM.

From these definitions it is straightforward to obtain the electromagnetic and muon energy fluxes at ground

$$\mathcal{F}_{\text{em}} = \frac{1}{\lambda - \beta} \left(\frac{S_{\text{SSD}}}{\mathcal{A}_{\text{SSD}}} - \frac{S_{\text{WCD}}}{\mathcal{A}_{\text{WCD}}} \right), \quad (2.2)$$

$$\mathcal{F}_\mu = \frac{1}{\lambda - \beta} \left(\lambda \frac{S_{\text{WCD}}}{\mathcal{A}_{\text{WCD}}} - \beta \frac{S_{\text{SSD}}}{\mathcal{A}_{\text{SSD}}} \right). \quad (2.3)$$

An approximation of the resolution on those quantities can be obtained assuming that the variance of the signal in the WCD and the SSD is equal to the signal itself when using their respective units (VEM and MIP), as expected from a Poisson law. As an example the relative resolution on the muon energy flux is

$$\sigma_\mu = \frac{\sqrt{\text{Var}[\mathcal{F}_\mu]}}{\mathcal{F}_\mu} = \frac{\sqrt{\lambda^2 \frac{S_{\text{WCD}}}{\mathcal{A}_{\text{WCD}}^2} + \beta^2 \frac{S_{\text{SSD}}}{\mathcal{A}_{\text{SSD}}^2}}}{\lambda \frac{S_{\text{WCD}}}{\mathcal{A}_{\text{WCD}}} - \beta \frac{S_{\text{SSD}}}{\mathcal{A}_{\text{SSD}}}} \sim \frac{K}{(\lambda - \beta) \sqrt{\bar{s}}}. \quad (2.4)$$

The resolution evolves as expected as $1/\sqrt{(\bar{s})}$ where \bar{s} is the average of the signals per unit area in both detectors. From simulations we find that λ is about 2.8β in MIP/VEM for EAS of energies above 10 EeV. Preliminary MC studies have shown that both λ and β evolve in similar ways with zenith angle and have little dependence on interaction models and primary mass. This allows to reconstruct the muon signal in the WCD in a nearly model independent way, as given by

$$S_{\text{WCD},\mu} = \mathcal{A}_{\text{WCD}} \mathcal{F}_\mu = \frac{\lambda}{\lambda - \beta} S_{\text{WCD}} - \frac{\beta}{\lambda - \beta} \frac{\mathcal{A}_{\text{WCD}}}{\mathcal{A}_{\text{SSD}}} S_{\text{SSD}} = \delta S_{\text{WCD}} - \gamma S_{\text{SSD}}. \quad (2.5)$$

More details on the use of this method to extract $S_{\text{WCD},\mu}$ from S_{WCD} and S_{SSD} will be discussed in Sec. 3.5.

¹ β is the ratio of the horizontal WCD surface to its surface perpendicular to the zenith direction θ . $\beta(\theta) = S(\theta)/S(0) = \cos \theta + 2h/(\pi R) \sin \theta$ where h and R are the height and radius of the water volume in the WCD. For the Auger WCD geometry: $\beta(\theta) = \cos \theta + 0.42 \sin \theta$.

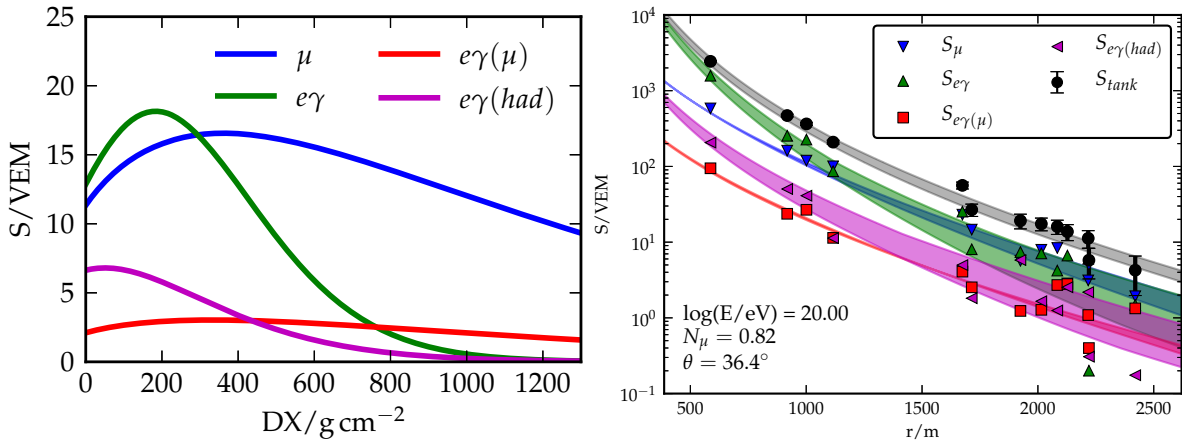


Figure 2.17: Left: The simulated average signal of the 4 different components as a function of DX (the slant depth between X_{\max} and ground level) at a distance of 1000 m and a zenith angle of 36° for fixed energy, $E = 10 \text{ EeV}$. Right: The lateral shape of the simulated signal of a 10^{20} eV shower. The upper band indicates the model prediction based on the fitted parameters. Round markers refer to the total simulated signal. The lower bands show the prediction for the four signal components compared to the simulated values. The size of the azimuthal signal asymmetry is indicated by the width of the bands.

Shower universality approach

The shower universality method predicts for the entire range of primary masses the air-shower characteristics on the ground using only three parameters: E , X_{\max} and N_μ . Therefore, from the integrated signal and the temporal structure of the signal measured in the individual stations, one can estimate these three parameters on an event-by-event basis.

The main advantage of this method is that it exploits all experimentally collected information of an air shower for deriving the physics observables. In this sense a universality-based reconstruction can be considered as a very advanced multivariate analysis of the shower data that employs parameterized physics relations to combine the different measured quantities. A weakness of the universality approach is that it has systematic uncertainties that are difficult to control. The parameterization of the universality relations between the energy, shower age (i.e. X_{\max}), and muon number, and the different signal components at ground (for different lateral distances), can only be derived from libraries of simulated showers and depends to some degree on the hadronic interaction models used for the simulations.

To fully exploit the universality features of air showers, four shower components have to be introduced: (a) the muonic component, (b) the electromagnetic component stemming from muon interactions and muon decay, (c) the purely electromagnetic component, and (d) the electromagnetic component from low-energy hadrons (the collimated beam component).

Splitting the electromagnetic component into component (c), originating from the decay products of high energy π^0 that have been produced in the first generations of hadronic interactions in a shower, and component (d) which is stemming from hadronic interactions at low energy taking place close to the individual detectors, allows us to include the correlation between muons and electromagnetic particles arising from such low energy interactions.

The contributions of the different universality components to the overall signal are illustrated in Fig. 2.17. Each component has a different dependence on the observation depth X

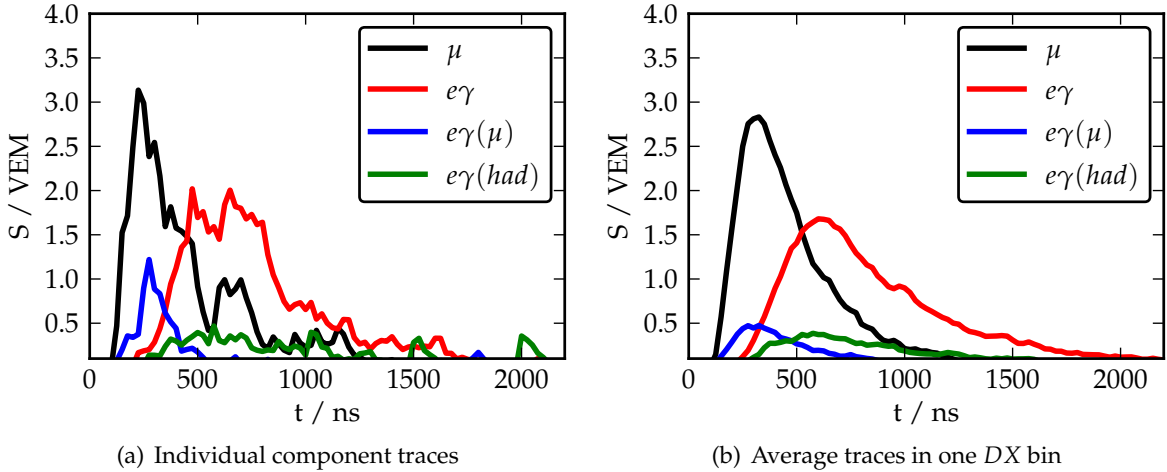


Figure 2.18: Time dependence of the signal of the different universality components in the Auger surface detectors for proton showers of $10^{19.5}$ eV simulated with QGSJet II-03.

relative to X_{\max} , $DX = X - X_{\max}$, and also the slopes of the lateral distributions differ. In addition, there is a dependence on the azimuthal angle about the shower axis that leads to an asymmetry of the ground signals. The colored bands reflect the predicted range of the asymmetry effect of individual components (black being the sum of all others). The markers indicate the simulated total signal (black) and the reconstructed component signals given by the reconstruction algorithm (see below).

For each of the individual universality components the expected arrival time profile of the particles can be parameterized. An example of the simulated time response of a water-Cherenkov detector of the Auger array is shown in 2.18(a) for a particular station far from the shower core. The average trace of the components at the same distance and for a given DX of about 200 g/cm^2 is shown in Fig. 2.18(b).

The total expected signal in a station at position r and relative depth DX is given by

$$S_{\text{tot}} = S_{\text{em}}(r, DX, E) + N_{\mu}^{\text{rel}} \left[S_{\mu}^{\text{ref}}(r, DX, E) + S_{\text{em}}^{\mu}(r, DX, E) \right] + (N_{\mu}^{\text{rel}})^{\alpha} S_{\text{em}}^{\text{low-energy}}(r, DX, E), \quad (2.6)$$

where we have not written the dependence on the azimuthal asymmetry for sake of clarity. The muonic contributions (both from muons directly and the decay/interaction products of the muons) are scaled with the factor N_{μ}^{rel} relative to the expectation values for proton primaries. The contribution from low-energy interactions to electromagnetic particles through π^0 production, $S_{\text{em}}^{\text{low-energy}}$, is scaled with $(N_{\mu}^{\text{rel}})^{\alpha}$. The parameter α is determined in simulations with different hadronic interaction models, resulting in $\alpha \approx 1$ to a very good approximation. The integrated signal as well as the time trace of each individual detector station is fitted by adjusting the parameters E , DX , and N_{μ}^{rel} .

Unfortunately, the primary energy E and relative muon number N_{μ}^{rel} are very strongly correlated and cannot be determined independently from the data of the water-Cherenkov detectors alone, except for very few high-energy events with an exceptionally large number of stations. Therefore, two approaches have been developed within the Auger Collaboration. In the first approach, the energy is taken from the standard reconstruction of $S(1000)$ (the WCD signal 1000 m from the shower core, see Sec.3.2) and the corresponding conversion

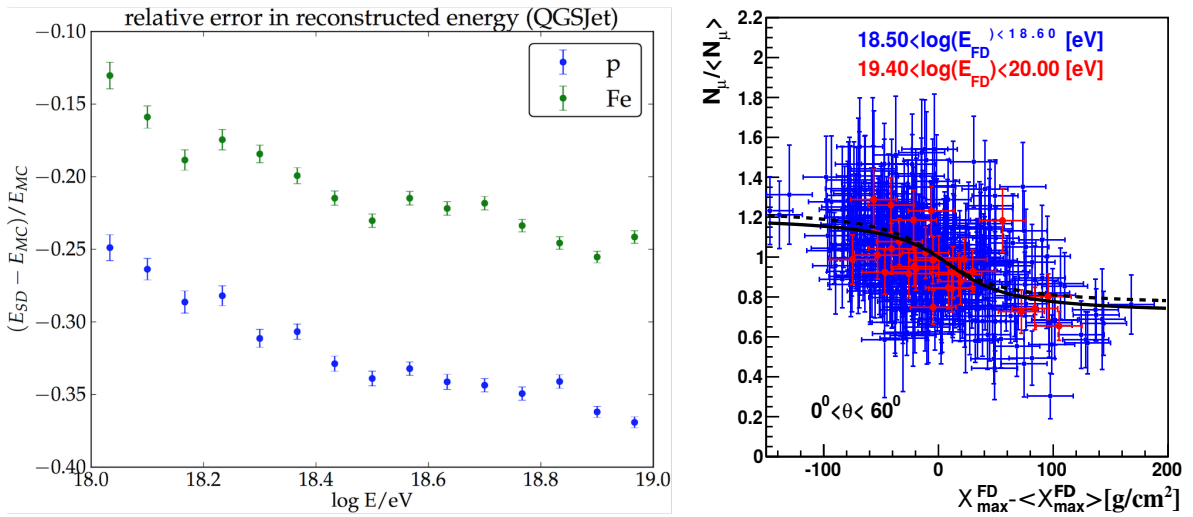


Figure 2.19: Left panel: Expected bias in the energy reconstruction if the signal at 1000 m is used as energy estimator. Right panel: Correlation between the relative number of muons and X_{\max} derived from the universality interpretation of hybrid events. The line shows a phenomenological parameterization for the mean of the distribution.

from $S(1000)$ to energy, which is calibrated by events measured independently with both the surface detector and the fluorescence telescopes. Then DX and N_{μ}^{rel} can be reconstructed. In the second approach the number of muons is parameterized as a function of energy and X_{\max} using hybrid events. Knowing the number of muons, the energy E and the depth of shower maximum X_{\max} can be reconstructed. The results obtained with the two approaches for X_{\max} are very encouraging.

An independent determination of the number of muons is required for the full potential of these universality methods to be exploited. Such a measurement will also give a handle on better understanding of the systematic uncertainties. Considering the first universality approach, this can be understood by looking at the bias of the energy reconstruction if $S(1000)$ is used as energy estimator. The reconstructed energy differs by more than 10% between proton and iron primaries, see Fig. 2.19 (left), making the corresponding estimate of the muon number quantitatively unreliable. In the case of the second approach, the key input is the parameterization of the relative number of muons as function of X_{\max} , see Fig. 2.19 (right). While it is possible to derive such a parameterization for showers with $E < 10^{19.5}$ eV from hybrid data with sufficient statistics, one has to assume that this relation does not change at higher energies. In particular, any sensitivity to a possible, unexpected change of the properties of hadronic interactions would be lost without a direct measurement of the muon densities. Another general weakness of certain applications of these universality parameterizations is the discrepancy in the number of muons found in data in comparison to the simulation predictions. It is not clear whether simply increasing the relative muon number N_{μ}^{rel} by an overall factor does indeed properly account for the physics missing in the hadronic interaction models and possibly air shower simulations.

The extension of the existing universality parameterization for water-Cherenkov detectors to scintillators is straightforward and has been done in preparation of the Auger Upgrade. Results obtained by applying this universality-based reconstruction simultaneously to both detectors will be discussed in Sec. 3.5.

Cross-checks using a direct muon detector

Both the matrix inversion method and the universality reconstruction depend at some level on air shower simulations. With one major aim of the Auger upgrade being the reduction of systematic uncertainties, it is highly desirable to cross-check the performance of both reconstructions. Such a cross-check will improve our understanding of the upgraded detectors and will allow us to reduce the systematic uncertainty of the derived number of muons. For example, discrepancies in the number of muons as currently observed at the 2σ level could be established beyond any doubt.

We will measure muons directly with an Underground Muon Detector. The AMIGA array of muon counters, covering almost 24 km^2 with sixty-one 30 m^2 detector stations at a spacing of 750 m, offers an ideal means for measuring the number of muons directly and, moreover, in a totally independent way. However, buried under a layer of 1.3 m of soil, as needed for a direct measurement, the effective energy threshold for muon detection will be higher than that of the scintillator-water-Cherenkov detector combination.

Chapter 3

Expected Physics Performance

3.1 Introduction

In this chapter we give an overview of the physics reach of the planned Upgraded Detector. We begin with the Surface Detector, first describing the three complementary detector elements and their performance, and then how the observations with these detector elements will be combined to reconstruct events and estimate composition, to vet shower modeling and different reconstruction approaches, and serve as cross-calibrating tools.

In order to assess the physics performance expected for the upgraded ground array, the expected number of events per year, as well as the cumulative number for a data taking period from 2018-2024, are shown in Table 3.1, for both the 750 m array and the 1500 m array. Given a data taking period of the upgraded detector of 7 years we can expect about 700 events above 3×10^{19} eV and more than 60 above 6×10^{19} eV for zenith angles less than 60° . Horizontal air showers ($60^\circ < \theta < 80^\circ$) will add about 30 % to the exposure and thus to the number of expected events. Accounting for a detector resolution of 15 % or better in determining the number of muons, this would allow e.g. for a separation of a fraction as small as 10 % of protons from intermediate and heavy primaries.

Taking data until end of 2024 will double our present SD event statistics and reduce the total statistical uncertainty significantly at highest energies. We have recently improved considerably our scheme for triggering individual stations. Predominantly low electromagnetic signals of physics events are additionally recorded. Not only do the new triggers lower the energy threshold of the 750 m and 1500 m arrays by half a decade in energy, but we gain additional stations far from the shower core in individual events, which will give a better handle on identifying different shower components. The gamma/hadron and neutrino/hadron separation will clearly benefit from an increased station multiplicity per event.

The three elements of the upgraded detector discussed below are (Sec. 3.2) the WCD which – apart from the electronics upgrade – is Auger’s current, well-performing Surface Detector, essentially untouched. Data from this detector are now powerful tools for optimizing the rest of the upgrade. In Sec. 3.3, we introduce the main component of the Upgrade, the Surface Scintillator Detector which consists of a 4 m^2 plastic scintillator detector which will be mounted on top of every WCD. Engineering aspects of the SSD are deferred to a later chapter; here we concentrate on its measurement capabilities and how those will contribute to the analysis. In Sec. 3.4 we describe the sub-array of 30 m^2 underground muon detectors, the current AMIGA project. The UMD, in tandem with the WCD+SSD will both constrain

Table 3.1: Expected number of events per year and cumulative number of events for a data taking period from 2018 until 2024 for events up to zenith angles of $\theta = 60^\circ$. Horizontal air showers ($60^\circ < \theta < 80^\circ$) add about 30 % to the exposure. Moreover, the new trigger scheme implemented in 2013 will allow us to significantly lower the energy threshold of both the 750 m and 1500 m arrays.

$\log_{10}(E/\text{eV})$	$dN/dt _{\text{infill}}$	$dN/dt _{\text{SD}}$	$N _{\text{infill}}$	$N _{\text{SD}}$
	$[\text{yr}^{-1}]$	$[\text{yr}^{-1}]$	[2018-2024]	[2018-2024]
17.5	11500	-	80700	-
18.0	900	-	6400	-
18.5	80	12000	530	83200
19.0	8	1500	50	10200
19.5	~ 1	100	7	700
19.8	-	9	-	60
20.0	-	~ 1	-	~ 9

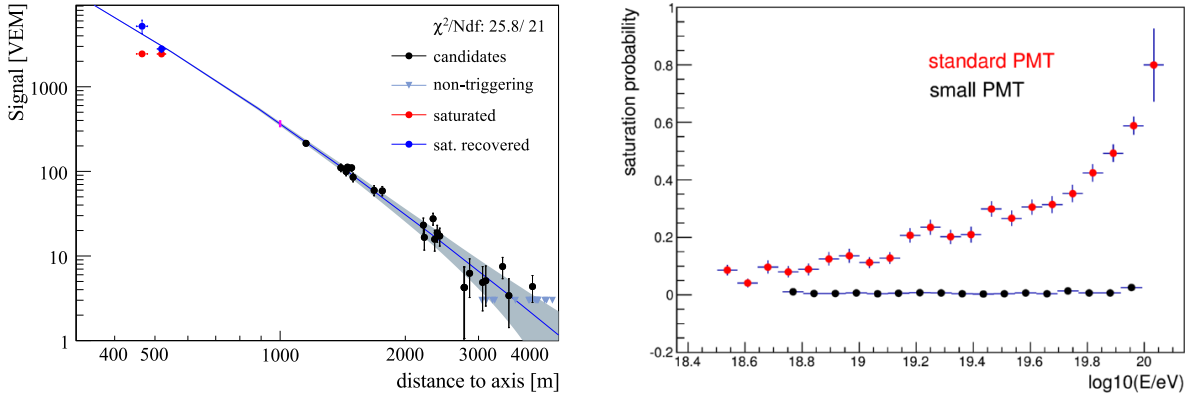


Figure 3.1: Left panel: Lateral distribution of the signal sizes recorded in the water-Cherenkov detectors. The two stations closest to the shower core are saturated (filled red circles). A procedure to recover the signal is applied (filled blue circles). Right panel: Probability of having at least one saturated station in an event as function of energy, obtained from simulations, for the standard PMT configuration (red) and for the small PMT option (black).

muon energy spectrum and serve as a cross-check of the muon estimation techniques.

3.2 Water Cherenkov Detector global performance parameters

Air-showers produced by cosmic rays with energies above 10 EeV produce a footprint on the ground extending over more than 20 km². The surface detector samples the arrival times and the signals produced by the particles reaching the ground. The reconstruction of the energy of the primary cosmic ray is based on the determination of the shower size, the signal interpolated at a certain distance to the air shower axis. In case of the 1500 m array the shower size is defined at 1000 m. An example of the lateral distribution of an event produced by a cosmic ray with an energy of 100 EeV is illustrated in Fig. 3.1 (left).

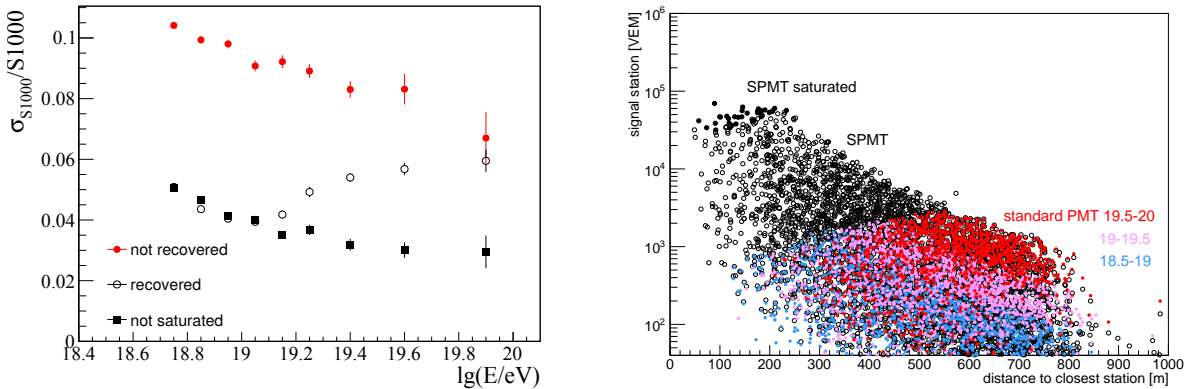


Figure 3.2: Left panel: Resolution of the reconstructed $S(1000)$ that is related to the uncertainty of the lateral distribution function. Shown is the estimated resolution for events without any saturated station (black squares) and for events with at least one saturated station (red circles). The open symbols show the improvement obtained if the currently available procedures for saturation recovery during reconstruction are applied. Right panel: The distribution of simulated signals as a function of the distance to the air-shower axis for different energies in the case of the standard PMT (opened colored circles) and in the case of the small PMT for the same air-showers (black markers).

3.2.1 Dynamic range and saturation

A drawback at present is the limited dynamic range of the SD electronics and PMTs for the very large signals at highest energies. At energies above 3×10^{19} eV more than 40% of the events suffer from saturated signals in at least the station closest to the shower core, see Fig. 3.1(right). A large fraction of these signals are recovered based on the PMT and FADC response and the time dependence of the signal [136].

Simulations show that the expectation value of reconstructed observables such as $S(1000)$, energy, and the arrival direction are not affected by having a station with a saturated signal trace in the event. Only the reconstruction resolution is affected to some extent. This is shown in Fig. 3.2 (left) for the resolution of $S(1000)$. The optimum distance of 1000 m is determined mostly by the spacing between the surface detectors and it provides a robust estimate of the shower size with respect to the assumptions about the functional form of the lateral distribution [137]. In the case of events with a saturated signal, the optimal distance is 1400 m and therefore the choice of a particular LDF induces a systematic uncertainty in $S(1000)$. At $10^{19.5}$ eV, the contribution to the reconstruction resolution of $S(1000)$ from the lateral distribution fit alone is less than 4% for events without saturated stations and increases to 8% if a signal trace is saturated. The software procedures developed for recovering the saturated signals work very well for energies below 10^{19} eV and are increasingly less effective at higher energies.

However, the detailed study of the whole lateral distribution requires us to reach an accuracy of better than 15% on the recovered signal, which can only be obtained with a detailed knowledge of the individual PMT responses in the non-linear region (a non feasible solution, which needs a measurement of the deep saturation curve of each of the 5000 PMTs and monitoring of their constancy in time). Due to the current limited information, the accuracy of the recovered signals larger than 10 kVEM (close to the core) can be worse than 70%.

The proposed equipping of the water-Cherenkov detector with an extra small PMT (SPMT)

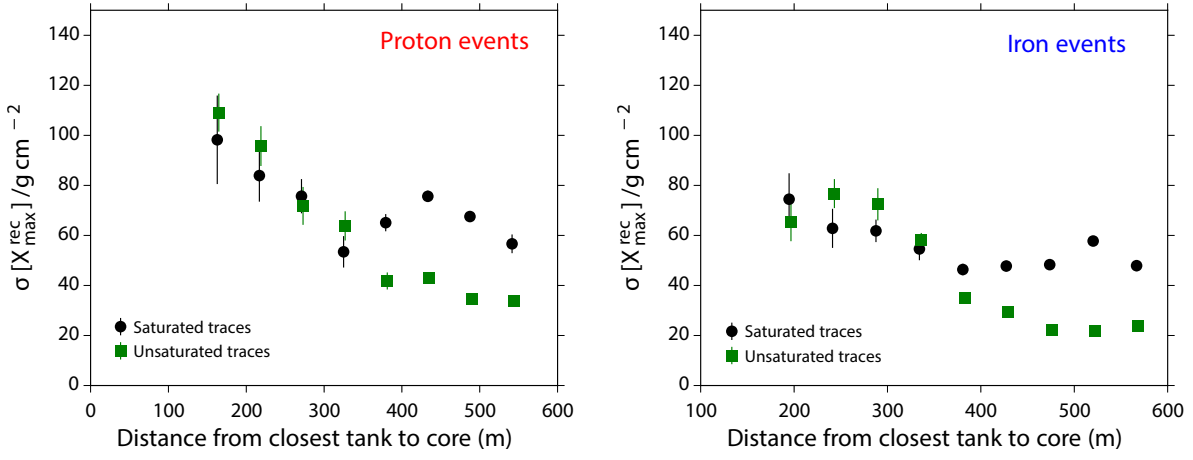


Figure 3.3: Resolution of X_{\max} reconstructed from data of the water-Cherenkov detectors only. The same simulated events have been reconstructed using the signal trace without saturation effects (unsaturated traces) and with saturation (saturated traces). If the saturated station is at a distance of more than 300 m the resolution of the reconstructed X_{\max} can be improved considerably by increasing the dynamic range of the detectors.

will increase the dynamic range from about 600 VEM to more than 30,000 VEM (for details see Sec. 4.4.1). With the new configuration we expect less than 2% of saturated events at the highest energies. The distribution of the expected signals as a function of the distance between the shower axis and the closest station is shown in Fig. 3.2 (right). The predicted measured signals for the current PMTs (colored filled circles) and for the SPMT (black circles) were obtained from CORSIKA simulations of air-showers induced by primary protons with an energy between 3 and 100 EeV. The increased dynamic range will allow measurement of complete signals at a distance as close as 300 m from the core. The signal variance in the extended dynamic range interval will be reduced significantly, being dominated by the calibration uncertainties of 6%. Event selections based on cuts in energy will be more accurate and flux corrections of the energy spectrum due to resolution-dependent migrations will be smaller.

Another example of the importance of measuring the signal traces close to the shower core is shown in Fig. 3.3. In this simulation study the resolution of the universality reconstructed X_{\max} is shown reconstructing the same events twice, once with saturated stations as one would have with the current surface detector, and once with increased dynamic range preventing any saturation of the time traces. The resolution of the reconstructed X_{\max} is significantly worse for showers with a saturated station close to the core. It should be noted that the gain of information by having non-saturated traces is, however, limited to distances larger than 300 m. At smaller distances the uncertainty of the core position limits the usefulness of the measured signal.

3.2.2 Angular and energy resolution

The energy resolution of the surface detector can be retrieved from the events used for the energy cross-calibration, i.e. events with coincident measurements by the FD and the SD [32, 138]. It is illustrated in Fig. 3.4 (left) for different energy thresholds. Above 10 EeV the energy resolution is 12%, with contributions from the detector resolution, reconstruction algorithms

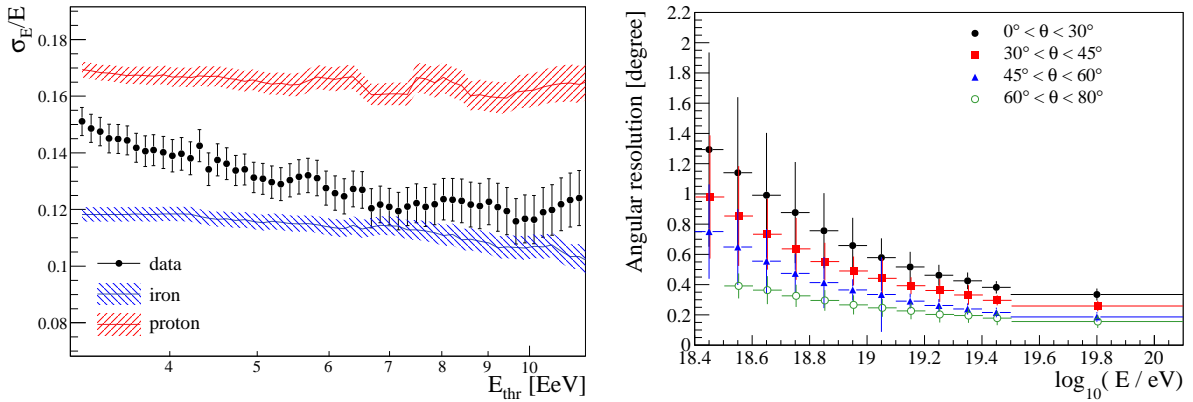


Figure 3.4: Left panel: The cumulative energy resolution above a threshold energy E_{thr} vs threshold energy for data, compared with CORSIKA (QGSJet) simulations of proton and iron induced air-showers. Right panel: The mean angular resolution of the surface detector as a function of energy for different angular ranges. The error bars represent the RMS of the distributions.

and from the shower-to-shower fluctuations. At the highest energies the resolution of the reconstructed impact point on the ground is highly correlated with the resolution on the shower size. A larger dynamic range, used together with the universality principles will improve the core location and the energy determination (for more details see Section 2.3.4). In the same figure the energy resolutions for proton and iron simulations are shown, the difference between them being the dependence of the intrinsic shower fluctuations on the primary mass. The proposed upgrade used with the universality principle will diminish the mass dependency of the energy assignment.

The incident direction of the cosmic rays is obtained from the reconstruction of the air-shower front based on the arrival time of the particles in the detectors. The angular resolution is determined mainly by the number of the stations participating in the event and by the variance of the arrival times. In a single station the accuracy on the determination of the arrival of the shower front is given by the sum of the intrinsic fluctuations of the air-showers, the absolute time given by the GPS, and by the FADC sampling. The current angular resolution as a function of energy for different zenith angle intervals is depicted in Fig. 3.4 (right). For events above 10 EeV, for which the majority have triggered more than 6 detectors, the current angular resolution is better than 1 degree. Switching to a faster ADC sampling of 120 MHz and a GPS RMS accuracy of about 2 ns (see Section 4.3.3) is expected to slightly improve the reconstruction of the direction of the cosmic rays.

3.3 Scintillator Detector performance considerations

3.3.1 Dynamic range

In order to benefit in an optimal way from the surface scintillator detector (SSD) information together with the water-Cherenkov detector (WCD) signal, the dynamic range of both detectors should be similar. The requirements on the SSD dynamic range could be slightly smaller, since close to the EAS core the signals of both detectors will be dominated by the electromagnetic component and therefore the two measurements do not bring as much information as at an intermediate distance to the core. However, at the highest energies a

significant signal is expected even at intermediate distances from the core.

For a shower at 10^{20} eV and a zenith angle of 38 degrees, the peak signal in a 4 m^2 SSD at 200 m from the core is expected to be around 12,000 MIP (Minimum Ionizing Particles), with the contribution of the muons to the SSD signal of less than 10% (and less than 20% for the WCD). A maximum signal of 12,000 MIP seems therefore a reasonable upper bound for determining the dynamic range. It has furthermore the advantage of being achievable with a single PMT, if it is linear enough. See section 4.2.3 for more details on the electronics designed to achieve such a dynamic range.

3.3.2 N_μ and X_{\max} resolutions using Universality based reconstruction

One of the main issues found when extracting physics quantities from an event observed by two detectors is the correlation of the signals in them. For example, if one applies an LDF fit to the signals, the WCD LDF and the SSD LDF will be strongly correlated, as it is the same shower. Also, the slope of these LDFs will be correlated with, for example, the radius of curvature of the shower front, as they both indicate the age of the EAS.

An appealing framework to solve this issue is shower universality where a parameterization of the detectors signals is made as a function of EAS macro-parameters. In the reconstruction process, these macro-parameters are adjusted and any change in them directly translates to the expected change in signal in both detectors. This allows therefore to properly take into account the correlations between the measurements of the SSD and the WCD. Adding an extra detector adds extra information to the global fit reducing the number of parameters to be reconstructed.

A description of the response of the WCD and SSD to EAS has been done, parameterizing both the integral signal deposited, and the timing structure of the signals as a function of the geometry and macro-parameters of the EAS. More details on universality can be found in Sec. 2.3.4. The parameterization is model independent but depends on more parameters than just the X_{\max} and N_μ . For example, the parameterizations are dependent on X_{\max}^μ instead of X_{\max} , and while in all models X_{\max} and X_{\max}^μ are strongly related, the relation between them is dependent on the hadronic interaction model.

Using a full set of MC showers, based on EPOS-LHC and QGSJetII-04, including the simulation of the detector response, it was shown that the combination of WCD and SSD are sensitive enough to reconstruct all the macro-parameters on a statistical basis. However, to get the best event-by-event characterization, it is beneficial to fix some of the very strong correlations between macro-parameters (such as the one between X_{\max} and X_{\max}^μ) and then let only one of them free in the reconstruction. The calibration of the correlation can be made by the WCD+SSD data set, and furthermore cross-checked with hybrid events. In the 750 m array region, FD will provide a direct X_{\max} measurement, while AMIGA will deliver a X_{\max}^μ measurement applying the muon production depth (MPD) technique, allowing a cross-check and a proper calibration of the universality parameterization. The accuracy in the X_{\max}^μ reconstruction using WCD and SSD data has been found to be 70 g/cm^2 at 10 EeV and 50 g/cm^2 at 63 EeV. While these values are somewhat large to be used for composition on an event by event basis, they are well suited to make a statistical measurement of the X_{\max} - X_{\max}^μ relation obtained in real data in order to calibrate properly the universality reconstruction and perform a reconstruction with only X_{\max} and N_μ as free parameters. In Figure 3.5 the X_{\max}^μ reconstruction based on simulations and the obtained X_{\max} - X_{\max}^μ correlation is shown.

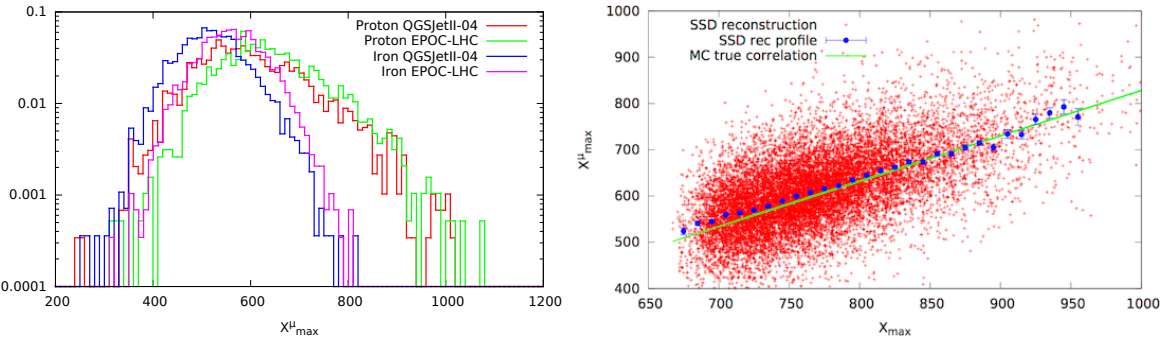


Figure 3.5: X_{\max}^μ distribution reconstructed at 10 EeV for proton and iron showers simulated with EPOS-LHC and QGSJetII-04 (left), and $X_{\max} - X_{\max}^\mu$ correlation obtained using SSD reconstructed values of X_{\max}^μ (right). Some small systematics can be seen for low X_{\max} (corresponding to lower energy EAS).

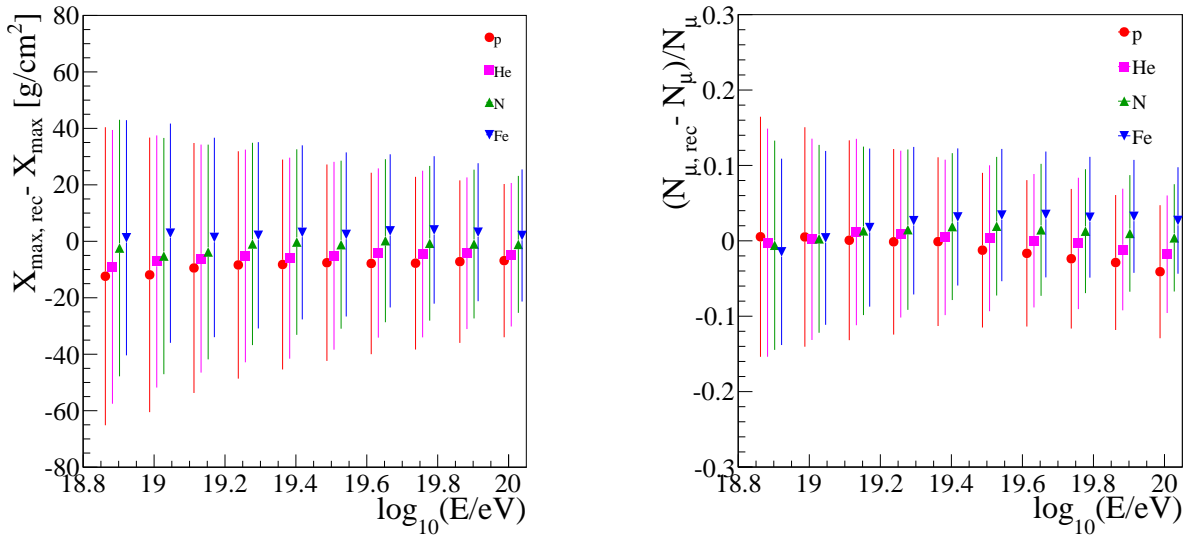


Figure 3.6: Left panel: The reconstructed X_{\max} compared with the true X_{\max} as a function of energy. Error bars represent the RMS of the distributions. Right panel: The reconstructed N_μ compared with the true N_μ as a function of energy. Error bars represent the RMS of the distributions. The resolutions are obtained from parameterizations and interpolations of EPOS-LHC simulations at fixed energies and zenith angles and are shown for events up to 60°.

Once the $X_{\max}^\mu - X_{\max}$ relationship is determined from the calibration described in the previous section, the remaining composition sensitive parameters to fit are just X_{\max} and N_μ . In order to properly determine the resolution of the SSD, the Monte Carlo simulations were treated as real data, and the $X_{\max}^\mu - X_{\max}$ relationship determined with reconstructed values. The events were then reconstructed again using this calibration and the resolution on X_{\max} and N_μ , and systematic biases, were derived. Figure 3.6 shows both resolution and bias for both variables as a function of composition and energy. Biases are small, below 15 g/cm² for X_{\max} and 5% for N_μ , and the resolution is about 40 g/cm² at 10 EeV, down to 25 g/cm² at 100 EeV for X_{\max} , and 15% at 10 EeV down to 8% at 100 EeV for N_μ . Of interest is also the energy resolution for the reconstruction of around 10% at 10 EeV down to 7% at 100 EeV.

3.3.3 Some results from scintillator (ASCII) prototypes

SSD units have been operating on top of an Auger WCD since 2010, under the name of ASCII, standing for Auger Scintillator for Composition II. At first a 0.25 m^2 scintillator was operated for a year, mainly to check the concept, by turning off one of the WCD PMTs and plugging in the SSD PMT instead. In 2012 a 2 m^2 detector was installed at the Central Radio Station with an independent DAQ in order to study the calibration. From its operation it was checked that the Minimum Ionizing Particle (MIP) peak in the charge histogram clearly stands out when a trigger is requested in coincidence with the WCD. After completion of these tests an array of $7 \times 2\text{ m}^2$ detectors was deployed in 2014 on the central 750 m array hexagon. All these detectors were built using scintillator bars similar to those of the MINOS experiment, including the procedures of gluing the fiber, cutting one of their ends and collecting light only on one side. They are inferior to the design described in Sec. 4.2, both in terms of total light collection and uniformity. As the upgraded electronics was not available for the detectors, again it was decided to remove one PMT of the WCD and use the channels for the SSD PMT. The PMT base had to provide the PMT with high voltage, and had to extract two signals, a low gain and a high gain, with a gain ratio of roughly 32, to make it compatible with the current local station electronics. Furthermore, some signal shaping was needed due to the frequency of the current FADC, 40 MHz, slower than the typical light response of the scintillator. The prototype PMT (R1463) and base electronics did behave reasonably, but displayed important non-linearity, limiting the effective dynamic range of the prototypes to less than 200 MIP.

The operation of 2 m^2 SSD units for more than one year went without issue and no intervention was needed. The support and double roof system was validated in strong wind conditions, and the temperature of the SSD was found to be similar to the temperature on the base of PMTs inside the WCD. The MIP peak was found to be clearly determined. More details on the calibration can be found in Sec. 4.2.7, including Figure 4.13 showing a histogram of a MIP from real data recorded with the ASCII prototypes.

While no real physics output could be obtained in the prototype phase due to the non-linearity of the detectors, some checks of the data quality could be performed. The comparison of the signal in ASCII with the signal in the WCD can be seen in Figure 3.7. In a 2 m^2 detector, the signal in units of a single MIP is roughly half the signal of the WCD in VEM. As the signal fluctuations in a WCD are of the order of \sqrt{S}/VEM , and the fluctuations in an SSD are of the order of \sqrt{S}/MIP , a size of around 4 m^2 for the SSD would imply a similar accuracy in the measurement for both detectors, allowing an optimal global reconstruction. Another test of the data can be done even at low energy, by doing the usual SD reconstruction of the WCD signals and taking the average X_{\max} and N_μ at the energy obtained to estimate the signals expected in the SSD using the universality parameterization. Doing so allows us to compare the observed signal to the predicted one, even for low energy events where the number of stations and the total signals are not enough to allow a reconstruction based on the universality parameterization on event-by-event basis. One can also do the same exercise but using different values for N_μ , or assuming a systematic error in the energy scale of for example 15% in one or the other direction. All these tests are summarized in Figure 3.7.

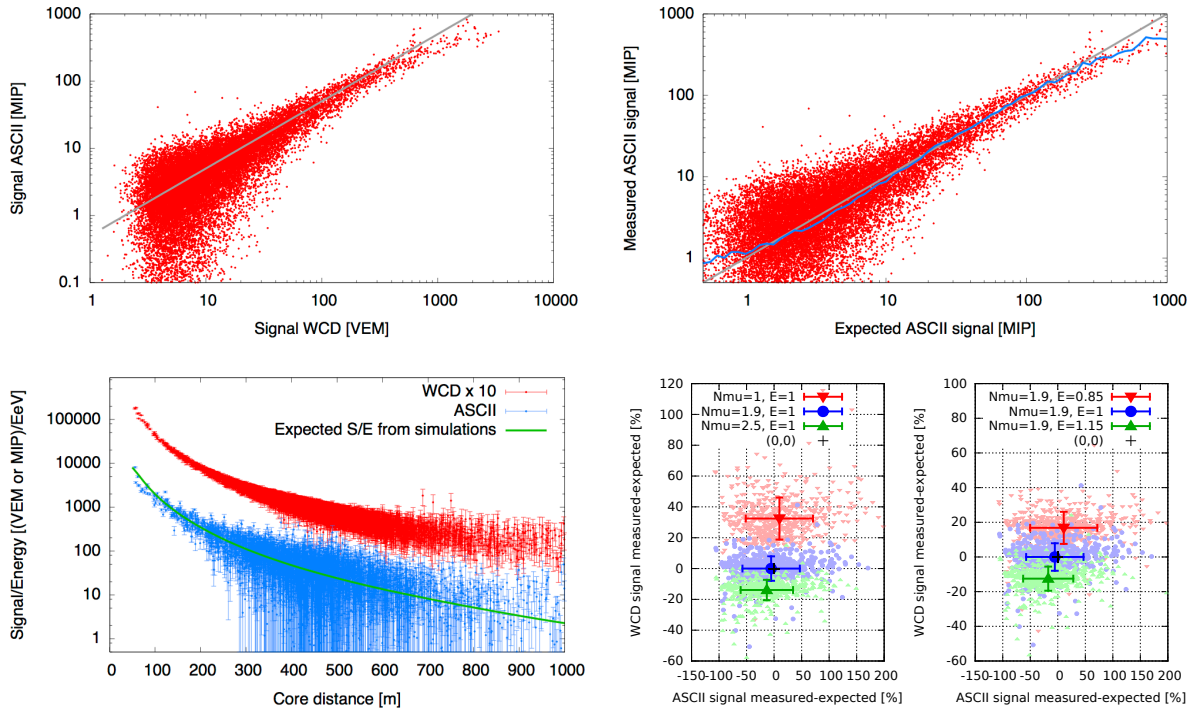


Figure 3.7: Results for the prototype SSD detectors (ASCII). Top left, ASCII signal compared to the WCD. The signal of a 2 m^2 SSD is roughly half the signal of the WCD. Non-linearity of the prototypes detectors can be seen for large WCD signals. Top right: comparison of measured signal with expected one from universality and average X_{\max} and N_μ at the reconstructed energy. The agreement is very good. The profile of the data points is also indicated. The non-linearity at large signals is again visible. Bottom left: LDF from WCD (scaled $\times 10$) and SSD for low energy events from 25 to 30 degrees of zenith angle, normalized to reconstructed energy, compared to prediction from simulations. Bottom right: measured signals in SSD and WCD compared to predicted ones from the universality parameterization, changing N_μ or the energy scale. A similar study, once systematics are understood, will allow to determine the muon numbers of real data and any systematic in the FD-based energy scale.

3.4 Underground Muon Detector performance considerations

The AMIGA muon detectors are buried scintillator counters optimized to perform a direct measurement of the air shower muon component at energies of $\sim 10^{17.5}\text{ eV}$ and higher. The detectors will be co-located with the WCDs of the 750 m array, i.e. at 750 m spacing and covering an area of 23.5 km^2 . A single station will have an area of 30 m^2 and consist of 3 modules of 10 m^2 . One key element for this direct measurement is the absorption of the electromagnetic shower component by the overburden. Results of a detailed simulation study of the punch-through are given in table 3.2. The optimal depth is found to be in the range 110 – 150 cm. The detectors will be deployed at a depth of 1.3 m. At this depth the effective energy threshold for muons is $600\text{ MeV} / \cos \theta_\mu$ with θ_μ being the zenith angle of the muon. As an important cross-check of the absolute efficiency and threshold energy of detected muons, a small precision muon-counter with several threshold energies will be installed on the surface at the Observatory, to monitor reference rates of unaccompanied atmospheric muons.

To validate this design, a Unitary Cell of AMIGA was built, consisting of a full 7 station

Table 3.2: Relative punch-through (PT) for vertical showers of 10^{19} eV and number of muons for detectors at different depths in the Pampa soil ($\sim 2.4 \text{ g/cm}^3$ average density).

Detector depth	70 cm		110 cm		150 cm	
	170 g/cm ²	$N_\mu/10 \text{ m}^2$	265 g/cm ²	$N_\mu/10 \text{ m}^2$	360 g/cm ²	$N_\mu/10 \text{ m}^2$
r_{core} (m)	Rel. PT	$N_\mu/10 \text{ m}^2$	Rel. PT	$N_\mu/10 \text{ m}^2$	Rel. PT	$N_\mu/10 \text{ m}^2$
200	88%	512	14%	493	2.3%	461
600	38%	49	7%	43	1.1%	40
1000	16%	10	3%	9	0.5%	8.4
1400	3%	3	0.6%	2.6	0.1%	2.4

hexagon where counters of different sizes were installed at depths of 2.3 m.

Direct counting of the muons through segmentation has the significant advantage that each channel counts pulses above a given threshold, without a detailed study of signal structure or peak intensity. This method is very robust since it does not rely on deconvolving the number of muons from an integrated signal. It does not depend on the PMT gain or gain fluctuations nor on the muon hitting position on the scintillator strip and the corresponding light production and attenuation along the fiber track. Neither does it require thick scintillators to control Poisson fluctuations in the number of photo-electrons per impinging muon. This *one-bit* electronics design relies on a fine counter segmentation to prevent under-counting due to simultaneous muon arrivals. The advantage of counting is however lost close to the core in the saturation region, where integration is needed. AMIGA will therefore include a channel for signal integration to cope with saturated stations.

To summarize, the main features of the muon counters are (i) sturdy plastic-scintillator based detectors proven to support up to 2.3 m of soil load without any mechanical failure and having long term stability (the first counter was buried in the Pampas in November 2009); (ii) segmented system to count muons on a very reliable and fast basis. The counting efficiency is shown in Fig. 3.8 for a simulated proton shower. (iii) dedicated channel for a summed analog signal to cope with high muon counts close to shower core (resolution $\approx 1.12/\sqrt{N_\mu}$ for more than 20 muons); (iv) cross calibration of the summed analog signal to segmented counting in the region of overlap (~ 30 to 70 muons).

The AMIGA detectors are described briefly in Chapter 5 and a detailed description is given in Appendix B.7.2.

3.5 Primary Particle Identification with Surface Detector

We will exploit several methods of measuring the muon density, which, combined with other observables, will enable us to estimate the mass of the primary particle.

The matrix inversion method (see Sec. 2.3.4) will allow us to derive the muon density for stations close to the shower core (i.e. below 1200 m) in a transparent and almost model-independent way. While being limited to detector stations with high electromagnetic and muonic signal, this method will enable us to derive the average number of muons in air showers of different energies and zenith angles unambiguously. As will be elaborated below, it is a robust technique for estimating the separate contributions of the electromagnetic and muonic shower components to the overall detector signal.

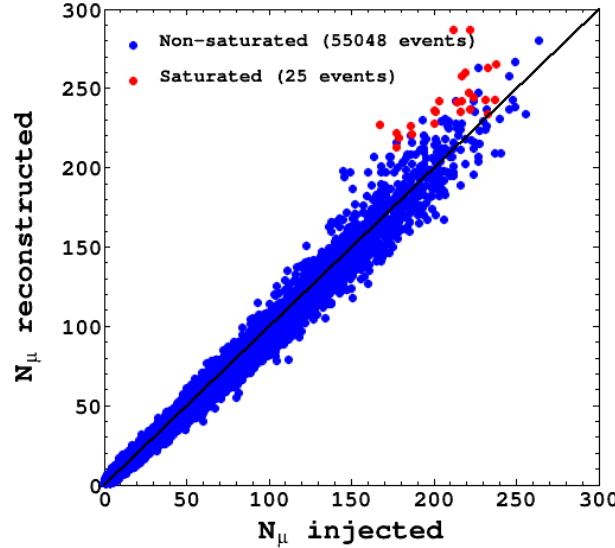


Figure 3.8: Muon counting efficiency of a 30 m^2 scintillator module for a proton initiated shower at an energy of $10^{18.5}\text{ eV}$ and a zenith angle of 21° .

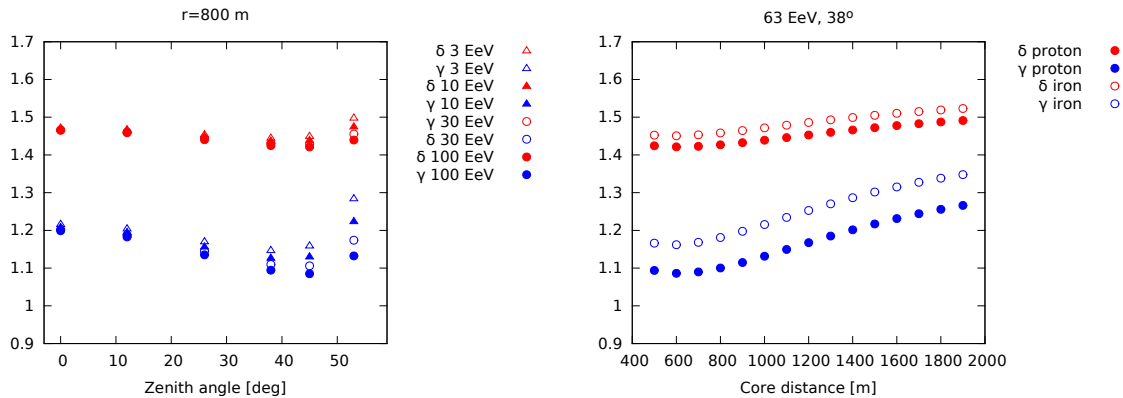


Figure 3.9: Coefficients for the matrix inversion approach. The values of δ and γ were calculated from showers simulated with QGSJet II.04 and EPOS-LHC using the GEANT-based detector simulation of the signals in the water-Cherenkov and scintillator detectors.

The coefficients δ and γ , introduced in Sec. 2.3.4, are shown in Fig. 3.9 for different lateral distances, zenith angles, and primary particles. A small dependence on the mass of the primary particle and similarly on the hadronic interaction model can be seen. To check the impact of this small dependence, the resolution and the mass-dependent bias in the reconstruction of the muon density for individual detector stations is given in Fig. 3.10. The resolution is about 20 – 30% on the single detector level for showers in the flux suppression region if stations with a lateral distance up to 1000 m are considered. This value is the result of a first implementation of the matrix inversion method without any optimization. It is ex-

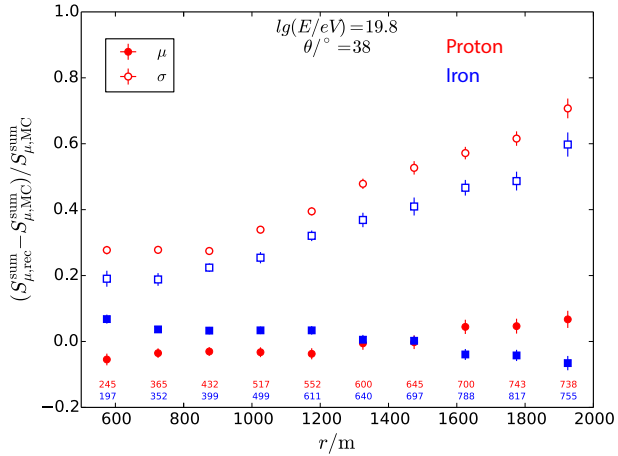


Figure 3.10: Reconstruction bias (solid symbols) and resolution (open symbols) of the muonic signal contribution for individual detector stations. The results for proton and iron showers are shown in red and blue, respectively. The number of detector stations analyzed for the different lateral distance intervals is also given.

pected that the resolution can be improved for large lateral distances by using the constraint that the detector signal is dominated there by muons.

In the following we will use constant values for δ and γ . Including the dependence of the coefficients on lateral distance and zenith angle, even if it is small, will help to improve the results and is foreseen once enough data is available to characterize the SSD response to the electromagnetic and muonic shower particles in more detail.

3.5.1 Event-based observables and merit factors

It is convenient to parameterize the discrimination power between the primary particles i and j in terms of the merit factor, defined as

$$f_{\text{MF}} = \frac{|\langle S_i \rangle - \langle S_j \rangle|}{\sqrt{\sigma(S_i)^2 + \sigma(S_j)^2}}. \quad (3.1)$$

Merit factors of 1.5 or higher allow a comfortable separation of the respective elements.

Single station estimate

The simplest, but at the same time least powerful method for distinguishing different primaries is the use of the muon density measured in individual detectors in a given lateral distance range. Due to the limited resolution of the matrix inversion method the corresponding merit factors for distinguishing between proton and iron primaries are only about 0.9 for stations at a lateral distance of 800 m from the core and shower energies $E > 10^{19.5}$ eV.

Muon lateral distribution

Fitting first a lateral distribution function (LDF) to the signals of the scintillator detectors in an event allows the estimate of the muon density at a given distance with very much reduced

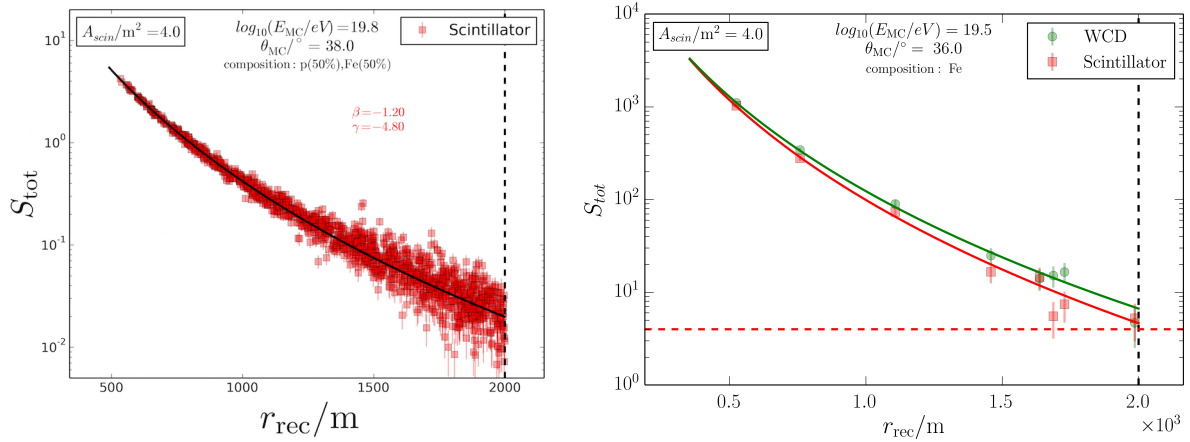


Figure 3.11: Left: Simulated showers for deriving the mean lateral distribution of the scintillator detectors. Right: Example of the LDFs of one iron shower using the shape parameters derived before. Both the results for the WCD and the SSD are shown. The horizontal dashed line indicates the single station trigger threshold and the vertical line the range up to which stations are used in the LDF fit.

statistical uncertainty. In the following we have used simulated showers (50% proton and iron primaries) to first derive a parameterization of the LDF for the SSD. The slope of this parameterization,

$$\text{LDF}(r) = C \left(\frac{r}{800 \text{ m}} \right)^\beta \left(\frac{r + 700 \text{ m}}{800 \text{ m} + 700 \text{ m}} \right)^\gamma, \quad (3.2)$$

is kept fixed in the subsequent analysis of another, independent set of Monte Carlo generated showers. Only the normalization is fitted on an event-by-event basis. The showers were selected from a sample simulated with a continuous energy distribution and the energy derived from $S(1000)$ using the standard energy conversion of the Auger Observatory. The Monte Carlo data for deriving the LDF for SSD and its application to one example event are shown in Fig. 3.11.

The matrix inversion algorithm is then applied to the LDF values for the WCD and SSD to calculate the muonic signal expected in a water-Cherenkov detector at 800 m core distance, $S_\mu(800)$. A reconstruction resolution of the muonic signal of, for example,

$$\left. \frac{\sigma[S_\mu(800)]}{\langle S_\mu(800) \rangle} \right|_{\text{proton}} \approx 22\% \quad \text{and} \quad \left. \frac{\sigma[S_\mu(800)]}{\langle S_\mu(800) \rangle} \right|_{\text{iron}} \approx 14\% \quad (3.3)$$

is reached at $E \approx 10^{19.8}$ eV and $\theta = 38^\circ$. Using $S_\mu(800)$ as composition estimator, the obtained merit factors for distinguishing between proton and iron primaries are above 1.5 at high shower energies ($E > 10^{19.5}$ eV) and small zenith angles.

Universality and multivariate analyses

A universality-based analysis, or a sophisticated multivariate analysis, allows one to correlate the detector signals at different lateral distances and also takes advantage of the arrival time (shower front curvature) and temporal structure of the signal measured in the detectors. At this stage we are only at the beginning of developing a reconstruction using all these observables. Nevertheless, some results are given in the following, but it should be kept in

Table 3.3: Fisher discriminant merit factor f_{MF}^{F} for fixed energy simulations. In addition, merit factors $f_{\text{MF}}^{\text{Rec}}$ are shown after accounting for the degradation due to the resolution of the energy reconstruction.

Model	Energy	Composition	Zenith angle	f_{MF}^{F}	$f_{\text{MF}}^{\text{Rec}}$
QGSJetII-04	10 EeV	Proton-Iron	All	1.49	1.31
QGSJetII-04	10 EeV	Proton-Helium	All	0.47	0.34
QGSJetII-04	10 EeV	Nitrogen-Iron	All	0.6	0.46
QGSJetII-04	63 EeV	Proton-Iron	All	1.86	1.59
QGSJetII-04	63 EeV	Proton-Helium	All	0.46	0.38
QGSJetII-04	63 EeV	Nitrogen-Iron	All	0.94	0.66
EPOS-LHC	10 EeV	Proton-Iron	All	1.59	1.35
EPOS-LHC	10 EeV	Proton-Helium	All	0.4	0.29
EPOS-LHC	10 EeV	Nitrogen-Iron	All	0.75	0.62
EPOS-LHC	63 EeV	Proton-Iron	All	1.82	1.45
EPOS-LHC	63 EeV	Proton-Helium	All	0.38	0.23
EPOS-LHC	63 EeV	Nitrogen-Iron	All	1.07	0.79
QGSJetII-04	10 EeV	Proton-Iron	21°	1.52	1.15
QGSJetII-04	10 EeV	Proton-Iron	38°	1.55	1.43
QGSJetII-04	10 EeV	Proton-Iron	56°	1.5	1.43
QGSJetII-04	63 EeV	Proton-Iron	21°	2.08	1.56
QGSJetII-04	63 EeV	Proton-Iron	38°	1.97	1.67
QGSJetII-04	63 EeV	Proton-Iron	56°	2.14	2.1

mind that the corresponding merit factors should be considered as lower limits to what will be reached after having a better understanding of the detectors.

The universality-based reconstruction provides the depth of shower maximum with a resolution of about 35 g/cm². If one were to use only the X_{max} derived from universality one would obtain a merit factor of 1.2 for the separation of proton and iron primaries over a wide range in energy and zenith angle. Conversely, if one would use only the relative muon number from the universality reconstruction the merit factor would be just above 1.4. The merit factors derived from the LDF fit are larger because of the different energy reconstructions used. In the case of the universality reconstruction the energy is obtained together with X_{max} and N_{μ}^{rel} . The current implementation of the universality reconstruction exhibits a composition-dependent bias in the energy reconstruction that reduces the merit factors. Work is ongoing to reduce this bias and correspondingly increase the merit factors.

A summary of merit factors for the separation of different primary particles at different energies and zenith angles is given in Tabs. 3.3 and 3.4. The merit factors are consistently higher for showers simulated with EPOS-LHC in comparison to QGSJET II-04. This is related to the higher muon multiplicity of EPOS showers. As even EPOS predictions of the muon number are lower than those observed in data, the merit factors will be higher when applying universality to real data. Finally it should be mentioned that advanced multivariate analysis methods are expected to reach similar merit factors as shown here.

Table 3.4: Fisher discriminant merit factor for a set of simulated showers with continuous energy distribution. The reconstructed showers have a mean energy of $10^{19.6}$ eV.

Model	Composition	Merit Factor (C)
QGSJetII-04	Proton-Iron	1.54
QGSJetII-04	Proton-Helium	0.41
QGSJetII-04	Nitrogen-Iron	0.64

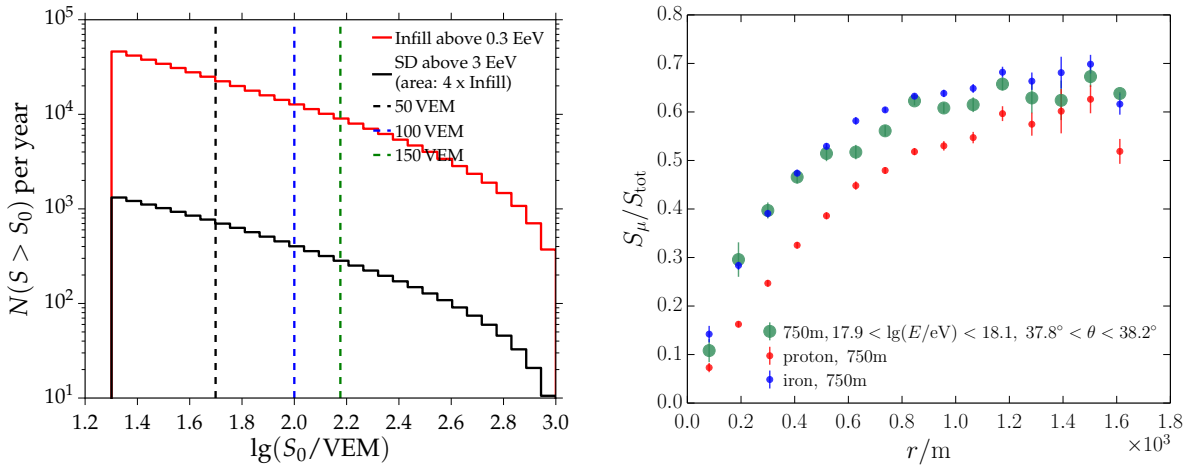


Figure 3.12: Left: Number of stations per year whose signal exceeds S_0 . Shown is the comparison of the rate detected in the 750 m array and the regular array if 61 stations are considered in both cases. Right: Ratio between the muonic and electromagnetic contributions to the signal of the WCD as function of the lateral distance, and for shower energies typical for the 750 m array. Shown are the expectations for proton and iron showers (small red/blue symbols) and the ratio reconstructed for Auger data using universality (large green circles).

3.5.2 Cross-checks with an underground muon detector

There are different kinds of cross-checks that can be performed with an array of additional, independent muon detectors. With the upgraded surface detectors being fully efficient for muon separation only above 10^{19} eV, however, one would need an array of independent muon detectors of the size of 200 to 300 km² to collect enough statistics to do an event-by-event comparison of the muon content of the showers.

A much more economic option is to limit the cross-checks to individual detector stations. This can be done with the 30 m² AMIGA counters foreseen to be deployed in the region of Auger's 750 m array. The trigger threshold for full efficiency of the 750 m array is below $10^{17.5}$ eV, in comparison to $10^{18.5}$ eV for the regular array. A comparison of the statistics of the number of detectors having a WCD signal larger than S_0 in the 750 m array region (61 detectors with 750 m spacing) and in the regular array (61 detectors with 1500 m spacing) is shown in Fig. 3.12 (left). More than 10,000 times per year a station in a shower will exceed a signal of 100 VEM in the 750 m array region. The corresponding rate would be well below 1000 for the regular array and the same number of additional muon detectors.

Showers detected with the 750 m array have typically a much lower energy, and the stations with the highest signal will be closer to the core than in the regular array. For example,

a station with $S \sim 100$ to 200 VEM will have a typical lateral distance of 1000 m in the regular array and 400 m in the 750 m spacing array. The different distances and shower energies lead to a different ratio between the muonic and electromagnetic signal contributions. This ratio is about 0.5 to 0.6 at 1000 m for showers of $10^{19.5}$ eV. The corresponding value for the 750 m array is shown in Fig. 3.12 (right). The ratio between the muonic and electromagnetic shower signals will be about 20 to 30% smaller than that of ultra-high energy showers. This difference is not too large and will allow us to use the AMIGA counters for cross-checking the muon measurement with the upgraded surface array.

3.6 Fluorescence Detector performance parameters

3.6.1 Geometry, energy, X_{\max} reconstruction

In the FD, cosmic ray showers are detected as a sequence of triggered pixels in the camera. The first step in the analysis is the determination of the shower-detector plane (SDP). The SDP is the plane that includes the location of the FD station and the line of the shower axis. Next, the timing information of the pixels is used for reconstructing the shower axis within the SDP. The accuracy of the monocular reconstruction is limited. More accurate reconstruction is obtained by combining the timing information from the SD stations with that of the FD telescopes. This is called hybrid reconstruction. A hybrid detector achieves the best geometrical accuracy by using timing information from all the detector components, both FD pixels and SD stations. As can be seen in Fig. 3.13, the angular resolution for hybrid events above $10^{18.5}$ eV is better than 0.5° .

The FD provides a nearly calorimetric energy measurement as the fluorescence light is produced in proportion to the energy dissipation by a shower in the atmosphere. The reconstruction of the fluorescence events is a complex process that requires the knowledge of several parameters, e.g. the absolute calibration of telescopes, the fluorescence yield, light attenuation and scattering in the atmosphere, optical properties of telescopes and an estimate of the invisible energy. The current systematic uncertainty on the energy scale for hybrid events (i.e. at least one SD station is used in the reconstruction) is 14%.

The energy evolution of the X_{\max} resolution is shown in the left panel of Fig. 3.14. As can be seen, the total X_{\max} resolution is better than 26 g/cm^2 at $10^{17.8}$ eV and improves with energy to reach about 15 g/cm^2 above $10^{19.3}$ eV. The systematic uncertainty of the X_{\max} scale, i.e. the precision with which the absolute value of X_{\max} can be measured, is shown in the right panel of Fig. 3.14. As can be seen, this uncertainty is $\leq 10 \text{ g/cm}^2$ at all energies. At low energies, the scale uncertainty is dominated by the uncertainties in the event reconstruction and at high energies the atmospheric uncertainties prevail.

3.6.2 Estimated event numbers

The selection efficiency after including the quality and fiducial cuts is between 40 and 50% above 10^{19} eV, see Fig. 3.15. A potential bias from these selection cuts can be checked by comparing its efficiency as a function of energy for data and simulated events. For this purpose, we use the independent measurement of air showers provided by the SD and measure the fraction of events surviving the quality and fiducial cuts out of the total sample of pre-selected events. This estimate of the selection efficiency is shown in Fig. 3.15 as a function of SD energy above 10^{18} eV. Below that energy, the SD trigger efficiency drops below 50%. The

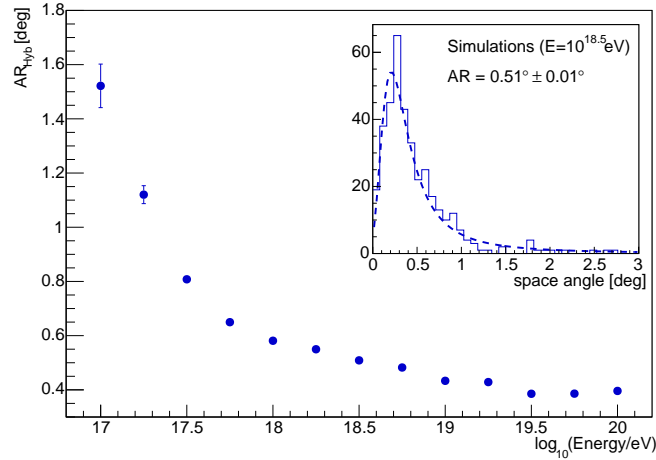
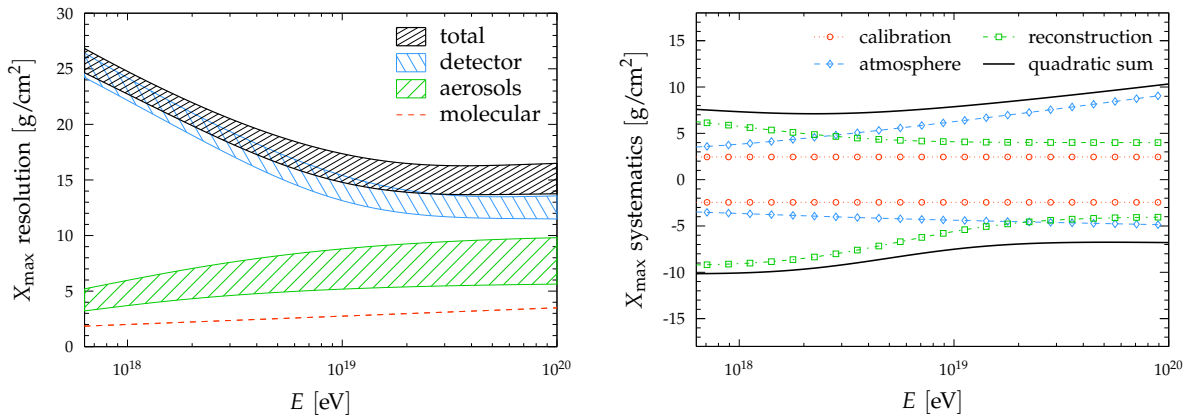


Figure 3.13: Angular resolution for hybrid events.

Figure 3.14: Left panel: X_{\max} resolution as a function of energy. Bands denote the estimated systematic uncertainties. Right panel: Systematic uncertainties in the X_{\max} scale as a function of energy.

comparison to the simulated data shows a good overall agreement and we conclude that the selection efficiency is fully described by our simulation.

The expected number of events after seven years of the standard FD measurement is 510 and 37 above energy 10^{19} eV and $10^{19.5} \text{ eV}$, respectively. An additional increase up to about 40% at the highest energies can be achieved by extending the FD operation to periods with higher night sky background. For more details see Chapter 6.

3.7 Benefits of hybrid (multi-detector) measurements

There are many benefits of having scintillator detectors in addition to the existing array of WCD that have not been discussed so far.

First of all, a direct comparison of the data of Telescope Array (TA) and the Pierre Auger Observatory can be made because it will be possible to implement the reconstruction procedures of TA also at the Auger Observatory. For example, the energy calibration of the surface arrays can be compared directly if mapped to the scintillator signal at a given lateral distance. Furthermore, the different indications for muon discrepancies can be compared be-

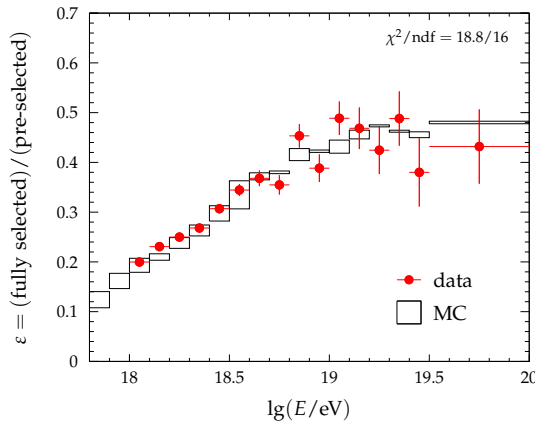


Figure 3.15: Efficiency of the quality and fiducial selection for data and MC. The χ^2 of the sum of the (data-MC) residuals is quoted on the top right.

tween both experiments. Many other comparisons will be possible, including composition-sensitive quantities such as shower front curvature or signal rise times.

Another important application of the multi-detector measurements possible with the upgraded array are detailed investigations of detector aging effects and possible drifts in the detector calibration. In general, the reduction of existing systematic uncertainties will be one of the main aims of installing the detector upgrade.

Last but not least, we hope to further improve our understanding of shower physics and, in particular, of universality based and multivariate reconstruction techniques in the end by such a degree that we will be able to re-analyze the data taken with the Auger Observatory before the upgrade was installed, and derive reliable composition information from the data taken so far.

3.8 Application to physics goals

In the following we will apply the universality reconstruction to simulated data of the water-Cherenkov and scintillator detectors to demonstrate the ability to derive composition sensitive observables with the upgraded Auger Observatory.

Without knowing what composition to expect in the GZK suppression region it is difficult to demonstrate the potential of the upgraded Auger Observatory. Therefore, we will use the two flux models introduced in Chap. 2 and shown in Fig. 2.10 to illustrate the discriminative power of the additional muon information. Mock data sets were generated for these scenarios that reproduce the predicted energy distribution and energy-dependent composition. The event number of each of these artificial data sets corresponds to that expected for 7 years of data taking with the upgraded Auger Observatory.

3.8.1 Composition sensitivity and measurement of the muon number

One of the key questions of the physics reach of the Auger Upgrade is that of being able to discriminate different composition and, hence, physics scenarios in the energy range of the flux suppression. Using only the surface detector data of the upgraded array we have reconstructed the number of muons and the depth of shower maximum. The mean X_{\max}

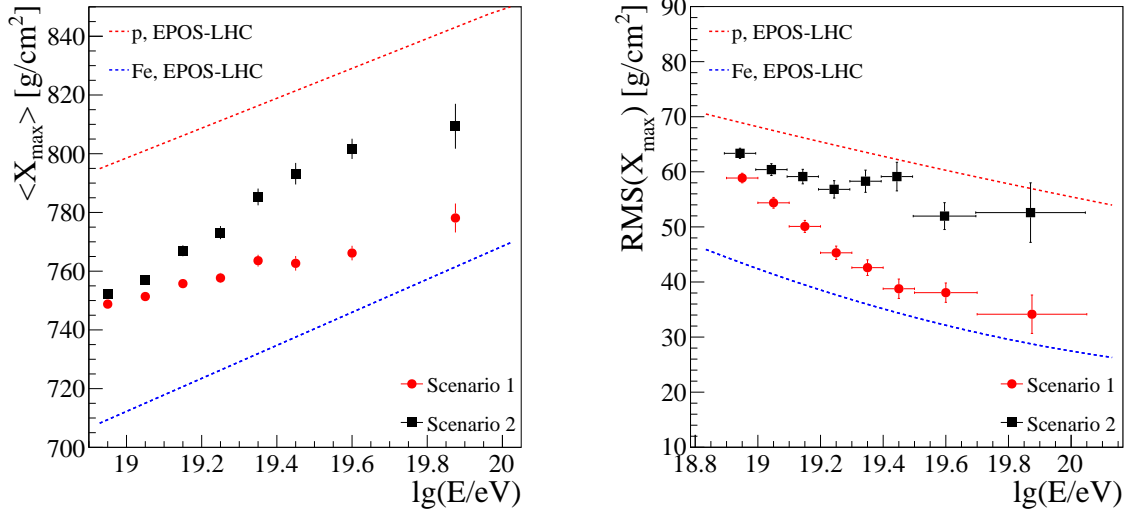


Figure 3.16: Reconstructed mean depth of shower maximum X_{\max} and its fluctuations for the two scenarios: (1) maximum-rigidity model; (2) photo-disintegration model. The $\text{RMS}(X_{\max})$ contains the intrinsic air-shower fluctuations and the detector resolution. The same quantities as expected for pure p and pure Fe compositions are illustrated. The difference in the evolution of the mass compositions of the two models in the energy range of the flux suppression can be distinguished with high significance.

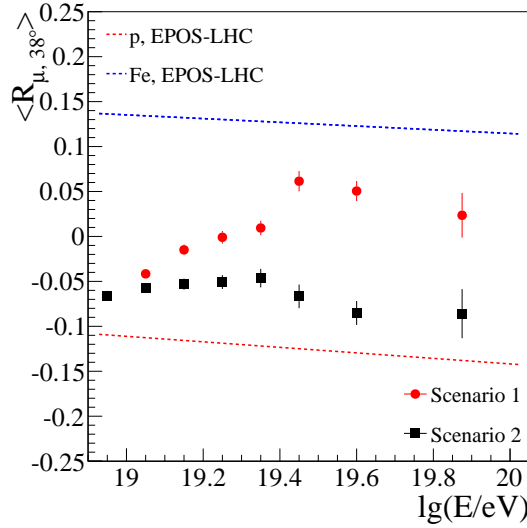


Figure 3.17: Reconstructed mean relative muon number R_μ for an equivalent shower at 38° zenith angle. The expectations for pure p and pure Fe compositions are shown together with the two scenarios: (1) maximum-rigidity model; (2) photo-disintegration model. In the energy range of the flux suppression the models can be distinguished with high significance.

and the $\text{RMS}(X_{\max})$ are depicted in Fig. 3.16. The RMS contains the intrinsic air-shower fluctuations and the reconstruction resolution. The number of muons, R_μ , relative to that expected for an equal mix of p-He-CNO-Fe as primary particles, is shown in Fig. 3.17. The

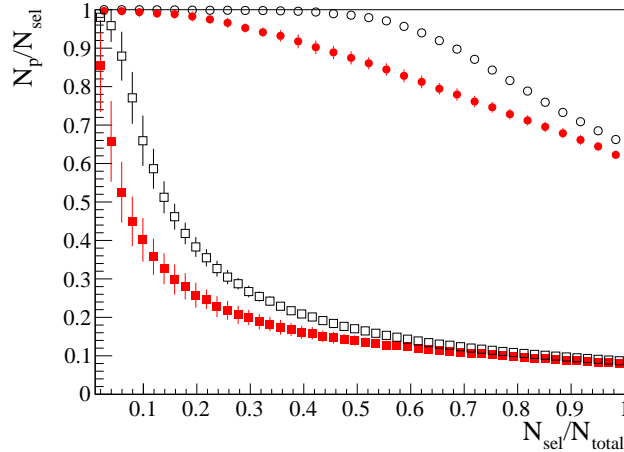


Figure 3.18: Purity of the selected proton-enriched sample (N_p/N_{sel}) as function of the fraction of events selected with the cut ($N_{\text{sel}}/N_{\text{total}}$). There are 10% protons added to both model scenarios to ensure that there is non-vanishing number of protons in the initial data sample. Squares are scenario 1, and circles are scenario 2. The solid symbols show the selection using the reconstructed observables and the open symbols corresponding to the theoretical limit, i.e. a selection based on the generated (true) X_{max} and R_μ .

expectations for pure p and pure Fe compositions for the same variables are also illustrated. While the mean X_{max} , $\text{RMS}(X_{\text{max}})$ and R_μ are very similar up to $10^{19.2}$ eV, the energy range that is well covered by data of the fluorescence telescopes, the models predict significantly different extrapolations into the GZK suppression region. This difference is well reproduced with the reconstructed X_{max} , $\text{RMS}(X_{\text{max}})$ and R_μ and the two scenarios can be distinguished with high significance and statistics.

Selection of light primaries

Another very important feature of the upgraded array will be the possibility of selecting data sets enriched with light or heavy primaries. Such a selection will be needed for searching for a proton component in the primary flux at the highest energies, and for carrying out anisotropy studies with light/heavy primaries.

Using the reconstructed X_{max} and R_μ in a Fisher discriminant analysis, one can apply event by event a selection cut and study the purity of the selected data sample as function of the selection efficiency. The result of such a selection is shown in Fig. 3.18 for energies greater than $10^{19.4}$ eV with the aim of selecting a proton-enriched data sample. As the reference model 1 (maximum-rigidity scenario) does not predict any protons at such a high energy we have added proton events equivalent to 10% of the flux at all energies. The open symbols show the result if the selection is applied to the true X_{max} and R_μ values, i.e. for a perfect detector with vanishing resolution. The difference between the solid symbols and the open symbols shows the effect of the limited detector and reconstruction resolution. For example, in the model of scenario 1 there are exactly 10% protons at this energy. Therefore a purity of 0.1 is expected if one selects all events $N_{\text{sel}}/N_{\text{total}} = 1$. And selecting the 10% most proton-like events, the purity of the sample will be 40%. These numbers are very different for model 2 (photo-disintegration scenario). Due to the presence of a large fraction of protons, a purity

Table 3.5: Examples of parameters for which the correlation of observed arrival directions with selected astrophysical objects is the strongest (i.e. maximum departure from isotropy). The energy threshold for event selection is E_{th} and the maximum angular difference is $\Delta\Psi$. The second section of the table shows the parameters for luminosity-selected AGNs with \mathcal{L}_{min} . The nominal p value and the chance probability accounting for the parameter scans are given as f_{min} and $\mathcal{P}_{\text{scan}}$. For details see [21].

Objects	E_{th} [EeV]	$\Delta\Psi$ [°]	D_{max} [Mpc]	\mathcal{L}_{min} [erg/s]	f_{min}	$\mathcal{P}_{\text{scan}}$
2MRS Galaxies	52	9	90	-	1.5×10^{-3}	24%
Swift AGNs	58	1	80	-	6×10^{-5}	6%
Radio galaxies	72	4.75	90	-	2×10^{-4}	8%
Swift AGNs	58	18	130	10^{44}	2×10^{-6}	1.3%
Radio galaxies	58	12	90	$10^{39.33}$	5.6×10^{-5}	11%
Centaurus A	58	15	-	-	2×10^{-4}	1.4%

of 90% is already reached by selecting 40% of the most proton-like events. These studies show that the upgraded surface array of the Auger Observatory does indeed allow us to detect a proton component in the primary flux with a relative contribution of 10% or more.

3.8.2 Composition enhanced anisotropy

In the following we will consider anisotropy studies applied to a data set with the statistics collected by the Auger Observatory until now [21]. To illustrate the gain in sensitivity we will have due to adding scintillator detectors to the surface array we will compare analyses of the same simulated data sets with and without the additional information provided by the upgraded array.

The improvement of the sensitivity of the upgraded Auger Observatory for searching for source correlations can be demonstrated by studying the expected correlations with sources, first without making any specific assumptions. In this study the arrival direction is considered to correlate by chance with an object of a reference catalog of sources with the probability p_{iso} , i.e. if the arrival direction distribution were isotropic. This probability follows from the number of sources times the solid angle around the sources that is taken for defining a correlation, and also depends on the source distribution within the sky exposure of the Auger Observatory. For example, for AGNs of the Véron-Cetty–Véron catalog [139] within a distance of up to 75 Mpc ($z < 0.018$) and considering a particle as correlated if it arrived with an angular distance of less than 3.1° to an AGN, one has $p_{\text{iso}} = 0.21$ [18]. Other examples taken from the latest correlation study are given in Tab. 3.5, see also [21]. The results of this generic study are given in Fig. 3.19 for three scenarios and assuming a merit factor of 1.5, see Tabs. 3.3 and 3.4. The assumed statistics of 155 events above an energy threshold of about 5.5×10^{19} eV corresponds to the currently collected exposure of the Auger Observatory [21]. In all cases it is assumed that heavy elements are distributed isotropically and only protons contribute to the correlation beyond random coincidences. The scenarios differ in the fraction of protons that correlate with the sources, which are 100%, 75% and 50%. For example, in the 75% scenario it is assumed that 25% of all protons are distributed isotropically. In all

cases the sensitivity to sources is improved by being able to select light elements with the separation power given by the merit factor of the proposed upgrade. The improvement is the largest for the 100% scenario. For example, having a 10% fraction of protons correlating with sources corresponding to $p_{\text{iso}} = 0.2$ will result in a deviation from isotropy of about 2.5σ if the primary particles masses cannot be discriminated. Having a merit factor of 1.5 for discriminating light from heavy particles will increase this signal to more than 4.5σ .

As a next step we want to illustrate the increased sensitivity of the upgraded Auger Observatory with a more specific example. We use the arrival directions of the 454 measured events with $\theta < 60^\circ$ and energy higher than 4×10^{19} eV (see [21]) and randomly assign each event an X_{max} value according to model 1 (maximum-rigidity scenario). To implement a 10% proton contribution we assigned 10% of the events a proton-like X_{max} . Half of these randomly chosen, proton-like events were given arrival directions that correlate with AGNs with a distance of less than 100 Mpc of the Swift-BAT catalog [140] within 3° . The other half were chosen with larger angular distances. By construction, this artificial data set reproduces many arrival direction features found in the Auger data while at the same time having a model-predicted mass composition.

Analyzing this data set without using any composition information a correlation with the AGNs of the Swift-BAT catalog is found at a level similar to that reported in [21]. The improvement of the sensitivity to find the correlation with AGNs in this data set is shown in Figs. 3.20 and 3.21. The top row of plots shows the results of the complete data sets with the energy thresholds 4×10^{19} eV and 5.5×10^{19} eV. The middle row shows what one would obtain in a correlation study if the proton-like events are removed from the data set. This is done by selecting events with a reconstructed X_{max} of less than 770 g/cm^2 at 10^{19} eV, adjusted to the event energies with an elongation rate of 55 g/cm^2 per decade. By selecting events with X_{max} larger than 770 g/cm^2 a proton-enriched data sample is selected. While the correlation of the arrival directions with that of AGNs in the Swift-BAT catalog is not significant for the complete data sets, a correlation well in excess of 3σ can be found for the proton-enriched samples. Furthermore the proton-deprived selections exhibit no correlation with the AGNs at all, as one would expect for an angular correlation that is just a statistical fluctuation.

These conservative examples of composition-improved anisotropy studies underline the large gain of sensitivity achieved by adding scintillation detectors to the water-Cherenkov detectors of the Pierre Auger Observatory.

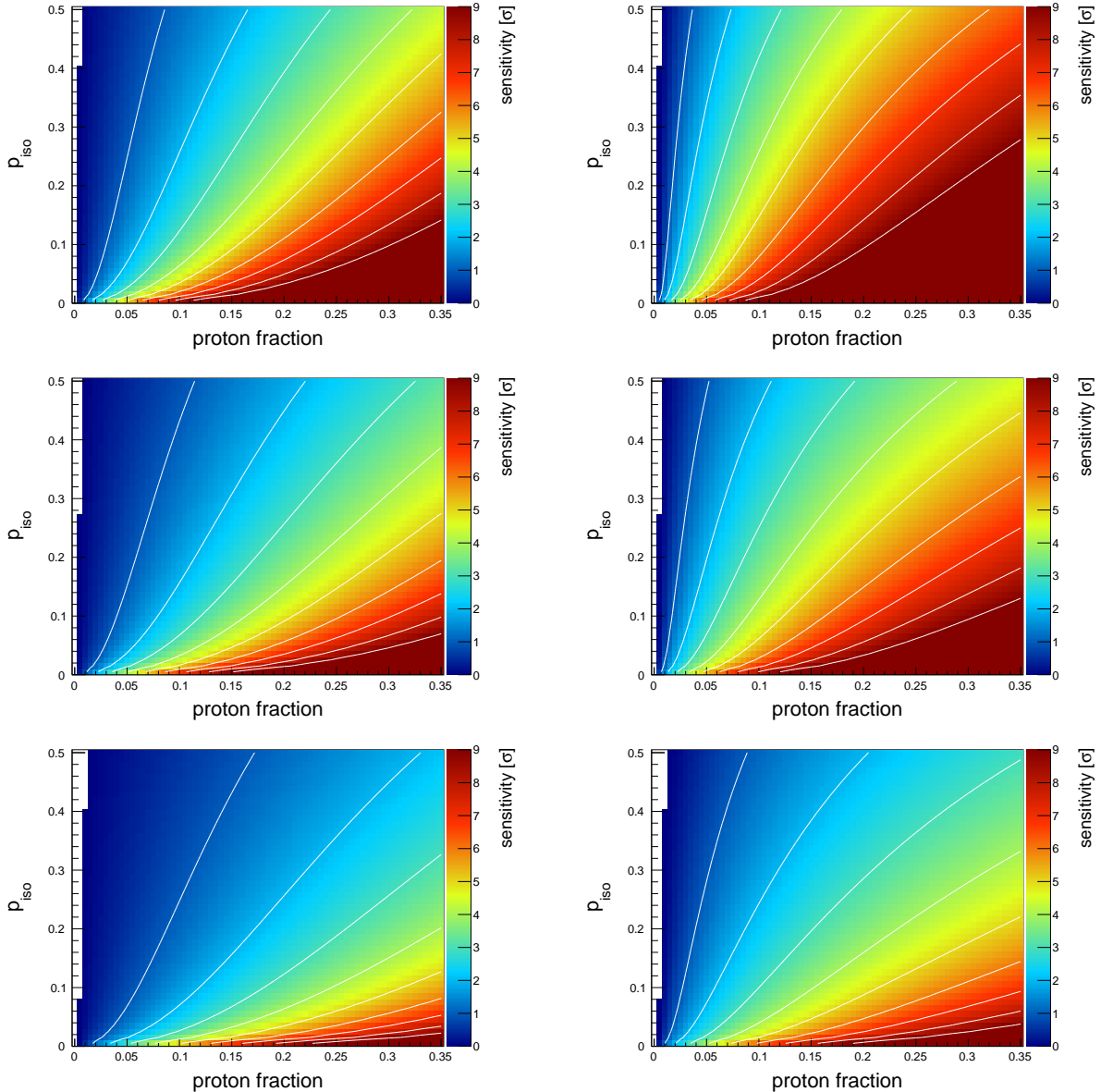


Figure 3.19: Expected correlation of the observed arrival direction distribution with a source catalog and selection criteria characterized by p_{iso} (see text) to a given proton fraction in the data. The upper row shows the scenario in which 100% of all protons are correlated with the sources of the catalog. The middle and lower rows are calculated for 75% and 50%, respectively. The plots on the left hand side are showing the correlation expected for the current surface array, and the ones on the right hand side for the upgraded array, both calculated for the same exposure. The white lines show the 1 σ to 9 σ thresholds from left to right.

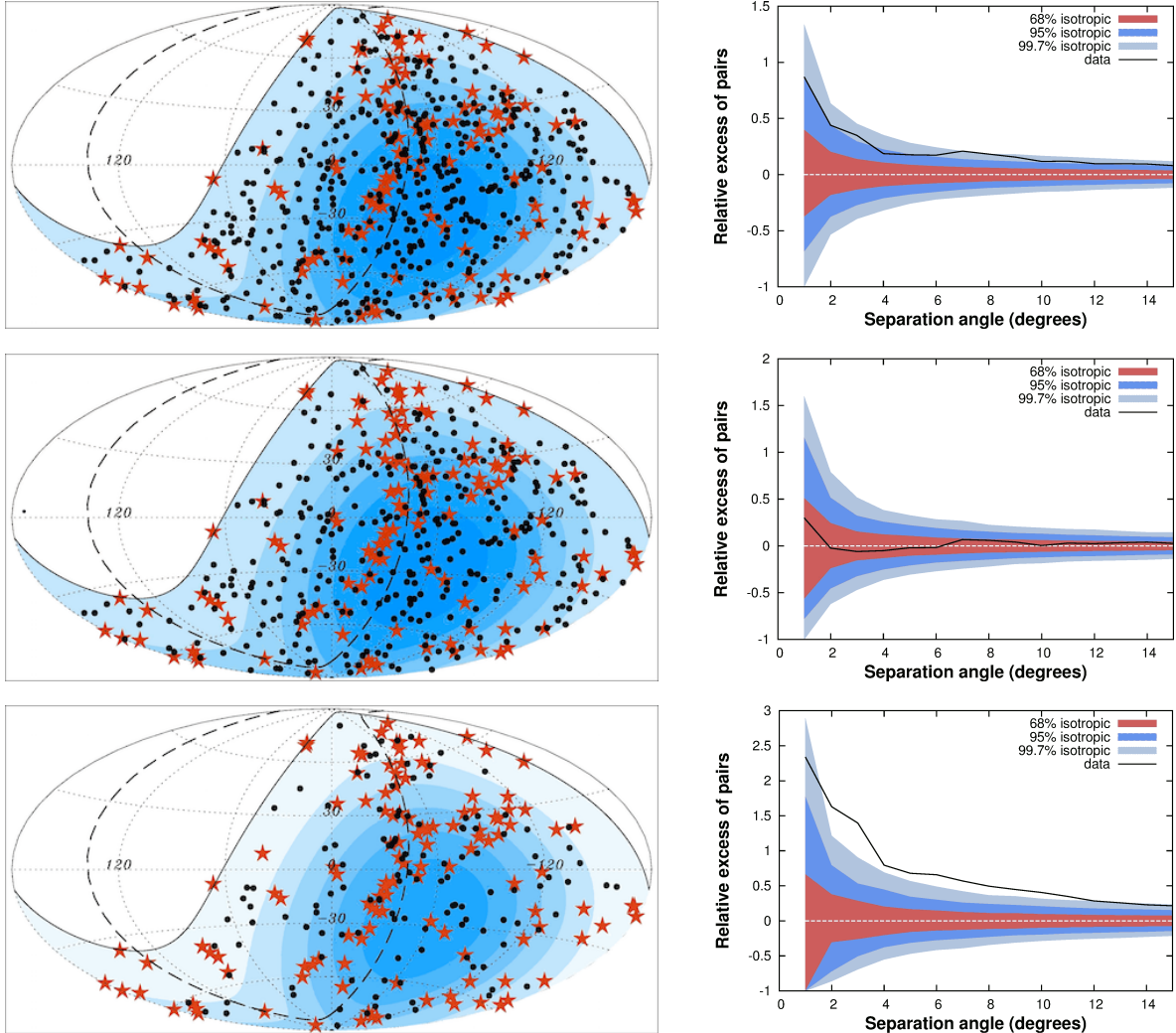


Figure 3.20: Arrival distribution and angular correlation of cosmic rays of the modified Auger data set (black circles) with AGNs of the Swift-BAT catalog [140] (stars). Shown are events with $E > 4 \times 10^{19}$ eV. The top row of plots show the complete data set (454 events), the middle row the selection deprived of light elements (326 events), and the bottom row the proton-enriched selection (128 events).

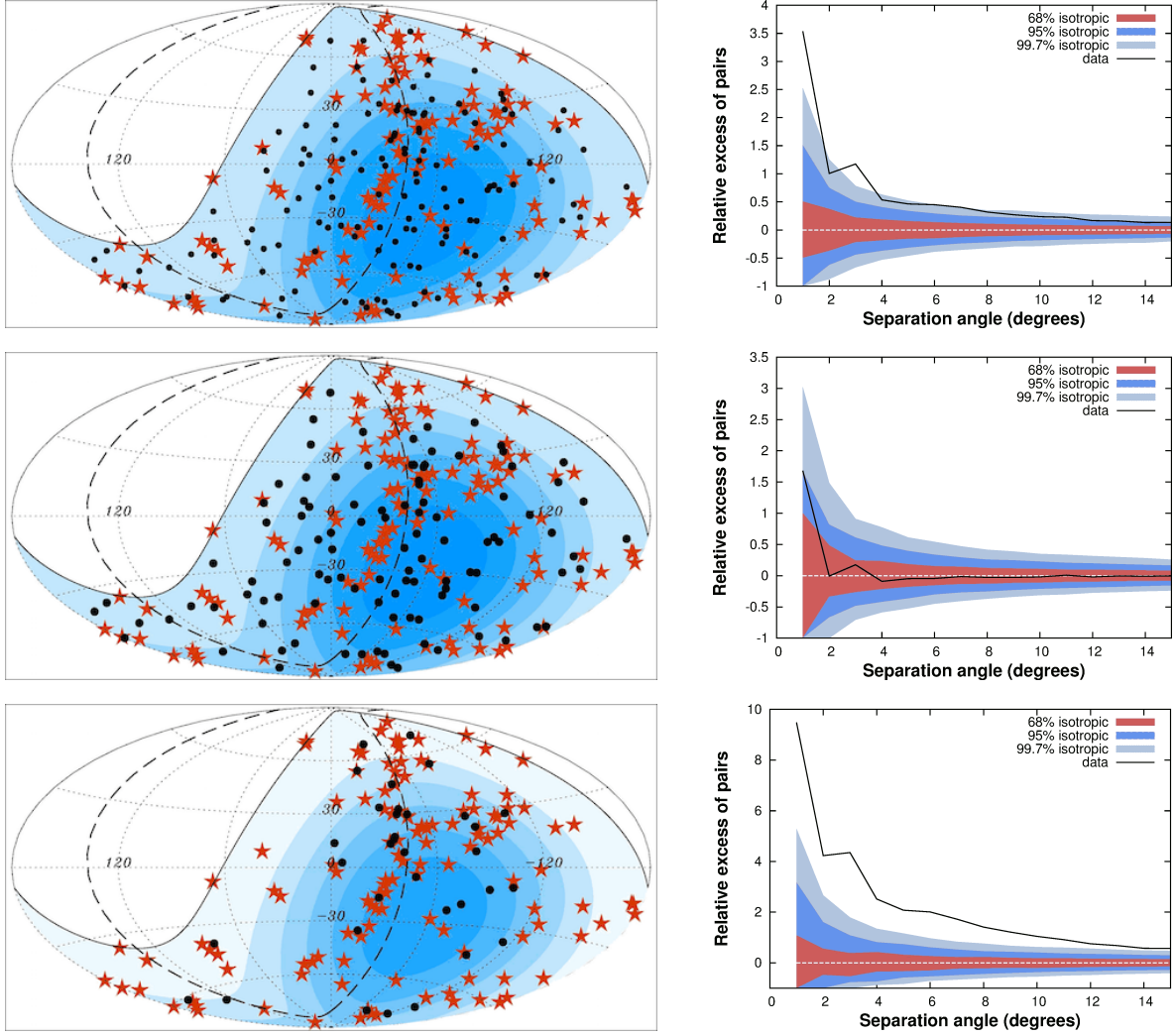


Figure 3.21: Arrival distribution and angular correlation of cosmic rays of the modified Auger data set (black circles) with AGNs of the Swift-BAT catalog [140] (stars). Shown are events with $E > 5.5 \times 10^{19}$ eV. The top row of plots show the complete data set (141 events), the middle row the selection deprived of light elements (107 events), and the bottom row the proton-enriched selection (34 events).

Chapter 4

The Surface Detector

The operating surface detector (SD) of the Pierre Auger Observatory comprises 1660 stations on a 1500 m triangular grid covering 3000 km². Each station is a water-Cherenkov detector (WCD) which samples the particle content of the extensive air showers (EAS) falling on the array (see Appendix B.2). The SD is overlooked by four fluorescence detector sites (FD), each with 6 fluorescence telescopes viewing an aggregate 180° azimuth by 30° elevation field of view. Additional detectors and a region with reduced detector spacing, known as the *infill* array, focus on lower energies, muon detection, and radio R&D.

The SD stations will be upgraded with new electronics for faster sampling of the PMT signals, better timing accuracy and enhanced triggering and processing capabilities, new light sensors for increased dynamic range, and improved calibration and monitoring capabilities.

New surface scintillator detectors (SSD) will be placed on top of each WCD to sample the EAS in another way. Given the different sensitivities of plastic scintillators and water-Cherenkov detectors to the electrons, photons, and muons of EAS, the combination of measurements will provide EAS muon content information, vital for cosmic ray mass composition studies and improved energy determination.

4.1 The Water Cherenkov Detector

Each WCD is a rotomolded polyethylene tank filled with purified water that produces Cherenkov light when crossed by energetic charged particles associated with CR showers. A flexible Tyvek liner inside the tank provides an interface between the water volume and the light sensors that collect Cherenkov light (PMTs) and the light sources that produce calibration pulses (LEDs). Access to the liner, the PMTs and the LEDs is through three hatches located on the top of the tank. An electronics box containing front-end charge amplifiers, shapers, trigger logic, signal buffers, power control, radio transmitter and receivers is located on the top roof of the tank on one of the hatch-covers and is protected by a dome. All the cables connecting the electronics and the light sensors run inside the tank and connect to the electronics via feed-throughs in the hatch covers. Figure B.4 shows a picture of an operating WCD.

Table 4.1: Basic properties of the SD photomultiplier tubes

Specification	Unit	LargePMT (LPMT)	SmallPMT (SPMT)
Diameter	mm	230	<30
Height (glass)	mm	256	<90
HV (max)	V	1950	1500
Gain (max)	10^6	3	40
QE (peak)	%	>16% 420nm	>16% 420nm
Anode dark current	nA	15 to 50	2 to 15
Anode rise time	ns	<5	<3
Anode pulse linearity ($\pm 5\%$)	mA	50	60 ¹

4.1.1 Photomultipliers

The WCDs in the field have a redundant set of three identical, large collecting area (230 mm diameter) Photonis XP1805 photomultipliers. We refer to these as the *Large PMTs* (LPMT), for which we are not envisaging upgrades.

In addition, a fourth, new phototube with a significantly smaller cathode surface, called the *Small PMT* (SPMT), will be added to the WCD to extend its dynamic range. An empty liner window facing the water volume, located near the center of the tank and originally planned for a spare LED, can be used for a straightforward installation of the SPMT, the diameter of which is therefore constrained to be less than 30 mm in order to fit in this window.

The new electronics (Section 4.3) will read and digitize the SPMT anode signals with a dedicated input, analogous to those for the LPMTs. As the single muon signal peak (VEM, see Section B.2) is not visible in the SPMT signal response, the scale of the SPMT signal in physical units (VEM) will be determined by cross-calibrating the SPMT and LPMT signals that occur in their overlapping region before saturation, and monitored with LED signals in the same signal region.

By fine tuning the SPMT gain and the signal overlap with the standard PMTs we expect to be able to extend the WCD dynamic range by an adjustable factor ranging from ~ 10 to ~ 60 .

We summarize in Table 4.1 the basic mechanical and electrical parameters of the SD PMTs.

We have qualified three models with the required performance for the SPMT (Hamamatsu R8619, Hamamatsu R6094, ETL9107B). The R8619 is our current baseline SPMT model, as it satisfies all technical requirements and is industrially produced in large quantities, with benefits on yield and cost. We will use the first field tests to verify the performance of all candidates in realistic conditions.

Prototype mechanics for supporting the SPMT in the LED window were successfully built with 3D printers and tested in the field. Molds will be engineered for cost-effective mass fabrication.

¹with tapered ratio divider

Table 4.2: Basic properties of HV power supplies for the Small PMT and the Scintillator Detector

Specification	Unit	SensTech-PS2010/12	CAEN-A7501P
Input Voltage	V	11.75 to 12.25	$12 \pm 5\%$
Max High Voltage	V	2000	2100
Output current (at Max HV)	μA	100	110
Output voltage temperature stability	$10^{-5}/^\circ\text{C}$	4.7	2.5
Output voltage Ripple	ppm	15 to 39	1.9 to 3.8
Power dissipation (at Max HV)	mW	400 ± 13	398 ± 4
Operating Temperature range	$^\circ\text{C}$	-10 to 60	-40 to 70

4.1.2 High Voltage Modules and Control

The operating LPMTs are equipped with an active base which includes the High Voltage (HV) resistive divider, a HV DC-DC converter module and a charge amplifier for the dynode readout. The base is soldered to the PMT leads and protected with insulating silicone potting. Given the high level of moisture and severe temperature cycles inside the WCD, the potting proved to be far from ideal, resulting in a low but visible number of failures in the field, which we plan to minimize in the upgrade with an improved design for the SPMT, with the goal to reducing the necessary maintenance operations to a negligible level.

We therefore designed a simpler, passive resistive base for the new SPMT, and moved the HV DC-DC converter to a separate module that can be conveniently located outside the WCD and away from the moisture. The base will be located inside the WCD and will not be potted, but simply coated. The HV module will be housed in a dedicated box next to the station electronics.

We have qualified a new model for the HV DC-DC converter (CAEN-A7501P), with slightly better thermal stability, operational temperature range and power consumption with respect to the module used for the LPMTs (SensTech-PS2010/12) [141]. Specifications and test results for the two HV systems considered are illustrated in table 4.2.

We plan to use the same HV system for the Scintillator Detector. The LPMTs in the field will not be modified, but only repaired in case of failures, with replacement bases identical to the operating ones except for the dynode amplifier, which is no longer needed.

The Slow Control of the existing Unified Board handles High Voltage (HV) control and monitoring of the existing standard PMTs. The Upgraded Unified Board (UUB) (Section 4.3.5) will implement a new version of the Slow Control (Section 4.3.4) that will be able to handle up to six HV lines, and will be used to drive the large PMTs, the new Small PMT and up to two additional PMTs for the Scintillator Detector (Section 4.2). Separate HV boxes for the Small PMT and the Scintillator Detector will connect to the Slow Control on the one hand and to the PMTs on the other.

4.1.3 Calibration and control system

Absolute calibrations with physics events

With a large number of stations on the field, scattered over a very large area and often difficult to reach, it is important to be able to routinely calibrate and monitor each station remotely, with stable and robust procedures, and ensure a uniform response of the array in

terms of trigger rates and performance.

This is achieved by using trigger rates as proxies of the signal charge recorded by the tank PMTs. We vary each LPMT high voltage until we reach a target rate of 100 Hz, with a fixed threshold set at the signal of ~ 3 vertical and central through-going muons. The Vertical Equivalent Muon (VEM) signal is the baseline reference unit of the SD calibrations, and was determined on a test tank with an external trigger hodoscope to give on average 95 photoelectrons at the cathode of the LPMTs, corresponding roughly to 150 integrated ADC counts above pedestal after signal digitization. We then verified *a posteriori* that the rate proxy is an accurate approximation at the 5 to 10% level, and can be further refined to 3% using off-line analysis of the charge histograms taken from each PMT with a dedicated high-rate, low-threshold, short-duration trigger primitive.

When completed, this calibration provides uniform trigger rates, by definition, and an average LPMT gain of 3.4×10^5 , with a $\sim 5\%$ spread over the whole array.

This algorithm ensures quick convergence, it does not require complex algorithms to run on the local station processor, nor transmission of large data-sets through the communication system and can be easily repeated when large deviations from the reference VEM signal are recorded, for example from aging of the PMTs.

The calibration of the large signal range of the LPMTs, given by the anode readout, is not covered by this procedure due to poor statistics of large enough signals. Additionally, in the existing SD, the dynode signal is amplified on the LPMT base, causing relative delays with the anode signal which make the signal ratio time dependent and more complex than a simple scaling factor of 32, which could be simply calibrated by dividing the anode and dynode peaks of the signal distribution.

Therefore the anode signal is currently converted to physical units using the dynode calibration described above and a model of the relative time development of anode and dynode signals. Instead, for the SD Upgrade, a much simpler and direct cross-correlation of the signals in the overlapping regions will be possible, as the dynode signal will no longer be used, and the WCD dynamic range will be spanned by the amplified anode signal ($32\times$), the anode signal ($1\times$) and the Small PMT (we consider a nominal factor of $1/32$ over the anode signal, but this is adjustable being a signal from an independent light sensor).

We envisage similar rate-based calibrations for the upgraded WCDs, and will revisit the target rates with dedicated field measurements.

Monitor and control with Light Emitting Diodes

In addition to routine calibrations with physics events, each WCD is equipped with two Light Emitting Diodes (LEDs). While these are not stable sources of calibrated light, they are very useful for monitoring and control. We will use the LEDs already installed in the tanks for several different purposes:

- setup the initial working point of the SPMT, to be refined later with physics events, possibly with rate-based techniques;
- quickly cross-calibrating the three ranges of the upgraded WCD with arbitrary high rates;
- testing the linearity of each PMT by recording the difference between the signals of the two LEDs, when switched on with the same trigger pulse, and the sum of the two

- LEDs switched on independently;
- creating artificial extensive shower events on the SD array with arbitrary topology for verification of the acquisition and reconstruction chains.

We have integrated a new controller circuit into the Upgraded Unified Board (Section 4.3.5) that builds on the existing controller for driving separate and simultaneous triggers to the two LED flashers, but includes better timing of the trigger signals. In particular, it offers a hardware synchronization of the LED trigger pulses with the GPS-PPS signal, to be able to synchronize LED triggers simultaneously over all the WCDs in the array. The new controller drives software triggers with custom delays between tanks as to emulate any EAS topology over the SD. Finally, the Slow Control now provides an increased bias voltage on the LED to give enough light output to sample the full WCD dynamic range.

4.1.4 Solar power system

Power for the Surface Detector stations is provided by a solar photovoltaic system. The power system provides 10 W average power. A 24 V system has been selected for efficient power conversion for the electronics. The system consists of two 55 Wp solar panels and two 105 Ampere-hour (Ah), 12 V batteries. The batteries are lead acid batteries designed for solar power applications. Power is expected to be available over 99% of the time. Even if after long term operation the capacities of the solar panels and batteries are degraded to 40 Wp and 80 Ah, respectively, power would be available 97.8% of the time.

One of the requirements for the new electronics was to have a sufficiently low power consumption to be able to use the existing power system. Current estimates of the power consumption indicate that the existing power system is sufficient to operate both the WCD and the SSD detectors. An additional power system is needed only in the infill area to accommodate the Underground Muon Detector.

4.2 The Scintillator Detector

4.2.1 Introduction and design objectives

The main objective of this additional array of detectors is to add an extra measurement of the particles in the EAS independent of the measurements made with the water-Cherenkov detectors. To achieve the maximum advantage from this additional measurement, the shower should be sampled in the position of the WCD with a detector that has a different response to the basic components of the EAS compared to the present stations. Additionally, the additional detector has to be reliable, easy to realize and install, and has to have minimal maintenance.

The design chosen consists of a detector based on a plane of plastic scintillator positioned on top of the existing surface detectors, and read in an integral way using only one photodetector. With this technique, the signal collected with the scintillator unit can be compared directly with the signals collected in the WCD. In particular, the amplitude and time distribution of the collected signal in the scintillator are different from those coming from the signals collected by the WCD tanks due to the fact that the signal in the scintillator will be dominated by signals from electrons while the WCD will be dominated by photons and muons.

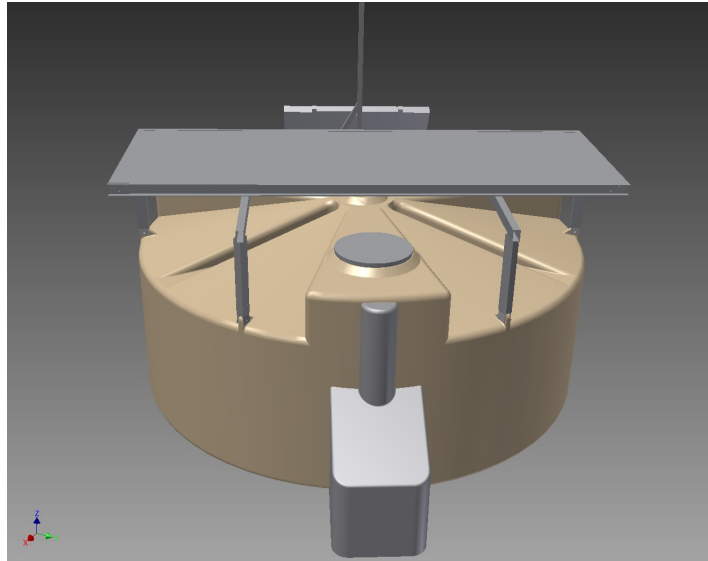


Figure 4.1: 3D view of a water-Cherenkov detector with a scintillator unit on top.

The scintillator units have to be precisely calibrated with a technique similar to the calibration procedure of the WCD (cf. section 4.2.7). The size of the detector and its intrinsic measurement accuracy should not be the dominant limitations for the measurement. The dynamic range of the units has to be adequate to guarantee the physics goals of the proposed upgrade.

The detector will be assembled and tested in parallel in multiple assembly facilities to reduce the production time and, therefore, has to be easily transportable. The mechanical robustness of the scintillator units must be ensured. The units will be shipped after assembly, and validated at the Malargüe facilities of the Pierre Auger Observatory before being transported to their final destination on top of a WCD in the Pampa. They will then have to operate for 10 years in a hostile environment, with strong winds and daily temperature variations of up to 30°C.

4.2.2 Detector design

The baseline design relies only on existing technology for which performance measurements have been made. The Surface Scintillator Detectors (SSD) basic unit consists of two modules of $\approx 2 \text{ m}^2$ extruded plastic scintillator which are read out by wavelength-shifting (WLS) fibers coupled to a single photo-detector. Extruded scintillator bars read by wavelength-shifting fibers have already been employed in the MINOS detector [142]. The active part of each module is a scintillator plane made by 12 bars 1.6 m long of extruded polystyrene scintillator. Each bar is 1 cm thick and 10 cm wide. The scintillator chosen for the baseline design is produced by the extrusion line of the Fermi National Accelerator Laboratory (FNAL) [143].

The bars are co-extruded with a TiO_2 outer layer for reflectivity and have four holes in which the wavelength-shifting fibers can be inserted. The fibers are positioned following the grooves of the routers at both ends, in a “U” configuration that maximizes light yield and allows the use of a single photomultiplier (at the cost of a widening of the time response of the detector by 5 ns, which has a totally negligible impact). The fibers are therefore read

out from both ends. Figure 4.2 shows a sketch of two bars with the fiber readout. The two-ended readout of the scintillator strips also provides a better longitudinal uniformity in light response.

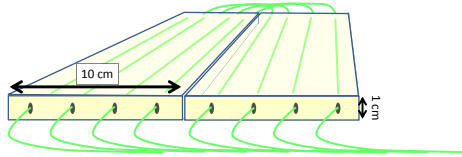


Figure 4.2: Sketch view of bars with the fiber readout.

Two companies, Kuraray and Saint Gobain, produce suitable WLS multi-clad optical fibers for our application. The Kuraray fibers have a higher light yield and are more readily available. They have also been used for optical read-out in most large area scintillator counter experiments. For these reasons they were chosen as the baseline design option. However the Saint Gobain WLS fiber may have a lower cost and the possibility to make use of them is currently under investigation.

For the baseline design, the Kuraray Y11 WLS multi-clad optical fiber with 1 mm diameter is chosen, with a concentration of fluorescent dye at either 200 or 300 parts per million. As shown in Figure 4.3, the absorption spectrum of the K27 dye (Y11 fiber) matches perfectly the scintillator emission [144]. On the other hand, the WLS fiber emission is shifted toward longer wavelengths than the absorption peak of a standard bialkali photocathode, thus suggesting some caution during the selection of the read-out photodetector.

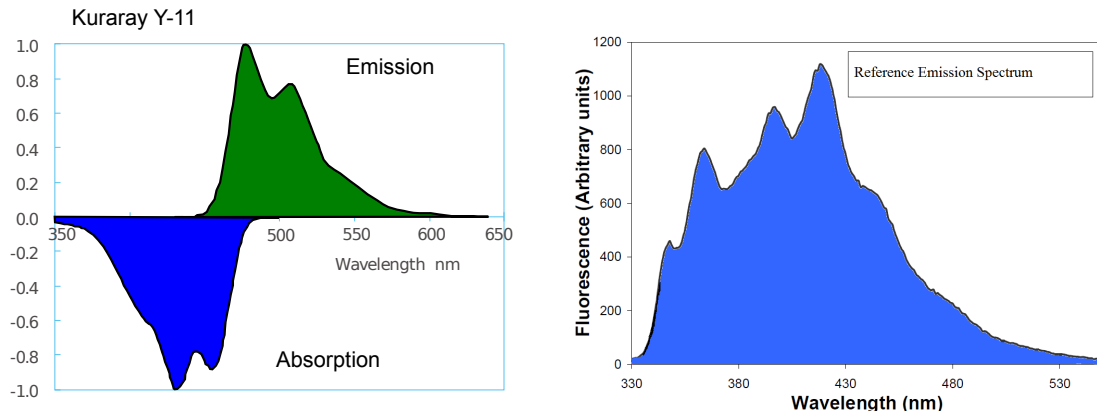


Figure 4.3: Left: emission and absorption spectra for Kuraray Y11 WLS fiber. Right: Reference emission spectrum of the chosen extruded scintillator.

The WLS fibers will be of S-Type to allow shorter bending diameter (Figure 4.4) and minimize the risk of damage during the detector assembly. In fact, the S-type fiber core has a molecular orientation along the drawing direction. This fiber is mechanically stronger against cracking at the cost of transparency; the attenuation length of this type is nearly 10% shorter than the standard type. Kuraray conservatively recommends a bend diameter 100 times the fiber diameter. Accordingly, the fiber routers have been designed with curvature

radii of 5 cm. The chosen “U” shape design means each fiber goes through two holes of the scintillator bars. To keep the proper radius of curvature, the same fiber has to pass from one bar to its neighbor.

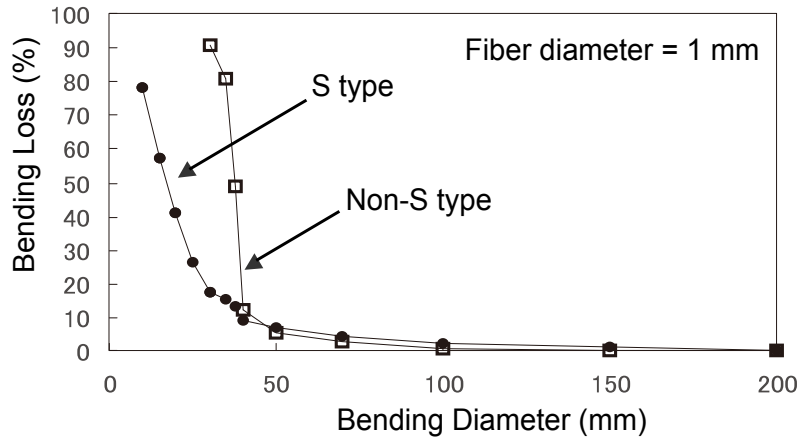


Figure 4.4: Light yield loss due to fiber bending.

A 6% non-uniformity [145] of the module can be obtained by cutting the fibers at the same length and forcing them to follow a particular route (a “snake” route) from the bars to the photo-detector (see Figure 4.5). Given this design, the length of each fiber is 1.6 m (bar length) $\times 2 + 1.2$ m (module width) $\times 2 + 0.16$ m (“U” shape) $+ 0.24$ m $\times 2$ (“snake” route) $+ 0.10$ m (tolerance at the two edges of the scintillator bars and for merging into the optical connector). The total length of each of the 24 fibers is therefore 6.3 m.

The performance of the SSD comes mainly from calibration requirements and, then, from the width of the MIP distribution, which is dominated by Poisson fluctuations of the number of photoelectrons (see Sec. 4.2.7). Therefore, the non-uniformity of the module can be increased up to 10% without deteriorating the performance of the SSD. This permits the possibility that the fiber lengths in the module need not be all equal, and a consequent cost saving.

The bars within a module are glued to an extruded polystyrene foam (XPS) plane, forming a rigid structure for easy handling and mounting. The ends of the modules have XPS manifolds which route the WLS fibers to bulk optical connectors.

A schematic view of the two basic modules that make up one detector is shown in Figure 4.6. The scintillator bars are hosted inside a vessel that will be provided, ready to use, by specialized companies. The bottom part will be delivered with the routers for the optical fibers already embedded to simplify the detector assembly.

The fiber bundle termination of one module is then inserted and glued inside (one half of) a special optical connector designed to allow the optical junction of the two modules. After the assembly and testing, the XPS vessel is hermetically sealed; a short fiber bundle tail is left free in one corner. The surface of the optical connector needs to be machined with a fly-cutter when the epoxy glue used for the fiber bundles is hardened. Six extra holes for fibers will be machined in the optical connector to allow replacement of fibers that may be broken during construction or shipping.

The optical connector with the 48 fibers of the two modules (24 each) is connected by a soft silicon pad to a single photo-detector, integrating the total charge of all the bars (see



Figure 4.5: Pictures of the extruded polystyrene manifold used in the prototype to route the WLS fiber. Left: external side of each module with the “U” shape. Right: internal side of each module with the “snake” shape.

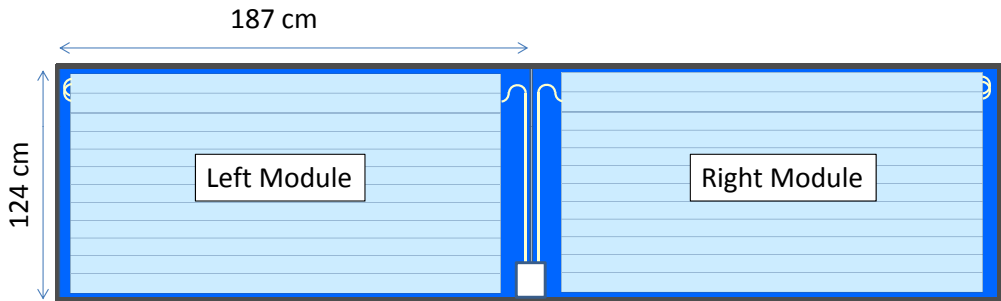


Figure 4.6: Schematic view of the two modules in the extruded polystyrene foam vessel. The dimensions of the vessel are quoted in the figure.

Figure 4.7). The signal of the photo-detector is then split in two: one is attenuated by a factor of 4, while the other is amplified by a factor of 32 to achieve a sufficient dynamic range. The power needed for operation is close to 1 W and can be taken directly from the current power system without the need of an extra solar panel.

As will be discussed in more detail in section 4.2.5, the external detector enclosure is made from aluminum to guarantee light tightness, robustness for 10 years of operation in the field, and enough rigidity for transportation. The access to the PMT is obtained with a mobile door in one side of the detector box. A double aluminum roof is installed, separated by 2 cm, to allow air flow and therefore reduce the temperature changes. This design for temperature has been checked with previous prototypes named ASCII as can be seen in Figure 4.8. The temperature control is of extreme importance not only for the correct behavior of the electronics but also with respect to the aging of the detector. Extensive studies have

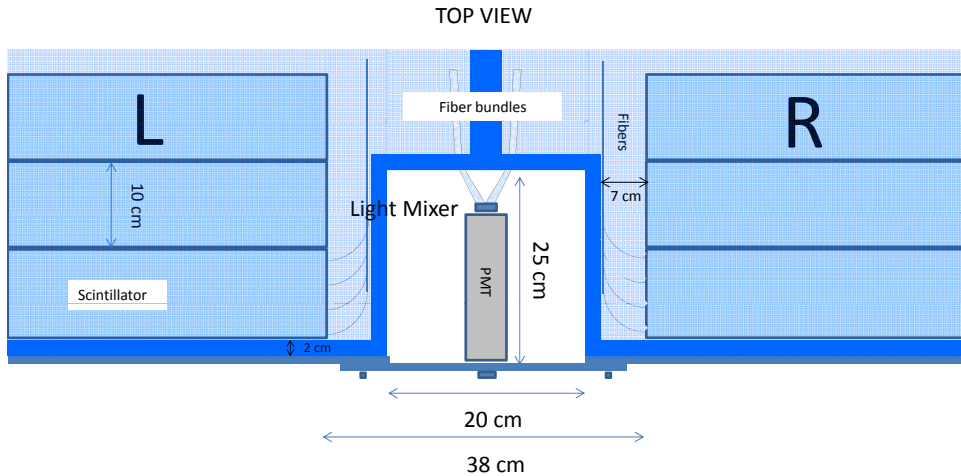


Figure 4.7: The photo-detector that collects the light produced by the two bundles of fibers.

been made for the MINOS detector [142], and the aging was found to be directly related to the temperature. Using the results from the MINOS team, which have been validated during 10 years of operation of their detector, and using the temperatures observed in 2014 from Figure 4.8, we obtain an expected light loss due to aging of 2.8% per year. For the design we will therefore assume a 30% light loss over 10 years of operation. While the MINOS team reports no effect during tests of temperature cycling, different groups in the collaboration are repeating these cycling measurements given the sometimes-strong 30 degree day-night temperature variations observed in Malargüe.

The total weight of one SSD unit is about 150 kg.

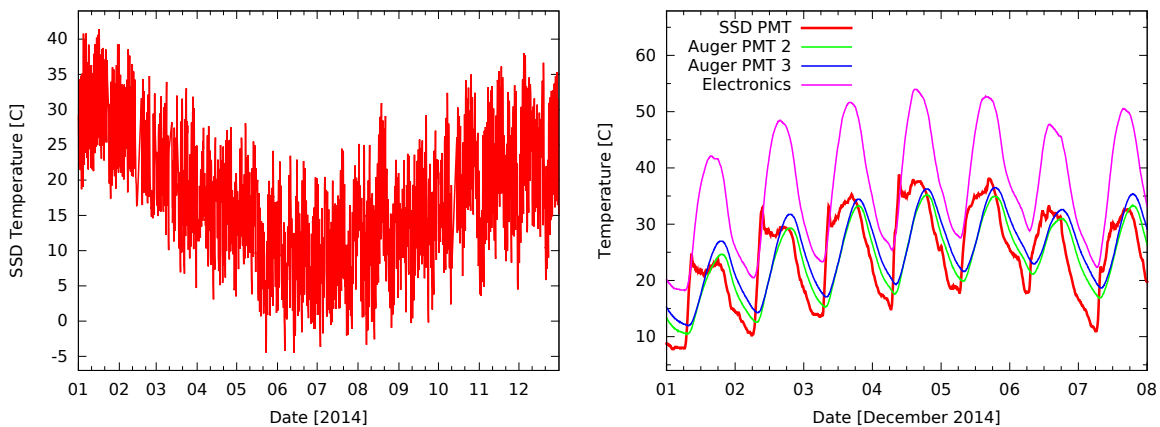


Figure 4.8: Left: one year of temperature measurements inside a 2 m^2 prototype of SSD in operation in the Pampa. The double roof keeps the detector below 40°C , even under the harsh direct sun of Malargüe. Right: temperature for the first week of December 2014 compared to the temperature of the WCD PMTs and of the electronics enclosure. The small peak in the SSD temperature in some mornings is due to direct sunlight reaching the PMT box which was exposed in the prototype design.

4.2.3 PMTs and HV power supply

The baseline SSD photomultiplier is the Hamamatsu R9420, head-on type, 8-stage PMT with a 38 mm bialkali photocathode. This PMT shows good quantum efficiency at the wavelength of interest (in the green region) associated with an excellent linearity range (when the PMT is supplied through a tapered ratio divider) of up to 200 mA of peak anode current for an operating gain of 7×10^5 (Figure 4.9). As an alternative, the performance of the lower cost Hamamatsu R8619 PMT is being investigated.

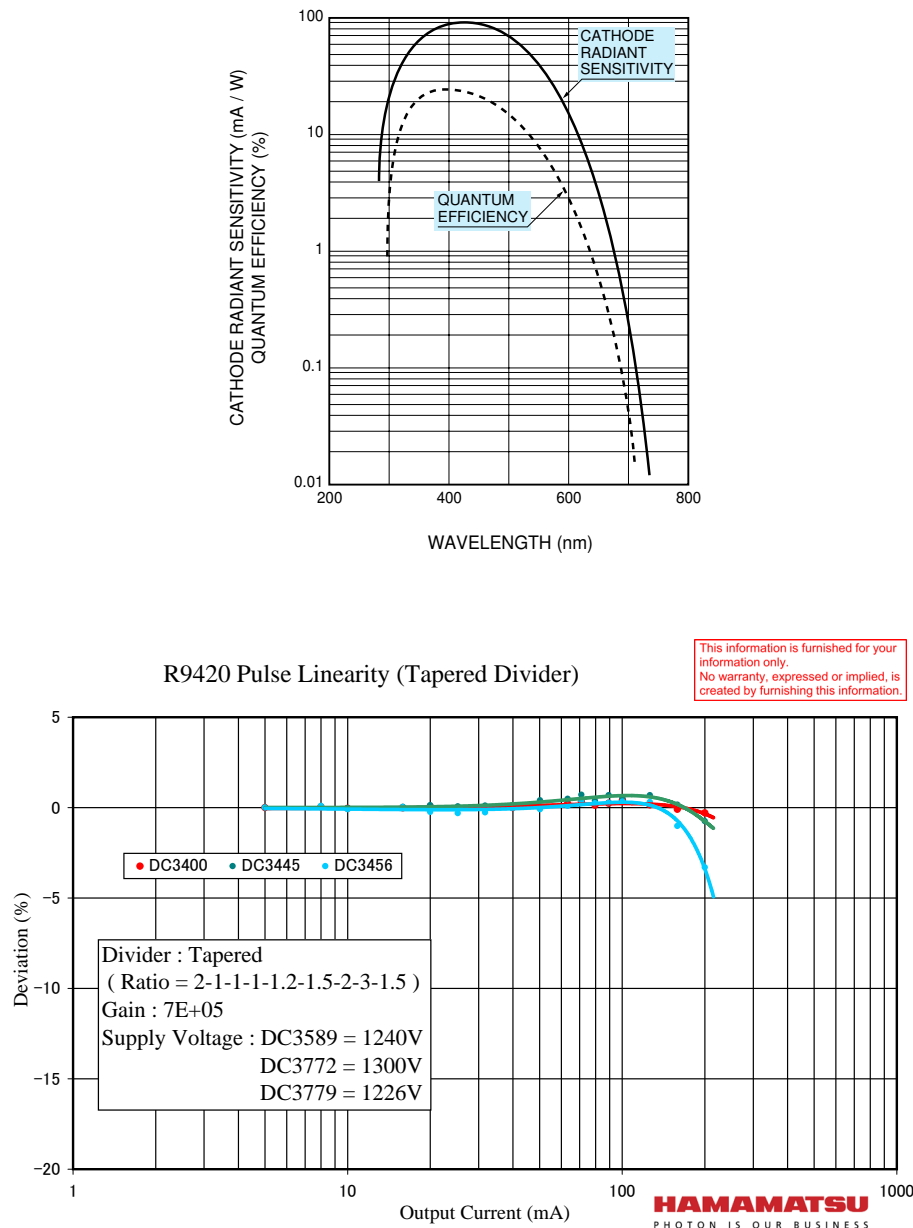


Figure 4.9: Top: Hamamatsu R9420 quantum efficiency. Bottom: Hamamatsu R9420 linearity.

The tapered divider has been designed, according to suggestions of Hamamatsu, with a large value of the total impedance, $60\text{ M}\Omega$, allowed given the very low average signal current. This design minimizes the consumption of high voltage power.

The HV module, which is produced by CAEN expressly for the proposal, has a power dissipation of less than 0.5 W with a maximum current of $110\text{ }\mu\text{A}$ (see table 4.2). It will located in a small box situated on top of the Upgraded Unified Board (UUB) enclosure, and be controlled by the UUB slow control signals. Cables with length less than 3 meters are required to connect the SSD unit to the companion WCD. No electronic buffers are required for signal transmissions. A RG59 type coaxial cable will be used for the PMT high voltage, and RG58 type cables will be used for all the other signals.

4.2.4 UUB integration

The SSD module will be integrated to the Upgrade Unified Board as an extra PMT. The Slow Control of the UUB will be able to handle up to six HV lines. One of these lines will be used to control the SSD HV with the same connection as for an existing PMT (including a temperature sensor).

The anode signal of the R9420 photo-detector will be filtered and split into two in a similar way to the signal from the standard WCD photo-detectors, Sec. 4.3.2. To achieve the required dynamic range after the splitting, one of the two signals is attenuated by a factor of 4 while the other is amplified by a factor of 32. Figure 4.18 shows the full dynamic range of the SSD ranging from 1 to 20,000 MIP (minimum ionizing particles).

4.2.5 Mechanical assembly

The availability of important complex components ready to be assembled is of primary importance to simplify the detector production and reduce the time needed to complete the project.

One of the detector components that can be manufactured by external companies is the vessel hosting the scintillators. For its realization, extruded polystyrene foam (XPS) was preferred because its mechanical properties well fit our application. Indeed, XPS is waterproof, sufficiently strong and durable for a long period, and furthermore, it is very light and easy to model.

Following our design, the first prototype vessels were produced by a specialized company in Italy. They were built starting from commercial, 10 cm thick XPS slabs, commonly used for thermal insulation. The vessels will be delivered to the assembly factories ready to use, saving work and time in the module construction.

The external aluminum structure of the baseline design is realized to guarantee enough robustness for 10 years of operation in the field and enough rigidity for transportation. A schematic view of the external structure is shown in Figure 4.10. The aluminum box consists of four "I" bars that form the external frame of the box. The top and bottom surface are made of two sheets of aluminum that are riveted to the frame. The choice to rivet the aluminum skin to the "I" bars gives the advantage of isolating the internal modules from water and dust and guarantees a better light tightness. The bottom part of the box is reinforced with extra aluminum bars (one every 36 cm) to support the scintillators.

The second aluminum roof is installed, separated by 2 cm, to allow air flow. The roof consists of a aluminum sheet of the same dimension of the box that is placed in position on

top the scintillator unit with five square tubes 2 cm wide (one every 1 m).

Inside the box the scintillator bars of each module are firmly fixed to the external frame with two tensioned bars per module (see Figure 4.11).

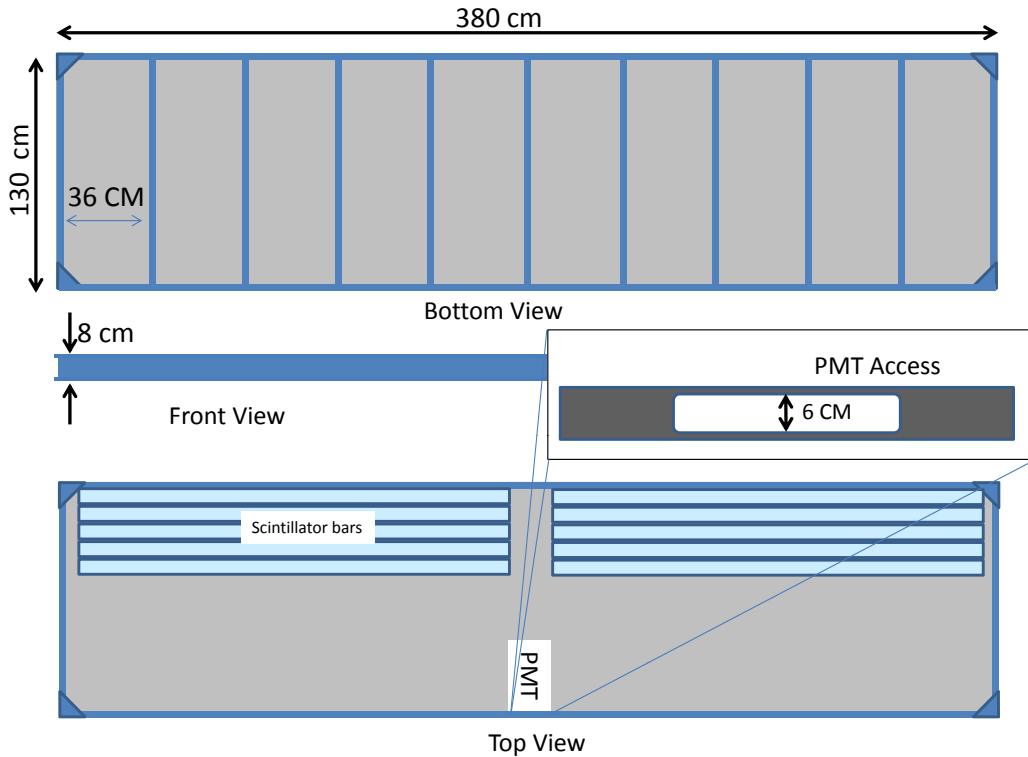


Figure 4.10: Schematic view of the aluminum external box.

The two scintillators modules are assembled together in the aluminum box. The photo-detector will be positioned in the center of the box between the two modules. A small hatch will guarantee the access to the photo-detector for maintenance.

The rigidity and robustness of the aluminum box reduces the complexity of the infrastructure needed to fasten the SSD unit onto the water-Cherenkov detector. Only few aluminum bars are needed because the box supports itself (see section 9.2). The supporting bars are attached to the WCD through the lifting lugs present on top of the tank structure (see Figure 4.12).

4.2.6 Detector testing

Two steps in testing are foreseen for an SSD unit. The first upon completion at any assembly site and the second in Malargüe before deployment. In both cases, as the fibers are not glued in the detector, the points of failure to explore are simply broken fibers. This means that no full scanning of the detector is needed, only a lateral scan of all bars. This can be done with a scanning table and a radioactive source, but given no longitudinal scan is needed, it can also be done with a simplified muon telescope, as long as the track of each muon detected by the SSD unit tested can be pinpointed to a specific bar.

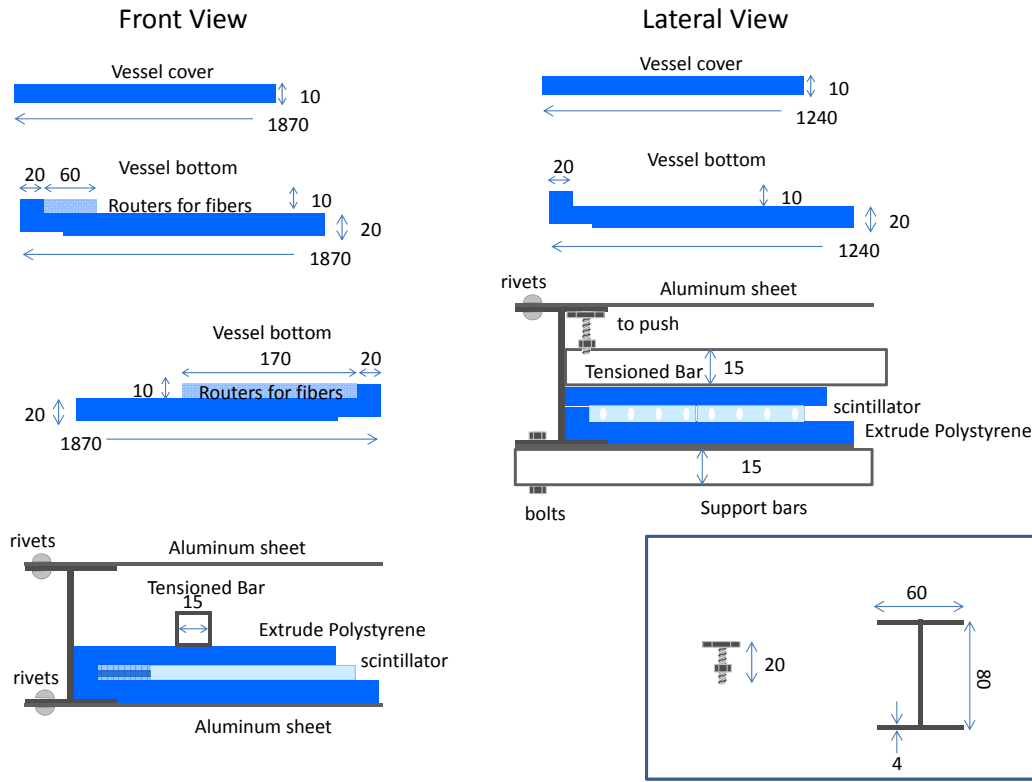


Figure 4.11: Box design of the scintillator unit. Left: detail of the front view. The different layers of the unit and the vessel can be seen with their relative dimensions. Right: detail of the lateral view. The complete unit is shown at the bottom. The module inside the box is fixed to the frame with tensioned bars. In the inset window the dimension of the "I" bars and of the bolt used to push the tensioned bars are indicated. All dimensions are in mm.

In order to do such a test, a muon telescope built from 2 RPCs with cell size smaller than the width of the bars can be used. There is a great deal of experience in RPCs in the collaboration and similar muon telescopes are taking data with groups in Portugal and Spain, and are being built in Brazil. Each SSD unit would be tested by being placed inside a double muon telescope, each telescope overlooking one half of the unit. The event rate per bar is expected to be about 5 Hz. About 5000 events per bar would be obtained in a 15 minute data taking run, allowing a proper check of the response of each individual bar. In case a specific fiber is found to be broken, it can be identified, removed and replaced. The extra holes in the optical connector are used in this case. Where available, a radioactive source scan table could be used instead of the RPC telescopes. A simple lateral scan of both sides of an SSD can be done in less than 5 minutes.

All the results of the tests, and of any repairs made, are kept in a central database. It should be noted that PMT testing (dark current, afterpulses, linearity) will occur before the final SSD unit testing, so that after the SSD is tested it can safely be deployed in the Pampa.

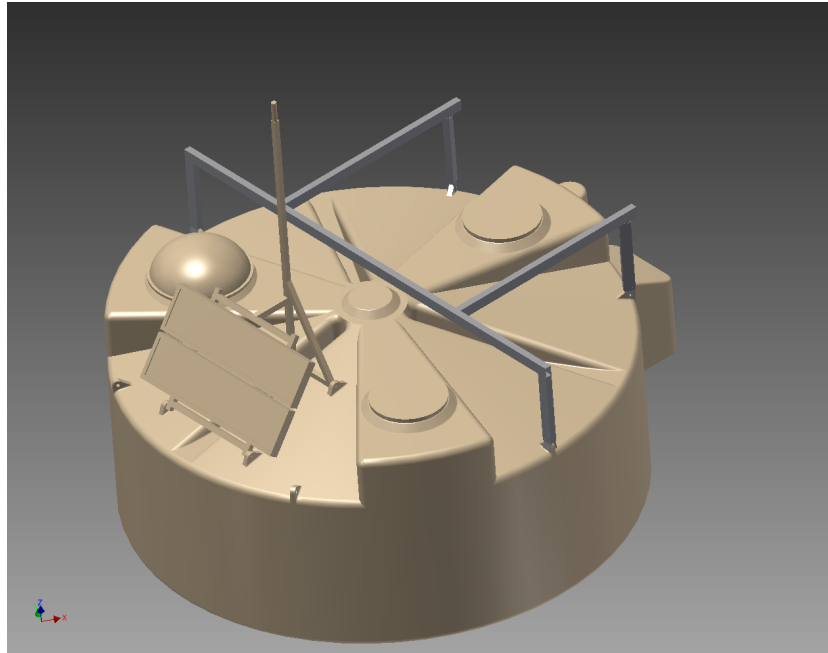


Figure 4.12: 3D view of the SSD module with the support bars. The bars are connected to the tank using lifting lugs present in the tank structure.

4.2.7 Calibration and control system

The SSD calibration is based on the signal of a minimum ionizing particle going through the detector, a MIP. Since this is a thin detector, the MIP will not necessarily be well separated from the low energy background but, being installed on top of the WCD, a cross trigger can be used to remove all of the background. About 40% of the calibration triggers of the WCD produce a MIP in the SSD. The statistics of calibration events recorded in a minute, the normal WCD calibration period, are therefore enough to obtain a precise measurement of the MIP. Figure 4.13 shows the MIP calibration histogram from a 2 m^2 test module, obtained in one minute of acquisition. The MIP is clearly defined, and will allow an absolute calibration of the SSD to better than 5%.

The performance requirements for the SSD come mainly from calibration requirements: in shower measurement mode, the dominant measurement errors are due to Poisson fluctuations of the number of particles detected, and the overall calibration constant determination. Detector non-uniformity contributes a small error when compared to the Poisson error, as long as non-uniformities are below 20%. While the FWHM of the WCD calibration histogram will be clearly smaller than that of the SSD (the calibration unit for the WCD, the VEM, is at about 100 pe), the fact that the SSD can be cross-triggered by the WCD means that the MIP is clearly visible against very little background. The width of the MIP distribution is mostly determined by Poisson statistics of the number of photoelectrons per MIP, the non-uniformity of the detector, and the intrinsic fluctuation of the response to a single particle, mainly due to different track lengths in the scintillator. The latter factor was determined from simulations to be around 18%. The baseline design chosen for the SSD produces 12 photoelectrons per MIP [145], which would degrade to 8 photoelectrons after 10 years of operation due to aging. This amounts to a 35% contribution to the MIP distribution width.

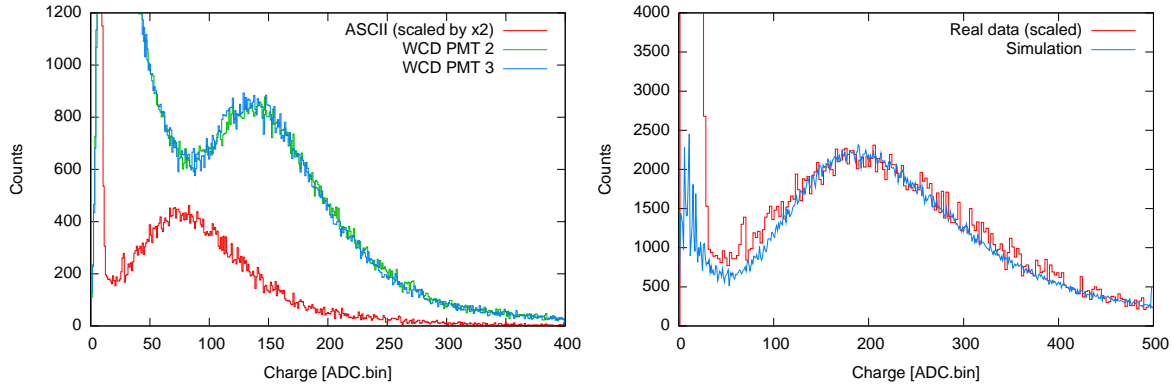


Figure 4.13: MIP histogram of a 2 m² prototype running in the Pampa, together with VEM calibration histograms of the WCD over which it is installed (left), and comparison to a simplified simulation (right). These histograms correspond to one minute of data taking. Given the clean separation of the MIP from the low energy background, no calibration issue is foreseen. These results were confirmed with the detailed codes discussed in section 8, including a Geant4 [146] based simulation of the response of the SSD and WCD to low energy showers simulated with CORSIKA [147].

Non-uniformity is very well controlled with the U-shape for the fibers and the “snake” routing of the fiber up to 6% [145]. The total width expected after 10 years of operation is 40%, assuring a MIP determination at better than 1.5% statistical accuracy. The expected MIP histogram can be seen in figure 4.14.

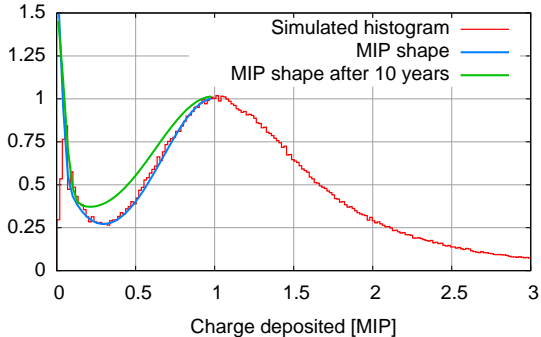


Figure 4.14: MIP histogram obtained from simulation and extrapolation of its shape after 10 years of aging. The MIP can still be easily determined with a foreseen 1.5% statistical accuracy.

In addition to these calibration histograms, which are taken in real time but used only offline, a rate-based method will be developed to get an estimate of the value of the MIP at the level of the local station controller. The advantage of a rate based algorithm, stabilized with a sigma-delta method, is that it is extremely robust. It is the same algorithm that has been running in the WCD for more than 10 years.

Finally, extra calibration information will also be determined for the SSD as is done for the WCD: high gain/low gain ratio, baseline noise and average pulse shape. In addition to these calibration data, monitoring values will also be sent to the central data acquisition system together with the WCD monitoring block (every 400 seconds). These monitoring data will include for the SSD unit the DAC settings for the HV supply of the PMT, the effective

voltage at which it is run, the monitoring current from the PMT, and the temperature inside the SSD unit. They will all be integrated into the online and offline monitoring systems.

4.3 Surface Detector Electronics

4.3.1 Introduction and design objectives

The Surface Detector Electronics (SDE) records the tank signals, makes local triggering decisions, sends timestamps to the central data acquisition system for the global triggers, and stores event data for retrieval when a global trigger condition is satisfied (see Sec. B.2). Because of the small bandwidth (1200 bits/s) available to each tank, the station must operate semi-autonomously, performing calibrations and taking action in response to alarm conditions at the station level.

The current SDE was designed 15 years ago using the technology available at that time. Evolution in processors, power consumption of electronics components, and timing systems make it possible today to design and implement a higher performance electronics system for the Surface Detector array. Furthermore, the proposed electronics provides an interface to allow the scintillator detectors co-located with the surface detector stations to make use of the data processing and communications infrastructure of the stations.

The design objectives of the SDE Upgrade (SDEU) globally aim to increase the data quality (faster sampling for ADC traces, better timing accuracy, increased dynamic range), to enhance the local trigger and processing capabilities (more powerful local station processor and FPGA) and to improve calibration and monitoring capabilities of the Surface Detector stations. Backwards-compatibility with the current data-set will be maintained by retaining the current time span of the PMT traces and providing for digital filtering and downsampling of the traces to emulate the current triggers in addition to any new triggers. The design objectives also aim for higher reliability and easy maintenance. An important feature in the design of the upgraded SD electronics is a facility for interfacing not only the SSD but also any other additional detectors.

The proposed upgrade involves the main electronics boards: the Unified Board (UB) and the front-end board of the current electronics. The interface board to the power system, the Tank Power Control Board (TPCB), will not be upgraded, and the interface to the communication system will also remain unchanged. Furthermore, new functionalities will be added to the tank calibration LED system and to the monitoring system. The dynamic range will be increased by adding a small PMT (SPMT) to the current 3 large 230 mm XP1805 PMTs. All the functionalities will be implemented in a single board, called the Upgraded Unified Board (UUB). The detailed specifications can be found in ref. [148].

4.3.2 Front-end electronics

The signal from the anode of the PMTs is split and the high-gain channel is amplified by using a dual channel ADA4927 Operational Amplifier (OA) yielding an amplification of about a factor of 5. Signals are filtered by a 5-pole low-band pass filter using passive components (inductances and capacitors). Finally the last amplification stage is implemented by using the same ADA4927 OA to obtain a total amplification of 30 dB corresponding to a voltage amplification factor of about 32 for the high-gain channel. The signals are digitized by commercial 12 bit 120 MHz AD9628 FADCs, which achieve this performance with minimal

power consumption, an important consideration due to the 10W station power budget. The pulse response of the PMT, when expressed in terms of bandwidth, is ~ 70 MHz. This is well matched to a 120 MHz FADC and associated 60 MHz Nyquist filter. A block diagram of the design is shown in Fig. 4.15.

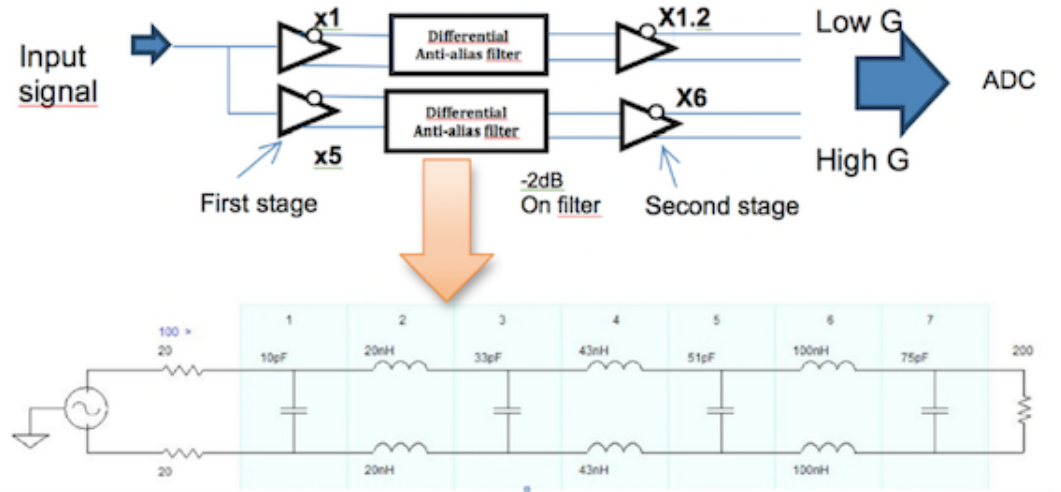


Figure 4.15: Block diagram of the front-end electronics.

The design of the filter was simulated and the response shows the correct cutoff at 60 MHz and a noise level of 400 μV RMS. The measured filter response is shown in Fig. 4.16 for both the high-gain and low-gain channels. The cut-off frequency is 60 MHz and the high gain is 30 dB.

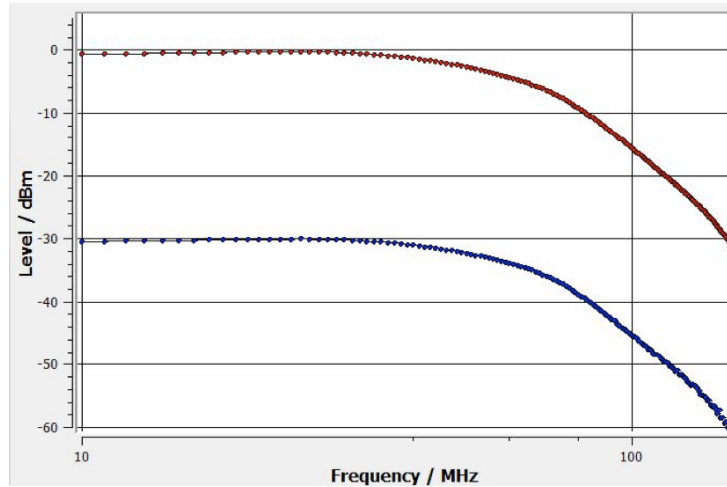


Figure 4.16: Filter response.

The large PMTs in the WCD deviate from linearity for peak currents in excess of ~ 50 mA. Conservatively assuming a maximum current of 40 mA for any PMT in the field, the corre-

sponding maximum signal in the WCD before saturation, for an operating gain of 3×10^5 and a single VEM peak signal of ~ 100 photoelectrons, is ~ 600 VEM. This is well matched via standard 50Ω termination resistors to the 2V input range of the Front End digitizers. In the upgraded WCD, the dynode signal is replaced by the anode, amplified by a factor of 32. The full WCD signal range of 600 VEM is then conveniently mapped into a full 17-bits digital range by the two WCD signals, namely the amplified anode, for single VEM resolution, and the direct anode signal, each spanning the 12 bits available in the new electronics and with 7 bits overlap. In such a configuration a single bit is worth $\sim 0.3\text{ }\mu\text{A}$. The WCD dynamics is further extended by other 5 bits using the SPMT signal, the gain of which is tuned to have a signal 32 times smaller with respect to the anode, corresponding to $600 \times 32 \sim 19\text{ kVEM}$. As discussed in Sec. 4.1.1, the SPMT gain and its overlap with the LPMT signals can be modified, and the overall dynamic range can comfortably exceed 40 kVEM.

The global dynamic range for the WCD PMT signals is shown in Fig. 4.17. The signal from the large PMT, operated at the current gain of 3×10^5 , is split into an amplified *LowGain* range for single muon resolution and a *HighGain* range for measurements of shower signals. Events closer to the core have a larger signal that is collected by the small PMT and input into a dedicated *VeryHighGain* range. The dynamic range scheme will allow moving the trigger threshold two bits higher and increasing the current dynamic range by a factor of 32 and up to 20 kVEM. The muon peak will be in channel 200.

Range	Intent	Dynamic Range																					
		1	2	3	4	5	6	7	8	9	10	11	12	13	14	15	16	17	18	19	20	21	22
bits																							
LowGain	VEM																						
HighGain	Showers																						
VeryHighGain	Cores																						
Ipeak (mA)		0.0006			0.02	0.08			1.2									40					
Vpeak (mV)		0.03			1	3.9			64									2000					
Ipeak SPMT (mA)									0.02									1.25				40	
Vpeak SPMT (mV)										1								64				2000	
Npart (VEM)		0.01			0.3	1.2			10									600				20000	

Figure 4.17: WCD dynamic range. The maximum signal before saturation corresponds to 20k particles with the operating settings specified in the text.

The anode signal from the SSD PMT will be split into two ranges (*LowGain* and *HighGain*), filtered and sampled in a similar way to the signals from the WCD PMTs. Like with the WCD, the SSD dynamic range is determined by the maximum peak current of the readout PMT, the number of bits available and the amplification factor of each channel. Assuming a peak current of 160 mA, as measured for the proposed R9420 PMT, we plan to match this to the 2V input range of the ADCs by reducing the signal by a factor of 4. Reducing the overlap of the low and high SSD gain ranges to 5 bits, we can count on a full 19 bits range,

with each bit worth $0.6 \mu\text{A}$. Using an amplification factor of 32 for the low gain signal, we place the MIP signal around 30 ADC counts ($\sim 0.5\text{mV}$), and stretch the linearity range up to 20 kMIP for the full 19 bits, matching the WCD range. Considering 12 photoelectrons per MIP at the scintillator, this implies working at a gain of 4×10^4 . It should be noted that while the availability of a dedicated PMT for very high range provides further margins to extend the WCD dynamics, the comparably large SSD dynamics relies on the properties of the chosen PMT, which exhibits high peak current and low operational gains. The global dynamic range for the SSD is shown in Fig. 4.18.

Range	Intent	Dynamic range																		
		1	2	3	4	5	6	7	8	9	10	11	12	13	14	15	16	17	18	19
bits																				
LowGain	MIP	AnodeX32																		
HighGain	Showers													Anode/4						
Ipeak (mA)		0.0006		0.01		0.1		1.25		10		160								
Vpeak (mV)		0.03		0.5		4		62.5		500		8000								
Npart (MIP)		0.07		1.2		10		156		1250		20000								

Figure 4.18: SSD dynamic range. The maximum signal before saturation corresponds to 20k particles with the operating settings specified in the text.

4.3.3 Timing

For the upgraded electronics we have selected the I-Lotus M12M Timing GPS Receiver manufactured by I-Lotus, LLC (Singapore) [149]. The M12M Timing receiver is designed to be functionally compatible with the Motorola Oncore UT+ GPS receiver that is currently used within the Auger SDE Unified Board. Choosing a compatible unit means that fewer and simpler modifications to the basic time-tagging system design. Specifically, the M12M provides the same 1 PPS timing output with serial control and data. The specified intrinsic device accuracy after the applied “granularity correction” (the so-called “negative saw tooth”) is about 2 nanoseconds. This accuracy is very good relative to the UUB specification to achieve better than 5.0 nanoseconds RMS accuracy.

Fig. 4.19 shows a histogram indicating the RMS timing accuracy as measured for twenty of the newer M12M Timing receivers during multi-hour thermal test chamber testing meant to mimic extreme temperate variations recorded on actual SD stations in the Auger SDE. No particular dependence of the temperature variation is observed, and all twenty of the test receivers demonstrate accuracy better than the 5.0 ns specification required.

The fundamental architecture of the time-tagging firmware module parallels the time-tagging design concept used in the original UB and is implemented in the UUB board FPGA.

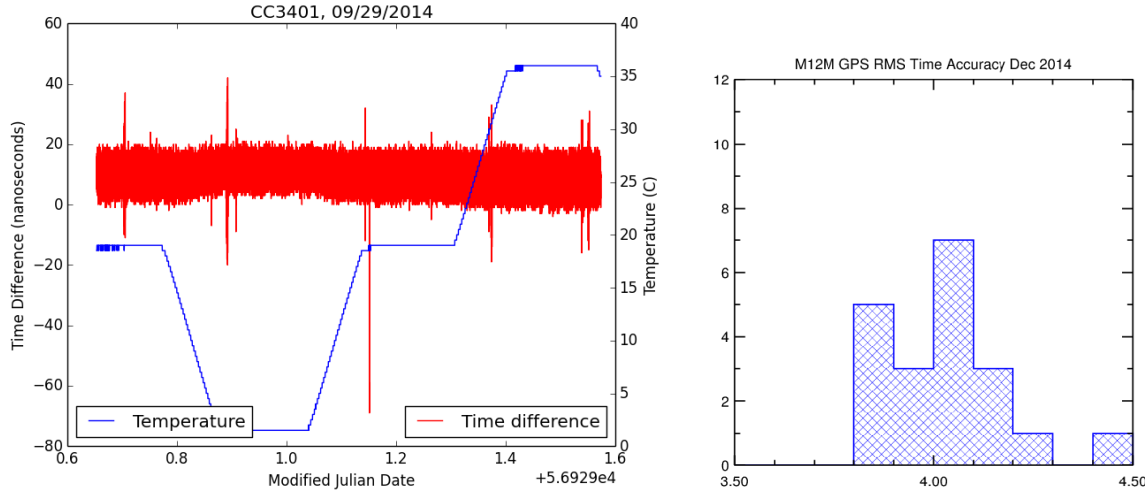


Figure 4.19: **Left:** Timing residuals (red: residuals in nanoseconds) for a typical I-Lotus M12M Timing GPS receiver as measured second-by-second during a 22 hour thermal test cycle (blue: temperature). The offsets are demonstrated here to be stable with extreme temperature variations to within 4.0 ns. [Note: short red vertical “spikes” indicate momentary GPS tracking glitches corresponding to less than 0.01 percent of all time-stamps which will have no impact on GPS time-tagging accuracy as implemented within the UUB.] **Right:** Histogram showing distribution of measured RMS residuals (in nanoseconds) for 20 I-Lotus M12M units tested within the thermal chamber. All measurements are well within the required specification of 5.0 ns or better.

The on-board software for initialization of the time-tagging modules, GPS hardware control, and timing data is implemented on the original UB as a framework, forking changes and modifications as needed for the new UUB.

4.3.4 Slow Control

A slow control system similar to that of AERA (The Auger Engineering Radio Array), incorporating a separate micro-controller (MSP430), will be used. There are sixty-four 0 to 5 V analog inputs, 16 logic IO's and eight 0 to 2.5 V analog outputs. The module also provides a USB serial connector. There are currently several free channels for test purposes and for additional detectors such as the SSD. Additional water temperature and pressure sensors will also be implemented. Fig. 4.20 shows a block diagram of the slow control.

The slow control software provides access to more than 90 monitoring variables. These include currents and voltages of the subsystems of the UUB, environmental sensor values and PMT currents and voltages. Also the PMT high voltages are controlled by the slow control. For maintenance there is a human interface implemented via USB serial connection. In case of trouble, the micro-controller can be instructed by the COMMS to perform a complete UUB reset. Care is taken in monitoring the solar power system, and in the case of battery under-voltage, some parts or all components of the UUB may be switched off.

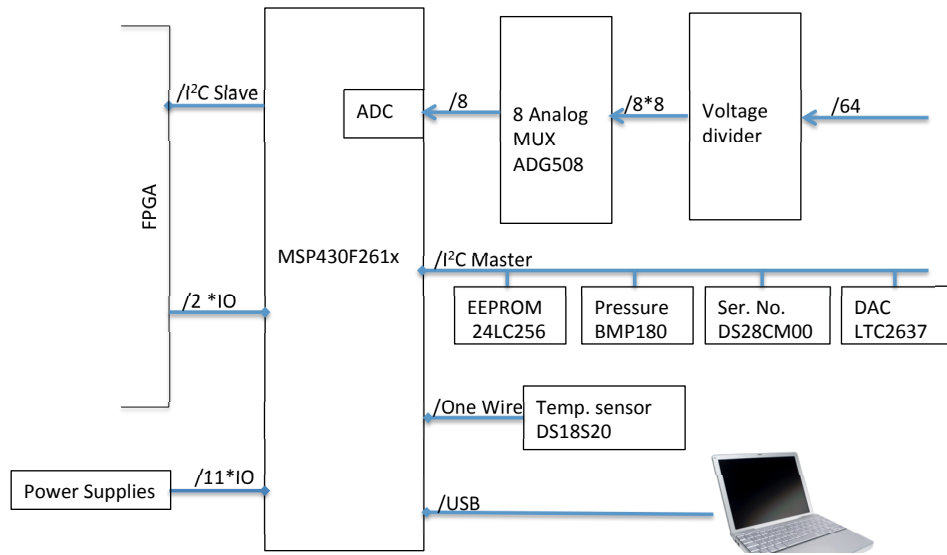


Figure 4.20: Slow control block diagram.

4.3.5 Upgraded Unified Board

All the different functionalities described in the previous sections are implemented on a single board, called the Upgraded Unified Board (UUB). The architecture of the UUB includes a Xilinx Zynq FPGA with two embedded ARM Cortex A9 333 MHz micro-processors, 4 Gbit LP-DDR2 memory and 2 Gbit Flash memory (storage memory). The general architecture is shown in Fig. 4.21.

The processor manages several devices including front-end electronics, slow control, LED controller, GPS receiver, clock generator, memory and various connectors (Fig. 4.22). The SSD PMT signal will be connected like the other PMTs by using SMA connectors. Two digital connectors are provided for future additional detectors. These connectors provide 8 differential lines, each of which can be individually defined as input or output in the FPGA. An example of such allocation could be: Trigger out, Clock out, PPS out, Busy in, Data in, Sync in, Data out, Sync out, etc. Moreover, this connector will provide unregulated +24 V, switched, limited, with a current monitor. The addition of accessible trigger IN/OUT and GPS 1 PPS signals will simplify time synchronization with future detectors. High speed USB interfaces and direct connection to the trigger FPGA will allow interfacing a variety of additional detectors.

The currently estimated peak power consumption (including radio and PMTs) is about 16 W. This is similar to the peak power of the current electronics running with an average power below 10 W. More accurate estimation of the power consumption will be done with the integrated prototype.

The design will be implemented on a 10 layer PCB board having the same size as the current UB board ($340 \times 240 \times 1.8$ mm). Global specifications for the components are: availability until 2020, operating temperature range from -20 to $+70^\circ\text{C}$, and preferably SMD packaging. A conformal coating will be used to protect the UUB board. The UUB will be installed in the current RF-enclosure, only the front panel will be changed. This will allow a smooth mechanical integration of the electronics kit between the radio and the tank power control board under the current weather enclosure.

4.3.6 Local trigger and Data Acquisition System

The existing UB software will be ported to LINUX and will be implemented in the FPGA. The data acquisition will be simplified by extending the use of FPGA firmware. The trigger and time tagging functionalities will also be implemented in the FPGA. The speed of the upgraded CPU will be >10 times faster than the current one, with a commensurate increase in memory. This will allow much more sophisticated processing in the local station.

The current local triggers (threshold trigger, time-over-threshold trigger (ToT), multiplicity of positive steps (MoPS) trigger, etc.) will be adapted to the 120 MHz sampling rate. The increased local processing capabilities will allow new triggers to be implemented such as asymmetry based triggers, and combined SSD and WCD triggers. The current muon memories and scalers will be retained. GPS synchronized LED pulses will be implemented which will improve calibration and monitoring of the detectors. The trigger scheme includes the ability to downsample and filter the data to the current 40 MHz rate which will facilitate the detectors to run with new electronics emulating the current detectors. This will allow deployment of new electronics during the maintenance of the current system without disturbance to the data taking.

4.3.7 Manufacturing and tests

The upgraded electronics will be fabricated and tested following the Quality Management Plan [150] of the current electronics. The specific design of the different parts of the SDEU (front-end, slow control, UUB) have been verified by using evaluation boards. The first integrated prototypes are currently being fabricated and will be tested in laboratories. The final validation of the design will be performed by an Engineering Array of 10 detector stations on site. This array will allow us to test triggers, validate various resolutions and test the local data processing and transmission.

Currently 4 manufacturing sites are foreseen (two in Europe, one in the USA and one in South America). All fabrication sites need to be ISO certified. For each production site, a pre-production run of about 30 to 50 units is planned. This will allow us to fine-tune the production parameters prior to the final production run. Component procurement will be centralized and controlled. Only one manufacturer is foreseen for the PCB procurement.

Each manufacturer will perform electric continuity tests and some simple functionality tests. The complete functionality tests including temperature stress testing will be done afterwards in laboratories. A specific test bench has been developed for this purpose. A description of the test procedure can be found in ref. [151]. All test results will be stored in a database. Tested UUB boards will be shipped on site where they will be assembled into electronics kits (Ekits). The procured GPS receivers will be tested following similar test procedure and shipped to the site for assembly. For details of assembly and tests on site see Chapter 9.

4.4 Surface Detector expected performance

4.4.1 Increased dynamic range

The Auger Upgrade will allow extension of the dynamic range of the SD enough to measure shower properties as close as about 300m from the core, both with the WCD and the SSD

(see Sec. 3.2). This is achieved in the WCD with the addition of the SPMT, dedicated to the readout of large signals and providing considerable margin to extend the dynamics even more. As discussed in Sec. 4.1.1, the SPMT gain and its overlap with the LPMT signals can be modified, and the overall dynamic range can comfortably exceed 40 kVEM. This is shown in Figure 4.24, where the VEM spectrum of shower particles is shown, measured by a test WCD equipped with a SPMT operated at a signal ratio of ~ 13 with respect to the anode. The saturation of the LPMT is clearly visible at the expected value of ~ 600 VEMs, while the overall spectrum of the SPMT extends well beyond 40 kVEM.

Currently half of events in the energy range $10^{19.5}$ to $10^{19.6}$ eV have at least one saturated station. The SDE upgrade extends the linear non-saturated measurement range to 32 times larger signals than currently achieved. This reduces the fraction of events in that energy range that have a saturated station by a factor of 10. Furthermore, the increased dynamic range will allow measurement of the LDF function at distances closer to the shower core than is now possible.

In the SSD a single light sensor is used measuring both single particles for calibration and high density CR shower signals. This is achieved by taking advantage of the very high-linearity PMT chosen as baseline for the SSD. This will allow measurement with both WCD and SSD detectors at distances as close as about 300 m from the shower core.

4.4.2 Faster timing and increased processing capability

The typical time distribution asymmetry between the PMTs of the WCD is of the order of 6 ns (light transit time between the PMTs). With the current electronics time bin width of 25 ns and $\sigma = 7.2$ ns it is difficult to extract much information from the time distribution asymmetries between the PMTs. However, with 8.3 ns bin width and $\sigma = 2.4$ ns it becomes possible to extract some directional information on a station by station basis, and to consider improved triggers for horizontal showers that take advantage of the arrival time differences in the PMTs.

While the SSD, in combination with the WCD, is required to accurately determine the muon content of the showers, the existing detector stations can already count muons in the regions far enough from the shower core where the interval between muons is more than a few FADC time bins. The various counting techniques that have been used rely on sensing the fast upward transitions in the FADC traces. Increasing the FADC sampling rate improves these techniques, allowing one to more reliably count larger numbers of muons per station and probe closer to the shower core.

Our current photon limits are no longer background free. Improved muon discrimination provided by the faster sampling will help reduce the background of hadronic events in our photon candidate sample.

Substantial additional resources available in the trigger FPGA will also provide the possibility of more sophisticated triggers tuned for photon and neutrino searches and may allow us to extend the energy range to lower energies, e.g. the expected number of events seen in the detector given the flux prediction by Waxman and Bahcall is improved by about 10% while only readjusting the original trigger condition to the increased sampling rate.

As the SSD and WCD signals are both provided to the same FPGA, it also becomes possible to implement dedicated SSD triggers or combined SSD and WCD triggers. The combination of these triggers may help to further monitor and understand efficiency and biases of the triggers.

As the PMT signals are AC coupled into the FADCs, the baseline level can fluctuate on time scales of milliseconds due to the preceding signals. The current low threshold triggers (ToT, ToTd), are set at a per bin threshold level of 0.2 VEM. The VEM peak is nominally set to be 50 counts above baseline, but some in PMTs it may go as low as 20-30 counts, before a HV adjustment is made. Thus the per bin trigger threshold may correspond to only 5 or 6 counts above baseline, which results in significant trigger rate fluctuations for those triggers. Baseline tracking by the FPGA has already been tested in the current electronics, but the coarse trigger threshold granularity precluded using that information to stabilize the trigger rates. The addition of 2 more bits of precision in setting the trigger threshold in the SDEU resolves that issue, and will allow the FPGA to dynamically track the baseline and make the corresponding trigger threshold adjustment on the timescale of $\approx 100 \mu\text{s}$, reducing the trigger rate fluctuations.

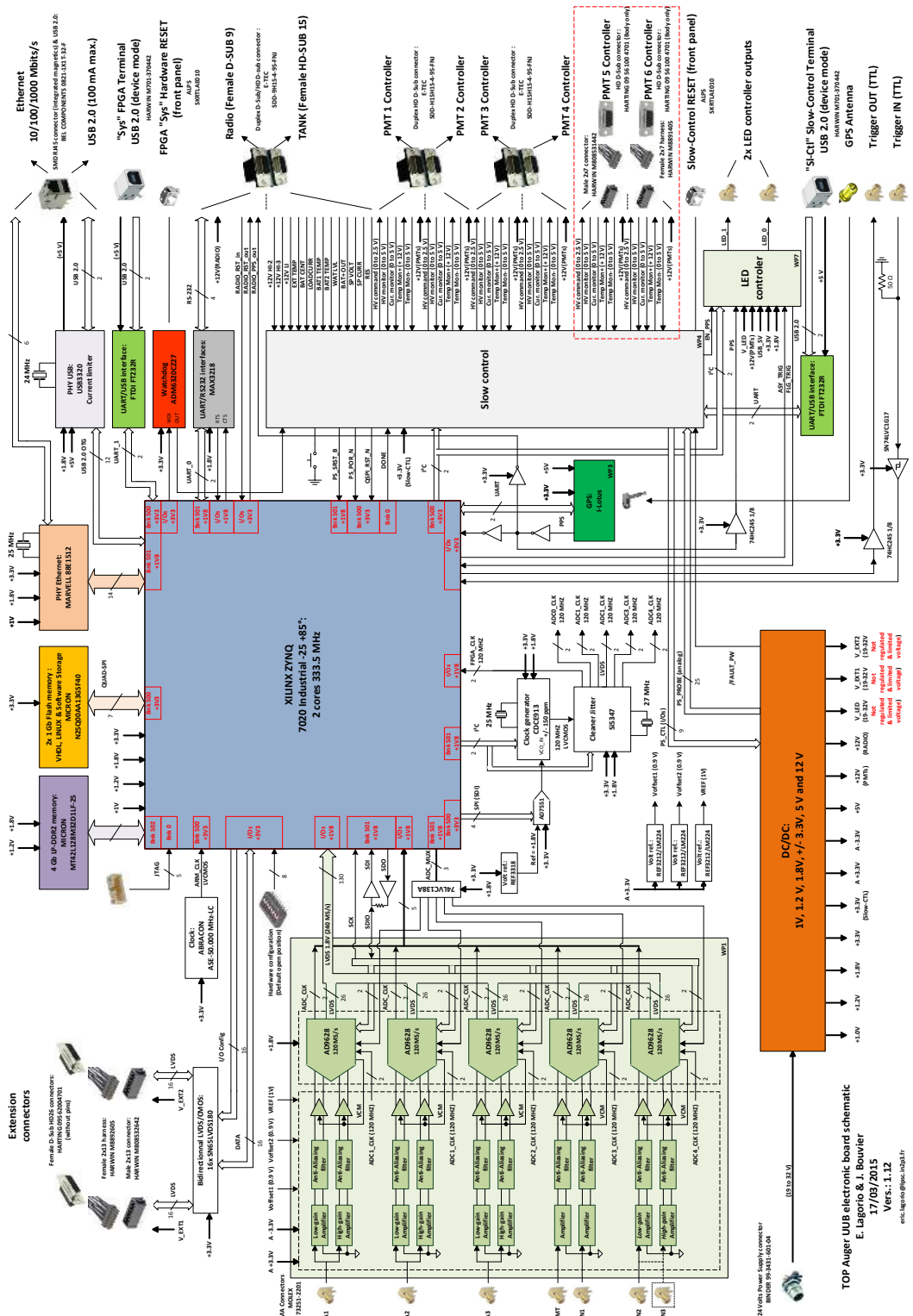


Figure 4.21: General architecture.

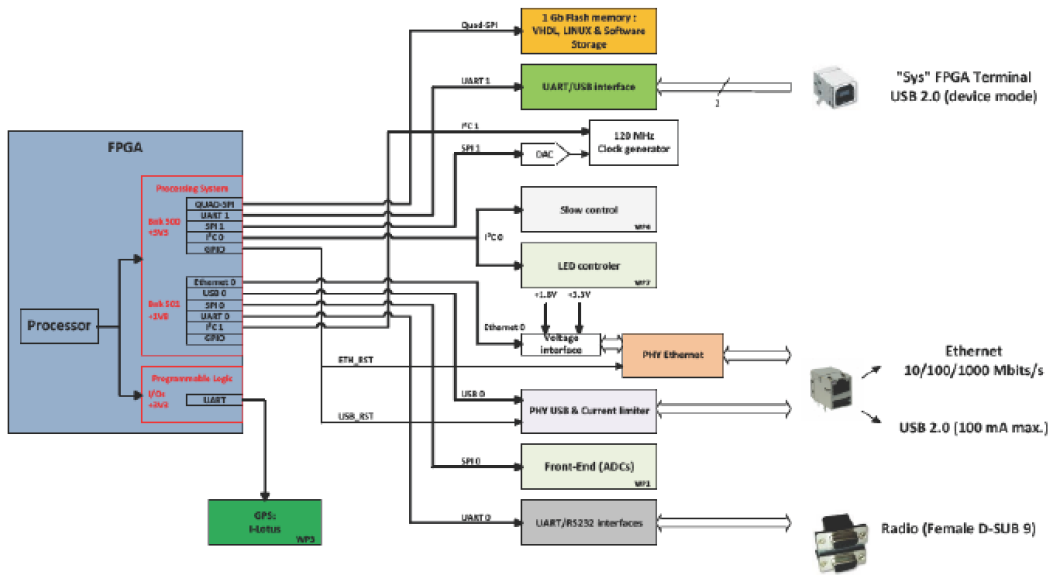


Figure 4.22: Devices managed by the UUB processor.

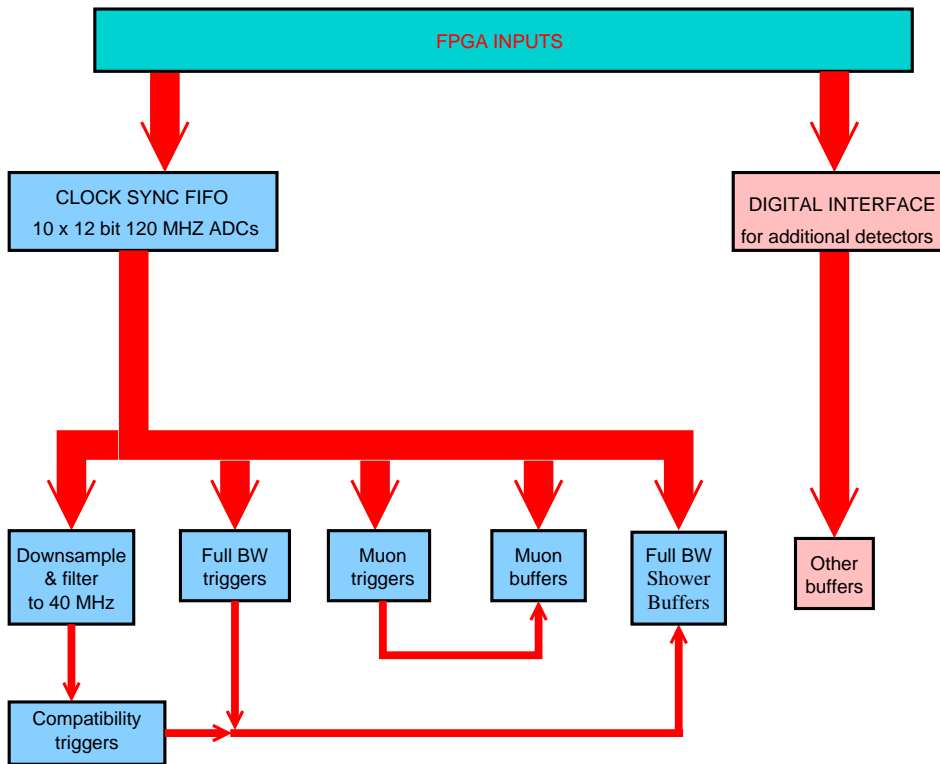


Figure 4.23: Conceptual diagram for local trigger.

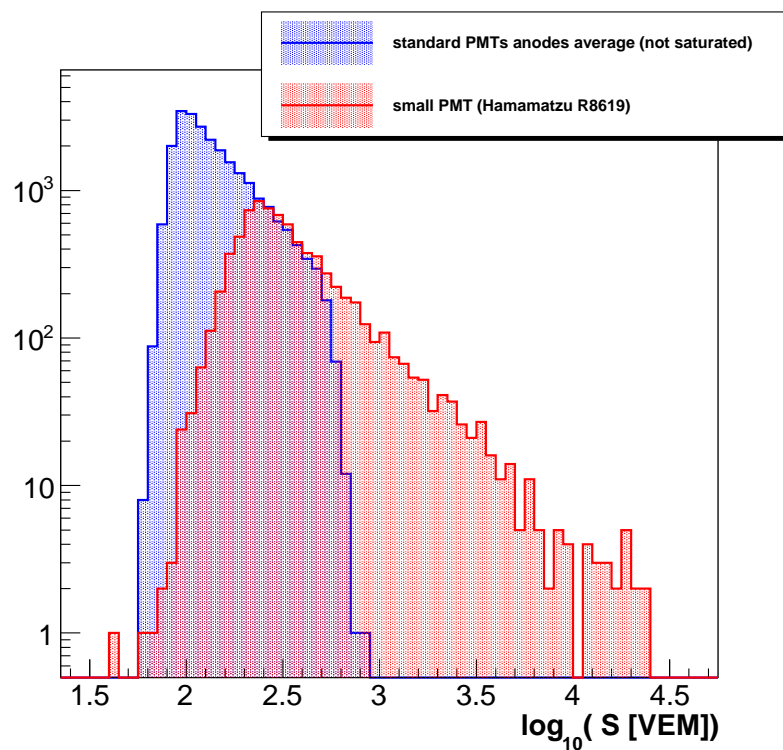


Figure 4.24: Comparison of the spectra measured by the standard PMT and the small PMT. The small PMT allows to extend the dynamic range above 30 kVEM.

Chapter 5

The Underground Muon Detector

5.1 Introduction and design objectives

The Underground Muon Detector (UMD) will provide a direct measurement of the muon content of a sub-sample of showers observed by the upgraded Auger surface detector. In the Upgrade plan this serves as verification and fine-tuning of the methods used to extract shower muon content using the SSD and WCD stations. As described in Sect. 3.4, the performance and characteristics of the AMIGA underground muon detectors match these requirements. The UMD will therefore consist of 61 AMIGA muon detectors deployed on a 750 m grid in the infill area of the Surface Detector, instrumenting a total area of 23.5 km².

The use of the AMIGA muon detectors in this verification role is additional to the rich physics investigations planned for AMIGA in the ankle-region of the energy spectrum [152].

The following sections provide an overview of the design and the implementation of the AMIGA muon detectors, with more detailed information given in Appendix B.7.2.

5.2 Detector design

Each muon detector station will have an area of 30 m² and will be buried at the side of a surface detector station at a depth of approximately 1.3 m. The distance to the station will be large enough to avoid shadowing from the water tank, guaranteeing uniform shielding, but small enough to represent the same physical point inside the shower front, and allowing shared use of GPS time signals and telecommunications with its associated surface detector.

The baseline design for the muon detectors uses the same extruded plastic scintillators already developed and used by the MINOS experiment. They will work as counters (i.e. signals above a tunable threshold are counted) having an appropriate segmentation to prevent pile-up, together with an integrated signal for large muon densities. The light collected in a scintillator will be guided towards a 64 channel Hamamatsu PMT.

An AMIGA prototype is displayed in Fig. 5.1. It consists of 64 4 m long scintillator strips. The strips are 4.1 cm wide and 1.0 cm thick and therefore the detector modules have an active area of 10 m². The strips have a middle groove which accommodates a wavelength shifter (WLS) fiber of 1.2 mm diameter which is glued into the groove and covered with reflective foil. The scintillator is co-extruded with a TiO₂ reflective coating which prevents light from leaving the material.



Figure 5.1: Left: An AMIGA 10 m² module being manufactured. The black optical connector concentrates the 64 optical fibers coming from the 32 scintillator bars at each side. Right: Deployment of a Unitary Cell AMIGA station with two 10 m² and two 5 m² modules at a depths of 2.3 m underground. The big tubes are to provide access to the electronics for development and maintenance purposes, to be replaced by tubes of 31 cm diameter for AMIGA production.

The fibers end at an optical connector matched and aligned to a 64 channel multi-anode photomultiplier tube. Muon counters sample scintillator signals at a frequency of 320 MHz, meaning that every 3.125 ns 64 bits are acquired. Each bit stores the digitized value (either a “0” or “1” if the signal was below or above a predefined threshold) associated to one scintillator bar of the counter.

Muon counting and the digitization of the integrated signal is implemented in the AMIGA electronics, including an FPGA with three main functional blocks: counting, data codification, and external communications. The data are sent to the CDAS using an independent, commercial radio communications system. The power for the counters is provided by a solar panel system similar to that used for the existing SD. The measured power consumption of one detector station is currently about 37 W. For more details about the module design and deployment see Sec. 9.5 and Appendix B.7.2.

5.3 Implementation

A unitary cell formed by 7 AMIGA muon stations and 7 associated surface detectors has been successfully installed in the field, with elements of the cell taking data for up to two years. The performance and physics results from the unitary cell are very encouraging and the procedure for deploying underground detectors in the infill area has been verified. Some R&D is still in progress, mainly aimed at reducing costs and increasing the integration of muon detectors with the SD. In particular, a common communications system is needed for the infill area detectors, which will be adapted either from the AMIGA or the AERA communication systems. Furthermore, some R&D is ongoing on the use of silicon photomultipliers (SiPM) and electronics improvements. This would allow a reduction in the power consumption and the cost of the detectors.

Chapter 6

Extending the Duty Cycle of Fluorescence Detector Observations

The fluorescence detector provides exceptional information about extensive air showers such as a model-independent energy reconstruction and direct measurement of the longitudinal development profiles. The main limitation of the FD is its duty cycle, currently at the level of 15%. Our goal is to increase the exposure for cosmic ray events above 10^{19} eV by extending the FD measurement into hours with high night sky background (NSB). The current setup allows this novel operation and we have performed several tests that successfully demonstrate that it is feasible.

Safety limits on the long and short term illumination of PMTs by the NSB, and particularly scattered moonlight, define the data taking period of the current FD operation. The duty cycle is therefore limited to about 19%, which is reduced to 15% by bad weather conditions, power cuts and malfunctions. A significant increase of the duty cycle is possible by the extension of the FD operation to times at which a large fraction of the moon in the sky is illuminated. However, during such operations the PMT gain must be reduced by lowering the supplied high voltage (HV) to avoid an excessively high anode current leading to an irreversible deterioration of the PMT sensitivity. The HV power supplies installed in the FD buildings allow switching between two high voltage levels and the PMTs can be operated at the nominal gain and a lower gain.

6.1 Laboratory test measurements

The FD PMTs (Photonis, model XP 3062) have been extensively tested at the nominal [153] and lowered gain levels in the laboratory. The nominal PMT gain and HV are 5×10^4 and 850 to 1050 V, respectively. A special test setup for the planned operation at higher NSB has been constructed. A uniform UV light source, which can be simultaneously operated in the DC and pulsed mode, illuminates a few FD PMTs and the HEAT electronics is used to read-out measured signals.

The PMTs were tested at HV as low as 400 V and their gain changes were measured as a function of HV over the whole studied range of HV. The PMT response to different light fluxes at different gain levels is a linear function of the light flux as is shown in Fig. 6.1. The PMT aging (i.e. loss of sensitivity) was also studied at the lower gain and results for a PMT at a gain of 5×10^3 (HV of 644 V) are shown in Fig. 6.1. After the initial aging phase the PMT

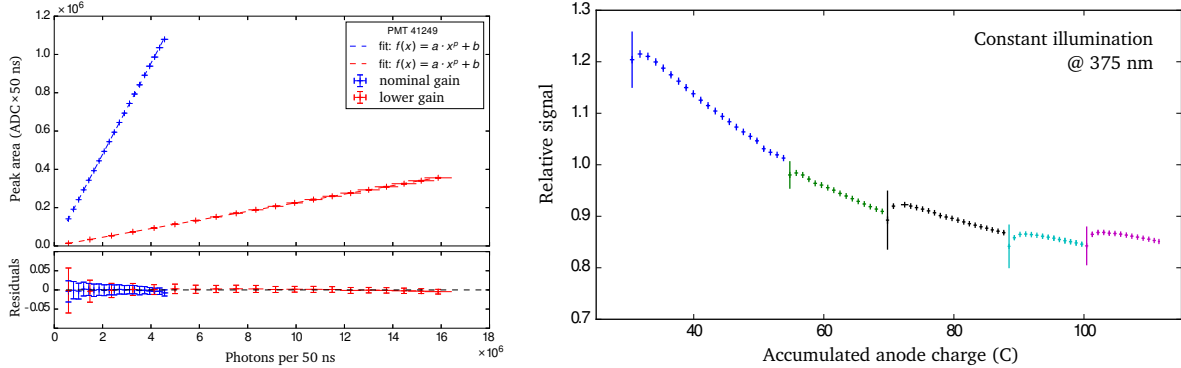


Figure 6.1: Left: The PMT response to photon flux up to the saturation level measured at the nominal (blue) and reduced (red) gain. The exponent p is 1.0 for both gains. Larger error bars at lower light fluxes are caused by the small amplitude of measured pulses. Right: The PMT response as a function of the accumulated anode charge measured in a dark box at ten times lower gain. Jumps correspond to a recovery phase after breaks in our measurement.

response changes very slowly as has also been measured for PMTs operated at the nominal gain.

A continuous change of the background light level was used to simulate the expected evolution of the NSB during nights with a highly illuminated moon moving across the sky. The PMT gain was automatically changed according to the measured light flux. Because of the AC-coupling of the read-out electronics, the DC light level can only be obtained from the variances of the measured signal. At a gain as low as 4000 the ADC variance is above the electronic noise level and it can provide information on the DC light level. The DC light level obtained from the PMT has been cross checked with a photodiode.

Thus, we have verified that the PMTs can be operated at more than ten times lower gain than the nominal value of 5×10^4 , and that no acceleration of the aging has been detected at lower gains with high NSB. Moreover, the measurement of the NSB by the FD PMTs is possible using variances even at lower gain, which is a necessary requirement for automatic changes of the HV level in the telescopes.

6.2 Test measurement with an FD telescope

The first test measurement outside the standard FD data taking period was performed with one FD telescope in the austral autumn of 2015 [154]. Telescope 1 at Los Leones was operated during six nights with a highly illuminated moon above the horizon. We have confirmed that the HV change can be done remotely and that the HV stabilizes within a few seconds after its change.

The PMT performance can be monitored with the existing calibration setup in exactly the same way as during the standard data taking, so no change in the system is required. The PMT performance obtained for one test night is shown in Fig. 6.2. An evolution of the PMT response studied every half an hour is shown in the left panel. We can see a fast change of the PMT response during the three hours after opening the shutters. A similar evolution of the PMT response has been observed during standard data taking at the nominal gain. In the right panel is the camera-averaged response to four light intensities measured at two gain

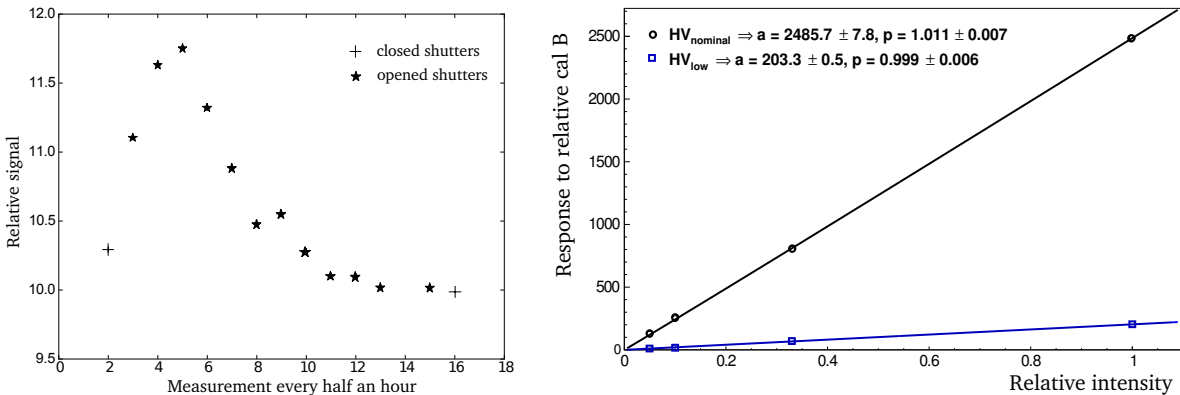


Figure 6.2: Left: The response of the PMTs operated at reduced gain during data taking. Shown is the ratio of the response measured before data taking at the nominal gain, to the response during data taking. Crosses and stars indicate closed and open shutters, respectively. Right: The camera-averaged response to calibration B as a function of calibration B intensity for nominal HV (black circles) and reduced HV (blue squares). Results of both HV settings are fitted with a power law and in both cases the exponent p is compatible with 1 (i.e. a linear fit).

settings. A linear fit is compatible with the data within uncertainties.

During these test runs a couple of air showers were measured despite a NSB ten times higher than is normal during the standard FD operation. The trigger rate was lower, but this can be explained by a lack of low energy events buried in the higher NSB.

We will continue test measurements during 2015 in order to study the FD performance in greater detail. We plan to also use a roving laser, which is available at the Observatory, in front of the telescope.

6.3 Air showers measured during high night sky background

The effect of a higher NSB on the reconstruction of air showers has been also studied. Existing measured air showers have been analyzed with the standard reconstruction chain after adding random noise to the ADC traces. A camera image and a longitudinal profile of a real FD event before and after the addition of noise is shown in Fig. 6.3.

The reconstruction and selection efficiency, resolutions and biases for various NSB levels have been evaluated. For this study, the noise in ADC traces of events in our current FD data set was artificially increased. Modified events were reconstructed in the same way as in the standard FD reconstruction and the same selection criteria were applied. In Fig. 6.4 we show that the reconstruction and selection efficiency increases with energy and is 75% at $10^{19.6}$ eV even for the most extreme NSB considered for the duty cycle extension (a variance of 1000 (ADC counts)²). In Fig. 6.5 we show the resolution for energy and X_{\max} . Our results show that good quality data can be obtained for air showers above 10^{19} eV measured in the presence of a NSB which is ten times higher than the maximum level allowed for the standard FD data taking.

Even though the PMT electronics is AC-coupled, we have studied a possible effect of a non-uniform NSB on the air shower reconstruction. The non-uniform NSB is caused by a highly illuminated moon shining in the sky close to the field of view of the detector. For an extreme gradient of the NSB the reconstruction biases in energy and X_{\max} were found

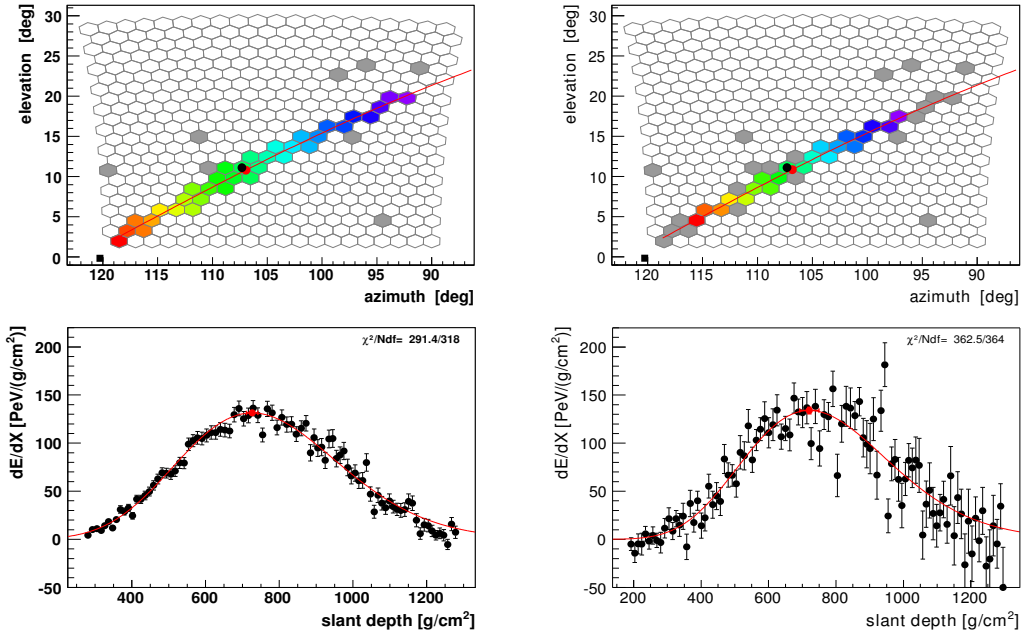


Figure 6.3: A real FD event with reconstructed energy 7×10^{19} eV. In the left panel are measured data (clear sky and no scattered moonlight, a baseline variance of 25 (ADC counts)²) and in the right panel the same data after adding random noise corresponding to a 40 times higher NSB.

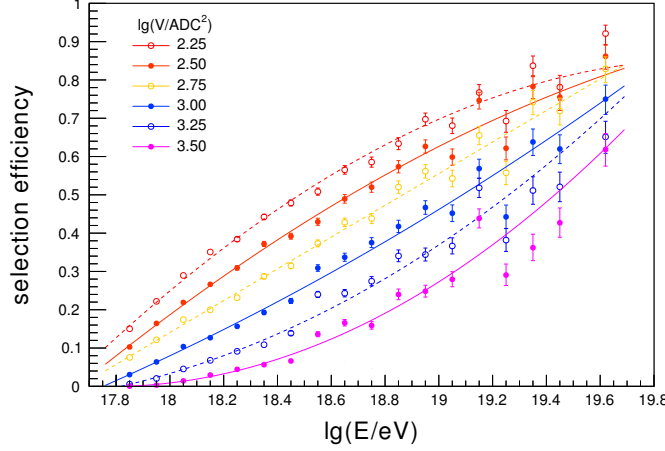


Figure 6.4: The combined reconstruction and selection efficiency as function of the energy for various levels of the NSB. The NSB is expressed as the variance of the PMT baseline signal V in (ADC counts)² and all studied levels are above the current limit for the standard FD operation which is less than 100 (ADC counts)². The level of 1000 (ADC counts)² corresponds to the NSB in the presence of a 90% illuminated moon.

not to exceed 2% and 5 g/cm², respectively, at energies above 10^{19} eV. Such biases can be considered acceptable taking into account that the events observed in the presence of the extreme NSB gradient will not dominate the overall data sample.

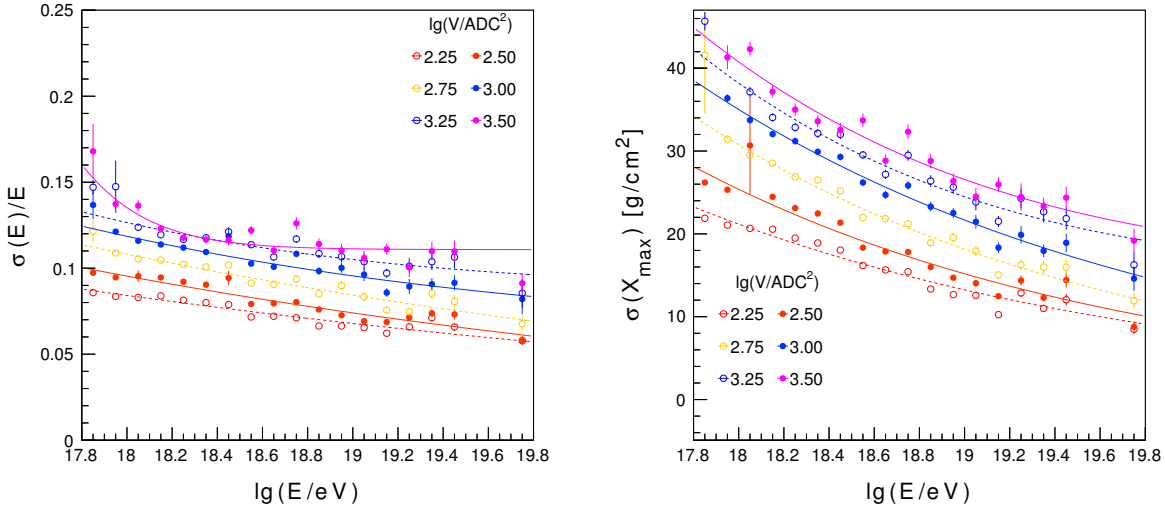


Figure 6.5: The energy (left) and X_{\max} (right) resolution as function of energy for various NSB levels. The NSB levels are explained in fig. 6.4.

6.4 Increase of the duty cycle

We are currently considering a PMT gain ten times lower than the nominal one for the FD duty cycle extension. We have verified in all our test measurements that the PMTs operated at reduced gain satisfy the criteria required for the FD performance (such as a linearity, stability and lifetime). At a gain of 5×10^3 the FD operation can be extended to nights with a moon fraction of 90%, where we expect ADC baseline variances of about 1000 (ADC counts)². This translates to about 29% FD duty cycle (without accounting for reductions caused by bad weather conditions and malfunctions), or in other words, a 50% increase of the current observation period of 19%.

Expected number of events for seven years are shown in Table 6.1: for the standard FD operation we can expect about (514 ± 27) and (52 ± 9) events above 10^{19} eV and $10^{19.5}$ eV, respectively. By extending the FD operation to higher NSB we can gain up to 40% more events above $10^{19.5}$ eV, see Fig. 6.4. Moreover, by applying less strict selection cuts for high quality events [22], we expect in total about 102 ± 14 events above $10^{19.5}$ eV after including the standard and extended FD operation. This will allow us to improve the cross check of results of the upgraded SD array with the FD up to the energy of the flux suppression in the cosmic ray flux.

We will maintain precautions to avoid dramatic changes of the PMT sensitivity (long-term aging) and to have a safe margin for another ten years of operation. The first step is a continuous monitoring of PMTs during each night. The illumination of the PMTs is also continuously monitored and the average accumulated anode charge by the PMTs is about 2.7 C per year during standard observations. Our estimate is 5 C per year for the extended data taking during nights with higher NSB. After another ten years the accumulated anode charge will stay well below the value corresponding to the half-lifetime of the FD PMTs, which is typically 250 C.

Table 6.1: Expected cumulative number of events for a data taking period from 2018 until the end of 2024 for the FD measurement during the standard operation only, after including the extended operation and after applying less strict selection criteria for both operations. Compare with the SD Table 3.1.

$\log_{10}(E/\text{eV})$	$N _{\text{std}}$	$N _{\text{ext}}$	$N _{\text{cuts}}$
	[2018-2024]	[2018-2024]	[2018-2024]
19.0	514 ± 27	668 ± 35	1425 ± 51
19.5	52 ± 9	73 ± 12	102 ± 14
19.7	11 ± 4	16 ± 5	29 ± 8

Chapter 7

Communication System and Data Acquisition

7.1 Communications System

The existing two-layer telecommunications system designed by the University of Leeds that currently provides bi-directional data transfer and control for both the Fluorescence Detector (FD) and the Surface Detector (SD) will continue to operate without significant modification within the Auger Upgrade. See B.4.1 for details on the existing system. The Leeds communication system will continue to receive data from the four individual FD sites and from the approximately 1600 SD stations deployed into the field, exclusive of those SD stations that are located within the infill region.

Individual surface detector stations are connected by a custom wireless network which is sectorized and supported by four concentration nodes. The wireless network is serviced by a high capacity microwave backbone network which also supports communications between the four fluorescence detector sites and the main campus data acquisition and control center. Figure 7.1 shows a conceptual schematic of the overall layout of the data communication system for the Auger Observatory. Table 7.1 lists the main performance characteristics.

7.1.1 The microwave backbone network

The backbone for the Auger data communications system is a 34 Mbps network operating in the 7 GHz band. Receivers and transmitters are mounted on five communications towers located at the perimeter of the array. The microwave backbone provides high speed network communications to nodes at all four FD sites and the main campus.

The microwave backbone, depicted schematically in figure 7.2, consists of a set of paired links providing sufficient capacity to stream data to and from each of the FD sites as well as for collecting data from the individual surface stations.

We note that the current microwave backbone system has worked reliably for many years, and therefore the baseline design calls for the existing system to serve for the Auger Upgrade. However, the specific transmitter/receiver hardware units deployed in the field are now obsolete. Therefore, we are exploring a range of possible equivalent replacements for the microwave communication system based on more up-to-date technology. Although

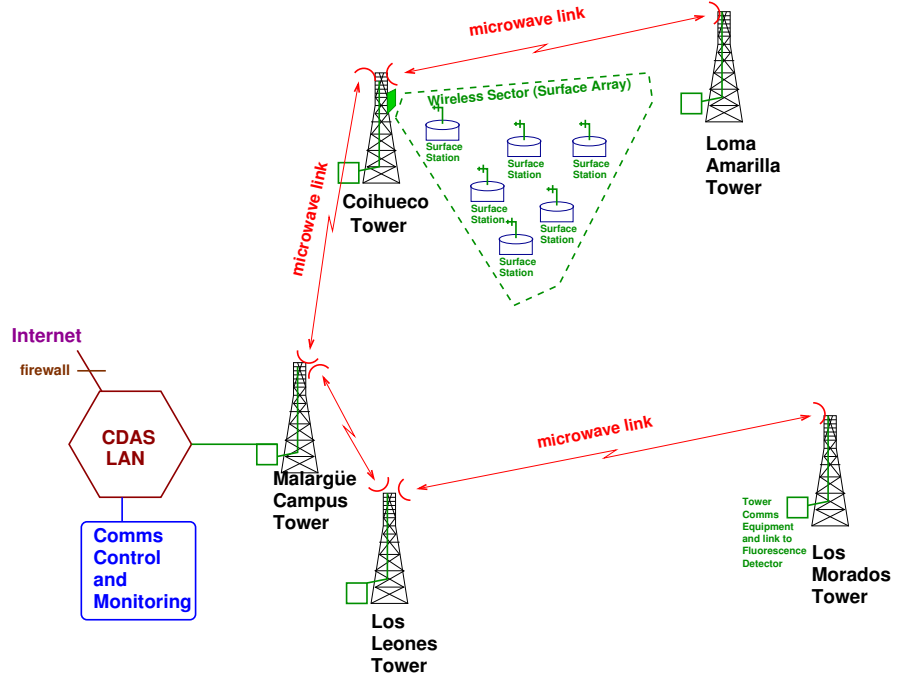


Figure 7.1: Conceptual schematic of the overall radio telecommunications system for the Pierre Auger Observatory.

Table 7.1: Performance summary for the radio data communications system for the Pierre Auger Observatory.

Microwave backbone network	
Links	4
Frequency	7 GHz
Data rate	24 Mbps
Wireless LAN	
Nodes	1660
Frequency	902 to 928 MHz ISM band
Protocol	TDMA, custom
Subscriber Unit over-air rate	200 kbps
Effective payload rate	1200 bps uplink
Typical daily data packet loss rate	less than 0.002%

the exact solution has not been identified, high-speed tower-to-tower communication links correspond to a very standard and common communication solution, and there exist several viable Commercial-Off-The-Shelf (COTS) solutions that can meet our bandwidth requirements at a cost that is rather lower than the original implementation. Our plan is to reduce costs and disruptions by gradually replacing obsolete units with modern COTS equivalents for increased reliability and bandwidth.

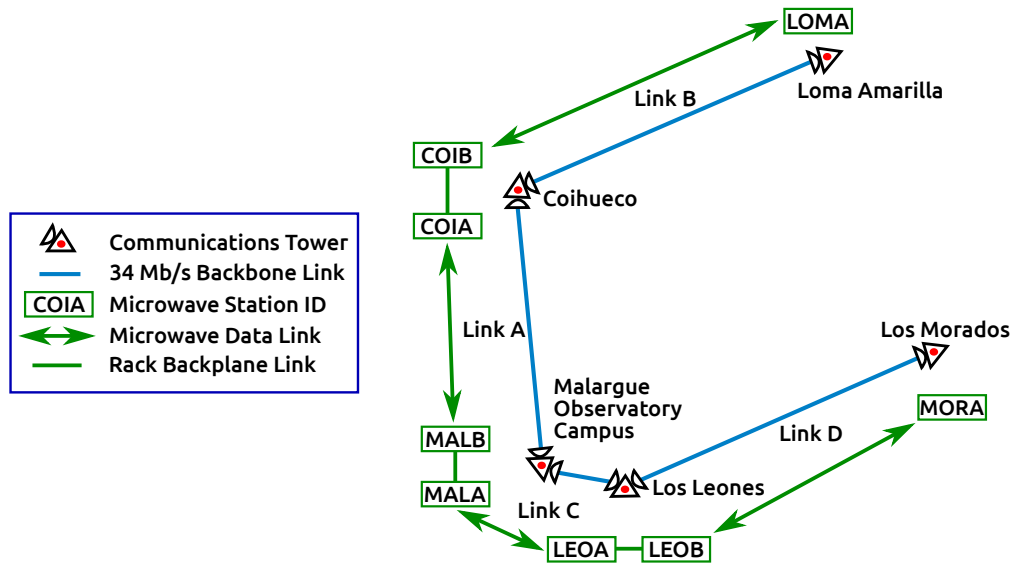


Figure 7.2: Configuration of the high capacity microwave backbone network that connects the four FD sites with the main campus control and data acquisition center in Malargüe.

7.1.2 The Leeds Wireless Network

Tower-to-surface-station communications are accomplished with custom designed units operating in the 902 to 928 MHz ISM band. A point-to-point bidirectional communications link is established between each surface detector station and one of four communication concentration nodes mounted on the four towers located at each of the fluorescence detector sites. Communication to the SD stations is achieved in a manner similar to a cellular telephone system by dividing the array into 28 sectors, each of which contains up to 68 stations.

Communications operations at each surface station are governed by a custom-built programmable Subscriber Unit (SU) used to mediate the transmission and reception of digital data between the electronics board of a surface detector and the concentrator node. An analogous custom-built unit, called a Base Station Unit (BSU), controls data transfer between each concentrator node and the backbone network connection at each tower.

Time division multiple access

Transmissions to and from the stations are synchronized by GPS timing so that each station is assigned a particular time slot during which it is available to send and receive data. This Time Division Multiple Access (TDMA) scheme provides a contention free communication environment within the array. A one-second data frame includes 68 uplink slots for collecting data from the array and 6 downlink slots for sending trigger requests and other commands to the stations. An additional 11 slots are reserved for network management, monitoring, and packet error control. The assignment of individual time slots within the one-second TDMA frame is shown in figure 7.3. This provides an effective bandwidth of at least 1200 bps uplink for each surface station and a 2400 bps for broadcast downlink.

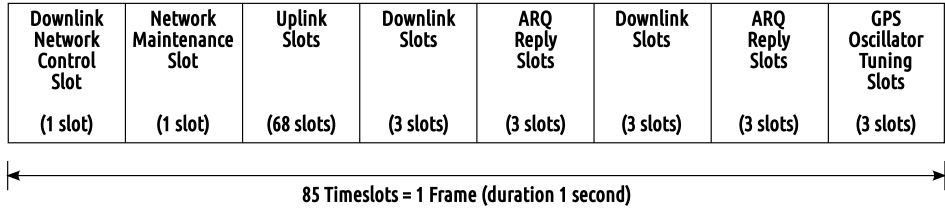


Figure 7.3: A single GPS synchronized one-second TDMA frame is broken in time slots as shown.

Error handling

A central requirement of the Auger WLAN system for collecting data from the surface detector stations is very high reliability. In response to an array trigger, digitized data from PMT traces and other detector information must be relayed promptly to the central controller (CDAS) so that the event can be built and recorded. Data from a single event trigger will be broken into several dozens packets transmitted by each station on request, a process that can continue for as long as two minutes. If even a single data packet is missing or corrupt, the entire trace from the station is lost. A custom packetization protocol that includes Cyclic Redundancy Checking to detect transmission errors is used at every level.

For the custom wireless network itself, an advanced re-transmit-on-error scheme, commonly called an Automatic Repeat Request (ARQ), is also employed. The ARQ scheme is especially designed to prevent data loss in the case of variable signal fluctuations, external sources of interference or any other episodic environmental influences. If a packet is flagged as missing or corrupt at the monitoring concentrator of the central network, a request to re-transmit the packet is automatically initiated and collected via the subsequent data frame reserved TDMA time slots. The ARQ request will be sent once per frame and will be repeated so that at least six attempts are made to retrieve each missing or corrupt packet.

7.1.3 Communications Data Rates for the Auger Upgrade

The uplink data rate requirements for the Auger Upgrade are based on the expected performance of the Upgraded Unified Board (UUB) electronics associated with each Surface Detector station. Each station in the field reports data via uplink in several distinct forms:

- **T2 time-stamps:** Each individual station in the field has set of local second-level trigger conditions (so-called T2 triggers). Within the existing array, the T2 trigger rate is approximately 25 Hz. The time-stamps for each of these T2 events must be reported via uplink to the central controller (CDAS) which decides on array-wide triggers (so-called T3 triggers) corresponding to real cosmic ray events.

For the Auger Upgrade, we do not anticipate that the rate of T2 triggers will increase. Indeed, given the greater flexibility of the UUB, we anticipate tuning the overall T2 rate down to about 20 Hz. The T2 message has a 7 byte header, with each individual timestamp requiring 3 bytes. For margin, we budget 80 bytes for the T2 timestamps.

- **Array Trigger Event Data:** For array triggers (T3 events) participating stations are required to report all station data related to the requested trigger event. Due to the increase in the number of channels and the increased ADC digitization rate, the upgraded SDs will generate approximately five times as much data per T3 array trigger

as is currently being generated within the existing array. However, given the very low overall event rate for the part of the array that is outside of the infill (about 10 events per day per station) the increased data rate can be easily handled by the existing Leeds wireless system. We project each event to be approximately 15 kB after compression, yielding an average event data rate of 2 byte/sec.

- **Monitoring/Calibration Data:** Stations also transmit calibration data, including the current estimates of the online energy calibration, as well as sensor and monitoring information. We conservatively budget 1 byte/sec for this data, which is more than twice the current rate.
- **Scaler Rate Data:** In addition to the event trigger data, stations also include a very low-threshold scaler trigger which provides a raw count of the number of these triggers per second. The rate of this data is also estimated to be not more than 1 byte/sec, several times less than the current rate.

In total, the estimated average data rate for the full array is 84 bytes/sec, well under the 120 bytes/sec uplink bandwidth of the Leeds system.

We note that during normal operations, the download broadcast link is used for station control and for event trigger requests from the central controller for event data (T3 requests). Generally, the broadcast rate is much lower than the capacity of 2400 bps for the Leeds system. As a rule, the broadcast bandwidth is only filled during special operations, such as installing new station firmware.

7.1.4 Data Communication for the Infill Array Region

The original Leeds wireless communication system for the Surface Detector system was designed for the original configuration of the Auger Observatory and will be more than sufficient to handle the increased bandwidth for the Auger Upgrade within the field for the 1600 surface detectors deployed on the 1.5 km grid. However, the data rates for the region recently occupied by AMIGA, including the Auger Infill region, result in a substantially higher array trigger rate (by design). At present, a combination of re-deployed Leeds radios, together with a specially configured communications system for AMIGA are operating within the infill region. Although the Leeds radios are operating within this region, the substantially increased infill trigger rates use up virtually all of the spare bandwidth so that there is no additional margin for additional data. What this means is that while the existing Leeds radios will very nicely handle the increased data rates for the Auger Upgrade associated with the larger array, they are *not* be able to handle the larger rates within the infill region.

For the infill / AMIGA region of the array, we will need an alternative to the exiting Leeds radio communication system. Specifically, we will need to identify and implement a communications system that will independently provide an uplink bandwidth of at least 20 kbps for anywhere from 100 to 200 stations within the infill.

Fortunately, the Auger Collaboration already has some experience with the implementation of alternative communications systems for specific tests and enhancements. At present, we can identify at least two different options for communications systems tailored for the infill array region: either based on the AMIGA communication system [155], or based on the AERA communication system [156].

Both options use commercial off-the-shelf 802.11-based wireless links, and have similar bandwidth (\sim Mbps) and power consumption (\sim 3 W). Technology for both systems should be readily available, and both are currently deployed and operating well within the infill region. The exact configuration for each communication system option has not yet been developed.

7.2 Central Data Acquisition System (CDAS)

The CDAS has been running since March 2001. The system was designed to assemble the triggers from the surface array detectors, to allow control of these detectors and to organize the storage of data. It is constructed using a combination of commercial hardware and custom made, high level, software components. The system is designed to run continuously, with minimum intervention, with the full 1660 detector array. Data from the FD are recorded separately at the FD locations and transferred daily to the computer center at Malargüe, although hybrid coincidences are identified online within the SD data stream.

The primary role for the CDAS is to combine local trigger information from the SD stations in order to identify potential physical events generating an SD higher level trigger (T3). These triggers combined with the T3 from FD sites (FD T3) are used to generate a request for the relevant data from SD stations for these events. The CDAS is then used to combine and store these data to form a shower event. The CDAS also contains configuration and control mechanisms, the means to monitor system performance, and the tools to access and download SD monitoring, calibration, control and configuration data.

The Post Master (Pm) is the interface between the Surface Detector Array and the CDAS. It is the end point, at the Observatory Campus, of the *communication backbone*, and is aimed at dispatching information from the different *data streams* towards the CDAS applications. It serves also as a router between the CDAS applications and the Surface Detector Array. Pm maintains a routing table by trapping local station identifications in the incoming data flow.

The Post Master also implements the *backbone protocol*. Pm is a *server* for all the transactions across the data path, accepting requests from *clients*. Requests consist of messages. The Pm protocol defines how to connect to the server and the content of the messages to be exchanged for a given *data service*. This protocol is also used by the CDAS applications or any external client to gain access to the data streams.

The data sent by the local stations belong to several *streams*. The main streams are:

- Local triggers (T2): higher priority stream; time stamps and local trigger type; to be forwarded to the *Central trigger* (Ct); their occurrence rate is about 20 Hz per station.
- Shower data and calibration (*Event*): on request from the CDAS; the events are split into smaller pieces in order to be channeled into the communication path together with the T2 packets. Once completed, the events are forwarded to the *Event Builder* (Eb).
- Calibration and Monitoring information (*Monitoring*): low priority stream; same behavior as Events; to be forwarded to the *Monitoring client*.

The CDAS transmits to the local stations some commands and configuration parameters, event requests (i.e. T3 triggers from Ct), and monitoring requests. Software downloads are also possible across the backbone.

Pm is in charge of presenting well formatted, intelligible and complete data to its clients. It extracts the different data streams from the local station messages and processes each of them according to CDAS requirements:

- T2 data from stations present in the run are accumulated. Every second, all T2 data which are older than the maximum allowed delay (5 s) are sent to the candidate clients (e.g. Ct), then discarded.
- Event, calibration and monitoring data pieces are reordered and concatenated from successive local station messages, then sent to clients (e.g. Eb) and discarded. Incomplete data blocks are discarded.
- Initialization messages from the local stations are formatted, forwarded to clients and logged by the Information Kernel (Ik) of the CDAS.
- T3 triggers, commands and controls, monitoring requests and software downloads are routed to the appropriate Base Station Unit.

As mentioned in Sec. 4.3.6, the local station acquisition for the Auger Upgrade will be a direct port of the existing code base. Therefore, the basic messaging protocol between CDAS and the surface detectors will not change. This has the distinct advantage of allowing easy operation of a heterogeneous array during the upgrade process, allowing or both UUB-based surface detectors and UB-based surface detectors to coexist during data taking.

Data structures themselves, however, will be different, due to the expanded data format and increased number of detector data channels. Therefore, to accommodate the new data format, the ‘event’ portion of the messaging between the local station and CDAS will be restructured into a block-based format, allowing the CDAS data acquisition processes to gracefully handle the presence or absence of data in the event structure. In addition, this will allow data from the digital expansion connectors to be eventually added to the event structure.

7.3 Monitoring

The CDAS provides information to monitor its own operation, the communication status, the trigger rates, the surface detectors status, and various environmental parameters. As explained above, the CDAS scheme will be easily adapted to the detector upgrade, and this is also the case for the whole monitoring procedure. Here we recall the Auger Monitoring scheme, before pointing out what has to be modified.

Besides the information from the data acquisition and the communication systems, the CDAS handles 3 types of data managed by the water-Cherenkov detector (WCD) acquisition software and related to the WCD: event data files, T2 files, monitoring and calibration files. Moreover, information on the weather conditions at different points in the Observatory are stored in a 4th data stream.

Inside the CDAS network, all these data streams are parsed by programs to produce XML files, which are copied to the monitoring system. The XML files are processed to produce and execute SQL requests in order to fill the Auger Monitoring Data Base. The Observatory

monitoring web site uses the appropriate scripts (PHP, Ajax, etc.) developed to display the information retrieved from the database to control the online SD status and to raise alarms if needed.

The monitoring and calibration files contain information related to the WCD status (solar power system currents and voltages, temperatures) PMT status (voltage and current, baseline values, etc.), calibration procedure (for each PMT : the peak current corresponding to a VEM; the corresponding charge; the dynode/anode ratio, used to calibrate low gain relative to high gain) and the local trigger rates. Each WCD sends this monitoring and calibration information every 6 minutes.

One "T2" file is produced each day. It provides data on which WCD are participating in data acquisition every second of the day. This is particularly useful for the exposure calculation.

The weather files contain temperature, pressure, and wind speed measurements sent every 5 minutes by different weather stations located either at the FD sites, or at the Central Laser Facility.

For the Auger Upgrade, the new CDAS version will contain the following monitoring-related changes:

- Additional slow control and calibration parameters will be added for the SSD (e.g. PMT voltage, temperature).
- New sensors available in the upgraded electronics will be recorded (temperature/current measurements).
- Trigger configuration/versioning information will be included with each event.
- Compressed calibration histograms will be transmitted periodically (1/hour) with calibration data.
- Data frequency will be reduced for housekeeping parameters (voltage, current) to allow for the additional calibration data.

Calibration histograms will be a significant monitoring improvement relative to the existing Auger software. Currently, these histograms are transmitted only when an event occurs at an individual station, due to the limited bandwidth. A statistical lossy compression scheme will be used to reduce the histogram size, allowing for a detailed measurement of the surface detector performance every hour.

These changes do not affect the data treatment between the CDAS frame and the monitoring frame. The different software which produce XML files and send them to the monitoring server, and which construct the SQL requests, will be modified to deal with new parameters. Existing DB tables will be extended to store useful parameters. The web interface to display monitoring, calibration and triggers rates will be upgraded accordingly. During the Engineering Array deployment, monitoring features developed to consider the status and performance of a particular sub-array (Infill array, test array...) will be used.

Chapter 8

Data Processing and Offline

The Offline software of the Pierre Auger Observatory provides both an implementation of simulation and reconstruction algorithms, discussed later, and an infrastructure to support the development of such algorithms leading ultimately to a complete simulation, reconstruction and analysis pipeline. Indeed, when the Offline code was originally devised, the only existing systems were the SD and FD. It has since been extended to handle the radio and AMIGA extensions without requiring dramatic framework changes. The most recent extensions comprise the surface scintillator detector (SSD), the upgraded electronics chain for faster sampling, and the small PMT in the water-Cherenkov detector (WCD). The software has been designed with such flexibility in mind, and is meant to accommodate contributions from a large number of physicists developing C++ applications over the long lifetime of the experiment. The essential features include a “plug-in” mechanism for physics algorithms together with machinery which assists users in retrieving event data and detector conditions from various data sources, as well as a reasonably straightforward way of configuring the abundance of different applications and logging all configuration data. A detailed description of the Offline software design, including some example applications, is available in [157].

The overall organization of the Offline framework is depicted in figure 8.1. A collection of processing *modules* is assembled and sequenced through instructions contained in an XML file [158] or in a Python [159] script. An *event* data model allows modules to relay data to one another, accumulates all simulation and reconstruction information, and converts between various formats used to store data on file. Finally, a *detector description* provides a gateway to data concerning detector conditions, including calibration constants and atmospheric properties as a function of time.

8.1 Physics modules

Simulation and reconstruction tasks can be factorized into sequences of processing steps which can simply be pipelined. Physicists prepare processing algorithms in modules, which they register with the Offline framework via a one line macro. This modular design allows collaborators to exchange code, compare algorithms and build up a variety of applications by combining modules in various sequences. Run time control over module sequences is implemented with a *Run Controller*, which invokes the various processing steps within the modules according to a set of user provided instructions. We devised an XML-based lan-

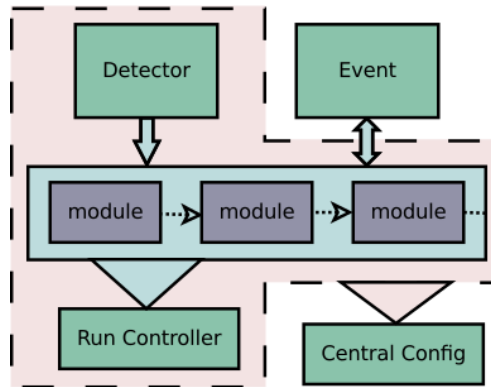


Figure 8.1: General structure of the *Offline* framework. Simulation and reconstruction tasks are enclosed in modules. Each module is able to read information from the detector description and/or the event, process the information, and write the results back into the event under the command of a *Run Controller*. A *Central Config* object is responsible for handing modules and framework components, their configuration data and for tracking provenance.

guage as one option for specifying sequencing instructions; this approach has proved sufficiently flexible for the majority of our applications, and it is quite simple to use.

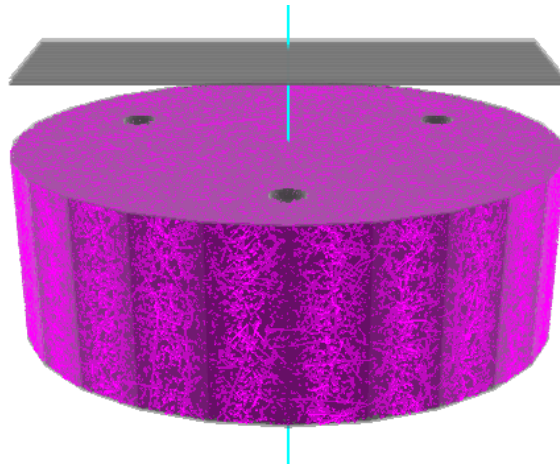


Figure 8.2: Visualization of a Geant4 simulation of the SSD/WCD combination. One can see a muon entering the SSD above the tank, the three 9-inch PMTs in the station, and the “gas” of reflected photons within the WCD.

Various simulation chains were prepared in the *Offline* framework for the battery of simulation challenges employed in arriving at the best, most cost-effective upgrade design. Figure 8.2 displays an image of a WCD with a scintillator positioned above it. A single muon is injected vertically for illustrative purposes. One can see the “photon gas” created as Cherenkov light is emitted in the WCD. The WCD/SSD simulation is based on the Geant4 [146] package, which supports detailed simulation of physics processes as well as relatively straightforward definition of complex detector geometries and materials.

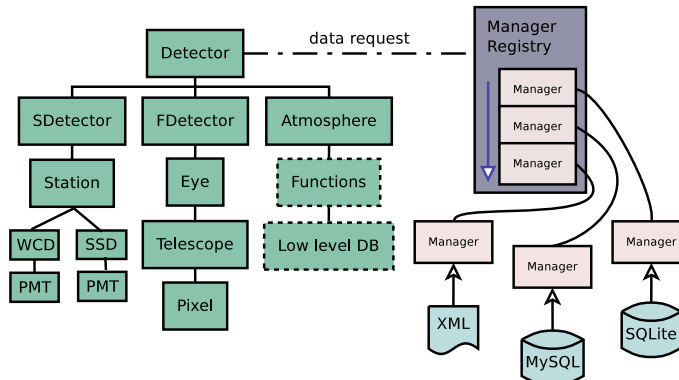


Figure 8.3: Machinery of the detector description. The user interface (left) comprises a hierarchy of objects describing the various components of the Observatory. These objects relay requests for data to a registry of managers (right) which handle multiple data sources and formats.

8.2 Data access

The `Offline` framework includes two parallel hierarchies for accessing data: the detector description for retrieving data about conditions, including detector geometry, calibration constants, and atmospheric conditions, and an event data model for reading and writing information that changes for each event.

The *detector description* provides a unified interface from which module authors can retrieve conditions data. Data requests are passed by this interface to a back end comprising a registry of so-called *managers*, each of which is capable of extracting a particular sort of information from a collection of data sources. The manager mechanism is highly configurable and relieves authors of the physics code from having to deal with the details of selecting and reading the correct data source. The general structure of the detector description machinery is illustrated in figure 8.3.

The event data model contains raw, calibrated, reconstructed and Monte Carlo information, and serves as the backbone for communication between modules. The event is instrumented with a protocol allowing modules to discover its constituents at any point in processing, and thereby determine whether the input data required to carry out the desired processing are available.

The transient (in memory) and persistent (on disk) event models are decoupled in order to avoid locking to a single provider solution for serialization, the process by which C++ objects are converted to a form that can be written to disk. When a request is made to write event contents to file, the data are transferred from the transient event through a *file interface* to the persistent event, which is instrumented with serialization machinery. We currently use the input/output portion of the ROOT [160] toolkit to implement serialization. Various file formats are interpreted using the file interface, including numerous raw event and monitoring formats as well as the different formats employed by the AIRES [161], CORSIKA [147], CONEX [162] and SENECA [163] air shower simulation packages.

8.3 Configuration

The *Offline* framework includes a system to organize and track data used to configure the software for different applications as well as parameters used in the physics modules. The *Central Config* configuration tool (figure 8.1) points modules and framework components to the location of their configuration data, and connects to Xerces-based [164] XML parsers to assist in reading information from these locations. We have wrapped Xerces with our own interface which provides ease of use at the cost of somewhat reduced flexibility, and which also adds functionality such as automatic units conversion and casting to various types, including commonly used containers.

The *Central Config* keeps track of all configuration data accessed during a run and stores them in an XML log file, which can subsequently be used to reproduce a run with an identical configuration. This allows collaborators to easily exchange and use configuration data for comparing results. The logging mechanism is also used to record the versions of modules and external libraries which are used for each run.

Syntax and content checking of the configuration files is afforded through W3C XML Schema [165] standard validation. Schema validation is used not only for internal configuration prepared by framework developers, but also to check the contents of physics module configuration files. This approach reduces the amount of code users and developers must prepare, and supports very robust checking.

8.4 Utilities, testing and quality control, and build system

The *Offline* framework is complemented by a collection of utilities, including an XML parser, an error logger and various mathematics and physics services. We have also developed a novel geometry package which allows the manipulation of abstract geometrical objects independent of coordinate system choice. This is particularly helpful for our applications since the Observatory comprises many instruments spread over a large area and oriented in different directions, and hence possesses no naturally preferred coordinate system. Furthermore, the Geometry package supports conversions to and from geodetic coordinates.

As in many large scale software development efforts, each low level component of the framework is verified with a small test program, known as a *unit test*. We have adopted the CppUnit [166] testing framework as the basis for implementing these tests. In addition to unit tests, a set of higher level acceptance tests has been developed which is used to verify that complete applications continue to function as expected, within some tolerance, during ongoing development. We employ a BuildBot system [167] to automatically compile the *Offline* software, run the unit and acceptance tests, and inform developers of any problems each time the code is modified.

The *Offline* build system is based on the CMake [168] cross-platform build tool, which has proven adequate for this project. In order to ease installation of *Offline* and its various external dependencies, we have prepared a tool known as APE (Auger Package and Environment) [169]. APE is a python-based dependency resolution engine, which downloads the external packages required for a particular application, builds them in whatever native build system applies for each package, and sets up the user's environment accordingly. APE is freely available, and has been adopted by other experiments, including HAWC, NA61/SHINE and JEM-EUSO.

8.5 Production

Data production methods are mature, as the Auger Observatory has been operational for over a decade. We employ GRID resources for simulation production, from generator-level shower simulation up through simulation of detector response and reconstruction of the resulting simulated data. The Auger collaboration has become one of the biggest non-LHC users of the European Grid Infrastructure (EGI), and at the recommendation of the EGI, a Virtual Research Community is being established for Auger. Simulations are transferred from GRID storage elements to the Computation Center - IN2P3 (CC-IN2P3) in Lyon, for easy availability to collaborators. Raw data from the Observatory site is also transferred to the CC-IN2P3, where it is available to collaborators for analysis and further processing. Reconstruction of real data is performed on a dedicated cluster located at the Karlsruhe Institute of Technology, and reduced data summary files are generated for end-user analysis.

The Collaboration is in the process of developing an extended program to release the full data sample to the general public. The relevant policies and technical issues are currently being addressed. At the moment 1% of high-quality data are made public regularly at [170].

Chapter 9

Reception Tests, Deployment and Maintenance

This chapter describes the equipment, facilities, and procedures for reception at the Central Campus in Malargüe of the detectors and components for the upgrade of the Pierre Auger Observatory. It also describes the testing, deployment, and maintenance for the next 8-10 years of operation.

9.1 Reception and testing of Scintillator Detectors

The scintillation detector modules will be prepared in distant facilities and shipped to Malargüe in crates, with three crates in each 40 foot (42G1) container. We presently estimate that we can load 16 modules resting on a side edge per crate for a total of 48 per container.

Upon arrival, the crates, which have a skid base, can be pulled from the container and moved by a forklift. The crates, still loaded with modules, will be stored in the yard under a protective cover until they are ready to be unloaded for testing and deployment. Individual modules can be lifted vertically out of the crates and moved in a straightforward manner, by forklift, or by light, portable cranes and on wheeled dollies. It will be necessary to buy these light, portable cranes and have at least two available to avoid conflicts resulting in delays. It may be desirable to rent or purchase an additional forklift for the duration of the upgrade activity.

Reception testing of the modules will consist of:

- a visual inspection of the exterior of the modules for any shipping damage;
- measurement of photomultiplier background in light- and dark-conditions to identify light leaks;
- measurement of individual scintillator strip response to cosmic rays.

The last measurement will be made using a cosmic ray telescope based on Resistive Plate Counters (RPCs) with readout pads sized and positioned to match the scintillator strip spacing in the modules. The module is placed horizontally on a 3.6m x 1.2m test bench between the RPCs. If four RPCs are provided per test bench, then every strip can be tested for efficiency and pulse size in a single “run” without having to move the module or the RPCs. We

would speed up the process by having two test benches operating in parallel. Based on our long experience in building and running the Auger Observatory, we estimate that with one team of two trained technicians we can expect a testing rate of 60 modules per week.

Following inspection and testing, the characteristics of the module and the serial numbers are recorded in a database. Cables, connectors, and the vent will be protected with plastic covers and the module placed in a vertical position, resting again on a side edge. The modules can then be stored in ad-hoc racks in the Assembly Building for ready deployment or, in the case where testing is well ahead of deployment activities, in longer term storage in the original crates in the yard under a protective cover. Modules which fail one or more of the incoming test procedures will be set aside for repair, to be done as quickly as possible in case feedback is needed to improve the manufacturing or shipping processes.

Each scintillator module will require a sunroof to be installed over it to reduce high temperature fluctuations during daytime. The engineering details of these sunroofs are not provided as of this writing but they are expected to be simple, corrugated sheet metal structures, spaced slightly above the scintillator modules to allow air to circulate between the module and the sunroof. They will not be installed on the modules when they arrive from the factory to reduce shipping costs but will be added in Malargüe or in the field during deployment. We may find it most cost effective to buy these materials in Argentina.

9.2 Deployment of Scintillator Detectors

The modules will be mounted over the existing surface detector water tanks on a frame attached to four of the six lifting lugs molded into the tank. This frame is shown in the rendering in Figure 9.1. To reduce corrosion and to minimize the weight loading on the tank and the weight to be lifted during installation, the mounting structure is made from aluminum beams. The structure consists of a main I-beam with vertical support columns at the ends and of two Unistrut® cross beams with one vertical column each. Although the nominal dimensional tolerances on the tanks is $\pm 1.5\%$, in practice the tanks are more uniform, with a few centimeters variation in the lug position being more typical. The mounting frame will have enough adjustment to allow for this variation by using the easy positioning ability of the Unistrut® cross beams and with slotted mounting holes in the attachment brackets at the ends of the main beam. Connection of the support frame to the tank is done with injection molded plastic feet at the four mounting lugs. These parts are inserted into vertical columns and their depth of insertion into the columns is controlled by thick plastic spacer washers, allowing the plane of the support frame to be adjusted to allow for warping of the tank top and subsequent non-planarity of the lugs. The scintillator module is fixed to the top of the cross beams and is supported at 25% and 75% of the length of the module. Additional support of the module at the ends of the main beam will be added to increase stability and resistance to wind-driven resonances in the structure.

The desired deployment rate requires that 1660 detectors be installed in 200 working days per year. A rate of six per day will allow us to complete installation in 1.5 years with margin for lost time due to weather, technician illness, and maintenance of the deployment equipment. Two teams of two people each will be able to deploy three detectors each day based on two hours of driving to/from the local site and 1.5 hours of work at each site. We considered the possibility of delivering a large number of modules to the field in a container, then deploying them from that “base”. It was concluded that the crew could easily take

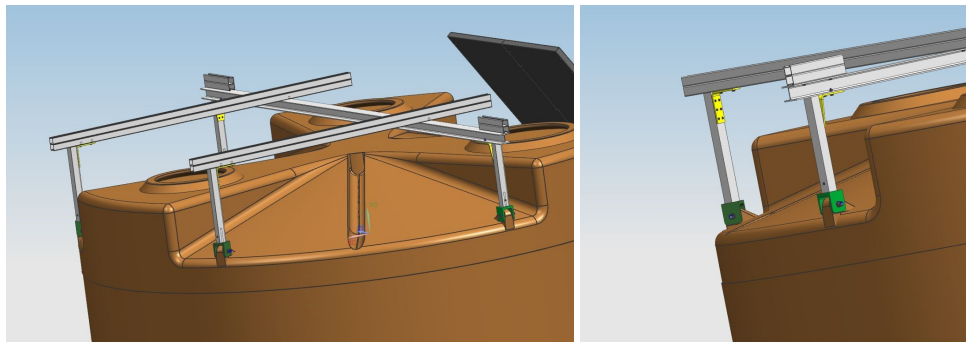


Figure 9.1: The module support structure designed for simplicity, light weight and simple installation. An overview is shown in the left panel, while a detail of the structure is shown on the right. An aluminum I-beam and two Unistrut channels are the main structure. Injection molded plastic feet connect the frame to the lifting lugs on the tank.

as many modules as required into the field each day, and that there was no advantage to providing a large local storage of modules in the field. The scintillator deployment, the electronics deployment with the small PMT, and the underground muon detector deployment will all be carried out independently. The electronics deployment requires a different skill set, a different deployment rate, and different equipment, so maximizing efficiency suggests that this deployment be done separately. The underground muon detectors are deployed in a very localized area of the detector array and require a very different technique and time scale from either the electronics or scintillator deployments.

Each scintillator deployment team will have a truck with a trailer. The trailer will be fitted with a rack that can hold five modules installed vertically, i.e., resting on the long edge. Each trailer will also be able to carry the mounting structure (in three pieces) and the sunroof, as well as any small parts and tools required for installation. Although the design deployment rate is three modules per day per team, it may be possible on some days to install more, so the trailer capacity was set at five modules to make this possible. Total loaded weight of the trailer will not exceed 1000kg, which can be pulled by a large pickup truck. If the sunroofs are mounted on the detectors in the Assembly Building, the trailer design would then be such that the modules are supported in a horizontal position on racks. As each module is removed the supporting cross-beams for the rack for that module are also removed.

The pickup truck will have a jib crane installed on the back with a capacity of 200 kg and a reach of at least 2.5 m. It will consist of a horizontal I-beam with a trolley from which is suspended a rolling electric hoist, powered by the truck electrical system. The horizontal beam is attached to a vertical column which pivots about a vertical axis, allowing the beam to swing over the trailer, pick up the module with the hoist, raise it and swing it over the tank and lower the module in position. There are other possibilities for a crane, such as the common “hydrogrua” hydraulic crane that was used for the deployment of the tanks, or other commercially available cranes designed for mounting in pickup trucks. Outriggers will be added to the truck to maintain stability during the lift. The mounting structure, especially considering that it will be in three large pieces (the beams) that can be lifted into position by two technicians by hand, will not require the crane for deployment.

Upon arrival at the site, the support structure is installed first. The three large components, the main beam and the two cross beams, will be lifted by hand onto the tank and fitted

to the lifting lugs. Adjustments will be made as needed for irregularities in tank dimensions. One vertical column needs to have adjustability (by selection of bolt holes, for example, or by selection from a set of vertical columns of varying lengths) to maintain the module in a plane. This plane may not be quite horizontal and we will have to determine based on physics analysis requirements what an acceptable deviation from horizontal might be.

The module is then lifted from the trailer using the crane on the truck. The module perimeter consists of a wide-flange I-beam so this is a strong point which can allow lifting fixtures to be attached for lifting in either a horizontal or a vertical orientation, and which can be used to transition between one orientation and the other. If the module is horizontal with the sunroof attached, it is simply lifted into position on the mount and connected with the attachment brackets to the beams. If the module is vertical without the sunroof attached, it needs to be rotated to a horizontal position, either by setting the module down on the ground on a temporary bench, or by setting it on the already-installed mounting structure and lowering to a horizontal position. After fixing the module to the mount, the sunroof can be installed.

The installation can then be inspected visually and manually to verify the proper installation of the module, mount, and connections for proper installation and stability. The cables can be connected to the module and sealed (if a separate weather/light seal is provided) and the CDAS operator contacted. The CDAS operator will verify proper operation of the new module. It is expected that the number of defective installations will be very low, and modules that fail will be retrieved from the field and repaired in the Central Campus later. Calibration of the detectors occurs remotely by CDAS. If the CDAS operator is not able to give a quick evaluation of performance, the installation crew will move on to the next station for the next deployment. In those rare occasions when the CDAS operator later reports a problem, it is a simple matter to return to the site and retrieve the module. We hope to learn a lot about deployment rates early in the Engineering Array deployment experience and adjust the plan and equipment requirements accordingly.

9.3 Reception and testing of Surface Detector Electronics kits

The integrated electronics board will be fabricated in 3-4 fabrication sites by following the Quality Management Plan of the current electronics [150]. The boards will be conformally coated and tested (including thermal stress testing) following the test plan described in [151] after which the boards will be shipped to the Auger Observatory. The GPS receivers will be procured and tested and also shipped to the Observatory. The front panel of the electronics enclosure and the cables and other loose parts will be fabricated and shipped to the Observatory.

In the Auger Observatory the various electronics parts are stored in a specific building called SDEco. They will first be visually inspected and then assembled into the electronics enclosure (Ekit). The final end-to-end tests are performed following the SDE test plan [151] after which the Ekits are ready for deployment. All test results will be stored in a database, as with the previous electronics test procedure.

9.4 Deployment of new SDE kits and small PMTs

As mentioned earlier, the electronics and small PMT deployment will be separate from scintillator deployment because the time scale and talent requirements are different. The electronics deployment is very similar to what is currently done for the electronics maintenance. Therefore, Ekits with new electronics can be deployed during the regular maintenance of the Surface Detector, when the old electronics Ekit will be simply replaced by a new Ekit. The new electronics can be downgraded to the function of the current electronics. In particular, the data can be compressed to 40 MHz traces which would allow application of the same trigger and data analysis routines as with the current electronics. This would allow a continued maintenance of the Surface Detector by using new electronics with no noticeable effect on data. The small PMT can be very easily deployed whenever a new Ekit is installed. On average, about 18 detector stations are maintained per week or about 800 per year. This would allow an upgrade of the array in two years.

In addition to the maintenance deployment, a dedicated deployment of electronics will be done. The strategy is to gradually increase the area of surface detectors with new electronics. In particular, this deployment will include pre-production phases corresponding to different electronics production sites (a total of about 100 detectors). The experience from the previous deployment of the Surface Detector electronics suggests that new electronics and small PMT installation will require 35 minutes. Therefore, typically 8 Ekits and 8 small PMTs can be deployed during one trip with a crew of two technicians. This would allow a deployment of about 100 Ekits and small PMTs per month and shorten the total deployment time to about one year. The addition of these 100 Ekits and small PMTs per month in a contiguous pattern will allow the subsequent installation of scintillator modules to also occur in a contiguous pattern, therefore maximizing the number of showers that can be detected with all triggered stations belonging to the upgraded array.

It is estimated that the additional deployment of the new electronics and small PMTs would require the hiring of one additional technician for the period of two years (see the WBS). Additional help will be provided by students as was done in the previous electronics deployment.

9.5 Reception and testing of Underground Muon Detectors

The underground detectors have a modular design in order to speed up the assembly process and to allow easy handling and transportation [171]. The modules are divided into three main parts: i) WLS fibers and optical connector, ii) scintillators and fiber routing components, and iii) PVC casing (see Fig. 9.2).

The fiber package has 64 WLS fibers threaded into the optical connector, which is identical in all detector modules. Fibers have different lengths (varying from approximately 4.3 m to 4.9 m) according to their routing in the PVC manifold towards the optical connector (see Fig. 9.2). Also, each fiber far-end (i.e., away from the optical connector and PMT, see Fig. 9.2 upper corner) is painted black to avoid reflections that would impoverish both timing and pile-up accuracies. The nearside is leveled and polished with a fly-cutter which is instrumented with two diamond tool bits. This fiber package is the most sensitive part of the detector to mechanical stress, so it is to be built in laboratories with testing facilities. It might be packed into a special transportation tube if the module is finally to be assem-

bled at the Observatory campus. The manufacturing laboratories must be clean and with a quality-assurance procedure plan. The testing of this critical package will include mechanical verification of the fibers (diameter, lengths, and fly-cutting quality) and of the optical connector dimensions and alignment. Light-transmission tests could be performed with a LED source fired directly onto the fibers and/or with a radioactive source on an already assembled module. A final quick test with background radiation is to be performed after the modules are deployed in the field for both quality assurance and calibration.



Figure 9.2: Two 10 m^2 AMIGA modules being manufactured. The 64 scintillator bars are grouped into two groups of 32 bars each, with the optical fibers curved up in the middle (see insert) onto an optical coupling device for the PMT.

The fiber routing parts, the scintillating bars, the fiber package, and the PVC casing sheets may be transported to the module assembly facility. This final assembling of the underground detector modules may be performed at different laboratories and at the Auger Observatory facilities. All parts are finally glued together to form a solid and robust plastic detector. The optical cement on the scintillator groove which glues fibers to scintillators is to be well controlled and inspected before closing the module in order to ensure no detector sectors have bad optical coupling.

9.6 Deployment of Underground Muon Detectors

The AMIGA engineering array has shown that an underground detector (three scintillating modules of 10 m^2 each) is easily deployed in two days, including the hole filling, cabling, electronics deployment, and final testing. In production, two machines might be required to perform in parallel the mentioned tasks in order to streamline the job. Deployment of a 10 m^2 module requires a 15 m^2 hole (5 m^2 are for maneuvering), and 10 m^2 for the excavated soil to be deposited alongside the hole. This hole would amount to 21 m^3 of removed soil.

The production deployment strategy consists of placing the three modules into a transportation container, mounting the container onto a cart provided with its own crane, and driving to the deployment destination with a pick-up truck. The three modules are lifted and deployed by a team of three technicians while the retro-digger machine opens another pit. After the modules are buried, the cabling is performed, electronics deployed, and a first diagnostic and calibration program is run. The experience with the engineering array



Figure 9.3: Left: 1.3 m deep hole for a 10 m² module; Right: photograph of final deployment.

has also shown that this diagnostic program is not needed to be run before the detector is buried. However, it could be performed for the first production modules, and then in a sampling mode, to check if good deployment conditions are maintained in the long term.

9.7 Maintenance of Surface Detector System

Maintenance of the present surface detector, surface detector electronics, and communications systems is done by a local crew of technicians at the Observatory. Two to three field trips per week are required, mainly to replace batteries, repair PMTs and electronics, to occasionally replace solar power regulators or solar panels, and to clear the detectors of (potentially flammable) vegetation and birds' nests.

The expected failure rate of the scintillation detectors is very low. A more precise estimate of the maintenance requirements will be available once some experience has been gained and the common failure modes have been identified.

It is expected that scintillator modules with a failure will be brought back to the Central Campus for repair, using the same equipment that was used for deployment. Perhaps the addition of one technician to the presently available crew will be an adequate allowance for the additional components (additional scintillator module, additional PMT in the tank) as well as for the aging of the existing equipment.

9.8 Maintenance of Underground Muon Detectors

Maintenance would mainly be performed on the electronics since the underground conditions at the Auger Observatory site seem to be convenient for the modules. The PVC casing does a very good job in providing water seal while the ground above the modules is a very good thermal insulator and a perfect light seal. Electronics is not to be repaired in the field but rather in trained laboratories. Removal of the electronics kit and PMT is performed from

the surface with a probe which hooks on to the system (Fig. 9.4, left). The electronics kit slides out on two thin metal rods (see Fig. 9.4, center). The PMT has two pins (Fig. 9.4, center and right) to match two conical holes bored into the optical connector. This procedure has already been practiced in the engineering array.

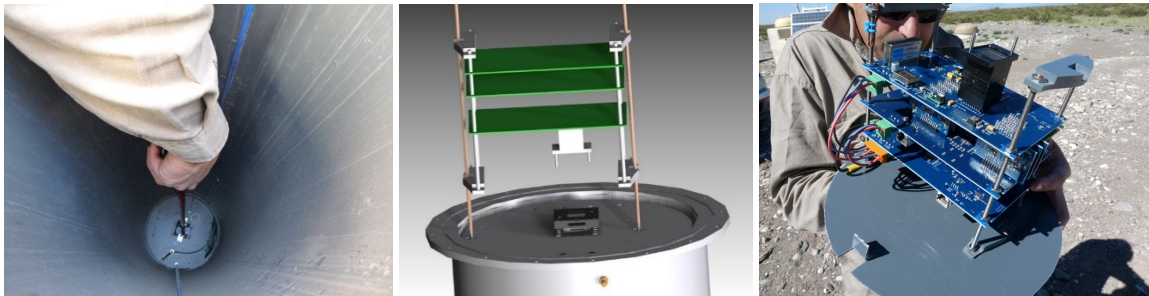


Figure 9.4: Electronics deployment and maintenance. Left: hook; center: diaphragm; right: electronics with PMT and pins.

The refilling of this small access tube can be done with small soil bags introduced into the tube. They would be light enough to be lifted without a crane.

Very few problems were found in both electronics kits and cabling since the first module was deployed in November 2009. No problems were found concerning PMTs, probably due to the favorable operating conditions of temperature and humidity.

9.9 Maintenance of the Upgraded FD

Four members of a local crew of technicians at the Observatory provide support for the operation and maintenance of the fluorescence detector including atmospheric monitoring devices. Currently, the regular maintenance work is done outside data taking periods and repairs are performed after each night in the case of a malfunction. An expert is needed during the data taking period to monitor the FD performance and provide support to shifters. We don't foresee any increase of manpower needed for the extended FD operation.

Travel to FD buildings by two crew members will be required in the case of a serious malfunction and a regular schedule of visits to the buildings will be maintained. The failure rate of various electronic components (typically moving mechanical parts and aging because of drying out capacitors), having been installed a decade ago, has been increasing in recent years and reparations are required by consuming still available spare parts. We expect higher failure rates after extending the FD operation, until most of the failing components have been renewed.

Very few problems have been experienced with PMTs and head electronics, but this system will be monitored closely during the longer data taking period. In addition, the slow control system will also require more attention as it almost doubles its operation time.

The costs of implementation of the FD extended operations do not appear in the WBS costing of the upgrade because no extra equipment is needed to extend operations into times of increased night sky background. Maintenance of the existing FD systems is covered by continuing memoranda of understanding with collaborating institutions.

Chapter 10

Upgrade Organization and Management

10.1 Introduction

An International Agreement, *The Agreement for the Organization, Management and Funding of the Pierre Auger Observatory* [172], approved in 1999, provides the basis for the organizational structure of the Auger Project. An extension of the International Agreement to 2025 has been approved by the Auger Finance Board and awaits final signatures.

The Auger Project Management Plan [1] has provided the basis for the detailed organization and management both for construction and operation of the Auger Observatory since its adoption by the Collaboration in 2001. The Auger Project employs the tools of management that have been learned over recent years from industry and large science projects like those at Fermilab and CERN. These include cost and schedule tracking, elements of systems engineering, quality assurance, risk management and ES&H programs. These tools were adapted to the particular needs of Auger, an international project based on an equal partnership of participating countries. Having successfully guided the Auger Project since its inception, the essential elements of the management structure will remain in place for the Observatory Upgrade. An updated version of the Auger Project Management Plan describes organizational and management features particular to the Upgrade.

10.2 Organization

The Pierre Auger Project has administrative oversight, both by the scientific collaboration through the Collaboration Board (CB), and by the funding agencies of the participating countries through the Finance Board (FB). The global project organization has been established by the International Agreement, a non-legally binding agreement among the funding agencies of the countries committing support to the construction, operation and upgrade of the Auger Observatory. The Agreement contains a statement of continuing support of the Auger Project, rules for the movement of experimental equipment through customs, a statement regarding ownership of Observatory property, tax status and related issues. The Pierre Auger global organization is shown in Figure 10.1.

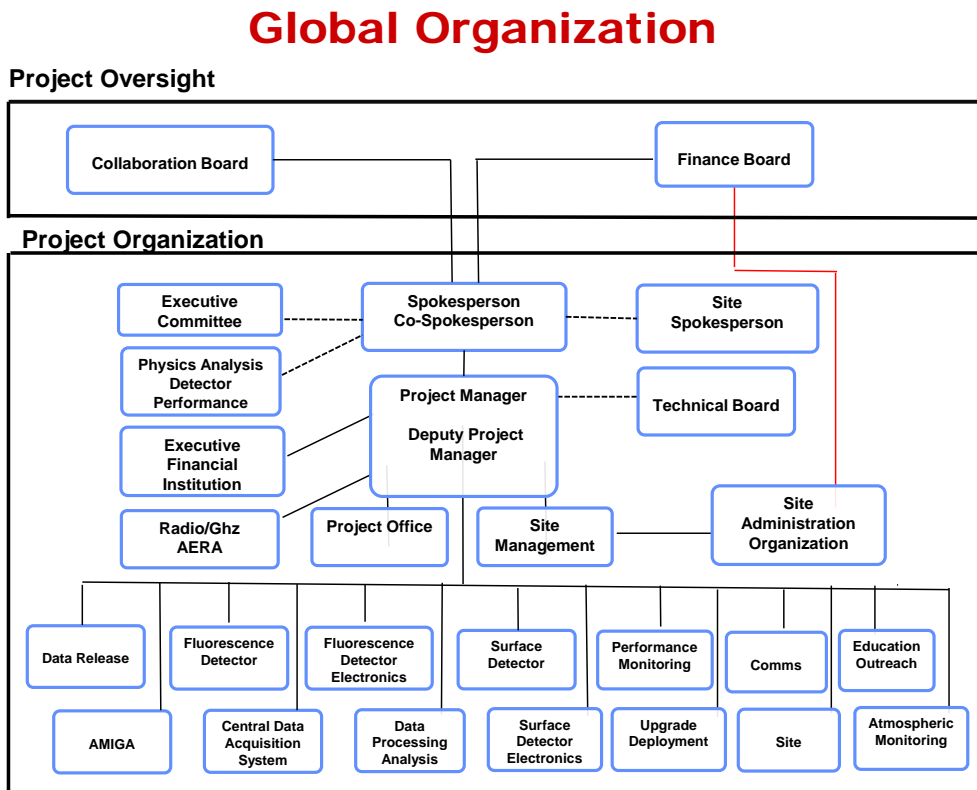


Figure 10.1: Auger Project organization and oversight

10.3 Management Structure

10.3.1 Project Oversight

The Finance Board is the oversight body for the financial aspects of the Project and is comprised of representatives of the funding agencies or their designees and works by consensus. The Finance Board assures the respective governments that the project is meeting its funding goals and furthermore provides a mechanism whereby funding problems associated with differences in accounting procedures, currency fluctuations, short term availability of funds within each country, etc. can be addressed. The Finance Board approves a yearly budget and financial reports presented by the Project Manager. It also receives status reports from the Project Manager and Spokesperson to ensure that schedule and budgetary goals are met. The Finance Board meets in-person on an annual basis and by phone conference as needed.

The Collaboration Board is the principal oversight body concerned with the scientific and technical aspects of the Project. It deals with issues including governance, scientific policy, admission policy of new members and institutions, publication policy and monitoring of the construction and operation of the Pierre Auger Observatory to ensure that the scientific objectives of the project are met. The members of the Collaboration Board are appointed by their home institutions among the scientists participating in the Pierre Auger Collaboration. Each institution with three or more active collaborators has one representative on the Collaboration Board. Institutions having fewer than three collaborators may join with other

institutions and have a common representative. Details on organization of the Collaboration Board are described in its bylaws that can be found in the Project Management Plan.

10.3.2 Project Organization

The scientific and technical direction of the project is invested in the Spokesperson and the Co-Spokesperson by the Collaboration Board. The Project Manager is responsible for the operation of the Observatory and reports to the Spokesperson. The Project Manager is supported by the Project Office staff and by the Technical Board. A Site Manager directs operations on-site and reports directly to the Project Manager. Task Leaders are responsible for the major components of the detectors.

The Auger Project Spokesperson and Co-Spokesperson are elected by the Collaboration via the CB and represent the Collaboration in scientific, technical, and management concerns. The Spokesperson speaks and negotiates on behalf of the Collaboration. The Spokespersons are responsible for establishing the scientific goals and the means for the Collaboration to pursue these goals successfully. They are also expected to pursue the identification of resources needed by the Auger Project and to seek the commitment of such resources toward the operation of and upgrades to the Observatory. These resources come from the scientific groups and institutions that collaborate in the Auger Project, as well as their various sources of funding for that purpose. The Spokespersons serve renewable three-year terms.

The Executive Financial Institution maintains an account for the operating funds and the operations reserve. The current Executive Financial Institution is the Karlsruhe Institute of Technology (KIT) in Karlsruhe, Germany. The operating and reserve funds are invoiced by KIT and disbursed at the request of the Project Manager.

The site spokesperson is the liaison between the Project Spokesperson and the host country.

The Project Manager is responsible for the operation of the Pierre Auger Observatory. The Project Manager's duties and responsibilities for operations include oversight of the day-to-day activities of the Observatory, preparation of budgets and tracking of expenditures, monitoring the environment, safety, and health program, serving as chair the Technical Board, carrying out technical reviews and preparation of MOUs for Operations with collaborating institutions. The Project Manager serves an indefinite term. The Project Manager reports to the Project Spokesperson. The Deputy Project Manager works with the Project Manager in carrying out Project Management responsibilities. They are assisted by personnel that make up the Project Office. These include a cost and schedule officer, an ES&H officer and clerical support. The Project Office is currently located at KIT.

The Task Leaders (level 2 managers) played a fundamental role in the construction and operation of the Observatory, and will also do so for the Upgrade. All tasks are broken down into a number of subtasks each with its own leader. These Subtask Leaders support the Task Leader in carrying out his/her duties. Task Leaders report to the Project Manager.

The Technical Board consists of scientists and engineers involved in leadership roles in the various technical areas of the Auger Project. The members of the Technical Board are the Spokesperson, Task Leaders and others appointed by the Spokesperson and the Project Manager. The Technical Board is chaired by the Project Manager. The Technical Board advises the Project Manager on technical issues pertaining to operation, maintenance and upgrades to the Observatory systems. The Technical Board also serves as the Change Control Board.

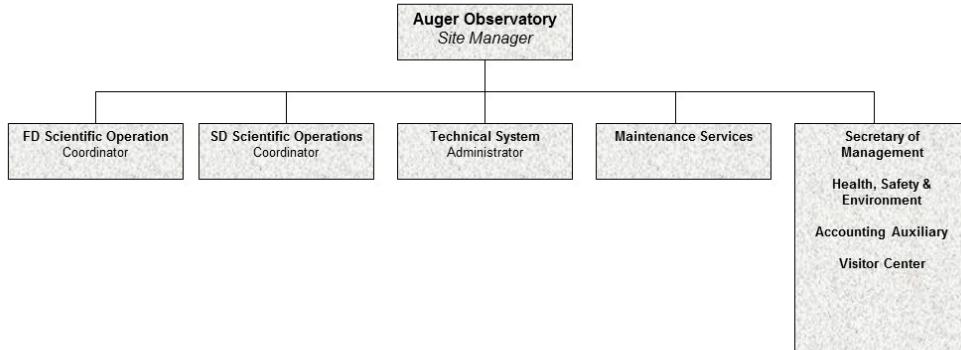


Figure 10.2: The Site Management

The Site Management staff is headed by the Site Manager. Operating funds for the Site Management are provided by the participating countries.

The responsibilities of the Site Manager include supervision of the site staff, writing contracts for local services needed for operations, maintenance of the buildings and infrastructure, assisting the Task Groups in receiving and storage of equipment, maintenance of the Visitor Center, serving as point of contact with land owners, local and state officials and ensuring that the environment is protected and the safety and health of staff and visitors is assured. The Auger Site Manager reports to the Pierre Auger Project Manager. The site organization is shown in Figure 10.2.

The Observatory Site Administrative Organization is responsible for contracting local personnel and for the local disbursement of funds in conformity with the laws of Argentina. The original Site Administrative Organization, Fundación Observatorio Pierre Auger Argentina (FOPAA), a non-profit foundation, was established in 2003, with bylaws as agreed to by the Pierre Auger Finance Board. The Site Administrative Organization is the only legally recognized entity directly related to the Auger Observatory, other than participating institutions and funding agencies in their respective countries. The Site Administration Organization will transition during 2015 to another not-for-profit foundation, *Ahuekna*, formed by a group of institutions in Argentina that support the Observatory.

In its role as part of the Auger Collaboration, the Site Administrative Organization reports annually to the Finance Board on its activities and funding. It handles operating funds on the basis of a budget approved by the Finance Board and the instructions of Auger Management. It also handles money and legal issues in consultation with the Project Management. Its responsibilities on behalf of the Auger Collaboration include employment of personnel, signing of contracts for services and maintenance, agreements for land usage and the handling of operating funds.

The Site Administrative Organization maintains legally required accounting and record of meeting books, hires lawyers, as needed, for labor and other legal issues, and utilizes computerized accounting and salary processing. It carries out the legal requirements from the tax and social services authorities and holds bank accounts and insurance policies.

10.4 Upgrade Management

The Auger Upgrade will be managed within the basic organizational structure under which the Observatory was successfully constructed. Minor changes will be made to the organization to reflect the specific responsibilities associated with the new elements of the Upgrade.

The revised Project Management Plan describes the management of the Upgrade. Associated management documents including Performance Requirements, Integrated Project Schedule, Work Breakdown Structure (WBS), WBS Dictionary, Quality Assurance Plan, Risk Management Plan, ES&H plan will be updated to reflect the particular needs of the Upgrade.

The Project Office will be strengthened to accommodate increased responsibilities of the Upgrade. In particular, project engineering, cost and schedule tracking, quality assurance, risk management and safety will require additional effort.

The management of the construction of the new scintillator detectors will take place within the existing Surface Detector Task. New subtasks will be added as necessary. Upgrades to the Surface Detector electronics will be carried out within the existing Surface Detector Task. Subtasks will be added as appropriate.

The MOUs with each institution participating in the Upgrade will include the commitment of institutional collaborators to the upgrade effort, their deliverables, and delivery schedule.

10.5 Quality Management

The Pierre Auger Project has a Quality Assurance Plan [2] to ensure the performance and reliability of the Observatory systems. Quality Assurance was an integral part of the Observatory design, procurement, assembly and test processes and the responsibility resides at all levels of the organization. The Auger Quality Assurance Plan was developed and will be updated by the Project Manager and the Project Quality Assurance Manager to accommodate the specific quality assurance/quality control requirements of the Upgrade.

Using the Quality Assurance requirements, each Task Leader has developed a quality system or plan that documents their approach and methods for achieving quality components and services. The Quality Assurance Manager assists the Project Manager and Task Leaders in developing their quality systems and audits their implementation.

As part of the Upgrade QA Plan a standard suite of internal technical reviews will be initiated early to ensure that the design and fabrication processes will achieve the physics goals of the Upgrade. The review panels will be made up of Auger collaborators, the project office (Project Manager, Project Engineer, QA manager, ES&H officer and Cost/Schedule officer) and outside experts as needed. The details of the each of the reviews below are contained in the Project Management Plan.

- Design Requirements Review (DRR)

- Preliminary Design Review (PDR)
- Critical Design Review (CDR)
- Production Readiness Review (PRR)
- Operations Readiness Review (ORR)

10.6 Risk Management

Risk management is a process of the Auger Upgrade activities project. It includes processes for risk management planning, identification, analysis, monitoring and control. It is the objective of risk management to decrease the probability and impact of events adverse to the project.

The Risk Management Plan (RMP) documents the processes, tools and procedures that will be used to manage and control those events that could have a negative impact on the Auger Upgrade activities. It is the controlling document for managing and controlling all project risks. This plan will follow the risk policy and will address:

- Risk Identification
- Risk Assessment
- Risk Response
- Risk Tracking and Reporting

The risk policy, described in the Risk Management Plan, defines the level-values scale for the risk impact on schedule, resources and performances, the scoring scheme for the likelihood of occurrence, and a risk index scheme to denote the magnitudes of the risks of the various risk scenarios.

For the Auger Upgrade project, the risks are defined in four classes:

- External
- Technical and Science
- Sub-Contractor and Industry
- Human and Organization

Risks can be identified from a number of different sources. Some may be quite obvious and are identified prior to project kick-off. Others are identified during the project life cycle, and can be identified by anyone associated with the project.

For each risk scenario, the risk assessment process should determine:

- The impact on the schedule, resources and performances
- The likelihood
- The risk index

- The risk magnitude (number of risk) per index

For each identified risk, a response is identified. The possible response options are:

Avoidance: Change the project to avoid the risk.

Transference: Shift the impact of a risk to a third party

Mitigation: Take steps to reduce the probability and/or impact of a risk.

Acceptance: Accept the impacts of the risk.

For each risk that will be mitigated, ways to prevent the risk from occurring or reduce its impact or probability of occurring are identified and defined in a mitigation plan. This may include prototyping, adding tasks to the project schedule, adding resources, etc. Note that even if a risk is acceptable, a reducing solution must be studied.

The level of risk on the Auger Upgrade project is tracked, monitored and reported throughout the project life cycle. A list of the major risks is maintained and is reported as a component of the project status reporting process. All major project change requests are analyzed for their possible impact on the project risks.

The results of the risk analysis for different upgrade components can be found in the risks analysis report [173]. No major risks have been identified. Component procurement and manufacturing will be done typically in at least two sites reducing the risk related to manufacturing. The design requirements for Surface Scintillator Detector (SSD), Surface Detector Electronics Upgrade (SDEU), and Underground Muon Detector (UMD) include easy deployment and maintenance reducing the risk related to the field access. The most important risk is related to funding.

Chapter 11

Cost, Schedule, and Funding

11.1 Introduction

The cost estimate and schedule for the Upgrade will be based on the Upgrade work breakdown structure (WBS). Task Leaders and, in turn, subtask leaders provide the details of the WBS for their subsystems from which the cost estimates and schedule are derived.

11.2 Cost estimation

The steps in cost estimate development are:

1. The WBS, a list of all components and tasks organized by subsystem, is developed and constitutes the work to complete the project. Each component and task is a WBS element.
2. A description for each WBS element is entered in the WBS dictionary.
3. The estimated cost of the components and activities which comprise the lowest level of the WBS is prepared and a basis of estimate document (BOE) is completed for each component and activity.

The total cost, including infrastructure costs, is included in the project cost. The cost of project scientists and their support (travel etc.) is borne by their home institution and *not* included in the project cost. Data analysis and associated hardware are *not* included in the project cost.

Labor rates are established for the institutions at which significant labor will be performed. For others, generic labor rates may be used. The labor rates are fully burdened. Typically a burdened labor rate includes direct labor, fringe, overhead, vacation, sick leave, and general and administrative costs.

Often labor estimates do not include all labor associated with manufacturing a product (e.g., manufacturing support, facility maintenance, etc.) because some of this effort is included in the overhead rate for that institution. A description of what is included in overhead at a given location should be provided in the BOEs.

Material costs include the purchase of raw materials for fabrication and the procurement of components, sub-assemblies, and tooling from outside sources, or items estimated in such

a way that only a total dollar amount can be identified. This includes detector hardware, equipment, fixtures, tooling, utilities, test and assembly equipment, computer hardware and software, raw materials, and procurement processing. The BOEs should indicate the basis for arriving at the materials cost estimate.

The Auger Cost and Schedule Officer is responsible for assisting the Project Manager in tracking costs and progress in the Upgrade to the Auger Observatory. The principal tools for tracking cost are the Project Schedule and the Work Breakdown Structure (WBS). Each task will be broken up into a suitable number of intervals or subtasks and milestones to allow effective tracking.

A preliminary WBS for the completion of the AMIGA muon counters that will be used for the Underground Muon Detector of the Auger upgrade is contained in Appendix A.

11.3 Upgrade Construction Funding

Each institution makes commitments for deliverables to the Upgrade project by way of a Memorandum of Understanding. Each country and the institutions within that country make commitments for deliverables with resources available within that country. Each institution then reports on a monthly basis to the Task Leaders. The Task Leaders will in turn report progress to the Cost and Schedule Officer. The Cost and Schedule Officer prepares reports for the Project Manager, Spokesperson, Collaboration and Finance Board. The Cost and Schedule Officer flags deviation from the project plan for corrective action by the Project Manager.

Country contributions will be primarily in-kind. Each country will also contribute to a common fund for such large procurements as scintillator and PMTs.

11.4 Schedule

The Upgrade project Work Breakdown Structure is the basis for the Upgrade schedule. Each task will be broken up into a suitable number of intervals or subtasks and milestones to allow effective tracking. Each Task Leader will be responsible for tracking scheduled activities within his/her own task using the same scheduling tool. Progress reports from the Task Leaders at the WBS level 4 and higher will be transmitted to the Project Cost and Schedule Officer on a monthly basis. The Cost and Schedule Officer will, in turn, prepare progress reports for use by the Spokesperson, Project Manager, Collaboration Board and Finance Board.

A preliminary schedule is contained in Appendix A. The components of the baseline design have been tested for their suitability for the upgrade. Some specific R&D is still in progress to optimize the performance/cost ratio, in particular for the scintillator detectors and the underground muon detectors. The final validation of the SSD and SDEU designs will be undertaken in an Engineering Array of 10 detector stations at the end of 2015. The production and deployment of the SSD, the SDEU and the UMD will be done in parallel and will extend over the period 2016-18. The production schedule is mainly driven by the funding profiles in the countries of the collaboration, not by the production or deployment rates.

11.5 Operating Funds

Contributions by participating countries to Observatory operating costs are based on the Operations Cost List (OCL) as is current practice. The OCL consists of authors of scientific papers excluding students. The Upgrade scintillation detectors will require little additional maintenance effort as they are simple in design. Based on previous experience we expect an upper limit of 10 PMT failures per year which can be repaired as part of our regular surface detector maintenance. Beyond gradual (acceptable) degradation of the scintillator and fiber performance, no other failures of the Upgrade scintillator detectors are expected. Additional maintenance for the revised operation of the FD is expected to be negligible. The overall increase in operating costs as a result of the Upgrade is expected to be less than five percent.

Chapter 12

Outreach and Education

The scale and scope of the physics explored at the Pierre Auger Observatory offer significant opportunities for outreach both to the local community and to the collaborating countries. Education, outreach and public relations have been an integral part of the Auger Observatory organization from the beginning when these activities were included as a level two management task group. The goals of the Outreach and Education Task are to encourage and support a wide range of efforts that link Auger scientists and the science of particle astrophysics, particle physics and related technologies to the public and especially to schools. Outreach focused on the communities surrounding the Observatory has fostered a remarkable amount of goodwill, which has contributed significantly to the success of the project. The Auger Collaboration initiated outreach first locally as a way to become better integrated into the community during the construction phase of the Observatory. Later outreach activities spread to the participating institutions but on a larger scale and to the Internet.

The heart of local outreach activities is the Auger Visitor Center (VC), located in the central office and data acquisition building on the Observatory campus in Malargüe. A staff member dedicated to outreach gives presentations and tours to visitors that are mostly from the area but often from all over Argentina and even from other countries worldwide. Many of the visitors are in the area because of the proximity of the Las Leñas ski area and other area tourist attractions. Almost 100,000 people have attended the lectures in the Visitor Center since it opened in 2001. The impact of these visits can be seen from the continuing interest and the comments in the guest book. The VC, which seats up to 50 people, is outfitted with multimedia equipment and contains a number of displays illustrating features of the Observatory. These displays include a full size SD station, a quarter sized model of an FD mirror, a spark chamber, a Geiger counter, a number of posters that explain the science and detectors of the Observatory and a library of books in several languages. Fig. 12.1(left) shows a visiting group of middle school students and teachers outside the Auger office building after their Visitor Center tour.

The Auger upgrade provides an excellent opportunity to modernize the VC, where the emphasis can be moved from a fully organized tour to a hands-on multimedia experience. Such a new setting will allow a continuously changing exhibition in which the physics of cosmic rays and the motivation for the upgrade of the Auger detector can be explained to the public at large. A more modern VC provides motivation to the local community to re-acquaint itself with the Observatory.

Every two years a Science Fair is organized by the Observatory which overlaps with a col-

laboration meeting in Malargüe. The fair targets both elementary schools and high schools, and is still growing. The latest fair hosted 33 entries with schools from all over Mendoza Province participating. The exhibits and presentations of the participants were judged by international members of the Auger Collaboration. The interaction of the participants with the Auger scientists reinforces the connection between Auger and surrounding communities. Fig. 12.1(right) shows a recent Science Fair in the Assembly Building.



Figure 12.1: Left panel: A group of middle school students and teachers after their Visitor Center tour. A surface detector station is visible in the upper right which visitors can inspect closely. Right panel: A recent Science Fair in the Assembly Building on the Auger campus.

The collaboration realizes the importance of making data available to the general public as well as other scientists. For this purpose a special Data Release task has been established. For outreach purposes, the Collaboration makes 1% of recorded surface detector events available on its public web page (www.auger.org), and this fraction is foreseen to increase to 10% in the near future. The current public data set contains over 38,000 events and has been analyzed by students worldwide for science fairs, classroom activities, and research projects. An explanation of how to handle this wealth of data, aimed at the high school level and beyond, is provided at the same web location. The online event display, coupled to the public data set, is a useful tool to provide insight to students on what is measured and how it is interpreted. Furthermore, an online analysis interface called VISPA [174] has been developed, which allows students to work with and analyze these data. The explanation, event display, and VISPA form a complete set of tools that allow students to work as scientists on the largest cosmic ray data set to become available to the general public.

Outreach has been an important part of the activities of the Auger Observatory that will continue through its lifetime. Our close relationship with the people of Malargüe and the other local communities as a result of our outreach activities has not only made our work comfortable and rewarding but has, indeed, contributed to the success of the Observatory. Among the collaborating institutions many innovative outreach ideas have sprung from our research, leading to, for example, institute open houses, public exhibitions to large audiences, and teacher workshops featuring the Observatory, its science and accomplishments. Because we can easily show their continuous presence around us, cosmic rays provide an effective vehicle to excite young people about the wonders and science of the cosmos.

Chapter 13

Acknowledgements

The successful installation, commissioning, and operation of the Pierre Auger Observatory would not have been possible without the strong commitment and effort from the technical and administrative staff in Malargüe. We are very grateful to the following agencies and organizations for financial support:

Comisión Nacional de Energía Atómica, Fundación Antorchas, Gobierno de la Provincia de Mendoza, Municipalidad de Malargüe, NDM Holdings and Valle Las Leñas, in gratitude for their continuing cooperation over land access, Argentina; the Australian Research Council; Conselho Nacional de Desenvolvimento Científico e Tecnológico (CNPq), Financiadora de Estudos e Projetos (FINEP), Fundação de Amparo à Pesquisa do Estado de Rio de Janeiro (FAPERJ), São Paulo Research Foundation (FAPESP) Grants No. 2010/07359-6 and No. 1999/05404-3, Ministério de Ciência e Tecnologia (MCT), Brazil; Grant No. MSMT-CR LG13007, No. 7AMB14AR005, and the Czech Science Foundation Grant No. 14-17501S, Czech Republic; Centre de Calcul IN2P3/CNRS, Centre National de la Recherche Scientifique (CNRS), Conseil Régional Ile-de-France, Département Physique Nucléaire et Corpusculaire (PNC-IN2P3/CNRS), Département Sciences de l'Univers (SDU-INSU/CNRS), Institut Lagrange de Paris (ILP) Grant No. LABEX ANR-10-LABX-63, within the Investissements d'Avenir Programme Grant No. ANR-11-IDEX-0004-02, France; Bundesministerium für Bildung und Forschung (BMBF), Deutsche Forschungsgemeinschaft (DFG), Finanzministerium Baden-Württemberg, Helmholtz Alliance for Astroparticle Physics (HAP), Helmholtz Gemeinschaft Deutscher Forschungszentren (HGF), Ministerium für Wissenschaft und Forschung, Nordrhein-Westfalen, Ministerium für Wissenschaft, Forschung und Kunst, Baden-Württemberg, Germany; Istituto Nazionale di Fisica Nucleare (INFN), Istituto Nazionale di Astrofisica (INAF), Ministero dell'Istruzione, dell'Università e della Ricerca (MIUR), Gran Sasso Center for Astroparticle Physics (CFA), CETEMPS Center of Excellence, Ministero degli Affari Esteri (MAE), Italy; Consejo Nacional de Ciencia y Tecnología (CONACYT), Mexico; Ministerie van Onderwijs, Cultuur en Wetenschap, Nederlandse Organisatie voor Wetenschappelijk Onderzoek (NWO), Stichting voor Fundamenteel Onderzoek der Materie (FOM), Netherlands; National Centre for Research and Development, Grants No. ERA-NET-ASPERA/01/11 and No. ERA-NET-ASPERA/02/11, National Science Centre, Grants No. 2013/08/M/ST9/00322, No. 2013/08/M/ST9/00728 and No. HARMONIA 5 - 2013/10/M/ST9/00062, Poland; Portuguese national funds and FEDER funds within Programa Operacional Factores de Competitividade through Fundação para a Ciência e a

Tecnologia (COMPETE), Portugal; Romanian Authority for Scientific Research ANCS, CNDI-UEFISCDI partnership projects Grants No. 20/2012 and No. 194/2012, Grants No. 1/ASPERA2/2012 ERA-NET, No. PN-II-RU-PD-2011-3-0145-17 and No. PN-II-RU-PD-2011-3-0062, the Minister of National Education, Programme Space Technology and Advanced Research (STAR), Grant No. 83/2013, Romania; Slovenian Research Agency, Slovenia; Comunidad de Madrid, FEDER funds, Ministerio de Educación y Ciencia, Xunta de Galicia, European Community 7th Framework Program, Grant No. FP7-PEOPLE-2012-IEF-328826, Spain; Science and Technology Facilities Council, United Kingdom; Department of Energy, Contracts No. DE-AC02-07CH11359, No. DE-FR02-04ER41300, No. DE-FG02-99ER41107 and No. DE-SC0011689, National Science Foundation, Grant No. 0450696, The Grainger Foundation, USA; NAFOSTED, Vietnam; Marie Curie-IRSES/EPLANET, European Particle Physics Latin American Network, European Union 7th Framework Program, Grant No. PIRSES-2009-GA-246806; and UNESCO.

Appendix A

Work Breakdown Structure (WBS) and Schedule

A.1 WBS

A summary of a preliminary WBS for the Auger upgrade including SDEU and SSD is shown in Fig. A.1.

Pierre Auger Observatory Upgrade - Cost Estimate - Preliminary Design Report							09 April 2015	5.4	
WBS	Activity	Total Cost ² with Contingency and Infrastructure cost (IFL)		Contingency Part	Infrastructure cost Part (IFL)	Total Cost ³ with Contingency only (No Infrastructure cost, IFL)		Infrastructure cost* only (IFL)	
		US \$	€			US \$	€	US \$	€
0	Pierre Auger Observatory Upgrade	15,175,050	14,416,298	13.9%	16.3%	12,694,152	12,059,445	2,480,898	2,356,853
1	Scintillator Surface Detector	14,811,450	14,070,878	13.9%	16.7%	12,330,552	11,714,025	2,480,898	2,356,853
1.1	Scintillator Surface Detector	10,300,788	9,785,749	14.2%	18.9%	8,356,898	7,939,053	1,943,890	1,846,696
1.1.1	Detector development	6,720,478.50	6,384,454.58	14.8%	1.2%				
1.1.2	Detector assembly and deployment	2,252,075.00	2,042,325.00	14.8%	3.2%				
1.1.3	Assembly, deployment and tests	2,252,075.00	2,139,471.25	14.8%	80.9%				
1.2	Surface Detector Electronics	4,510,662	4,285,129	13.1%	11.9%	3,973,654	3,774,971	537,008	510,158
1.2.1	Upgraded Uniform Board Production	3,065,750.28	2,913,547.27	12.2%	12.6%				
1.2.2	Small PMT	1,144,671.50	1,087,457.93	13.3%	3.6%				
1.2.3	Test Benches Production	22,710.00	21,574.50	20.0%	30.1%				
1.2.4	Assembly and deployment	277,020.25	263,169.24	22.0%	36.6%				
2	Preparation to Upgrade	363,600	345,420	16.7%	0.0%	363,600	345,420	0	0
2.1	Surface Detector Preparation	363,600	345,420	16.7%	0.0%	363,600	345,420	0	0
2.1.1	Photodetectors	363,600.00	345,420.00	16.7%	0.0%				

Notes:
1 - Exchange rate Euro/US Dollar = 0.95
2 - Total cost with contingency, spares, wastages, labor and infrastructure charges
3 - Total cost with contingency, spares, wastages.
4 - Infrastructures charges including labor

Figure A.1: Summary of the SDEU and SSD WBS.

The total cost with contingency, including infrastructure costs, is estimated to be US \$15.2 M, and the total cost with contingency, but without infrastructure costs (the so-called European accounting), is estimated to be US\$12.7 M. The overall increase in operating costs as a result of the upgrade is expected to be less than five percent. A more detailed WBS is available in ref. [175].

The costs of implementation of the extended FD duty-cycle (Chap. 6) do not appear in the WBS because no extra equipment is needed to extend operations into times of increased night sky background. Maintenance of the existing FD systems is covered by continuing memoranda of understanding with collaborating institutions. However, provision is made for purchasing 300 water-Cherenkov detector (WCD) photomultipliers as spares for future operation (Item 2.1.1 in Figure A.1). The WCD PMTs were originally purchased with the collaboration's Common Fund, and hence no single institution has explicit responsibility for

their maintenance.

A summary of a preliminary WBS for the completion of the AMIGA muon counters that will be used for the Underground Muon Detector of the Auger upgrade is shown in Fig. A.2.

Pierre Auger Observatory Upgrade - Cost Estimate - AMIGA										07 April 2015	2.0		
WBS	Activity	Total Cost ² with Contingency and Infrastructure cost (IFL)			Contingency Part		Infrastructure cost Part (IFL)		Total Cost ² with Contingency only (No Infrastructure cost, IFL)			Infrastructure cost ⁴ only (IFL)	
		Currency ¹ >	US \$	€	%	%	US \$	€	US \$	€	US \$	€	
3.1	AMIGA Completion	1 794 130	1 704 424		10.5%	8.7%	1 637 801	1 555 911	156 329	148 512			
3.1.1	Module	644 126	611 920		13.1%	16.9%	535 153	508 396	108 973	103 524			
3.1.2	Optics	459 292	436 328		8.9%	2.6%	447 317	424 952	11 975	11 376			
3.1.3	Electronics	491 848	467 256		3.6%	7.2%	456 468	433 644	35 381	33 612			
3.1.4	Photovoltaic System	74 988	71 239		22.7%	0.0%	74 988	71 239	0	0			
3.1.5	Deployment	123 875	117 681		23.1%	0.0%	123 875	117 681	0	0			

Notes:

- 1 - Exchange rate Euro/US Dollar = 0.95
- 2 - Total cost with contingency, spares, wastages, labor and infrastructure charges
- 3 - Total cost with contingency, spares, wastages
- 4 - Infrastructure charges including labor

INFO:	Modules to complete Infill	162
	Modules without scintillator/fiber purchased	81
	Solar Panels not purchased	0
	Batteries not purchased	71

Figure A.2: Summary of the AMIGA WBS.

The current cost estimate for the completion of the AMIGA counters, without the infrastructure cost, is US\$1.6 M. A more detailed WBS is available in ref. [175].

A.2 Schedule

The schedule for the Surface Detector Electronics upgrade is shown in Fig. A.3. The final

Work Packages	2014				2015				2016				2017			
	T1	T2	T3	T4	T1	T2	T3	T4	T1	T2	T3	T4	T1	T2	T3	T4
WP1 : PMTs signal conditioning	Design															
WP2 : Trigger	Design															
WP3 : Time Tagging	Design															
WP4 : Slow Control	Design															
WP5 : UUB hardware Design & Integration	Design	Prototypes & Eng. Array			Valid.		Pre Production		Valid.	Production						
WP6 : UUB software																
WP7 : Calibration & Control tools	Design															
WP8 : Deployment		winter				Eng. Array	winter			winter						
WP9 : Simulation and Science Validation																
Milestones Reviews->		Sub System Design Review														
		System Critical Design Review														
		Software Design Review														
		Pre-Production Readiness Review														
		Pre-Production Deployment Readiness Review														
		Production Readiness Review														
		Production Deployment Readiness Review														
		End of Deployment Review														

Figure A.3: SDEU schedule.

validation of the SDEU design will be done in an Engineering Array of 10 detector stations at the end of 2015. The production and deployment of the SDEU can be done in 2016-17. However, the production schedule is mainly driven by the funding profiles in different countries which typically extend over 3 years, and will therefore be extended up to 2018.

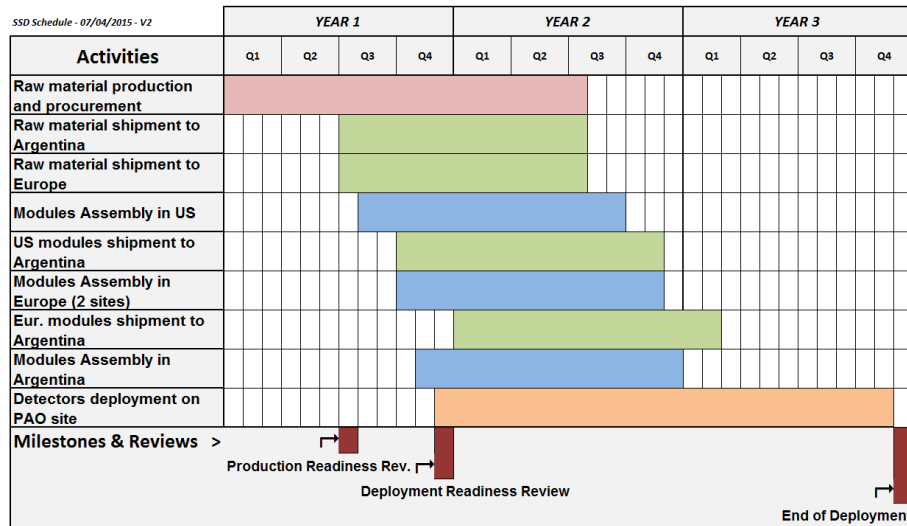


Figure A.4: SSD schedule.

The schedule for the Scintillator Surface Detector is shown in Fig. A.4. Similarly to the SDEU, the final validation of the SSD design will be done in an Engineering Array of 10 detector stations at the end of 2015. The production and deployment of the SSD will be done in 2016-18. Like the SDEU, the production and deployment schedule is mainly driven by the funding profiles.

Appendix B

The Current Pierre Auger Observatory

B.1 Introduction

The Pierre Auger Project was proposed in 1998 “to discover and understand the source or sources of cosmic rays with energies exceeding 10^{19} eV.” A unique partnership of 17 countries came together to pursue this science. To achieve its goals, the collaboration designed an experiment to achieve high-quality data in a high-statistics study of the most extreme cosmic rays. The Pierre Auger Observatory in the Province of Mendoza, Argentina, has been taking data since 2004, adding detectors as they became active until completion in 2008. Measured properties of air showers are used to determine the cosmic ray energy, direction and composition.

A powerful feature of the Auger design is the capability of observing air showers simultaneously by two different but complementary techniques. On dark moonless nights, air fluorescence telescopes record the development of what is essentially the electromagnetic shower that results from the interaction of the primary particle with the upper atmosphere. The surface array measures particle signals as the shower strikes the earth just beyond its maximum development. By recording the light produced by the developing air shower, fluorescence telescopes can make a nearly calorimetric measurement of the energy. This energy calibration can then be transferred to the surface array with its 100% duty factor and large event-gathering power. The energy conversion and subsequent determination of the spectrum can be done with minimal reliance on numerical simulations or on assumptions about the composition or interaction models.

The Observatory design features an array of 1660 water-Cherenkov surface detectors spread over 3000 km^2 and arranged on a triangular grid, with the sides of the triangles being 1.5 km (see Figure B.1). Four fluorescence detector stations, each containing six fixed telescopes designed to detect air-fluorescence light, overlook the surface array. (An additional three telescopes view higher elevations for lower energy air showers.) The surface detector stations measure the density distribution of the air shower cascade as it strikes the surface while the fluorescence telescopes measure the light produced by atmospheric nitrogen excited by the cascading shower. This dual approach is called the *hybrid technique*.

A water-Cherenkov particle detector was chosen for use in the surface array because of robustness, low cost, and sensitivity to showers at high zenith angles. A surface detector station (SD) consists of a 12,000 liter polyethylene water tank containing a sealed laminated polyethylene liner with a reflective inner surface. Cherenkov light from the passage

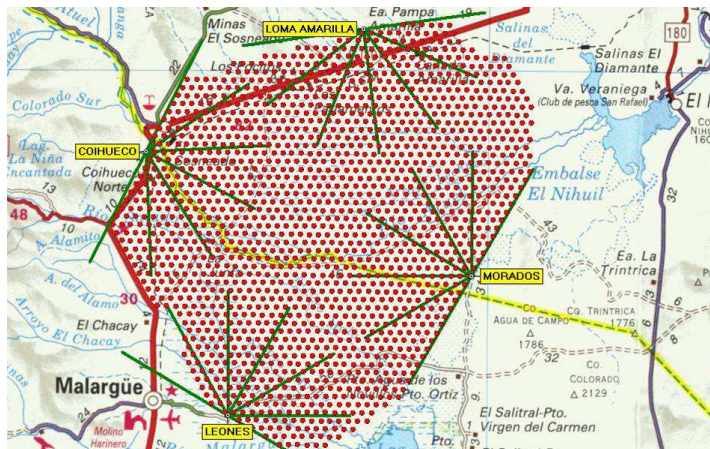


Figure B.1: The Auger Observatory layout. Each dot corresponds to one of the 1660 surface detector stations. The four fluorescence detector enclosures are shown, each with the field of view of its six telescopes.

of charged particles is collected by three 230 mm photomultiplier tubes (PMTs) that look through windows of clear polyethylene into highly purified water. The surface detector station is self contained. A solar power system provides power for the PMTs and electronics package. The electronics package, consisting of a processor, GPS receiver, radio transceiver and power controller, is mounted on the tank.

The Auger fluorescence detector (FD) operates in conjunction with the surface detector (SD). Its primary purpose is to measure the longitudinal profile of showers recorded by the SD whenever it is dark and clear enough to make reliable measurements of atmospheric fluorescence from air showers. The integral of the longitudinal profile is used to determine the shower energy, and the speed of the shower development is indicative of the primary particle's mass. The hybrid detector has better angular resolution than the surface array alone.

The Auger Project was conceived during the International Cosmic Ray Conference in Dublin in 1991 by J.W. Cronin of the University of Chicago and A.A. Watson of the University of Leeds. It had become clear to them that only the construction of a very large air shower array in both the northern and southern hemispheres would yield the statistical power and complete sky coverage necessary to address the question of the origin of the highest energy cosmic rays.

A six month long design workshop was held in early 1995 that produced a design report with a discussion of the science, a conceptual design and cost estimate. The design report became the basis for funding proposals by the Auger collaborators to their funding agencies.

Subsequent to the workshop, a team of scientists evaluated numerous prospective sites in both hemispheres. Site considerations included altitude, latitude, topography, and sky clarity. In 1995 and 1996 preferred sites were selected by the collaboration in the Southern and Northern hemispheres respectively. At the direction of the funding agencies, the project began by building the Auger Observatory in the southern hemisphere.

The site is in the Province of Mendoza near the city of Malargüe (pop. 18,000) and 180 km south-west of the city of San Rafael (pop. 100,000). The site is located at about latitude 35° south with a mean altitude of 1400 m a.s.l. The site is a relatively flat alluvial plain,



Figure B.2: *Left:* an aerial view of the Auger campus in Malargüe. *Right:* the office building and visitor center.

sufficiently large to easily encompass the required 3000 km^2 footprint of the array. There are convenient elevated positions on the edge of the array that allow placement of the four fluorescence telescope enclosures slightly above ground level. A campus area in Malargüe includes an office building with a visitor center, a detector assembly area, and a staging area for detectors (See Figure B.2).

After a period of research and development, the Engineering Array, consisting of 32 prototype surface array detectors and two prototype fluorescence telescopes, was built to validate the design [176]. At the end of 2001, before the end of the scheduled two years, the Engineering Array was able to record and reconstruct air shower events simultaneously with both the surface array and the fluorescence detectors. The Engineering Array was able to demonstrate the validity of the design and the performance of all of the detectors, communications equipment and data systems as well as the deployment methodology. Indeed, we found that the detectors performed even better than expected, substantially increasing our physics reach.

Installation of production detectors was started in 2002. While the Engineering Array was assembled and deployed almost completely by Auger collaborators, production deployment was transferred to trained Observatory staff. The scientists oversaw the quality of the work and carried out the commissioning of the completed detectors. The Observatory started collecting data in January 2004. The first physics results were presented during the 2005 conference season.

Many important results have now been published by the Auger Collaboration that have had a major impact on the field of cosmic ray physics. As of this writing, 55 full author list papers have been published or accepted, with another 2 submitted and about 15 more in preparation. The Auger Collaboration is also training a cadre of future scientists, with 218



Figure B.3: A fluorescence telescope enclosure, seen on the hill top, and a surface detector station, below.

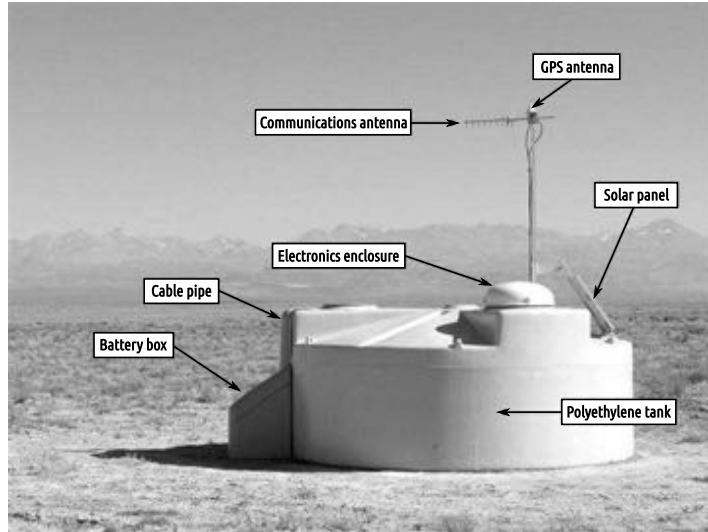


Figure B.4: A pictorial view of a surface detector station in the field, showing its main components.

students granted PhDs based on their work on Auger. Another 157 PhD students are in the pipeline.

B.2 The Surface Detector

B.2.1 Detector hardware

Each surface detector station of the Observatory consists of a 3.6 m diameter water tank containing a sealed liner with a reflective inner surface. The liner contains 12,000 l of ultra-high purity water. Three 230 mm diameter photomultiplier tubes are symmetrically distributed at a distance of 1.20 m from the center of the tank and look downwards through windows of clear polyethylene into the water to collect the Cherenkov light produced by the passage of relativistic charged particles through the water. The water height of 1.2 m makes it also sensitive to high energy photons, which convert to electron-positron pairs in the water volume.

The surface detector station is self-contained. A solar power system provides an average of 10 W for the PMTs and the electronics package consisting of a processor, GPS receiver, radio transceiver and power controller. The components of the surface detector station are shown in Fig. B.4. The hardware of the surface detector is described extensively in [176, 177].

The tanks are made of high-density polyethylene by the rotomolding process. The exterior is colored beige to minimize the visual impact. The resins are compounded with additives to enhance ultraviolet protection. The interior has added carbon-black to guarantee light-tightness. The tanks have a nominal wall thickness of 1.3 cm and a weight of 530 kg.

Three hatches, located above the PMTs, provide access to the interior of the tank for assembly, water filling and eventual servicing of the interior parts. The hatches are covered with light- and water-tight polyethylene hatch covers. Hatch cover 1 is larger and accommodates the electronics on its top. The electronics is protected by an aluminum dome. The tanks also possess lugs for lifting and four additional lugs to support the solar panel and antenna mast assembly.

Electrical power for the electronics is provided by two 55 Wp solar panels which feed

two 12 V, 105 Ah lead-acid low maintenance batteries. Batteries are charged through a commercial charge controller. The electronics assembly possesses a Tank Power Control Board (TPCB) which also monitors the charging and discharging of batteries and sets the system to hibernation mode if the charge of the batteries falls below a critical level. The batteries are accommodated in a thermally insulated battery box which is installed next to the tank at the shaded southern side.

The solar panels are mounted on aluminum brackets, which also support a mast of a height of 2.15 m. The communications and GPS antennas are mounted at the top of this mast.

The tank liners are right circular cylinders made of a flexible plastic material conforming approximately to the inside surface of the tanks. They enclose the water volume, provide a light-tight environment and diffusively reflect the Cherenkov light produced in the water volume. The liners are produced from a laminate composed of an opaque three-layer co-extruded low-density polyethylene (LDPE) film bonded to a layer of DuPont Tyvek® 1025-BL by a layer of Titanium-dioxide pigmented LDPE. The three-layer co-extruded film consists of a carbon black loaded LDPE formulated to be opaque to single photons, sandwiched between layers of clear LDPE to prevent any carbon black from migrating into the water volume.

The liner has 3 windows through which the PMTs look into the water volume from above. These windows are made of UV-transparent linear low-density polyethylene. The PMTs are optically coupled to the windows with optical silicone and protected with a light-tight plastic cover.

Once deployed in their correct position in the field, the tanks are filled with high purity water produced at a water plant owned by the Auger Project. Water quality exceeds $10 \text{ M}\Omega \text{ cm}$ at the output of the water plant and is transported in clean ad-hoc transport tanks. The water is expected to maintain its quality without degradation for the lifetime of the Observatory.

B.2.2 The existing surface detector electronics

The Auger Upgrade includes a major overhaul of the electronics of the surface detectors, as described in the body of this Report. Here we outline the existing SD electronics.

To collect the Cherenkov light produced in the water volume of the detectors by the air showers, three PMTs look at the water volume from the top. The PMTs (Photonis XP1805/D1) have a 230 mm diameter photocathode and eight dynodes, with the chemical composition of the dynode surfaces optimized by the manufacturer to maximize linearity. Due to their proximity to water they are operated with a positive anode voltage, the photocathode being grounded. The high voltage is provided locally from a module integrated in the PMT base, and is proportional to a DC control voltage provided by the slow control system. The PMTs are operated at a nominal gain of 2×10^5 , and are specified for operation at gains up to 10^6 . The PMTs are required to be linear within 5% up to 50 mA anode current. The base, including the high voltage supply, is attached to the tube by soldering to flying leads and is potted in GE silicone RTV-6136 to protect it from the high humidity present in the tank.

Each PMT has two outputs. An AC coupled anode signal is provided. In addition, the signal at the last dynode is amplified and inverted by the PMT base electronics to provide a signal with 32 times the charge gain of the anode. No shaping of the signal is performed on the PMT base.

Six identical channels of electronics are provided to digitize the anode and amplified dynode signals from each of the PMTs. Each channel consists of a 5-pole Bessel filter with a -3 dB cutoff at 20 MHz and a voltage gain of -0.5 . This filter is implemented using a pair of Analog Devices AD8012 current feedback op-amps. The filtered analog signals are fed to Analog Devices AD9203 10 bit 40 MHz semi-flash ADCs. The ADC negative inputs are biased to -50 mV to bring the input pedestal on scale and allow for amplifier section offsets. The choice of filter cutoff results in 5% aliasing noise while preserving the time structure of the signals. The use of two 10 bit ADCs with a gain difference of 32 extends the dynamic range of the system to 15 bits with a 3% precision at the end of the overlap region.

An LED flasher is mounted in a test port of the water tank liner. The LED flasher incorporates two LEDs which can be pulsed independently or simultaneously and with variable amplitude. This allows testing of the linearity of the photomultipliers to be conducted remotely.

Each SD station contains a GPS receiver with its corresponding antenna mounted at the top of the communications mast for event timing and communications synchronization. The receiver is a Motorola (OEM) Oncore UT+. This receiver outputs a timed one-pulse-per-second (1 PPS). The GPS 1 PPS signal is offset from the true GPS second by up to 50 ns , and a correction for this offset is provided periodically by the receiver. Event timing is determined using a custom ASIC which references the timing of shower triggers to the GPS 1 PPS clock. The ASIC implements a 27 bit clock operating at 100 MHz . This clock is latched on the GPS 1 PPS signal at the time of each shower trigger. A counter operating at the 40 MHz ADC clock is also latched on the GPS 1 PPS clock. These data, together with the timing corrections provided by the GPS receiver, are used to calibrate the frequencies of the 40 MHz and 100 MHz clocks and to synchronize the ADC data to GPS time within 10 ns RMS .

The digital data from the ADCs are clocked into a programmable logic device (PLD). In the first half of the deployment, we employed two ALTERA ACEX PLDs (model EP1-K100QI208-2) with $16k \times 36$ bits additional external static RAM. In later stations, an Altera Cyclone FPGA replaced the two ACEX devices and external memory. The PLD implements firmware that monitors the ADC outputs for interesting trigger patterns, stores the data in a buffer memory, and informs the station micro-controller when a trigger occurs. There are two local trigger levels (T1 and T2) and a global third level trigger, T3. Details of the local triggers are described in section B.2.4.

The front end is interfaced to a unified board which implements the station controller, event timing, and slow control functions, together with a serial interface to the communications system. The slow control system consists of DACs and ADCs used to measure temperatures, voltages, and currents relevant to assessment of the operation of the station.

The station controller consists of an IBM PowerPC 403 GCX-80 MHz, with a 32 MB DRAM bank to store data and executable code, and a 2 MB Flash EPROM for the bootstrap and storing of the OS9 operating system. The data acquisition system implemented on the station controller transmits the time stamps of the ~ 20 T2 events collected each second to CDAS (Central Data Acquisition System; see section B.4.2). CDAS returns T3 requests to the station within ~ 8 seconds of the event (including communications delays due to re-transmission). The station controller then selects the T1 and T2 data corresponding to the T3 requests and builds it into an event for transmission to CDAS. Calibration data are included in each transmitted event.

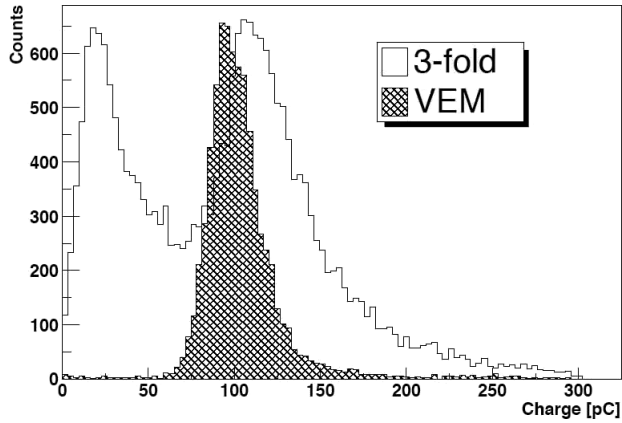


Figure B.5: Muon peak.

B.2.3 Surface Detector Calibration

The detector calibration is inferred from background muons. The typical rise time for a muon signal is about 15 ns with a decay time of the order of 60 to 70 ns. The average number of photoelectrons per muon collected by one PMT is 95. By adjusting the trigger rates, the gains of the three PMTs are matched within 6%. The measurement of the muon charge spectrum allows us to deduce the charge value for the signal produced by a single, central, vertical muon, Q_{VEM} , from which the calibration is inferred for the whole dynamic range. The cross calibration between the anode and dynode output channels is performed by using small shower signals in the overlap region [178].

The decay constant of the muon signal is related to the absorption length of the light produced. This depends of various parameters such as the Tyvek® reflectivity and the purity of the water. The signal decay constant correlates with the so called area-to-peak (A/P) ratio of the signal:

$$\text{A/P} = \frac{Q_{\text{VEM}}}{I_{\text{VEM}}} \quad (\text{B.1})$$

where I_{VEM} is the maximum current of the muon signal. This area-to-peak ratio is a routine monitoring quantity that is directly available from the local station software.

B.2.4 The SD local triggers

The front-end electronics implements three types of trigger functions. Shower triggers result in the recording of 768 samples (19.2 μs) of the six ADCs. Muon triggers result in the recording of 24 samples of the three high gain dynode channels for use in calibration. Double buffered scalers are also implemented for use in monitoring rates and for auxiliary physics purposes.

A shower trigger is generated when one of several conditions is satisfied. A single bin threshold trigger is generated when at least a specified number of the high gain signals (amplified dynode) are each above a threshold level. The standard trigger condition is 2 I_{VEM} on at least two of the high gain signals. The rate of this trigger is about 100 Hz, and is sensitive to showers near the core but subject to contamination due to small showers. A software selection of this trigger with a higher threshold at 3.2 I_{VEM} is also performed. In addition, a time-over-threshold (ToT) trigger is implemented. This trigger requires that single bin



Figure B.6: FD building at Los Leones during the day. Behind the building is a communication tower. This photo was taken during daytime when shutters were opened because of maintenance.

threshold trigger be satisfied for at least a minimum number of samples within a sliding time window. A ToT trigger is generated when at least 12 samples within a $3\text{ }\mu\text{s}$ window (120 samples) exceed a threshold of $0.2 I_{\text{VEM}}$ on at least two out of the three tubes. The ToT trigger is efficient for shower signals far from the core. The rate of the ToT trigger is a few Hz, and depends on the shape of the muon pulse in the tank. The shower triggers implemented in the PLD are collectively referred to as T1. The station controller (see below) transmits timestamps for the ToT and $3.2 I_{\text{VEM}}$ threshold triggers (collectively referred to as T2) to the CDAS for global (T3) trigger determination.

Two additional sophisticated triggers were introduced in 2013 to somewhat lower the energy threshold of the array, and improve sensitivity to photon and neutrino initiated showers. See [177] for details.

B.3 The Fluorescence Detector

The 24 telescopes of the FD overlook the SD array from four sites – Los Leones, Los Morados, Loma Amarilla and Coihueco [179]. Six independent telescopes are located at each FD site in a clean climate-controlled building [176], an example of which is seen in figure B.6. A single telescope has a field of view of $30^\circ \times 30^\circ$ in azimuth and elevation, with a minimum elevation of 1.5° above the horizon. The telescopes face towards the interior of the array so that the combination of the six telescopes provides 180° coverage in azimuth.

B.3.1 FD telescopes

The details of the fluorescence detector telescope are shown in figure B.7. The telescope design is based on Schmidt optics because it reduces the coma aberration of large optical systems. Nitrogen fluorescence light, emitted isotropically by an air shower, enters through a circular diaphragm of 1.1 m radius covered with a Schott MUG-6 filter glass window. The filter transmission is above 50% between 310 and 390 nm in the UV range. The filter reduces the background light flux and thus improves the signal-to-noise ratio of the measured air shower signal. It also serves as a window over the aperture and thus keeps the space containing the telescopes and electronics clean and climate controlled. The shutters seen in

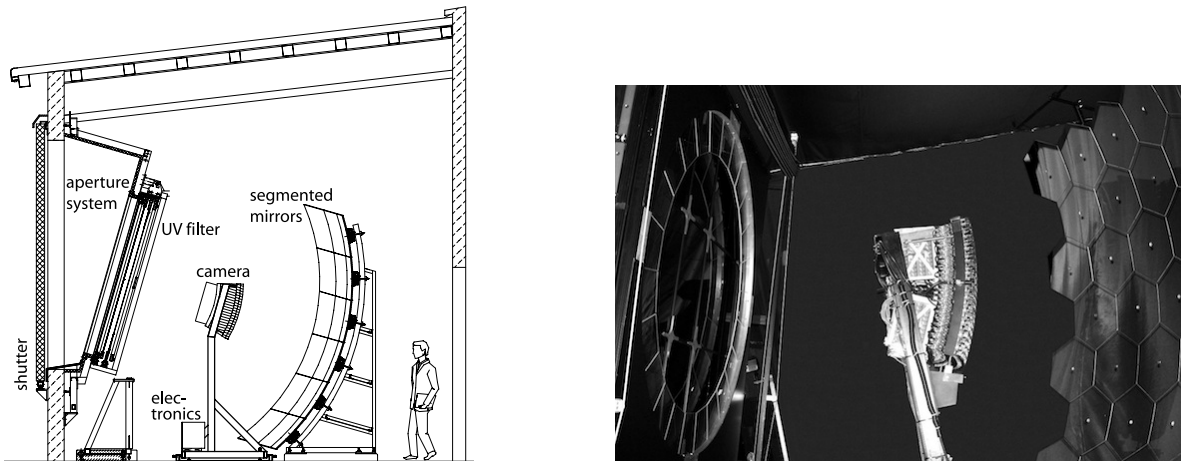


Figure B.7: *Left:* Schematic view of a fluorescence telescope with a description of its main components. *Right:* Photograph of a fluorescence telescope at Coihueco.

figure B.7 are closed during daylight and also close automatically at night when the wind becomes too high or rain is detected. In addition, a fail safe curtain is mounted behind the diaphragm to prevent daylight from illuminating a camera in case of a malfunction of the shutter or a failure of the Slow Control System.

A simplified annular lens, which corrects spherical aberration and eliminates coma aberration, is mounted in the outer part of the aperture. The segmented corrector ring has inner and outer radii of 850 and 1100 mm, respectively. Six corrector rings were made from Schott BK7 glass and Borofloat was used for the rest. More details about the corrector ring can be found in [176, 180].

The light is focused by a spherical mirror of ~ 3400 mm radius of curvature onto a spherical focal surface with radius of curvature ~ 1700 mm. Due to its large area ($\sim 13 \text{ m}^2$), the primary mirror is segmented to reduce the cost and weight of the optical system. Two alternative segmentation configurations are used: one is a tessellation of 36 rectangular anodized aluminum mirrors of three different sizes; the other is a structure of 60 hexagonal glass mirrors (of four shapes and sizes) with vacuum deposited reflective coatings [176]. The average reflectivity of cleaned mirror segments at a wavelength $\lambda = 370$ nm is more than 90%. Measurements have shown that dust layer deposits could reduce the mirror reflectivity by about 5% in the bottom part of the spherical mirror, where the segments are turned slightly upward (see, e.g., figure B.7). Therefore, careful mirror cleaning is performed as needed.

The camera body is machined from a single aluminum block of 60 mm thickness, with an outer radius of curvature of 1701 mm and an inner curvature radius of 1641 mm. The hexagonal photomultiplier tubes, model XP3062 manufactured by Photonis, are positioned inside 40 mm diameter holes drilled through the camera block at the locations of the pixel centers. The pixels are arranged in a matrix of 22 rows by 20 columns.

The PMT boundaries are approximate hexagons with a side to side distance of 45.6 mm. The PMTs are separated by simplified Winston cones secured to the camera body which collect the light to the active cathode of the photomultiplier tube. The light collectors serve to prevent photons from landing in the dead spaces between the PMT cathodes. The upper edge of the light collectors lie on the focal surface of 1743 mm radius. The pixel field of view defined by the upper edges corresponds to an angular size of 1.5° .

All support structures and cables are distributed so as to minimize any obscuration in the light path. The contribution of reflection and scattering inside the optical system of the telescope has been measured *in situ* and with an airborne remotely controlled platform carrying an isotropic and stabilized UV light source [181]. The measured point spread function of the light distribution in pixels has been implemented in the software used in the air shower reconstruction.

Cleaning and maintenance work has been required during years of detector operation. The cleaning of the UV filter from outside has been performed several times because of deposited dust layers. Less frequently, the inner side of the filter and the corrector ring were washed. Dry and wet methods of mirror cleaning have been adopted over the years and they both improve the reflectivity of mirrors by $\leq 1\%$ (in the case of mirror segments in the upper rows) up to about 5% for mirror segments in the bottom rows.

Alignment of individual mirror segments was cross-checked with a laser on site. Moreover, additional methods using data measured by telescopes were used, such as star tracking, Central Laser Facility (CLF) and eXtreme Laser Facility (XLF) shots (section B.3.4), or a comparison of FD and SD geometry reconstruction. Only in two cases were a realignment of a telescope and a readjustment of camera position needed.

B.3.2 FD Electronics

The FD electronics must provide a large dynamic range and strong background rejection, while accepting any physically plausible air shower. Moreover, the electronics is responsible for anti-alias filtering, digitizing, and storing signals from the PMTs.

The XP3062 photomultiplier tube is an 8-stage unit with a bi-alkaline photocathode with quantum efficiency of about 25% in the wavelength range 350 to 400 nm. The PMT high voltage is provided by a HV divider chain which forms a single physical unit together with the signal driver circuitry. This head electronics unit is soldered to the flying leads of the PMT [153].

The nominal gain for standard operation of the FD is set to 5×10^4 . Stabilization of the HV potential for large pulses, and in the presence of the low but not negligible light intensity of the dark sky background, is realized by employing an active network that uses bipolar transistors in the last three stages of the PMT. The active divider ensures that the gain shift due to the divider chain is less than 1% for anode currents up to about 10 mA. The normal dark sky background on moonless nights induces an anode current of about 0.8 μ A on each PMT.

The head electronics for each PMT is connected to a distribution board located just behind the camera body. Each board serves 44 PMTs, providing high and low voltage and receiving the output signals. The signal is then shaped and digitized in the front-end electronics (FE) unit, where threshold and geometry triggers are also generated. Analog boards in the FE unit are designed to handle the large dynamic range required for air fluorescence measurements; this means a range of 15 bits and 100 ns timing.

As the PMT data are processed, they are passed through a flexible three-stage trigger system implemented in firmware and software. The trigger rate of each pixel in a camera (first level trigger) is kept around 100 Hz by adjusting the pixel threshold level. The algorithm of the second level trigger searches for track segments at least five pixels in length within a camera. The typical trigger rate per camera fluctuates between 0.1 and 10 Hz. The third level trigger is a software algorithm designed to clean the air shower data stream of noise

events that survive the low-level hardware triggers. It is optimized for the fast rejection of triggers caused by lightning, triggers caused by cosmic ray muon impacts on the camera and randomly triggered pixels.

The events surviving all trigger levels are sent to the computer, which builds an event from the coincident data in all telescopes and generates a hybrid trigger (T3) for the surface array. The event rate is about 0.012 Hz per building for the 24 baseline telescopes.

B.3.3 FD Calibration

The reconstruction of air shower profiles and the ability to determine the total energy of a reconstructed shower depend on the conversion of ADC counts to light flux at the telescope aperture for each channel that receives a portion of the signal from a shower. To obtain this important relation, it is necessary to evaluate the response of each pixel to a given flux of incident photons from the solid angle covered by that pixel, including the effects of aperture projection, optical filter transmittance, reflection at optical surfaces, mirror reflectivity, pixel light collection efficiency and area, cathode quantum efficiency, PMT gain, pre-amp and amplifier gains, and digital conversion. This response is measured in a single end-to-end calibration.

The absolute calibration of the fluorescence detectors uses a portable drum shaped calibrated light source at the telescope aperture, providing uniform illumination to each pixel. The technique [182] is based on a 2.5 m diameter, 1.4 m deep, drum-shaped light source which mounts on the exterior of the FD apertures (see Figure B.8(a)). The source provides a pulsed photon flux of known intensity and uniformity across the aperture, and simultaneously triggers all the pixels in the camera. In the lab, light source uniformity is studied using CCD images and the intensity is measured relative to NIST calibrated photodiodes. Use of the drum for gain adjustment and calibration provides a known, uniform response for each pixel in a detector.

For calibration at wavelengths spanning the FD acceptance, a xenon flasher is mounted at the back of the drum, with a filter wheel containing 5 notch filters for selection of wavelengths. The xenon flasher [183] provides 0.4 mJ optical output per pulse covering a broad UV spectrum, in a time period of a few hundred nanoseconds. Relative drum intensity measurements at wavelengths of 320, 337, 355, 380 and 405 nm have been made with the same reference PMT used in the absolute measurements. The signals detected at the various wavelengths combine with the lab work to form a curve of relative camera response shown in Figure B.8(b). A new detailed measurement procedure was developed that utilized a monochromator and UV light source to measure the FD efficiency in 5 nm steps and found efficiencies consistent with the curve in Figure B.8(b) [184].

Three additional calibration tools are used at Auger. First, before and after each night of data taking a relative calibration of the PMTs is performed [179]. This relative calibration is used to track both short and long term changes in detector response. Secondly, the relative FD response has been measured at wavelengths of 320, 337, 355, 380 and 405 nm, defining a spectral response curve that has been normalized to the absolute calibration. Thirdly, an independent check of the calibration in some phototubes is performed using vertical shots from a portable laser in the field.

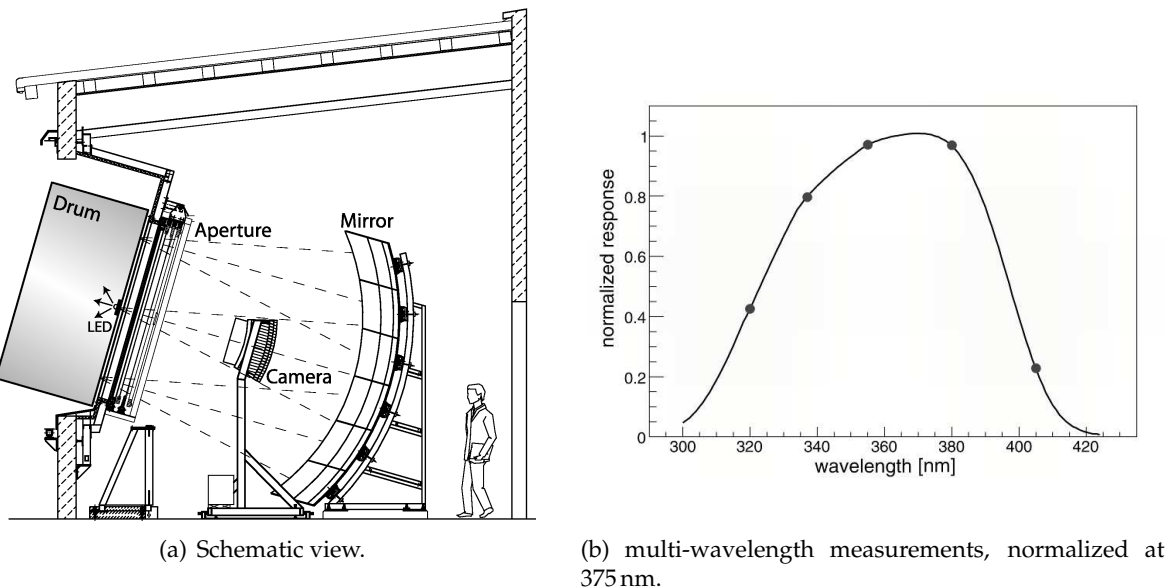


Figure B.8: Detector calibration with the 'drum'.

B.3.4 Atmospheric monitoring

The exploitation of the calorimetric measurement of the fluorescence signal in the atmosphere depends essentially on the efficiency of fluorescence light production and subsequent transmission to an FD telescope. In particular, the aerosol content of the atmosphere, in the form of clouds, dust, smoke and other pollutants, needs to be well characterized. The aerosol content of the atmosphere can be variable on short time-scales necessitating the routine monitoring of light transmission conditions in the atmospheric volume above the Pierre Auger Observatory. To account for possible horizontal non-uniformities in the aerosols the area enclosed by the observatory is divided into 5 sub-regions within which only the vertical characteristics of the aerosols are described. Within each region the aerosols are characterized in vertical slices of 200 m thickness, up to a height of 10 km. The aerosol parameters that are important for EAS reconstruction are the $\text{VAOD}(h)$, the vertical aerosol optical depth as a function of height, $\alpha(h)$, the aerosol scattering coefficient as a function of height and $d\sigma/d\Omega$, the aerosol differential cross section. The wavelength dependence of these parameters in the 300 to 400 nm sensitivity range of the FDs is also measured. Aerosol parameters are updated hourly during the periods of FD operation.

These measurements are accomplished using a complex set of instruments including backscatter LIDARS, two laser facilities (the Central Laser Facility, CLF and XLF) near the middle of the array, horizontal attenuation monitors, Aerosol Phase Function monitors, star monitors and cloud cameras. The location of these components is shown in Figure B.9 and are described in more detail in [177].

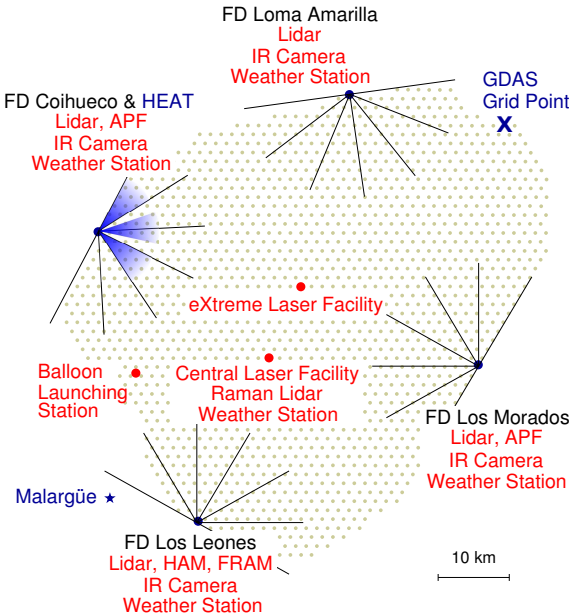


Figure B.9: Schematic overview of the atmospheric monitoring devices installed at the Pierre Auger Observatory. At each FD site, there is a lidar station, a ground-based weather station, and an infrared camera for cloud cover detection. In addition, there are devices for measuring the Aerosol Phase Function (APF) at FD Coihueco and Los Morados, a Horizontal Attenuation Monitor at FD Los Leones, and a ph(F)otometric Robotic Atmospheric Monitor also at Los Leones. A steerable backscatter elastic lidar system is installed at each of the 4 FD sites to measure aerosols and the positions of clouds near each site. At central positions within the surface detector array, two laser facilities are installed (CLF and XLF) to measure $\tau_{\text{aer}}(h)$ in the line of sight of each FD telescope 4 times per hour. In 2013 the CLF was upgraded with a Raman lidar. At the western boundary of the array, the Balloon Launching Site has been assembled together with a weather station. From this station, the weather balloons were launched so that they were typically carried across the entire array by westerly winds.

B.4 Communications System and CDAS

B.4.1 Communications system

Due to the large coverage area and widely dispersed nature of the 1660 Cherenkov detectors that make up the surface detector array, a communications system based on radio technology was deemed to be the only economically viable solution for the Pierre Auger Observatory. The system consists of two integrated radio networks organized as a 2-layer hierarchy: the individual detectors are serviced by the surface detector wireless LAN (WLAN), which is a sectorized network supported by 4 data-concentration nodes. These WLAN nodes are serviced by a high capacity microwave backbone network. The backbone also supports communications from the Fluorescence Detector sites.

The data-rate requirements of the surface detector array are determined primarily by the T2 triggering rate of the individual surface detectors. The presence of an analysis computer at each detector greatly reduces the required bandwidth as local events within the detector must pass through several stages of discrimination before they need to be communicated to the Central Data Acquisition System (CDAS) which is described below.

The design specification for the uplink from each detector to CDAS is a continuously

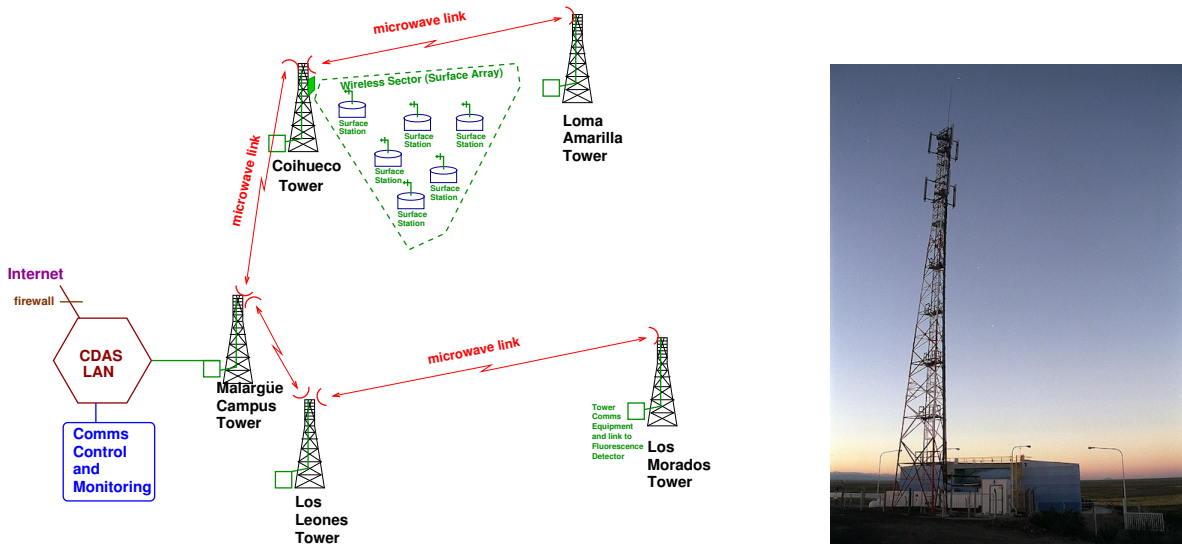


Figure B.10: *Left:* Conceptual schematic of the overall radio telecommunications system for the Pierre Auger Observatory. *Right:* One of the five communications towers: the one shown is deployed at the Los Leones site.

available capacity of 1200 bps. A reverse downlink data path is also required so that the CDAS system may request full T3 trigger readouts from those detectors that have collected relevant data. A downlink broadcast capacity of 2400 bps to all detectors is sufficient to meet this requirement.

A bi-directional 2.048 Mbps link is available to each fluorescence detector building via direct connection to the microwave backbone network.

Microwave Backbone Network The backbone network uses a standard 34 Mbps telecommunications architecture based on commercially available microwave point-to-point equipment operating in the 7 GHz band. The equipment consists of dish-mounted microwave transceivers installed on communications towers, together with secondary units located in shelters at the base of each tower. As shown in Fig. B.10 (left), the backbone network consists of two arms, both of which terminate at the Observatory Campus in Malargüe, at which point the data are routed to the central data acquisition system. The backbone network has sufficient capacity for the transfer of both the surface detector WLAN data and all FD data to and from the fluorescence detector sites.

Surface Detector WLAN The surface detector WLAN has been specially designed for the Auger project using custom radio hardware running proprietary network access protocols. This network operates in the 902-928 MHz industrial, scientific and medical (ISM) radio band and provides data communications to and from each of the 1660 surface detectors over a 3000 km² area. This is achieved in a manner similar to a cellular telephone system, whereby the area containing the detectors is divided into a number of sectors, and communications within each sector are coordinated by a base-station. Factorization is required in order to meet legislation pertaining to maximum transmitter powers and frequency re-use within the ISM band. It also greatly distributes the data processing load of the array, and reduces

the possibility that a failure at a data collection node will cause a total Observatory outage. A single sector typically contains 57 surface detectors.

Data Path from the Surface Detectors to Campus WLAN air-interface and related functions at each surface detector are performed by a subscriber unit. This unit communicates with the main surface detector electronics module via a serial link, and incorporates a proprietary digital radio transceiver running appropriate firmware on its control processor. The subscriber unit is connected to a 12 dBi Yagi antenna via a short low-loss feeder, with the antenna mounted on a short communications mast integrated into the detector's solar panel support. This can be seen in Fig. B.4, which shows a typical detector tank installation. The antenna is mounted at a height of 3 m above the ground.

Data are transmitted over a path of up to 30 km to a local data concentration tower, where the signal is received via a high-gain cellular-style panel antenna. The antenna is connected via very low-loss feeders to a base-station unit located in a shelter at the base of the tower. A single base-station can serve up to 68 detector tanks. A base-station incorporates the same digital radio transceiver platform employed in the subscriber units, with additional processing capability.

At each tower, data from several base-station units is concentrated onto an E1-ring and then processed by a custom interface before being passed on to the backbone microwave network for transmission to the Observatory campus in Malargüe. There the data passes from the E1 microwave network into the central data acquisition system via TCP/IP running on a conventional Ethernet network.

Digital Radio Transceiver Development The need to provide many highly robust data links over distances of 30 km and beyond using a minimal amount of power has presented some unique equipment performance challenges that could not be met with existing communications equipment. To meet the requirements, a low-power digital radio transceiver platform has been designed, the functionality of which is determined by re-configurable firmware stored in Flash memory and loaded into a digital signal processor (DSP) when the unit powers up. This reconfigurability not only allows the functionality of the transceiver to evolve and be refined over time, it also allows a common radio transceiver platform to be used for both subscriber units and base-station units, thereby reducing the hardware development time and simplifying long-term hardware support.

The transceiver uses very low power devices and a highly flexible architecture to provide reliable long range digital communications within the strict power budget of the solar-powered surface detectors. Power consumption is less than 1.1 W of DC power.

B.4.2 Central Data Acquisition System, CDAS

The CDAS has been running since March 2001. The system was designed to assemble the triggers from the surface array detectors, to allow control of these detectors and to organize the storage of data. It is constructed using a combination of commercial hardware and custom made, high level, software components. The system is designed to run continuously, with minimum intervention, with the full 1660 detector array, and can manage many more. Data from the FD are recorded separately at the FD locations and transferred daily to the

computer center at Malargüe, although hybrid coincidences are identified on-line within the SD data stream.

The primary role for the CDAS is to combine local trigger information from the SD stations in order to identify potential physical events generating an SD higher level trigger (T3). These triggers combined with the T3 from FD sites (FD T3) are used to generate a request for the relevant data from SD stations for these events. The CDAS is then used to combine and store these data to form a shower event. The CDAS also contains configuration and control mechanisms, the means to monitor system performance, and the tools to access and download SD monitoring, calibration, control and configuration data.

Except for triggering information (see section B.4.2), the CDAS and the FD data acquisition systems are completely independent. The merging of FD and SD data is made off-line during the daytime following an FD run. Data are synchronized on the central storage hardware after each night of observation. The newly acquired data within the central storage are mirrored at the primary data mirror located at the Lyon HEP Computer Center (France) every 3 hours; later these data can be transferred to secondary mirror sites such as Fermilab. The data may then be transferred from a convenient mirror site to over 50 participating institutions.

The communication between applications within the CDAS is controlled using a central message routine manager called the ‘Information Kernel’. This manager allows formatted messages to be broadcast by producer applications (applications that need to advertise their status), and for consumer applications (applications that need to know about the status of others) to receive them on demand. All data, with one exception, are exchanged between the CDAS applications in human readable formatted ASCII and go through the ‘Information Kernel’ manager. The exception is the large binary block of raw data coming from the SD stations. Data exchanged in raw format are calibration blocks and FADC traces (these comprise the event data), data from local triggers as well as the monitoring data.

Data Collection The data flow over the radio network, from individual SD stations to the central campus, is controlled by a dedicated application called the ‘Post Master’. The Post Master is the end point of the communication backbone at the Observatory Campus, and is designed to dispatch information extracted from the different data streams of a local station to the other applications of the CDAS. As its name suggests, the Post Master application is used to read the data type contained in a radio frame and to forward it to the proper application within the CDAS so that specific data can be handled. When the data received from individual SD stations are split into several radio frames, they are reassembled and forwarded to clients by the Post Master after all the frames have been received.

The Post Master is used also to route data between the applications of the CDAS and the SD. Commands and configuration parameters can be transmitted, along with event requests, such as the level 3 trigger identified by the ‘Central Trigger’ processor. Software downloads over the communications link are also possible, thus enabling upgrades of the local DAQ software at the stations without the need to travel many kilometers to each one.

Data received from each SD station belong to different data streams: Local triggers, forwarded to the Central Trigger application; Shower and calibration data, forwarded to the Event Builder application; Control data, forwarded to the Information Kernel application; and Calibration and monitoring data, forwarded to the Monitoring Recorder application.

Event Triggering System The triggering system of the Observatory fulfills two important conditions. First it must be able to detect showers with high efficiency across the SD, namely 99% efficiency for showers with energy above 3×10^{18} eV and zenith angle less than 60° . Secondly, it allows and identifies cross-triggers (hybrid events) between the FD and SD systems.

The local DAQ system of each SD station is designed to generate low level triggers (T2) as described in section B.2.4. The time stamps of these triggers are sent every second to the CDAS. The T2 requirements are such that the average rate per station is always around 20 to 25 Hz so that at least 50% of the bandwidth is free for data transmission.

The CDAS Central Trigger processor is used to identify groups of stations that are clustered in time and space as SD events. These are T3s, and are created if they fulfill one of the following conditions:

1. The main trigger condition is based on both the temporal and the spatial clustering of the local triggers (T2) received from each station. Basically, temporal clusters are sought by centering a time window on each T2. Clusters, with multiplicity of three or more, are then examined for spatial coincidences. For 3-fold coincidences, the triggered stations must lie within the first two crowns (hexagons) centered on the station whose T2 served as the center of the time window. For a 4-fold coincidence, one station with a T2 may be as far away as in the fourth crown. This condition is, however, stronger than the 3-fold coincidence requirement. Thus, all 4-fold triggers are also 3-fold triggers. Once the spatial coincidence is verified, final timing criteria is imposed: each T2 must be within $(3 + 8n)$ μ s of the central one where n represents the crown number.
2. A random trigger is generated every N minutes (with $3 < N < 30$) by selecting one of the T2s in an arbitrary manner and promoting it to a T3. The purpose of this trigger is to monitor randomly the FADC traces that satisfy the local trigger conditions and thus to verify the efficiency of the global trigger processor.

Once a trigger has been identified, a message requesting all FADC trace information recorded within a certain time of the central T2 sent to all stations in the array.

The DAQ system of the fluorescence detector is completely independent of the CDAS. Local triggers are generated at each camera and those identified as T3 FD event triggers are logged by a local processor if a shower track can be found. After each night of operation, details of events recorded at the FD telescopes are transferred to the CDAS.

To build the hybrid event set, the T3 information from the FD local DAQ system is transmitted in real time to the CDAS. This trigger information includes an estimate of the geometry of the shower candidate, including the time of arrival of the light front of the shower at the camera. The time of the shower impact at a ground position in the region of the SD stations is computed from this information, and a corresponding SD event T3 is constructed. All FADC traces recorded within a time window of the computed time are assembled as a normal “SD-only” event, with the addition of the identification of the corresponding FD T3 trigger. Data from these triggers forms the hybrid data set and is merged with the data collected by the FD DAQ and analyzed offline.

Monitoring The CDAS provides monitoring information for its own operation, as well as the slow control information of the SD stations and various environmental parameters. The operation of the CDAS is monitored using a low level application that routinely checks

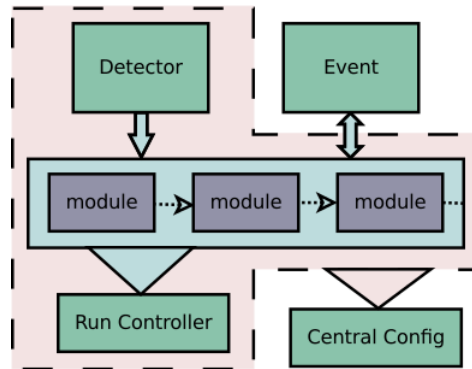


Figure B.11: General structure of the `Offline` framework. Simulation and reconstruction tasks are encased in modules. Each module is able to read information from the detector description and/or the event, process the information, and write the results back into the event under command of a *Run Controller*. A *Central Config* object is responsible for handing modules and framework components their configuration data and for tracking provenance.

that all software components are running correctly. This “watch dog” system is used to re-initialize and re-launch any application that may have failed.

SD station monitoring information is sent by the stations at regular intervals. This information consists mainly of “slow control” data, PMT and CPU board voltages and environmental parameters. Calibration data are also collected by the CDAS.

B.5 Data processing and `Offline` Software

The Pierre Auger Observatory `Offline` software provides an infrastructure to support development of hybrid event simulation and reconstruction. The software has been designed to accommodate contributions from a large number of physicists developing C++ applications over a long experimental run. The essential features include a “plug-in” mechanism for physics algorithms together with machinery which assists users in retrieving event and detector conditions data from various data sources. A detailed description of the `Offline` software design, including some example applications, is available in [157]; additional information is also given in [177].

The overall organization of the `Offline` framework is depicted in Fig. B.11. A collection of processing *modules* are assembled and sequenced through instructions contained in an XML file [158]. An *event* data model allows modules to relay data to one another, accumulates all simulation and reconstruction information, and converts between various formats used to store data on file. Finally, a *detector description* provides a gateway to detector conditions data, including calibration constants and atmospheric properties as a function of time.

Simulation and reconstruction tasks are factorized into sequences of processing steps which can simply be pipelined. Physicists prepare processing algorithms in modules, which they register with the `Offline` framework. This modular design allows collaborators to exchange code, compare algorithms and build up a variety of applications by combining modules in various sequences. Run-time control over module sequences is obtained through a *run controller*, which invokes the various processing steps within the modules according to a set of user-provided instructions written in XML.

The `Offline` framework includes two parallel hierarchies for accessing data: the detector description for retrieving conditions data, including detector geometry, calibration constants, and atmospheric conditions; and an event data model for reading and writing information that changes for each event.

The *detector description* provides a unified interface from which module authors can retrieve conditions data. Data requests are passed by this interface to a back end comprising a registry of so-called managers, each of which is capable of extracting a particular sort of information from a given data source.

The transient (in memory) and persistent (on disk) event models are decoupled. When a request is made to write event contents to file, the data are transferred from the transient event through a so-called *file interface* to the persistent event, which is instrumented with serialization machinery, currently using ROOT [160]. Various file formats are interpreted using the file interface, including raw event and monitoring formats as well as the different formats employed by the AIRES [161], CORSIKA [147], CONEX [162] and SENECA [163] air shower simulation packages.

The `Offline` framework includes a system to organize and track data used to configure of the software for different applications as well as parameters used in the physics modules. A *central configurator* points modules and framework components to the location of their configuration data, and creates Xerces-based [164] XML parsers to assist in reading information from these locations.

The central configurator keeps track of all configuration data accessed during a run and stores them in an XML log file, which can subsequently be used by the central configurator to reproduce a run with an identical configuration. The logging mechanism is also used to record the versions of modules and external libraries which are used for each run. Syntax and content checking of the configuration files is afforded through W3C XML Schema [165] standard validation. The configuration machinery can also verify configuration file contents against a set of default files by employing MD5 digests [185].

The `Offline` framework is complemented by a collection of utilities, including an XML parser, an error logger and various mathematics and physics services. We have also developed a novel geometry package which allows the manipulation of abstract geometrical objects independent of coordinate system choice.

Low-level components of the framework are verified with a small test program, known as a unit test, while full applications are vetted with more detailed acceptance tests. We employ a BuildBot system [167] to automatically compile the `Offline` software, run the unit and acceptance tests, and inform developers of any problems each time the code is modified.

B.6 Event Reconstruction and Aperture

Extensive air showers in the Auger energy range are such dramatic and large scale events that there is essentially no background to both SD and FD measurements. Triggers are easily set up to exclude virtually any possibility of chance coincidences of triggers of the individual SD stations and/or FD pixels that would mimic a real cosmic-ray shower. Therefore, the performance of the detector and its ability to produce high-quality data depend solely on the accuracy of the cosmic-ray shower reconstruction and of the computation of the acceptance of the detector.

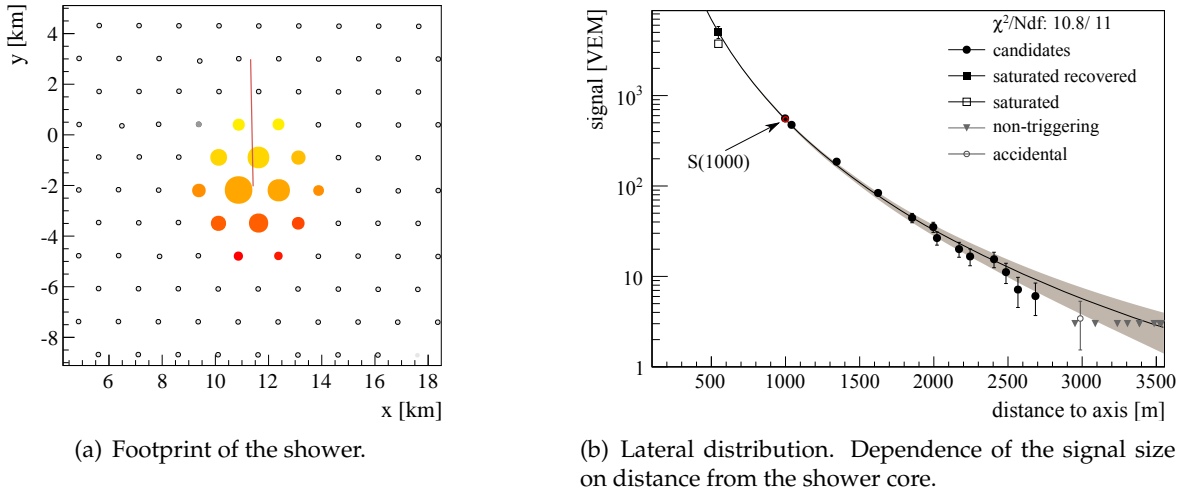


Figure B.12: Footprint and lateral distribution of a reconstructed SD event ($E = 104 \text{ EeV}$, $\theta = 25.1^\circ$). In the footprint plot, colors represent the arrival time of the shower front from early (yellow) to late (red) and the size of the markers is proportional to the logarithm of the signal. The line represents the shower arrival direction.

B.6.1 Surface Detector

Several experiments have proved successful in measuring extensive air shower parameters by use of a surface array. The quantities that can be measured directly are the geometry of the shower axis and the lateral distribution function (LDF), or the particle signal as a function of distance from the core. The primary energy can be inferred from the LDF, or, more specifically, from $S(1000)$, the detector signal at 1000 m from the core. At smaller distances, close to the core, fluctuations due to the nature of the first interactions of the primary with the atmosphere are dominating, while at larger distances statistical fluctuations become important. The relation between $S(1000)$ and the primary energy established by using shower simulations is therefore model dependent. The calibration of the zenith angle independent measure of $S(1000)$, S_{38} , with the FD energy is developed and used instead. The SD-only reconstruction takes place in three steps: event and station selection; determination of the shower geometry; and measurement of the shower lateral distribution function (LDF).

Event selection To ensure good data quality for physics analysis there are two additional off-line triggers. The physics trigger, T4, is needed to select real showers from the set of stored T3 data (see section B.4.2) that also contain background signals from low energy air showers. This trigger is mainly based on a coincidence between adjacent detector stations within the propagation time of the shower front. In selected events, random stations are identified by their time incompatibility with the estimated shower front. Time cuts were determined such that 99% of the stations containing a physical signal from the shower are kept. An algorithm for the signal search in the time traces is used to reject signals produced by random muons by searching for time-compatible peaks.

To guarantee the selection of well-contained events, a fiducial cut (called the 6T5 trigger) is applied so that only events in which the station with the highest signal is surrounded by all 6 operating neighbors (i.e., a working hexagon) are accepted. This condition assures an

accurate reconstruction of the impact point on the ground, and at the same time allowing for a simple geometrical calculation of the aperture/exposure [186], important for, e.g., the spectrum analysis [4]. For arrival-direction studies a less strict cut can be used (5T5 or even 4T5).

Geometry and Energy measurement An approximate shower geometry solution can be obtained from the simplified linear model assuming that all stations lie within some plane, i.e. here the tangential plane on the reference ellipsoid that contains the signal-weighted barycenter is chosen. In such a case one can expect $z_i \ll x_i, y_i$ for the station position (x_i, y_i, z_i) . The z-component is neglected and the linear χ^2 is obtained,

$$\chi^2 = \sum_i \frac{[ct_i - ct_0 + ux_i + vy_i]^2}{\sigma_i^2}, \quad (\text{B.2})$$

where t_i is the signal start time in tank i and t_0 is the time when the shower passes the barycenter. Equation B.2 can be expressed as a set of linear equations and is analytically solved. The approximate solution serves as starting point to more elaborate 3D-fitting attempts taking the varying altitude of the stations, and a more accurate core location from the LDF fit (below), into account.

An example of the footprint on the array of an event produced by a cosmic ray with an energy of (104 ± 11) EeV and a zenith angle of $(25.1 \pm 0.1)^\circ$ is shown in figure B.12. The lateral distribution of the signals is depicted in figure B.12(b). The function employed to describe the lateral distribution of the signals on the ground is a modified Nishimura-Kamata-Greisen function [187, 188],

$$S(r) = S(r_{\text{opt}}) \left(\frac{r}{r_{\text{opt}}} \right)^\beta \left(\frac{r + r_1}{r_{\text{opt}} + r_1} \right)^{\beta + \gamma} \quad (\text{B.3})$$

where r_{opt} is the optimum distance, $r_1 = 700$ m and $S(r_{\text{opt}})$ is an estimator of the shower size used in an energy assignment. For the SD array with station spacing of 1.5 km the optimum distance [137] is $r_{\text{opt}} = 1000$ m and the shower size is thus $S(1000)$. The parameter β depends on the zenith angle and shower size. Events up to zenith angle 60° are observed at an earlier shower age than more inclined ones, thus having a steeper LDF due to the different contributions from the muonic and the electromagnetic components at the ground. For events with only 3 stations, the reconstruction of the air showers can be obtained only by fixing the two parameters, β and γ to a parameterization obtained using events with a number of stations larger than 4.

The primary particle energy is determined from $S(1000)$ and the shower zenith angle θ . For a given energy, the value of $S(1000)$ decreases with θ due to the attenuation of the shower particles and geometrical effects. Assuming an isotropic flux of primary cosmic rays at the top of the atmosphere, we extract the shape of the attenuation behavior from the data using the Constant Intensity Cut (CIC) method [190]. An attenuation curve $f_{\text{CIC}}(\theta)$ has been fitted with a third degree polynomial in $x = \cos^2 \theta - \cos^2 \bar{\theta}$, i.e., $f_{\text{CIC}}(\theta) = 1 + ax + bx^2 + cx^3$, where $a = 0.980 \pm 0.004$, $b = -1.68 \pm 0.01$, and $c = -1.30 \pm 0.45$ [138].

The median angle, $\bar{\theta} = 38^\circ$, is taken as a reference point to convert $S(1000)$ to $S_{38} \equiv S(1000)/f_{\text{CIC}}(\theta)$. S_{38} may be regarded as the signal a particular shower with size $S(1000)$ would have produced had it arrived at $\theta = 38^\circ$.

High quality hybrid events, events seen by both the SD and FD, are used to calibrate S_{38} with the near-calorimetric measurement of the primary energy by the FD, E_{FD} . The 1475

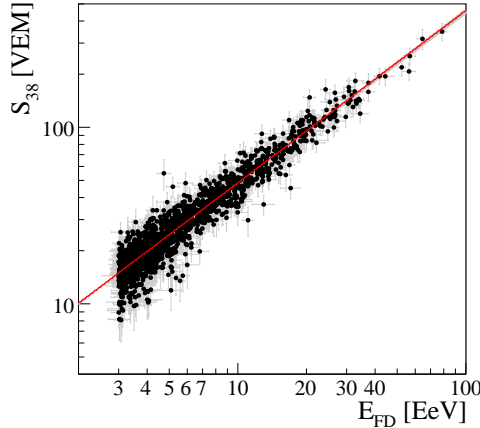


Figure B.13: Correlation between S_{38} and E_{FD} [138, 189].

high quality hybrid events recorded between Jan 2004 and Dec 2012 which have an energy above the SD full efficiency trigger threshold [186] are used in the calibration. The correlation between the two variables is obtained from a maximum likelihood method [189, 191] which takes into account the evolution of uncertainties with energy, as well as event migrations due to the finite energy resolution of the SD. The relation between S_{38} and E_{FD} is well described by a single power-law function,

$$E_{\text{FD}} = A (S_{38}/\text{VEM})^B \quad (\text{B.4})$$

where the resulting parameters from the data fit are $A = (1.90 \pm 0.05) \times 10^{17}$ eV and $B = 1.025 \pm 0.007$ [138, 192]. As can be seen in figure B.13, the most energetic event used in this analysis has an energy of 79 EeV.

The resolution of the final SD energy estimator,

$$E_{\text{SD}} = A(S(1000)/f_{\text{CIC}}(\theta)/\text{VEM})^B, \quad (\text{B.5})$$

can be inferred from the distribution of the ratio $E_{\text{SD}}/E_{\text{FD}}$. Using the FD energy resolution of 7.6%, the resulting SD energy resolution with its statistical uncertainty is $\sigma_{E_{\text{SD}}}/E_{\text{SD}} = (16 \pm 1)\%$ at the lower energy edge in figure B.13 and $(12 \pm 1)\%$ at the highest energies. Due to the large number of events accumulated until December 2012, the systematic uncertainty on the SD energy due to the calibration is better than 2% over the whole energy range. The systematic uncertainties are dominated by the FD energy scale uncertainty of 14% [192]. The main contributions to this uncertainty are related to the knowledge of the fluorescence yield (3.6%), the atmospheric conditions (3.4 to 6.2%), the absolute calibration of the telescopes (9.9%), the shower profile reconstruction (6.5 to 5.6%) and the invisible energy (3 to 1.5%).

B.6.2 Hybrid Reconstruction

Geometry Reconstruction A hybrid detector achieves the best geometrical accuracy by using timing information from all the detector components, both FD pixels and SD stations. Each element records a pulse of light from which one can determine the central time of the pulse and its uncertainty. Each trial geometry for the shower axis yields a prediction for the times at each detector component. Differences between actual and predicted times are

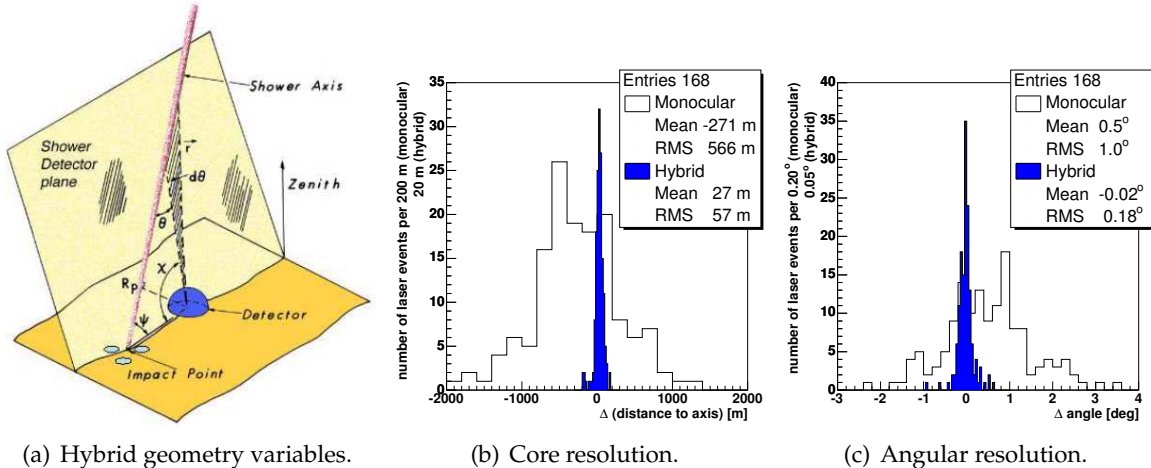


Figure B.14: Illustration of the geometrical shower reconstruction from the observables of the fluorescence detector (left) and Comparison of mono- and hybrid geometry reconstruction of vertical laser beams (right)

weighted using their corresponding uncertainties, squared, and summed to construct a χ^2 value. The hypothesis with the minimum value of χ^2 is the reconstructed shower axis. In the FD, cosmic ray showers are detected as a sequence of triggered pixels in the camera. The first step in the analysis is the determination of the shower-detector plane (SDP) that is the plane that includes the location of the eye and the line of the shower axis (cf. Fig. B.14(a)). Experimentally, it is determined by minimizing the signal weighted sum of scalar product of its normal and the pixel pointing directions.

Next, the timing information of the pixels is used for reconstructing the shower axis within the SDP. As illustrated in Fig. B.14(a), the shower axis can be characterized by two parameters: the perpendicular distance R_p from the eye to the track and the angle ψ that the track makes with the horizontal line in the SDP. Each pixel which observes the track has a pointing direction which makes an angle χ_i with the horizontal line. If t_0 is the time when the shower front on the axis passes the point of closest approach R_p to the eye, then the light arrives at the i th pixel at the time

$$t_i = t_0 + \frac{R_p}{c} \cot [(\psi + \chi_i)/2]. \quad (\text{B.6})$$

The shower parameters are then determined by fitting the data points to this functional form. The accuracy of the monocular (FD-only) reconstruction is limited when the measured angular speed $d\chi/dt$ does not change much over the observed track length. For such showers, degeneracy in the fitting parameters can be broken by combining the timing information from the SD stations with that of the FD telescopes. This is called the *hybrid* reconstruction. Example results are shown in Fig. B.14(b) and Fig. B.14(c) for reconstruction of a vertical laser beam at the Central Laser Facility (CLF) where some laser light is also injected into a neighboring SD station. There we compare the mono and hybrid reconstructions of the distance to the laser and the zenith angle. With the monocular reconstruction, the location of the CLF can be determined with a resolution of ~ 500 m. After including the timing information of the single SD station, the resolution improves by one order of magnitude with no systematic shift.

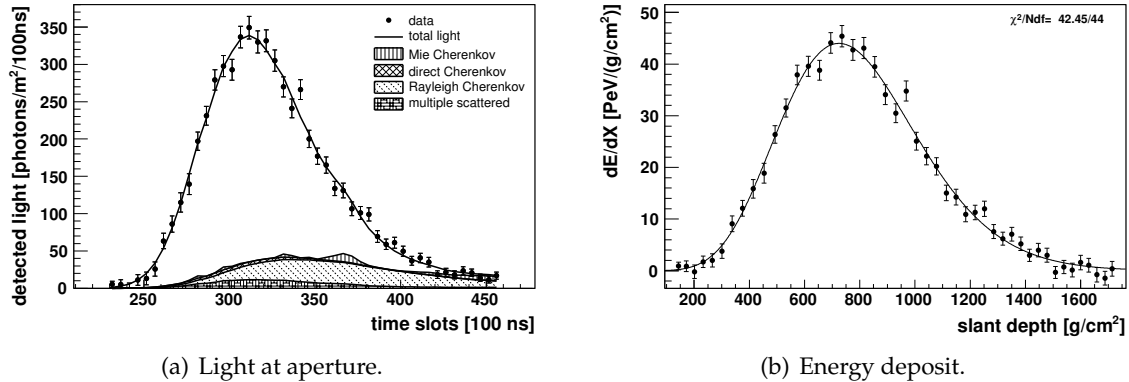


Figure B.15: Example of a reconstructed shower profile.

Profile Reconstruction and Energy Determination Once the geometry of the shower is known, the light collected at the aperture as a function of time can be converted to energy deposit, dE/dX , at the shower as a function of slant depth. For this purpose, the light attenuation from the shower to the detector needs to be corrected for and all contributing light sources need to be disentangled: fluorescence light [193–195], direct and scattered Cherenkov light [131, 196] as well as multiply scattered light [197–199]. Since the Cherenkov and fluorescence light produced by an air shower are connected to the energy deposit by a linear set of equations, the shower profile is obtained by an analytic linear least square minimization [200]. Due to the lateral extent of air showers, a small fraction of shower light is not contained within the optimal light collection area. This is corrected for by taking into account the universal lateral fluorescence [201] and Cherenkov light [202] distributions. The calorimetric energy, E_{cal} , of a shower is given by the integral over the longitudinal energy deposit profile,

$$E_{\text{cal}} = \int_0^{\infty} dE/dX(X) dX. \quad (\text{B.7})$$

Since usually the full profile cannot be observed within the field of view of the FD, this integral is evaluated from a Gaisser-Hillas function [203] that is fitted to the reconstructed energy deposit. In addition, this fit yields an estimate of X_{max} , the mass sensitive position of the shower maximum. An example of the measured light at aperture and the reconstructed light contributions and energy deposit profile is shown in Figs. B.15(a) and B.15(b). The total energy of the shower is obtained from E_{cal} by correcting for the ‘invisible energy’ carried away by neutrinos and high energy muons [204].

The resolution of the profile measurement can be determined by reconstructing simulated showers, that have passed a full detector simulation [205]. Moreover, at the high energies it can be determined from the data itself by comparing independent measurements of the same shower by different eyes (stereo events). Both studies show that the energy of a shower can be determined with a precision of 8% above 10 EeV. For the shower maximum, the resolution is 20 g/cm² [206].

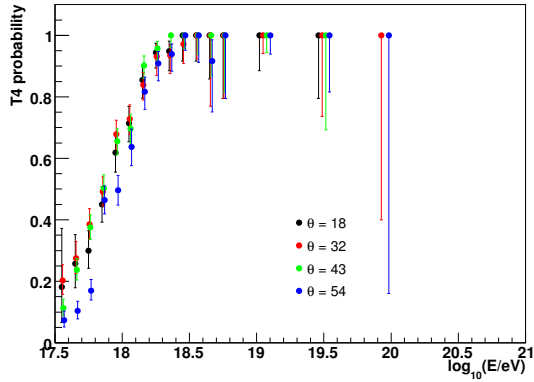


Figure B.16: Detection efficiency of the SD array, as a function of energy, as measured from the data using the hybrid data set, for different zenith angles (averaged over azimuths).

B.6.3 Aperture

An important feature of the SD is that it allows for a straightforward control of the shower detection volume. With the requirement that the shower core of the events be reconstructed within the limits of the region covered by the SD stations, the SD aperture can be obtained from a simple geometric calculation of the actual size of the active array on the ground, at any given time. This sets the effective detection surface on the ground, to be weighted by the energy-dependent detection efficiency of cosmic ray showers. The latter can be measured directly from the hybrid data: restricting oneself to conditions where the showers are known to be detectable with 100% efficiency in the 1-tank hybrid mode, one derives the SD detection efficiency at a given energy as the fraction of the corresponding showers that do trigger the SD, at the “physics trigger” level (T4) described above. This is shown in Fig. B.16, where the detection efficiency is seen to reach 100% at the *saturation energy* $E_{\text{sat}} \simeq 3 \times 10^{18}$ eV, in very good agreement with simulations and measurements based on the SD trigger probability and signal fluctuations as a function of distance to the shower axis.

Above E_{sat} , the instantaneous aperture of the SD is derived from the total surface covered by the array. In order to avoid border effects and a potentially degraded energy reconstruction for showers hitting the ground close to an edge of the array or in a region where some tanks are momentarily inactive, an additional cut is applied to the data (referred to as the *quality trigger*, or T5) to ensure nominal reconstruction accuracy. This T5 trigger requires that the station recording the highest signal in a given CR event be surrounded by at least 5 active stations (out of the 6 nearest neighbors). In the case when only 5 neighboring stations are active, the shower core must also be reconstructed inside an elementary triangle of stations that were active at that time. Figure B.17 illustrates this requirement, showing the core positions allowed for vertical showers arriving well inside the array (left) or near a missing station (right). The total detection area associated with the central station is then seen to be $D^2\sqrt{3}/2 \simeq 1.95 \text{ km}^2$ in the former case, and $2/3$ of this in the latter. A final integration over solid angle for showers with zenith angles between 0 and 60° gives the nominal aperture per active station: $A_0 \simeq 4.59 \text{ km}^2 \text{ sr}$.

The computation of the total SD aperture at any given time is then obtained by multiplying the elementary aperture by the number of active stations (with the required number

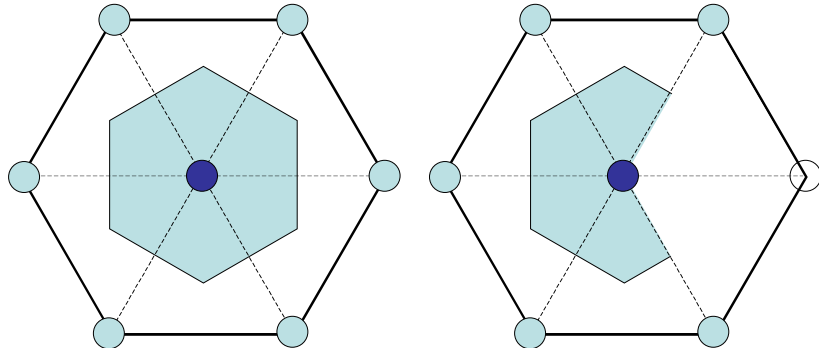


Figure B.17: Schematic view of the area (shaded region) where the core of a vertical shower must be located inside an elementary hexagonal cell of the SD array to pass the quality trigger (T5). Left: for a complete hexagon with 7 active tanks. Right: for a hexagon with one missing tank.

of active neighbors), obtained from a simple census using the SD monitoring data, which give the list of active stations on a second-by-second basis. Finally, the integrated SD exposure in *linsleys* ($1 \text{ L} = 1 \text{ km}^2 \text{ sr yr}$) is obtained by the time integration of the instantaneous aperture of the SD array, taking into account any changes in the array configuration, using the same monitoring data. In this way, the growth of the array during the SD deployment period could be automatically included in the exposure calculation, whatever the shape and duration of the intermediate configurations.

Overall, the above-mentioned technique provides a very accurate determination of the SD acceptance, with an uncertainty of $\sim 3\%$, which can be considered as negligible with respect to the uncertainty on the energy reconstruction.

B.7 Enhancements

Instrumental enhancements have been installed close to the Coihueco FD station. These include underground muon detectors, additional water Cherenkov detectors, and high-elevation fluorescence telescopes for a larger field-of-view. Also, research programs are underway to assess the utility of radio and microwave emission from air showers.

B.7.1 High Elevation Auger Telescopes (HEAT)

Three additional fluorescence telescopes with an elevated field of view were built at the FD site at Coihueco [207]. These telescopes are very similar to the original fluorescence telescopes but can be tilted by 29° upward with an electrically driven hydraulic system. These three telescopes work independently of other FD sites and form the “fifth site” of the Observatory. The HEAT telescopes were designed to cover the elevation range from 30° to 58° , which lies above the field of view of the other FD telescopes. The HEAT telescopes allow a determination of the cosmic ray spectrum and X_{\max} distributions in the energy range from below the second knee up to the ankle. The design of the HEAT telescopes is depicted in Figure B.18.

The main objective of this extension is to lower the energy threshold of hybrid data to enable an unbiased detection of nearby low-energy showers. In combination with the SD infor-

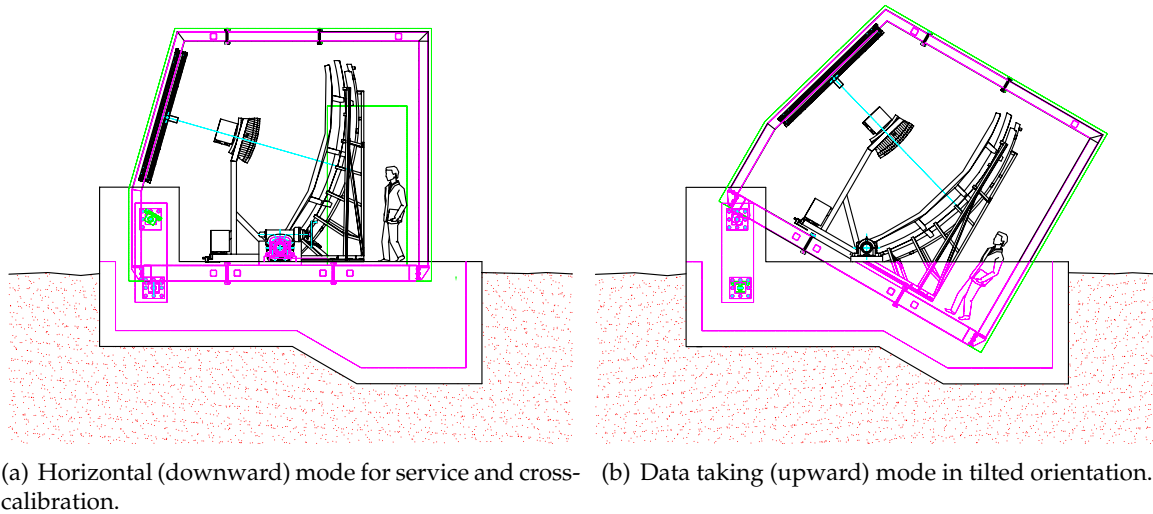


Figure B.18: Schematic view of the cross-section of one of the HEAT telescopes.

mation from an infill array of water-Cherenkov detectors on a 750 m grid (see section B.7.2) close to the HEAT site, the energy range of high quality hybrid air shower measurements has been extended down to 10^{17} eV.

The HEAT telescopes can be tilted using the hydraulic mechanism. The telescopes are parked in the horizontal position between the FD data taking periods to be accessible for maintenance. The same position is used for the absolute calibration of the HEAT telescopes and also for the cross-calibration with telescopes at Coihueco.

The Schmidt optics of the HEAT telescopes, camera body, PMTs, light collectors, etc., are the same as in the other sites. All three spherical mirrors are built up from hexagonal glass mirrors with vacuum-deposited reflective coatings.

A feature that sets HEAT apart from the classic Auger telescopes is its new electronics kit that can sample up to 40 MHz instead of 10 MHz. In practice, a sampling rate of 20 MHz (corresponding to a 50 ns FADC bin size) was chosen. The higher rate improves the measurement for close showers that have a correspondingly larger angular velocity – precisely the showers we are interested in observing with HEAT. From this it follows that the first level trigger interval was reduced to 50 ns, whereas the second level trigger continues to operate every 100 ns. The length (in time) of the FADC traces remains the same, so the number of bins doubles.

The trigger rate of the HEAT telescopes is high, particularly because of the Cherenkov light from low energy showers. Therefore the T4 trigger has been implemented to reduce the readout of the SD array for these low energy showers.

B.7.2 Auger Muon and Infill Ground Array (AMIGA)

A dedicated detector to directly measure the muon content of air showers is being built. The AMIGA enhancement [152, 208, 209] is a joint system of water-Cherenkov and buried scintillator detectors that spans an area of 23.5 km^2 in a denser array with 750 m spacing nested within the 1500 m array (see figure B.19). The area is centered 6 km away from the Coihueco fluorescence site. The infill array is fully efficient from 3×10^{17} eV onwards for air

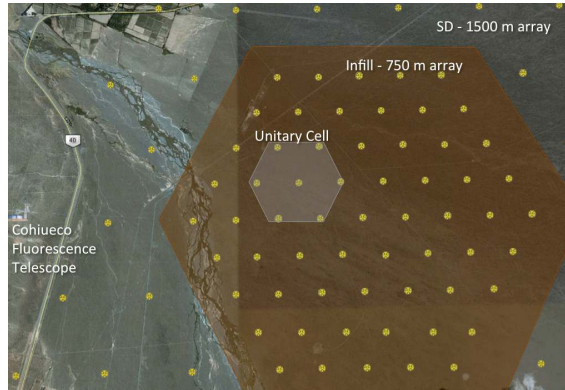


Figure B.19: AMIGA layout: an infill of surface stations with an inter-detector spacing of 750 m. Plastic scintillators of 30 m^2 are buried under $\approx 280\text{ g/cm}^2$ of vertical mass to measure the muon component of the showers. The small shaded area indicates the prototype hexagon (*Unitary Cell*) of the muon detector.

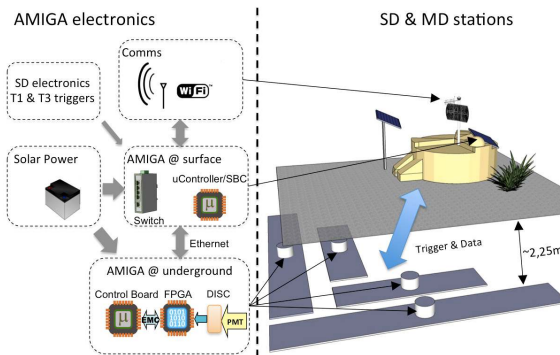


Figure B.20: AMIGA station: SD+MD paired detectors. During the MD prototype phase the 30 m^2 buried scintillators are segmented into 4 modules, $2 \times 10\text{ m}^2 + 2 \times 5\text{ m}^2$. For the production phase, only 3 modules of 10 m^2 will be used. To avoid shadowing effects by the water-Cherenkov detector, there are 5 m of sideways clearance. The buried front end electronics is serviceable by means of an access pipe which is filled with local soil bags. Data are sent by a dedicated WiFi antenna.

showers with zenith angle $\leq 55^\circ$ [210].

The SD infill array was completed in September 2011 while the first prototype hexagon of buried scintillators, the *Unitary Cell*, was fully operational at the end of 2014. This engineering array consists of seven water-Cherenkov detectors paired with 30 m^2 scintillators segmented in two modules of 10 m^2 plus two of 5 m^2 in each position. In addition, two positions of the hexagon were equipped with *twin* detectors (extra 30 m^2 scintillators) to allow the accuracy of the muon counting technique to be experimentally assessed [211] and one position has 20 m^2 of extra scintillators buried at a shallower depth to analyze the shielding features. The proven tools and methods used for the analysis of the 1500 m SD array data have been extended to reconstruct the lower energy events. The angular resolution for $E \geq 4 \times 10^{17}\text{ eV}$ is better than 1° and the energy reconstruction is based on the lateral density of shower particles at the optimal distance of 450 m from the core [212].

The buried scintillators are the core of the detection system for the muonic component of air showers (the muon detector, MD). To effectively shield the electromagnetic component,

the MD is placed under $\approx 280 \text{ g/cm}^2$ of vertical mass corresponding to a depth of 1.3 m in the local soil. This shielding imposes a cutoff for vertical muons of around 1 GeV. The layout of SD+MD paired stations is shown in figure B.20. The scintillator surface of each MD station is highly segmented. It consists of modules made of 64 strips each. Strips are 4.1 cm wide \times 1.0 cm thick and 400 cm long for the 10 m² modules. They consist of extruded Dow Styron 663W polystyrene doped by weight with 1% PPO (2,5-diphenyloxazole) and 0.03% POPOP (1,4-bis(5-phenyloxazole-2-yl)benzene). They are completely wrapped with a thin white reflective layer of titanium dioxide (TiO_2) except for a central groove into which a wavelength shifting (WLS) optical fiber is installed. The light output uniformity is $\pm 5\%$. Because the scintillators have an attenuation length of $\sim (55 \pm 5)$ mm, light is transported to a photomultiplier tube using the WLS fiber. The manifold of fibers of each module ends in an optical connector matched to a 64 multi-anode PMT from the Hamamatsu H8804 series.

The bandwidth of the front end electronics is set to 180 MHz to determine the pulse width. Signal sampling is performed by a Field Programmable Gate Array (FPGA) from the ALTERA Cyclone III series at 320 MHz. MD scintillator modules receive the trigger signal from their associated SD station. The lowest level trigger (T1) of the surface detectors is used. Once a T1 condition is fulfilled on the surface, its MD companion freezes a 6.4 μs data sample into a local buffer – 1.6 μs before and 4.8 μs after the T1. Data are then moved to an external RAM capable of storing 1024 triggers [213].

Incoming analog signals from each pixel of the PMT are digitized with a discriminator that provides the input to the FPGA. Samples can be either a logical “1” or “0” depending on whether the incoming signal was above or below a given (programmable) discrimination threshold. This method of *one-bit* resolution is very robust for counting muons in a highly segmented detector. This avoids missing muons due to simultaneous particle arrivals [214]. It relies neither on deconvolving the number of muons from an integrated signal, nor on the PMT gain or its fluctuations, nor on the point of impact of the muon and the corresponding light attenuation along the fiber. It also does not require a thick scintillator to control Poissonian fluctuations in the number of single photoelectron pulses per impinging muon [215]. The MD station power is supplied by an additional solar panel and battery box (see figure B.20).

B.7.3 Radio and Microwave Research Programs

Radio Research Program The observation of air showers with radio detection techniques can be done at all times (day and night). Moreover, radio signals are sensitive to the development of the electromagnetic component of particle showers in the atmosphere of the Earth and, in particular, to the depth of the shower maximum or mass of the incoming cosmic ray [216]. Radio detection of air showers started in the 1960s, and the achievements in those days have been presented in reviews by Allan [217] and Fegan [218]. More recent developments are based on initial studies performed by the LOPES [219] and the CODALEMA [220] collaborations and the LOFAR radio telescope [221]. In the last 10 years the radio detection technique in the MHz region has been revived and the present radio detector arrays for cosmic ray research are equipped with low noise and high rate analog-to-digital converters.

The Pierre Auger Collaboration has started a research program to examine the feasibility and quality of radio observations of air showers. Since 2009 the activities are coordinated within the Auger Engineering Radio Array (AERA), which is based on work within the Collaboration using various prototypes at the site of the Pierre Auger Observatory [222–



Figure B.21: Map of the Auger Engineering Radio Array (left) and a photograph of one station. AERA consists of 153 antenna stations at the Auger Infill array covering an area of $\approx 17 \text{ km}^2$.

[224]. As a first step the emission mechanisms need to be understood. Recently, AERA has measured the relative contribution of the two main emission processes in air showers [225]. As a second step the data obtained with radio detection stations deployed at the Observatory will be used to check their sensitivity with respect to the determination of the air shower parameters.

The scientific goals of the AERA project are as follows: 1) calibration of the radio emission from the air showers, including sub-dominant emission mechanisms; 2) demonstration at a significant scale of the physics capabilities of the radio technique, e.g., energy, angular, and mass resolutions; and 3) measurement of the cosmic ray composition from 0.3 to 5 EeV, with the goal of elucidating the transition from galactic to extragalactic cosmic rays.

At present, AERA consists of 153 radio detection stations. Each station is comprised of a dual polarization antenna, sensing the electric field in the north/south and east/west directions, associated analog and digital readout electronics, an autonomous power system and a communication link to a central data acquisition system. Nine of the stations are additionally equipped with a third, vertically aligned antenna to measure the full electric field. The antennas are sensitive between 30 and 80 MHz, chosen as the relatively radio quiet region between the shortwave and FM bands. AERA deployment began in 2010 with 24 stations. Stable physics data taking started in March 2011, and the first hybrid detection of cosmic ray events by radio, fluorescence, and surface particle detectors was recorded in April 2011. In May 2013 additional 100, and in March 2015 further 25 stations were installed (see figure B.21), where the stations are optimized compared to the first phase, in particular related to the antenna type used [226]. AERA covers an area of $\approx 17 \text{ km}^2$ and operates in self-trigger and at the same time in external (SD, FD, and minimum bias) trigger mode. The AERA data is merged with those of the other detector components and analyzed by Offline which enables detailed comparisons and hybrid reconstruction on a single event basis. Several thousands hybrid events are presently analyzed including tens of so-called super-hybrid (SD - FD - AERA - AMIGA- μ) events.

Microwave research program Recent results of a test beam experiment at SLAC [227] showed that it could be possible to use microwave radiation to detect extensive air showers. This radiation, expected to be isotropic and broad in frequency, is interpreted [227] as molec-

ular bremsstrahlung (MBR) produced by the scattering of low energy electrons in the weakly ionized plasma produced by the shower with the neutral molecules of the atmosphere. The Auger collaboration is pursuing an active R&D program to determine if a detector sensitive to MBR would be a suitable alternative for the study of ultra-high energy cosmic rays.

This R&D program [228, 229] consists of three different setups installed at the Observatory. The AMBER and MIDAS experiments use radio-telescope style detectors intended for the observation of the shower longitudinal development in the same manner as an FD. In the EASIER setup on the other hand, SD tanks are instrumented with smaller radio receivers that take advantage of the enhancement of the signal when the shower is observed close to its axis.

Installation of the microwave detectors was finalized in September 2012. A previous result by the MIDAS detector [230], obtained in Chicago, places tight constraints on the amount of microwave signal emitted and its scaling with the energy of the shower [231]. The ongoing work to identify showers detected at the same time in the SD and in one of the microwave detectors already yielded the first unambiguous detection of a cosmic ray shower in the EASIER setup in June 2011 [229].

B.8 Performance of the Observatory

B.8.1 Key performance parameters

In Table B.1 are summarized some of the important parameters that characterize the performance of the Observatory. These parameters include the event rate of the detectors and the resolutions of the different reconstructed observables.

B.8.2 Surface detector performance

Stable data taking with the surface detector array started in January 2004 and the Observatory has been running in its full configuration since 2008. As described in section B.4.2, various parameters are continuously monitored to optimize the performance of the detectors and ensure reliable data.

The monitoring tool includes so-called performance metrics to monitor the overall performance of the surface detector array. Relevant data useful for long term studies and for quality checks are stored in the Auger Monitoring database on a one-day basis. For example, mean values over one day of the number of active SD detectors and the number of active hexagons as well as the nominal value (expected value if all the detectors deployed were active) are available. As an example, figure B.22 shows the number of active SD stations normalized to the nominal number of stations in the array for the last 4 years. This plot is a convolution of the status of the active stations and of the efficiency of the CDAS, which since the beginning is better than 99.5%.

Figure B.23 shows the number of active hexagons for the same period. This variable is a key parameter since it is the basis of the exposure evaluation. Indeed, the off-line T5 fiducial trigger, described in section B.6.1 selects only events for which the hottest station is surrounded by an active hexagon. Thus, above 3×10^{18} eV, when the full efficiency of detection of the array is reached (at least three triggered tanks), the exposure is simply proportional to the integrated number of active hexagons during the period.

Table B.1: Key performance parameters for the Auger Observatory

SD	
SD Annual Exposure	$\sim 5500 \text{ km}^2 \text{ sr yr}$
T3 rate	0.1 Hz
T5 events/yr, $E > 3 \text{ EeV}$	$\sim 14,500$
T5 events/yr, $E > 10 \text{ EeV}$	~ 1500
Reconstruction accuracy ($S(1000)$)	22% (low E) to 12% (high E)
Angular resolution	1.6° (3 stations) 0.9° (>5 stations)
Energy resolution	16% (low E) to 12% (high E)
FD	
Duty cycle	$\sim 15\%$
Rate per building	0.012 Hz
Rate per HEAT	0.026 Hz
Hybrid	
Core resolution	50 m
Angular resolution	0.6°
Energy resolution (FD)	8%
X_{\max} resolution	<20 g/cm²

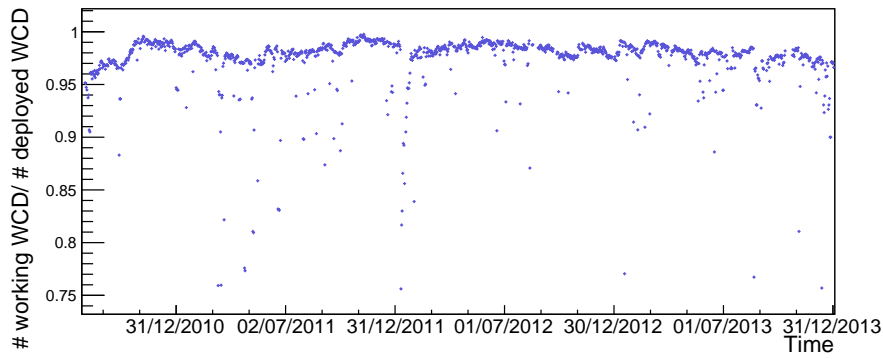


Figure B.22: Number of active SD stations normalized to the nominal number of SD stations in the array, as a function of time.

The rate of events (T5 events) normalized to the average number of active hexagons is expected to be stable in time above the energy threshold of $3 \times 10^{18} \text{ eV}$, which can be seen in figure B.24.

Finally the integrated exposure between 1 January 2004 and 31 December 2012 is shown in Fig. B.25. Since completion of the array in 2008, the increase of the exposure has been about $5500 \text{ km}^2 \text{ sr per year}$.

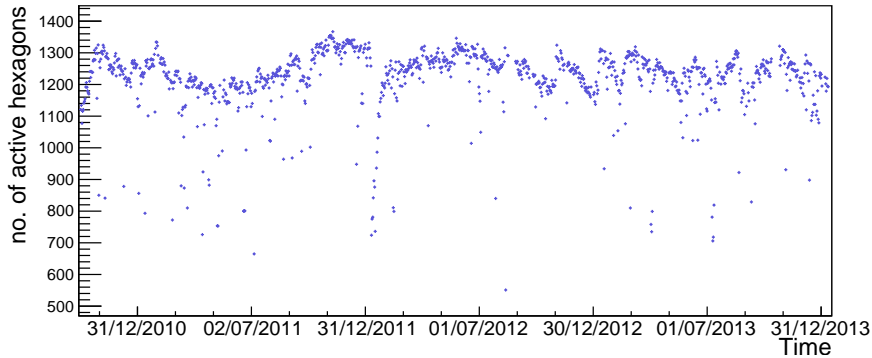


Figure B.23: Number of active hexagons as a function of time

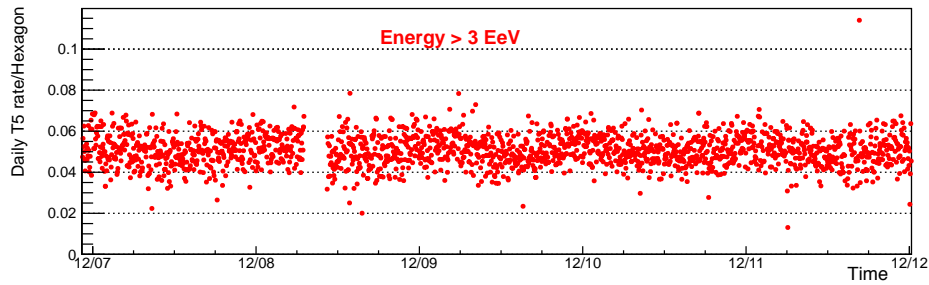


Figure B.24: Evolution of the daily T5 rate normalized to the number of hexagons for the period 2008 to 2012.

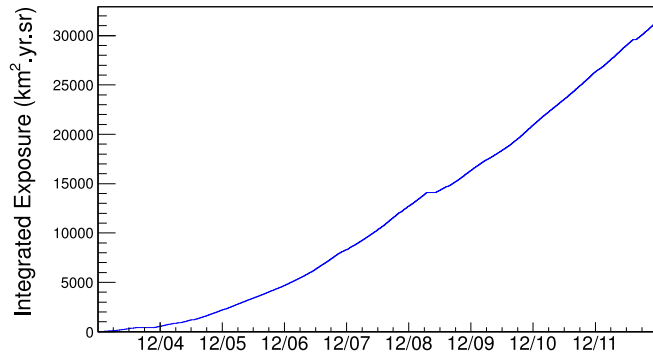


Figure B.25: Evolution of the exposure between 1 January 2004 and 31 December 2012.

B.8.3 Fluorescence detector performance

The data taking of the FD can only take place under specific environmental conditions and is organized in night shifts. The telescopes are not operated when the weather conditions are unfavorable (high wind speed, rain, snow, etc.) and when the observed sky brightness (caused mainly by scattered moonlight) is too high. As a consequence, the shifters have to continuously monitor the atmospheric and environmental conditions and judge the operation mode on the basis of the available information.

The performance of the fluorescence and hybrid data taking is then influenced by many

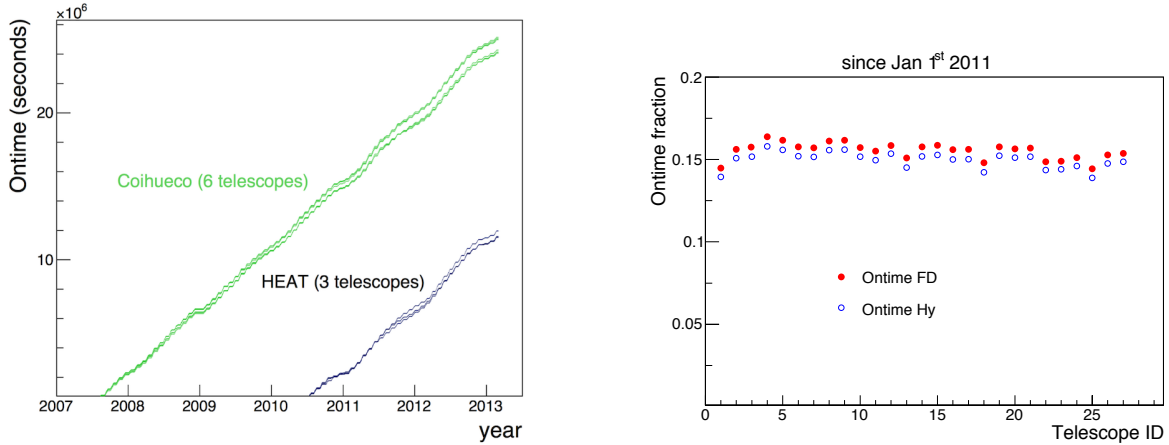


Figure B.26: *Left:* accumulated on-time since 1 Jul 2007 for the Coihueco and HEAT telescopes. *Right:* On-time of individual telescopes since 1 Jan 2011. (1–6), (7–12), (13–18), (19–24), (25–27) for the sites of Los Leones, Los Morados, Loma Amarilla, Coihueco and HEAT, respectively.

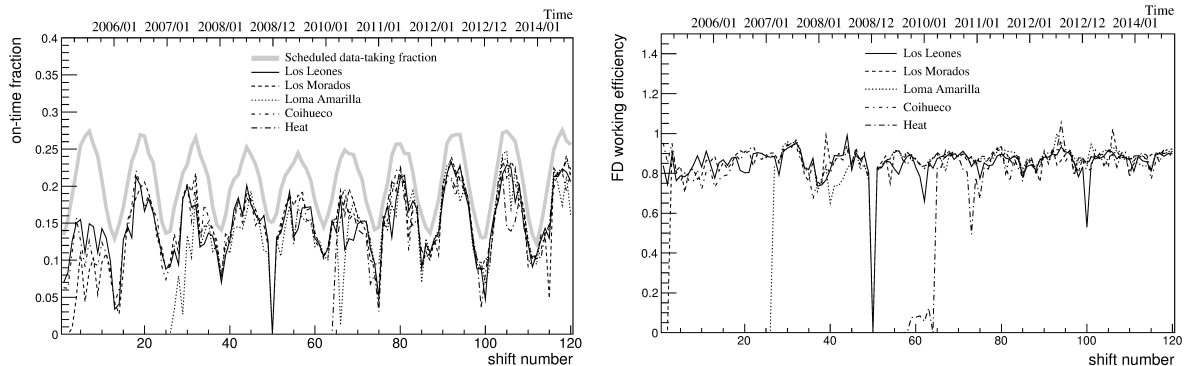


Figure B.27: *Left:* time evolution of the average hybrid on-time fraction over 9 years of operation of the Pierre Auger Observatory. The thick gray line defines the scheduled data taking time fraction defined as the time periods with moon fraction lower than 70% and with the moon being below the horizon for more than 3 hours. *Right:* readiness of the FD detector (see text for details).

effects. These can be external, e.g., lightning or storms, or internal to the data taking itself, e.g., DAQ failures. For the determination of the *on-time* of the Pierre Auger Observatory in the hybrid detection mode it is therefore crucial to take into account all of these occurrences and derive a solid description of the data taking time sequence.

Data losses and inefficiencies can occur on different levels, from the smallest unit of the FD, i.e., one single photomultiplier (pixel) readout channel, up to the highest level, i.e., the combined SD/FD data taking of the Observatory.

The active time of the FD data acquisition is calculated using a minimum bias data stream with a less restrictive trigger condition. Since July 2007, the relevant information concerning the status of the FD detector has been read out from the Observatory monitoring system. An on-time dedicated database has been set up by storing the average variances and the on-time fraction of individual telescopes in time bins of 10 minutes. The information on the veto due to the operation of the lidar or to an anomalous trigger rate on FD together with the status of the CDAS needed to form a hybrid event are also recorded. The method to calculate the

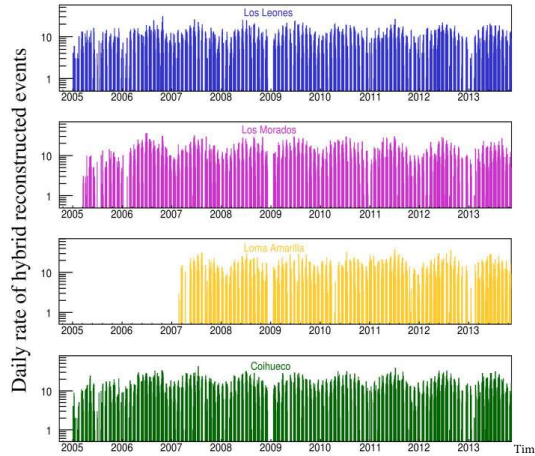


Figure B.28: Daily rate of hybrid reconstructed events as a function of year, starting in 2005, for (from top to bottom) Los Leones, Los Morados, Loma Amarilla and Coihueco, respectively.

on-time of the hybrid detector is described in detail in [232].

The accumulated on-time is shown in figure B.26 (left), for the six telescopes at Coihueco and for the three HEAT telescopes. The average FD on-time (full circles) of individual telescopes since 1 January 2011 is shown in figure B.26 (right). Requiring that the CDAS is active defines the hybrid on-time (empty circles).

The time evolution of the full hybrid duty cycle over 9 years of operation is shown in figure B.27 (left), for all FD sites. Time bins are taken as the time intervals elapsed between two subsequent FD data taking shifts. The performance of the hybrid detector is compared to the nominal DAQ time in the top panel of figure B.27. In the right-hand panel, the FD on-time is normalized to the time with high voltage ON, leading to an average FD detector readiness of about 85% for all telescopes. The remaining inefficiency can be ascribed to different factors such as bad weather conditions (high wind load and/or rain) or high variances due to bright stars/planets crossing the field of view of the FD.

It should be noted that the FD site of Los Morados became operational in May 2005, Loma Amarilla starting from March 2007 and HEAT since September 2009. After the initial phase due to the start up of the running operations, the mean on-time is about 15% for all of the FD sites. Additionally, a seasonal modulation is visible, since higher on-time fractions are observed in the austral winter during which the nights are longer.

B.8.4 Time stability of the hybrid detector response

The performance of the hybrid detector is demonstrated as a function of time using a sample of events fulfilling basic reconstruction requirements, such as a reliable geometrical reconstruction and accurate longitudinal profile and energy measurement. The daily rate of well-reconstructed hybrid events observed by individual FD sites is shown in figure B.28 as a function of time, starting in 2005.

An important benchmark for the time stability of the hybrid detector response is the study of the effective on-time, defined as the fraction of all events that are well reconstructed hybrids. Its time evolution, shown in figure B.29 (top), exhibits quite a stable behavior over time. Moreover the mean energy of the hybrid events above 10^{18} eV, with distance to the

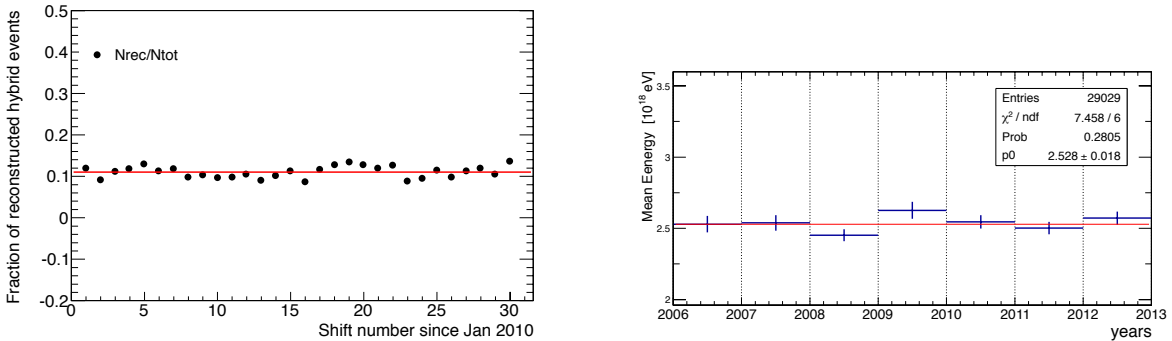


Figure B.29: *Left:* fraction of all events that are well reconstructed hybrids since 2010. *Right:* mean energy for reconstructed hybrid events.

shower maximum between 7 and 25 km (corresponding to the 90% of the entire hybrid data sample), is shown as a function of time in figure B.29 (bottom). All these features demonstrate the quality of the collected hybrid data and directly assess their long term stability.

B.9 Maintenance

Currently more than 1660 surface detector stations are operational. Concerning the water-Cherenkov detectors themselves, very few failures have been detected. Only a few liners were observed to leak shortly after installation. In this case, which constitutes the worst failure mode, the tank is emptied and brought back to the Assembly Building for replacement of the interior components. Similarly, only a few solar panels have been damaged. Solar power system parameters are recorded and analyzed using the central data acquisition system. The average battery lifetime is 4 years, and batteries are changed during regular maintenance trips.

The PMTs and electronic boards are the most critical elements of the Surface Detector stations. They are subject to very severe environmental conditions: temperature variations, humidity, salinity and dust. The failure rates of the PMTs are about 20 per year (about 0.5%). Some HV module and base problems have been detected as well as some problems due to bad connections. All other failures except those concerning the PMTs (such as broken photocathode) can be repaired on site. It is currently estimated that the number of spare PMTs is sufficient for about 10 to 15 more years of operation. The failure rate of electronic boards is about 1% per year. Some of the problems are repaired simply by reflashing the software. Most of the electronic problems can also be repaired on site. All the spare parts are stored on site.

The operation of the array is monitored on-line and alarms are set on various parameters. The maintenance goal is to have no more than 20 detector stations out of operation at any time. Currently the achieved number is less than 10 detector stations out of operation. It is currently estimated that the long-term maintenance (including the battery change) requires about 3 field trips per week. This maintenance rate is within the original expectations. The maintenance is organized by the Science Operation Coordinator and performed by local technicians. The Surface Detector Array does not require a permanent presence of physicists from other laboratories on site. However, remote shifts for the data quality monitoring will be implemented.

Bibliography

- [1] “Pierre Auger Observatory Project Management Plan.”
http://www.auger.org/admin/Management/PMP/PMP_updated_8May2013.pdf.
- [2] “Pierre Auger Observatory Project Quality Assurance Plan.”
http://auger.fnal.gov/upgrade_review/qa_plan_auger.pdf.
- [3] **Pierre Auger** Collaboration, J. Abraham *et al.*, “Observation of the suppression of the flux of cosmic rays above 4×10^{19} eV,” *Phys. Rev. Lett.* **101** (2008) 061101, [arXiv:0806.4302 \[astro-ph\]](https://arxiv.org/abs/0806.4302).
- [4] **Pierre Auger** Collaboration, J. Abraham *et al.*, “Measurement of the energy spectrum of cosmic rays above 10^{18} eV using the Pierre Auger Observatory,” *Phys. Lett. B* **685** (2010) 239–246, [arXiv:1002.1975 \[astro-ph.HE\]](https://arxiv.org/abs/1002.1975).
- [5] **Pierre Auger** Collaboration, A. Aab *et al.*, “Measurement of the cosmic ray spectrum above 4×10^{18} eV using inclined events detected with the Pierre Auger Observatory,” [arXiv:1503.07786 \[astro-ph.HE\]](https://arxiv.org/abs/1503.07786). Submitted to JCAP.
- [6] **Pierre Auger** Collaboration, J. Abraham *et al.*, “An upper limit to the photon fraction in cosmic rays above 10^{19} eV from the Pierre Auger observatory,” *Astropart. Phys.* **27** (2007) 155–168, [astro-ph/0606619](https://arxiv.org/abs/0606619).
- [7] **Pierre Auger** Collaboration, J. Abraham *et al.*, “Upper limit on the cosmic-ray photon flux above 10^{19} eV using the surface detector of the Pierre Auger Observatory,” *Astropart. Phys.* **29** (2008) 243–256, [arXiv:0712.1147 \[astro-ph\]](https://arxiv.org/abs/0712.1147).
- [8] **Pierre Auger** Collaboration, J. Abraham *et al.*, “Upper limit on the cosmic-ray photon fraction at EeV energies from the Pierre Auger Observatory,” *Astropart. Phys.* **31** (2009) 399–406, [arXiv:0903.1127 \[astro-ph.HE\]](https://arxiv.org/abs/0903.1127).
- [9] **Pierre Auger** Collaboration, M. Settimi *et al.*, “An update on a search for ultra-high energy photons using the Pierre Auger Observatory,” *Proc of 32nd Int. Cosmic Ray Conf., Beijing, China* **2** (2011) 55, [arXiv:1107.4805 \[astro-ph.HE\]](https://arxiv.org/abs/1107.4805).
- [10] **Pierre Auger** Collaboration, J. Abraham *et al.*, “Upper limit on the diffuse flux of UHE tau neutrinos from the Pierre Auger Observatory,” *Phys. Rev. Lett.* **100** (2008) 211101, [arXiv:0712.1909 \[astro-ph\]](https://arxiv.org/abs/0712.1909).
- [11] **Pierre Auger** Collaboration, P. Abreu *et al.*, “A Search for Ultra-High Energy Neutrinos in Highly Inclined Events at the Pierre Auger Observatory,” *Phys. Rev.* **D84** (2011) 122005, [arXiv:1202.1493 \[astro-ph.HE\]](https://arxiv.org/abs/1202.1493).

- [12] **Pierre Auger** Collaboration, P. Abreu *et al.*, “Search for point-like sources of ultra-high energy neutrinos at the Pierre Auger Observatory and improved limit on the diffuse flux of tau neutrinos,” *Astrophys.J.* **755** (2012) L4, [arXiv:1210.3143 \[astro-ph.HE\]](https://arxiv.org/abs/1210.3143).
- [13] **Pierre Auger** Collaboration, P. Abreu *et al.*, “Ultrahigh Energy Neutrinos at the Pierre Auger Observatory,” *Adv.High Energy Phys.* **2013** (2013) 708680, [arXiv:1304.1630 \[astro-ph.HE\]](https://arxiv.org/abs/1304.1630).
- [14] **Pierre Auger** Collaboration, A. Aab *et al.*, “Large scale distribution of ultra high energy cosmic rays detected at the Pierre Auger Observatory with zenith angles up to 80° ,” *Astrophys. J.* **802** no. 2, (2015) 111, [arXiv:1411.6953 \[astro-ph.HE\]](https://arxiv.org/abs/1411.6953).
- [15] **Pierre Auger** Collaboration, P. Abreu *et al.*, “Search for First Harmonic Modulation in the Right Ascension Distribution of Cosmic Rays Detected at the Pierre Auger Observatory,” *Astropart. Phys.* **34** (2011) 627–639, [arXiv:1103.2721 \[astro-ph.HE\]](https://arxiv.org/abs/1103.2721).
- [16] **Pierre Auger** Collaboration, P. Abreu *et al.*, “Large scale distribution of arrival directions of cosmic rays detected above 10^{18} eV at the Pierre Auger Observatory,” *Astrophys. J. Suppl.* **203** (2012) 34, [arXiv:1210.3736 \[astro-ph.HE\]](https://arxiv.org/abs/1210.3736).
- [17] **Pierre Auger** Collaboration, P. Abreu *et al.*, “Constraints on the origin of cosmic rays above 10^{18} eV from large scale anisotropy searches in data of the Pierre Auger Observatory,” *Astrophys. J.* **762** (2012) L13, [arXiv:1212.3083 \[astro-ph.HE\]](https://arxiv.org/abs/1212.3083).
- [18] **Pierre Auger** Collaboration, J. Abraham *et al.*, “Correlation of the highest energy cosmic rays with nearby extragalactic objects,” *Science* **318** (2007) 938–943, [arXiv:0711.2256 \[astro-ph\]](https://arxiv.org/abs/0711.2256).
- [19] **Pierre Auger** Collaboration, J. Abraham *et al.*, “Correlation of the highest-energy cosmic rays with the positions of nearby active galactic nuclei,” *Astropart. Phys.* **29** (2008) 188–204, [arXiv:0712.2843 \[astro-ph\]](https://arxiv.org/abs/0712.2843).
- [20] **Pierre Auger** Collaboration, P. Abreu *et al.*, “Update on the correlation of the highest energy cosmic rays with nearby extragalactic matter,” *Astropart. Phys.* **34** (2010) 314–326, [arXiv:1009.1855 \[astro-ph.HE\]](https://arxiv.org/abs/1009.1855).
- [21] **Pierre Auger** Collaboration, A. Aab *et al.*, “Searches for Anisotropies in the Arrival Directions of the Highest Energy Cosmic Rays Detected by the Pierre Auger Observatory,” [arXiv:1411.6111 \[astro-ph.HE\]](https://arxiv.org/abs/1411.6111). *Astrophys. J.* (in press).
- [22] **Pierre Auger** Collaboration, A. Aab *et al.*, “Depth of maximum of air-shower profiles at the Pierre Auger Observatory. I. Measurements at energies above $10^{17.8}$ eV,” *Phys. Rev. D* **90** no. 12, (2014) 122005, [arXiv:1409.4809 \[astro-ph.HE\]](https://arxiv.org/abs/1409.4809).
- [23] **Pierre Auger** Collaboration, A. Aab *et al.*, “Depth of maximum of air-shower profiles at the Pierre Auger Observatory. II. Composition implications,” *Phys. Rev. D* **90** no. 12, (2014) 122006, [arXiv:1409.5083 \[astro-ph.HE\]](https://arxiv.org/abs/1409.5083).
- [24] **Pierre Auger** Collaboration, P. Abreu *et al.*, “Measurement of the proton-air cross-section at $\sqrt{s} = 57$ TeV with the Pierre Auger Observatory,” *Phys. Rev. Lett.* **109** (2012) 062002, [arXiv:1208.1520 \[hep-ex\]](https://arxiv.org/abs/1208.1520).

- [25] **Pierre Auger** Collaboration, G. R. Farrar, “The muon content of hybrid events recorded at the Pierre Auger Observatory,” *Proc. of 33rd Int. Cosmic Ray Conf., Rio de Janeiro, Brazil*, #1108 (2013) , [arXiv:1307.5059](https://arxiv.org/abs/1307.5059) [astro-ph.HE].
- [26] **Pierre Auger** Collaboration, A. Aab *et al.*, “Muons in air showers at the Pierre Auger Observatory: Mean number in highly inclined events,” *Phys.Rev.D* (2014) , [arXiv:1408.1421](https://arxiv.org/abs/1408.1421) [astro-ph.HE].
- [27] **Pierre Auger** Collaboration, A. Schulz, “The measurement of the energy spectrum of cosmic rays above 3×10^{17} eV with the Pierre Auger Observatory,” *Proc. of 33rd Int. Cosmic Ray Conf., Rio de Janeiro, Brazil*, #0769 (2013) , [arXiv:1307.5059](https://arxiv.org/abs/1307.5059) [astro-ph.HE].
- [28] E. Armengaud, G. Sigl, T. Beau, and F. Miniati, “CRPropa: A numerical tool for the propagation of UHE cosmic rays, gamma-rays and neutrinos,” *Astropart. Phys.* **28** (2007) 463–471, [arXiv:astro-ph/0603675](https://arxiv.org/abs/0603675).
- [29] K.-H. Kampert, J. Kulbartz, L. Maccione, N. Nierstenhoefer, P. Schiffer, *et al.*, “CRPropa 2.0 – a Public Framework for Propagating High Energy Nuclei, Secondary Gamma Rays and Neutrinos,” *Astropart. Phys.* **42** (2013) 41–51, [arXiv:1206.3132](https://arxiv.org/abs/1206.3132) [astro-ph.IM].
- [30] R. Aloisio, D. Boncioli, A. Grillo, S. Petrera, and F. Salamida, “SimProp: a Simulation Code for Ultra High Energy Cosmic Ray Propagation,” *JCAP* **1210** (2012) 007, [arXiv:1204.2970](https://arxiv.org/abs/1204.2970) [astro-ph.HE].
- [31] **Pierre Auger** Collaboration, D. Ravignani, “Measurement of the energy spectrum of cosmic rays above 3×10^{17} eV using the AMIGA 750 m surface detector array of the Pierre Auger Observatory,” *Proc. of 33rd Int. Cosmic Ray Conf., Rio de Janeiro, Brazil*, #0693 (2013) , [arXiv:1307.5059](https://arxiv.org/abs/1307.5059) [astro-ph.HE].
- [32] **Pierre Auger** Collaboration, V. Verzi, “The Energy Scale of the Pierre Auger Observatory,” *Proc. of 33rd Int. Cosmic Ray Conf., Rio de Janeiro, Brazil*, #0928 (2013) , [arXiv:1307.5059](https://arxiv.org/abs/1307.5059) [astro-ph.HE].
- [33] R. J. Protheroe and P. A. Johnson, “Propagation of ultrahigh-energy protons over cosmological distances and implications for topological defect models,” *Astropart. Phys.* **4** (1996) 253, [arXiv:astro-ph/9506119](https://arxiv.org/abs/astro-ph/9506119).
- [34] T. Stanev, R. Engel, A. Mücke, R. J. Protheroe, and J. P. Rachen, “Propagation of ultra-high energy protons in the nearby universe,” *Phys. Rev.* **D62** (2000) 093005, [astro-ph/0003484](https://arxiv.org/abs/astro-ph/0003484).
- [35] V. Berezinsky, A. Z. Gazizov, and S. I. Grigorieva, “On astrophysical solution to ultra high energy cosmic rays,” *Phys. Rev.* **D74** (2006) 043005, [hep-ph/0204357](https://arxiv.org/abs/hep-ph/0204357).
- [36] L. Anchordoqui, T. Paul, S. Reucroft, and J. Swain, “Ultrahigh energy cosmic rays: The state of the art before the Auger observatory,” *Int. J. Mod. Phys.* **A18** (2003) 2229–2366, [hep-ph/0206072](https://arxiv.org/abs/hep-ph/0206072).

- [37] D. Hooper and A. M. Taylor, “On The Heavy Chemical Composition of the Ultra-High Energy Cosmic Rays,” *Astropart. Phys.* **33** (2010) 151–159, [arXiv:0910.1842 \[astro-ph.HE\]](https://arxiv.org/abs/0910.1842).
- [38] **Telescope Array** Collaboration, P. Tinyakov, “Latest results from the telescope array,” *Nucl. Instrum. Meth.* **A742** (2014) 29–34.
- [39] **Telescope Array** Collaboration, T. Abu-Zayyad, R. Aida, M. Allen, R. Anderson, R. Azuma, *et al.*, “The Cosmic Ray Energy Spectrum Observed with the Surface Detector of the Telescope Array Experiment,” *Astrophys. J.* **768** (2013) L1, [arXiv:1205.5067 \[astro-ph.HE\]](https://arxiv.org/abs/1205.5067).
- [40] **HiRes** Collaboration, R. U. Abbasi *et al.*, “First Observation of the Greisen-Zatsepin-Kuzmin Suppression,” *Phys. Rev. Lett.* **100** (2008) 101101, [astro-ph/0703099](https://arxiv.org/abs/0703099).
- [41] **Pierre Auger** Collaboration, P. Pieroni, “Ultra-high energy neutrinos at the Pierre Auger Observatory,” *Proc. of 33rd Int. Cosmic Ray Conf., Rio de Janeiro, Brazil*, #0697 (2013), [arXiv:1307.5059 \[astro-ph.HE\]](https://arxiv.org/abs/1307.5059).
- [42] **IceCube** Collaboration, M. Aartsen *et al.*, “Probing the origin of cosmic-rays with extremely high energy neutrinos using the IceCube Observatory,” *Phys. Rev.* **D88** (2013) 112008, [arXiv:1310.5477 \[astro-ph.HE\]](https://arxiv.org/abs/1310.5477).
- [43] **ANITA** Collaboration, P. Gorham *et al.*, “New Limits on the Ultra-high Energy Cosmic Neutrino Flux from the ANITA Experiment,” *Phys. Rev. Lett.* **103** (2009) 051103, [arXiv:0812.2715 \[astro-ph\]](https://arxiv.org/abs/0812.2715).
- [44] **ANITA** Collaboration, P. Gorham *et al.*, “The Antarctic Impulsive Transient Antenna Ultra-high Energy Neutrino Detector Design, Performance, and Sensitivity for 2006-2007 Balloon Flight,” *Astropart. Phys.* **32** (2009) 10–41, [arXiv:0812.1920 \[astro-ph\]](https://arxiv.org/abs/0812.1920).
- [45] **ANITA** Collaboration, P. Gorham *et al.*, “Erratum: Observational Constraints on the Ultra-high Energy Cosmic Neutrino Flux from the Second Flight of the ANITA Experiment,” *Phys. Rev.* **D85** (2012) 049901, [arXiv:1011.5004 \[astro-ph.HE\]](https://arxiv.org/abs/1011.5004).
- [46] **RICE** Collaboration, I. Kravchenko, S. Hussain, D. Seckel, D. Besson, E. Fensholt, *et al.*, “Updated Results from the RICE Experiment and Future Prospects for Ultra-High Energy Neutrino Detection at the South Pole,” *Phys. Rev.* **D85** (2012) 062004, [arXiv:1106.1164 \[astro-ph.HE\]](https://arxiv.org/abs/1106.1164).
- [47] **HiRes** Collaboration, R. U. Abbasi *et al.*, “An upper limit on the electron-neutrino flux from the HiRes detector,” *Astrophys. J.* **684** (2008) 790, [arXiv:0803.0554 \[astro-ph\]](https://arxiv.org/abs/0803.0554).
- [48] **Telescope Array** Collaboration, T. Abu-Zayyad *et al.*, “Upper limit on the flux of photons with energies above 10^{19} eV using the Telescope Array surface detector,” *Phys. Rev.* **D88** (2013) 112005, [arXiv:1304.5614 \[astro-ph.HE\]](https://arxiv.org/abs/1304.5614).
- [49] P. Bhattacharjee and G. Sigl, “Origin and propagation of extremely high energy cosmic rays,” *Phys. Rept.* **327** (2000) 109–247, [astro-ph/9811011](https://arxiv.org/abs/astro-ph/9811011).

- [50] M. Ahlers, L. Anchordoqui, M. Gonzalez-Garcia, F. Halzen, and S. Sarkar, “GZK Neutrinos after the Fermi-LAT Diffuse Photon Flux Measurement,” *Astropart. Phys.* **34** (2010) 106–115, [arXiv:1005.2620 \[astro-ph.HE\]](https://arxiv.org/abs/1005.2620).
- [51] K. Kotera, D. Allard, and A. Olinto, “Cosmogenic Neutrinos: parameter space and detectability from PeV to ZeV,” *JCAP* **1010** (2010) 013, [arXiv:1009.1382 \[astro-ph.HE\]](https://arxiv.org/abs/1009.1382).
- [52] K.-H. Kampert and M. Unger, “Measurements of the Cosmic Ray Composition with Air Shower Experiments,” *Astropart. Phys.* **35** (2012) 660–678, [arXiv:1201.0018 \[astro-ph.HE\]](https://arxiv.org/abs/1201.0018).
- [53] G. Gelmini, O. Kalashev, and D. V. Semikoz, “GZK Photons as Ultra High Energy Cosmic Rays,” *J. Exp. Theor. Phys.* **106** (2008) 1061–1082, [arXiv:astro-ph/0506128](https://arxiv.org/abs/astro-ph/0506128).
- [54] J. R. Ellis, V. E. Mayes, and D. V. Nanopoulos, “UHECR Particle Spectra from Crypton Decays,” *Phys. Rev.* **D74** (2006) 115003, [arXiv:astro-ph/0512303](https://arxiv.org/abs/astro-ph/0512303).
- [55] G. Sigl, S. Lee, P. Bhattacharjee, and S. Yoshida, “Probing grand unified theories with cosmic ray, gamma-ray and neutrino astrophysics,” *Phys. Rev.* **D59** (1998) 043504, [arXiv:hep-ph/9809242 \[hep-ph\]](https://arxiv.org/abs/hep-ph/9809242).
- [56] O. E. Kalashev, G. I. Rubtsov, and S. V. Troitsky, “Sensitivity of cosmic-ray experiments to ultra-high-energy photons: reconstruction of the spectrum and limits on the superheavy dark matter,” *Phys. Rev.* **D80** (2009) 103006, [arXiv:0812.1020 \[astro-ph\]](https://arxiv.org/abs/0812.1020).
- [57] E. Waxman and J. N. Bahcall, “High energy neutrinos from astrophysical sources: An upper bound,” *Phys. Rev.* **D59** (1999) 023002, [hep-ph/9807282](https://arxiv.org/abs/hep-ph/9807282).
- [58] J. N. Bahcall and E. Waxman, “High energy astrophysical neutrinos: The upper bound is robust,” *Phys. Rev.* **D64** (2001) 023002, [hep-ph/9902383](https://arxiv.org/abs/hep-ph/9902383).
- [59] M. Risse and P. Homola, “Search for ultra-high energy photons using air showers,” *Mod. Phys. Lett.* **A22** (2007) 749–766, [astro-ph/0702632](https://arxiv.org/abs/astro-ph/0702632).
- [60] M. Galaverni and G. Sigl, “Lorentz Violation and Ultrahigh-Energy Photons,” *Phys. Rev.* **D78** (2008) 063003, [arXiv:0807.1210 \[astro-ph\]](https://arxiv.org/abs/0807.1210).
- [61] M. Galaverni and G. Sigl, “Lorentz Violation in the Photon Sector and Ultra-High Energy Cosmic Rays,” *Phys. Rev. Lett.* **100** (2008) 021102, [arXiv:0708.1737 \[astro-ph\]](https://arxiv.org/abs/0708.1737).
- [62] S. Liberati and L. Maccione, “Quantum Gravity phenomenology: achievements and challenges,” *J. Phys. Conf. Ser.* **314** (2011) 012007, [arXiv:1105.6234 \[astro-ph.HE\]](https://arxiv.org/abs/1105.6234).
- [63] R. Horvat, D. Kekez, and J. Trampetic, “Spacetime noncommutativity and ultra-high energy cosmic ray experiments,” *Phys. Rev.* **D83** (2011) 065013, [arXiv:1005.3209 \[hep-ph\]](https://arxiv.org/abs/1005.3209).
- [64] F. Klinkhamer, “Potential sensitivities to Lorentz violation from nonbirefringent modified-Maxwell theory of Auger, HESS, and CTA,” *Phys. Rev.* **D82** (2010) 105024, [arXiv:1008.1967 \[hep-ph\]](https://arxiv.org/abs/1008.1967).

- [65] F. Girelli, F. Hinterleitner, and S. Major, “Loop Quantum Gravity Phenomenology: Linking Loops to Observational Physics,” *SIGMA* **8** (2012) 098, [arXiv:1210.1485 \[gr-qc\]](https://arxiv.org/abs/1210.1485).
- [66] G. Rubtsov, P. Satunin, and S. Sibiryakov, “Prospective constraints on Lorentz violation from ultrahigh-energy photon detection,” *Phys. Rev.* **D89** no. 12, (2014) 123011, [arXiv:1312.4368 \[astro-ph.HE\]](https://arxiv.org/abs/1312.4368).
- [67] D. M. Mattingly, L. Maccione, M. Galaverni, S. Liberati, and G. Sigl, “Possible cosmogenic neutrino constraints on Planck-scale Lorentz violation,” *JCAP* **1002** (2010) 007, [arXiv:0911.0521 \[hep-ph\]](https://arxiv.org/abs/0911.0521).
- [68] **Pierre Auger** Collaboration, A. Aab *et al.*, “Muons in air showers at the Pierre Auger Observatory: Measurement of atmospheric production depth,” *Phys. Rev.* **D90** (2014) 012012, [arXiv:1407.5919 \[hep-ex\]](https://arxiv.org/abs/1407.5919).
- [69] **Pierre Auger** Collaboration, P. Abreu *et al.*, “The Pierre Auger Observatory II: Studies of Cosmic Ray Composition and Hadronic Interaction models,” *Proc of 32nd Int. Cosmic Ray Conf., Beijing, China* (2011), [arXiv:1107.4804 \[astro-ph.HE\]](https://arxiv.org/abs/1107.4804).
- [70] **Pierre Auger** Collaboration, J. Abraham *et al.*, “Measurement of the Depth of Maximum of Extensive Air Showers above 10^{18} eV,” *Phys. Rev. Lett.* **104** (2010) 091101, [arXiv:1002.0699 \[astro-ph.HE\]](https://arxiv.org/abs/1002.0699).
- [71] R. Engel, D. Heck, and T. Pierog, “Extensive air showers and hadronic interactions at high energy,” *Ann. Rev. Nucl. Part. Sci.* **61** (2011) 467–489.
- [72] **Pierre Auger** Collaboration, P. Abreu *et al.*, “Interpretation of the Depths of Maximum of Extensive Air Showers Measured by the Pierre Auger Observatory,” *JCAP* **1302** (2013) 026, [arXiv:1301.6637 \[astro-ph.HE\]](https://arxiv.org/abs/1301.6637).
- [73] K. Werner, F.-M. Liu, and T. Pierog, “Parton ladder splitting and the rapidity dependence of transverse momentum spectra in deuteron gold collisions at RHIC,” *Phys. Rev.* **C74** (2006) 044902, [hep-ph/0506232](https://arxiv.org/abs/hep-ph/0506232).
- [74] T. Pierog and K. Werner, “Muon Production in Extended Air Shower Simulations,” *Phys. Rev. Lett.* **101** (2008) 171101, [astro-ph/0611311](https://arxiv.org/abs/0611311).
- [75] S. Ostapchenko, “Monte Carlo treatment of hadronic interactions in enhanced Pomeron scheme: I. QGSJET-II model,” *Phys. Rev.* **D83** (2011) 014018, [arXiv:1010.1869 \[hep-ph\]](https://arxiv.org/abs/1010.1869).
- [76] E.-J. Ahn, R. Engel, T. K. Gaisser, P. Lipari, and T. Stanev, “Cosmic ray interaction event generator SIBYLL 2.1,” *Phys. Rev. D* **80** (2009) 094003, [arXiv:0906.4113 \[hep-ph\]](https://arxiv.org/abs/0906.4113).
- [77] T. Pierog, I. Karpenko, J. Katzy, E. Yatsenko, and K. Werner, “EPOS LHC : test of collective hadronization with LHC data,” [arXiv:1306.0121 \[hep-ph\]](https://arxiv.org/abs/1306.0121).
- [78] S. Ostapchenko, “LHC data on inelastic diffraction and uncertainties in the predictions for longitudinal EAS development,” *Phys. Rev.* **D89** (2014) 074009, [arXiv:1402.5084 \[hep-ph\]](https://arxiv.org/abs/1402.5084).

- [79] D. d'Enterria, R. Engel, T. Pierog, S. Ostapchenko, and K. Werner, "Constraints from the first LHC data on hadronic event generators for ultra-high energy cosmic-ray physics," *Astropart. Phys.* **35** (2011) 98–113, [arXiv:1101.5596 \[astro-ph.HE\]](https://arxiv.org/abs/1101.5596).
- [80] J. Dias de Deus, M. C. Espirito Santo, M. Pimenta, and C. Pajares, "Percolation effects in very high energy cosmic rays," *Phys. Rev. Lett.* **96** (2006) 162001, [arXiv:hep-ph/0507227](https://arxiv.org/abs/hep-ph/0507227).
- [81] T. Wibig, "Ultra high-energy cosmic ray proton interactions," *Phys. Lett. B* **678** (2009) 60–64.
- [82] J. Allen and G. Farrar, "Testing models of new physics with UHE air shower observations," [arXiv:1307.7131 \[astro-ph.HE\]](https://arxiv.org/abs/1307.7131).
- [83] **HiRes** Collaboration, R. U. Abbasi *et al.*, "A study of the composition of ultra high energy cosmic rays using the High Resolution Fly's Eye," *Astrophys. J.* **622** (2005) 910–926, [astro-ph/0407622](https://arxiv.org/abs/astro-ph/0407622).
- [84] **Telescope Array** Collaboration, R. Abbasi, M. Abe, T. Abu-Zayyad, M. Allen, R. Anderson, *et al.*, "Study of Ultra-High Energy Cosmic Ray composition using Telescope Array's Middle Drum detector and surface array in hybrid mode," *Astropart. Phys.* **64** (2014) 49–62, [arXiv:1408.1726 \[astro-ph.HE\]](https://arxiv.org/abs/1408.1726).
- [85] **Pierre Auger, Telescope Array, and Yakutsk** Collaboration, E. Barcikowski *et al.*, "Mass Composition Working Group Report at UHECR-2012," *EPJ Web Conf.* **53** (2013) 01006, [arXiv:1306.4430 \[astro-ph.HE\]](https://arxiv.org/abs/1306.4430).
- [86] **Pierre Auger and Telescope Array** Collaboration, R. Abbasi *et al.*, "Report of the Working Group on the Composition of Ultra High Energy Cosmic Rays," [arXiv:1503.07540 \[astro-ph.HE\]](https://arxiv.org/abs/1503.07540).
- [87] D. Harari, S. Mollerach, and E. Roulet, "Anisotropies of ultrahigh energy cosmic rays diffusing from extragalactic sources," *Phys. Rev. D* **89** no. 12, (2014) 123001, [arXiv:1312.1366 \[astro-ph.HE\]](https://arxiv.org/abs/1312.1366).
- [88] **Pierre Auger** Collaboration, I. Sidelnik, "Measurement of the first harmonic modulation in the right ascension distribution of cosmic rays detected at the Pierre Auger Observatory: towards the detection of dipolar anisotropies over a wide energy range," *Proc. of 33rd Int. Cosmic Ray Conf., Rio de Janeiro, Brazil*, #0739 (2013), [arXiv:1307.5059 \[astro-ph.HE\]](https://arxiv.org/abs/1307.5059).
- [89] J. Linsley, "Fluctuation effects on directional data," *Phys. Rev. Lett.* **34** (1975) 1530–1533.
- [90] R. Bonino, V. Alekseenko, O. Deligny, P. Ghia, M. Grigat, *et al.*, "The East-West method: an exposure-independent method to search for large scale anisotropies of cosmic rays," *Astrophys. J.* **738** (2011) 67, [arXiv:1106.2651 \[astro-ph.IM\]](https://arxiv.org/abs/1106.2651).
- [91] **Telescope Array** Collaboration, R. Abbasi *et al.*, "Indications of Intermediate-Scale Anisotropy of Cosmic Rays with Energy Greater Than 57 EeV in the Northern Sky Measured with the Surface Detector of the Telescope Array Experiment," *Astrophys. J.* **790** (2014) L21, [arXiv:1404.5890 \[astro-ph.HE\]](https://arxiv.org/abs/1404.5890).

- [92] R. Ulrich, J. Blümer, R. Engel, F. Schüssler, and M. Unger, “On the measurement of the proton-air cross section using air shower data,” *New J. Phys.* **11** (2009) 065018, [arXiv:0903.0404 \[astro-ph.HE\]](https://arxiv.org/abs/0903.0404).
- [93] R. J. Glauber and G. Matthiae, “High-energy scattering of protons by nuclei,” *Nucl. Phys.* **B21** (1970) 135–157.
- [94] R. Ulrich, R. Engel, and M. Unger, “Hadronic Multiparticle Production at Ultra-High Energies and Extensive Air Showers,” *Phys. Rev.* **D83** (2011) 054026, [arXiv:1010.4310 \[hep-ph\]](https://arxiv.org/abs/1010.4310).
- [95] **Pierre Auger** Collaboration, B. Kegl, “Measurement of the muon signal using the temporal and spectral structure of the signals in surface detectors of the Pierre Auger Observatory,” *Proc. of 33rd Int. Cosmic Ray Conf., Rio de Janeiro, Brazil*, #0860 (2013), [arXiv:1307.5059 \[astro-ph.HE\]](https://arxiv.org/abs/1307.5059).
- [96] L. Cazon, R. A. Vazquez, and E. Zas, “Depth development of extensive air showers from muon time distributions,” *Astropart. Phys.* **23** (2005) 393–409, [astro-ph/0412338](https://arxiv.org/abs/astro-ph/0412338).
- [97] M. Ave, R. Vazquez, and E. Zas, “Modeling horizontal air showers induced by cosmic rays,” *Astropart. Phys.* **14** (2000) 91, [arXiv:astro-ph/0011490 \[astro-ph\]](https://arxiv.org/abs/astro-ph/0011490).
- [98] I. Valino, J. Alvarez-Muniz, M. Roth, R. Vazquez, and E. Zas, “Characterisation of the electromagnetic component in ultra-high energy inclined air showers,” *Astropart. Phys.* **32** (2010) 304–317, [arXiv:0910.2873 \[astro-ph.HE\]](https://arxiv.org/abs/0910.2873).
- [99] **Telescope Array** Collaboration, H. Sagawa highlight talk given at 33rd Int. Cosmic Ray Conf., Rio de Janeiro, Brazil, 2013.
- [100] **Pierre Auger, Telescope Array, and Yakutsk** Collaboration, J. Allen *et al.*, “Air Shower Simulation and Hadronic Interactions,” *EPJ Web Conf.* **53** (2013) 01007, [arXiv:1306.6090 \[astro-ph.HE\]](https://arxiv.org/abs/1306.6090).
- [101] V. S. Berezinsky, S. I. Grigorieva, and B. I. Hnatyk, “Extragalactic UHE proton spectrum and prediction for iron- nuclei flux at 10^8GeV to 10^9GeV ,” *Astropart. Phys.* **21** (2004) 617–625, [astro-ph/0403477](https://arxiv.org/abs/astro-ph/0403477).
- [102] T. Wibig and A. W. Wolfendale, “At what particle energy do extragalactic cosmic rays start to predominate?” *J. Phys.* **G31** (2005) 255–264, [astro-ph/0410624](https://arxiv.org/abs/astro-ph/0410624).
- [103] A. M. Hillas, “Can diffusive shock acceleration in supernova remnants account for high-energy galactic cosmic rays?,” *J. Phys.* **G31** (2005) R95–R131.
- [104] D. Allard, E. Parizot, E. Khan, S. Goriely, and A. V. Olinto, “UHE nuclei propagation and the interpretation of the ankle in the cosmic-ray spectrum,” *Astron. Astrophys.* **443** (2005) L29–L32, [astro-ph/0505566](https://arxiv.org/abs/astro-ph/0505566).
- [105] K. Greisen, “End to the cosmic ray spectrum?,” *Phys. Rev. Lett.* **16** (1966) 748–750.
- [106] G. T. Zatsepin and V. A. Kuzmin, “Upper Limit of the Spectrum of Cosmic Rays,” *J. Exp. Theor. Phys. Lett.* **4** (1966) 78.

- [107] D. Allard, "Extragalactic propagation of ultrahigh energy cosmic-rays," *Astropart. Phys.* **39-40** (2012) 33–43, [arXiv:1111.3290 \[astro-ph.HE\]](https://arxiv.org/abs/1111.3290).
- [108] T. K. Gaisser, T. Stanev, and S. Tilav, "Cosmic Ray Energy Spectrum from Measurements of Air Showers," *Front. Phys. China* **8** (2013) 748–758, [arXiv:1303.3565 \[astro-ph.HE\]](https://arxiv.org/abs/1303.3565).
- [109] K. Fang, K. Kotera, and A. V. Olinto, "Ultrahigh Energy Cosmic Ray Nuclei from Extragalactic Pulsars and the effect of their Galactic counterparts," *JCAP* **1303** (2013) 010, [arXiv:1302.4482 \[astro-ph.HE\]](https://arxiv.org/abs/1302.4482).
- [110] J. Candia, S. Mollerach, and E. Roulet, "Cosmic ray spectrum and anisotropies from the knee to the second knee," *JCAP* **0305** (2003) 003, [astro-ph/0302082](https://arxiv.org/abs/astro-ph/0302082).
- [111] G. Giacinti, M. Kachelriess, D. Semikoz, and G. Sigl, "Cosmic Ray Anisotropy as Signature for the Transition from Galactic to Extragalactic Cosmic Rays," *JCAP* **1207** (2012) 031, [arXiv:1112.5599 \[astro-ph.HE\]](https://arxiv.org/abs/1112.5599).
- [112] A. M. Taylor, "UHECR Composition Models," *Astropart. Phys.* **54** (2014) 48–53, [arXiv:1401.0199 \[astro-ph.HE\]](https://arxiv.org/abs/1401.0199).
- [113] R. Aloisio, V. Berezinsky, and P. Blasi, "Ultra high energy cosmic rays: implications of Auger data for source spectra and chemical composition," *JCAP* **1410** no. 10, (2014) 020, [arXiv:1312.7459 \[astro-ph.HE\]](https://arxiv.org/abs/1312.7459).
- [114] K.-H. Kampert and P. Tinyakov, "Cosmic rays from the ankle to the cutoff," *Comptes Rendus Physique* **15** (2014) 318–328, [arXiv:1405.0575 \[astro-ph.HE\]](https://arxiv.org/abs/1405.0575).
- [115] D. Allard, N. G. Busca, G. Decerprit, A. V. Olinto, and E. Parizot, "Implications of the cosmic ray spectrum for the mass composition at the highest energies," *JCAP* **0810** (2008) 033, [arXiv:0805.4779 \[astro-ph\]](https://arxiv.org/abs/0805.4779).
- [116] A. M. Taylor, M. Ahlers, and F. A. Aharonian, "The need for a local source of UHE CR nuclei," *Phys. Rev.* **D84** (2011) 105007, [arXiv:1107.2055 \[astro-ph.HE\]](https://arxiv.org/abs/1107.2055).
- [117] V. Berezinsky, A. Z. Gazizov, and S. I. Grigorieva, "Dip in UHECR spectrum as signature of proton interaction with CMB," *Phys. Lett.* **B612** (2005) 147–153, [astro-ph/0502550](https://arxiv.org/abs/astro-ph/0502550).
- [118] N. Shaham and T. Piran, "Implications of the Penetration Depth of Ultrahigh-Energy Cosmic Rays on Physics at 100 TeV," *Phys. Rev. Lett.* **110** (2013) 021101, [arXiv:1204.1488 \[astro-ph.HE\]](https://arxiv.org/abs/1204.1488).
- [119] A. Calvez, A. Kusenko, and S. Nagataki, "Role of Galactic sources and magnetic fields in forming the observed energy-dependent composition of ultrahigh-energy cosmic rays," *Phys. Rev. Lett.* **105** (2010) 091101, [arXiv:1004.2535 \[astro-ph.HE\]](https://arxiv.org/abs/1004.2535).
- [120] K. Kotera, "Ultrahigh energy cosmic ray acceleration in newly born magnetars and their associated gravitational wave signatures," *Phys. Rev.* **D84** (2011) 023002, [arXiv:1106.3060 \[astro-ph.HE\]](https://arxiv.org/abs/1106.3060).

- [121] P. L. Biermann and V. de Souza, “Centaurus A: the one extragalactic source of cosmic rays with energies above the knee,” *Astrophys. J.* **746** (2012) 72, [arXiv:1106.0625 \[astro-ph.HE\]](https://arxiv.org/abs/1106.0625).
- [122] G. R. Farrar and J. D. Allen, “A new physical phenomenon in ultra-high energy collisions,” *EPJ Web Conf.* **53** (2013) 07007, [arXiv:1307.2322 \[hep-ph\]](https://arxiv.org/abs/1307.2322).
- [123] F. R. Klinkhamer and M. Schreck, “New two-sided bound on the isotropic Lorentz-violating parameter of modified Maxwell theory,” *Phys. Rev. D* **78** (Oct, 2008) 085026. <http://link.aps.org/doi/10.1103/PhysRevD.78.085026>.
- [124] F. R. Klinkhamer and M. Risse, “Ultrahigh-energy cosmic-ray bounds on nonbirefringent modified Maxwell theory,” *Phys. Rev. D* **77** (Jan, 2008) 016002. <http://link.aps.org/doi/10.1103/PhysRevD.77.016002>.
- [125] F. Schmidt, M. Ave, L. Cazon, and A. S. Chou, “A Model-Independent Method of Determining Energy Scale and Muon Number in Cosmic Ray Surface Detectors,” *Astropart. Phys.* **29** (2008) 355–365, [arXiv:0712.3750 \[astro-ph\]](https://arxiv.org/abs/0712.3750).
- [126] S. Lafebre, R. Engel, H. Falcke, J. Hörandel, T. Huege, J. Kuijpers, and R. Ulrich, “Universality of electron-positron distributions in extensive air showers,” *Astropart. Phys.* **31** (2009) 243–254, [arXiv:0902.0548 \[astro-ph.HE\]](https://arxiv.org/abs/0902.0548).
- [127] M. Ave, R. Engel, J. Gonzalez, D. Heck, T. Pierog, and M. Roth, “Extensive Air Shower Universality of Ground Particle Distributions,” *Proc. of 31st Int. Cosmic Ray Conf., Beijing* (2011) #1025.
- [128] P. Lipari, “The Concepts of ‘Age’ and ‘Universality’ in Cosmic Ray Showers,” *Phys. Rev.* **79** (2008) 063001, [arXiv:0809.0190 \[astro-ph\]](https://arxiv.org/abs/0809.0190).
- [129] A. M. Hillas, “Angular and energy distributions of charged particles in electron photon cascades in air,” *J. Phys.* **G8** (1982) 1461–1473.
- [130] M. Giller, A. Kacperczyk, J. Malinowski, W. Tkaczyk, and G. Wieczorek, “Similarity of extensive air showers with respect to the shower age,” *J. Phys.* **G31** (2005) 947–958.
- [131] F. Nerling, J. Bluemer, R. Engel, and M. Risse, “Universality of electron distributions in high-energy air showers: Description of Cherenkov light production,” *Astropart. Phys.* **24** (2006) 421–437, [arXiv:astro-ph/0506729 \[astro-ph\]](https://arxiv.org/abs/astro-ph/0506729).
- [132] D. Maurel, M. Ave, J. Gonzalez, and M. Roth, “Universality of the time structure of ground particle distributions and its application to the reconstruction of extensive air showers,” *Proc. of 33rd Int. Cosmic Ray Conf., Rio de Janeiro, Brazil*, #600 (2013) .
- [133] B. Sarkar, K. Kampert, J. Kulbartz, L. Maccione, N. Nierstenhoefer, and G. Sigl *Proc. of 32rd Int. Cosmic Ray Conf., Beijing, China*, #1087 (2011) .
- [134] J. K. Becker, “High-energy neutrinos in the context of multimessenger physics,” *Phys. Rept.* **458** (2008) 173–246, [arXiv:0710.1557 \[astro-ph\]](https://arxiv.org/abs/0710.1557).
- [135] A. Letessier-Selvon, P. Billoir, M. Blanco, I. C. Mariş, and M. Settimi, “Layered water Cherenkov detector for the study of ultra high energy cosmic rays,” *Nucl. Instrum. Meth.* **A767** (2014) 41–49, [arXiv:1405.5699 \[astro-ph.IM\]](https://arxiv.org/abs/1405.5699).

- [136] **Pierre Auger** Collaboration, D. Veberič, “Estimation of the Total Signals in Saturated Stations of the Pierre Auger Observatory,” [233], p. 23. [arXiv:1307.5059](https://arxiv.org/abs/1307.5059) [[astro-ph.HE](#)].
- [137] D. Newton, J. Knapp, and A. A. Watson, “The optimum distance at which to determine the size of a giant air shower,” *Astropart. Phys.* **26** (2007) 414–419, [astro-ph/0608118](https://arxiv.org/abs/0608118).
- [138] **Pierre Auger** Collaboration, A. Schulz, “Measurement of the Energy Spectrum of Cosmic Rays above 3×10^{17} eV with the Pierre Auger Observatory,” [233], p. 27. [arXiv:1307.5059](https://arxiv.org/abs/1307.5059) [[astro-ph.HE](#)].
- [139] M. Veron-Cetty and P. Veron *Astron. Astrophys.* **455** (2006) 773–777.
- [140] W. Baumgartner, J. Tueller, C. Markwardt, G. Skinner, S. Barthelmy, *et al.*, “The 70 Month Swift-BAT All-Sky Hard X-Ray Survey,” *Astrophys. J. Suppl.* **207** (2013) 19, [arXiv:1212.3336](https://arxiv.org/abs/1212.3336) [[astro-ph.HE](#)].
- [141] M. Aglietta *et al.*, “Comparison of the performances of the PS2010/12 and A7501P DC-DC converters,” *Pierre Auger Observatory technical note GAP2015-026* (2015) . Available for reviewers at http://auger.fnal.gov/upgrade_review/.
- [142] D. Michael *et al.*, “The magnetized steel and scintillator calorimeters of the MINOS experiment,” *Nucl. Instrum. Meth.* **A596** no. 2, (2008) 190 – 228.
- [143] D. Beznosko, A. Bross, A. Dyshkant, A. Pla-Dalmau, and V. Rykalin, “FNAL-NICADD extruded scintillator,” *IEEE Nuclear Science Symposium* (2004) .
- [144] A. Dyshkant, D. Beznosko, G. Blazey, D. Chakraborty, K. Francis, *et al.*, “About NICADD extruded scintillating strips.” <http://inspirehep.net/record/682730/files/pub-05-010.pdf>.
- [145] M. Aglietta *et al.*, “Qualification of extruded plastic scintillators and WLS fibers,” *Pierre Auger Observatory technical note GAP2015-005* (2015) . Available for reviewers at http://auger.fnal.gov/upgrade_review/.
- [146] “Geant4.” <https://geant4.cern.ch>.
- [147] D. Heck, G. Schatz, T. Thouw, J. Knapp, and J. Capdevielle, “CORSIKA: A Monte Carlo code to simulate extensive air showers,” *Forschungszentrum Karlsruhe - Wissenschaftliche Berichte* (1998) . downloads and manuals to the software can be found at <https://web.ipk.kit.edu/corsika/>.
- [148] “SD electronics H/W Specifications.” https://atrium.in2p3.fr/nuxeo/nxdoc/default/90879bec-97c3-4dbc-a200-bfa7ec7bb231/view_documents.
- [149] “i-Lotus GPS.” http://www.ilotus.com.sg/m12m_timing_oncore/.
- [150] “SD electronics Quality Management Plan.” https://atrium.in2p3.fr/nuxeo/nxdoc/default/90879bec-97c3-4dbc-a200-bfa7ec7bb231/view_documents.
- [151] “SD electronics Tests and Verification Plan.” https://atrium.in2p3.fr/nuxeo/nxdoc/default/90879bec-97c3-4dbc-a200-bfa7ec7bb231/view_documents.

- [152] **Pierre Auger** Collaboration, F. Suarez, “The AMIGA muon detectors of the Pierre Auger Observatory: overview and status,” [233], p. 4. [arXiv:1307.5059](https://arxiv.org/abs/1307.5059) [astro-ph.HE].
- [153] K. Becker, A. Behrmann, H. Geenen, S. Hartmann, K. Kampert, *et al.*, “Qualification tests of the 11000 photomultipliers for the Pierre Auger Observatory fluorescence detectors,” *Nucl. Instrum. Meth. A* **576** (2007) 301–311.
- [154] J. Zorn *et al.*, “The first measurement with the FD operated at a reduced PMT gain,” *Pierre Auger Observatory technical note GAP2015-021* (2015) . Available for reviewers at http://auger.fnal.gov/upgrade_review/.
- [155] M. Platino *et al.*, “AMIGA at the Auger Observatory: The telecommunications system,” *Proc. of 33rd Int. Cosmic Ray Conf., Rio de Janeiro, Brazil* (2013) .
- [156] “Ubiquiti Networks.” <https://www.ubnt.com/airmax/bulletm/>.
- [157] S. Argiro, S. Barroso, J. Gonzalez, L. Nellen, T. C. Paul, *et al.*, “The Offline Software Framework of the Pierre Auger Observatory,” *Nucl. Instrum. Meth. A* **580** (2007) 1485–1496, [arXiv:0707.1652](https://arxiv.org/abs/0707.1652) [astro-ph].
- [158] E. Harold and W. Means, *XML in a Nutshell*. O'Reilly Media, 2004. ISBN 0-596-00764-7.
- [159] “Python.” <https://www.python.org/>.
- [160] “ROOT - Data Analysis Framework.” <https://root.cern.ch/drupal/>.
- [161] S. Sciutto, “AIRES: A System for air shower simulations. User's guide and reference manual. Version 2.2.0.” http://www2.fisica.unlp.edu.ar/auger/aires/eg_Aires.html, 1999.
- [162] T. Bergmann, R. Engel, D. Heck, N. Kalmykov, S. Ostapchenko, *et al.*, “One-dimensional Hybrid Approach to Extensive Air Shower Simulation,” *Astropart. Phys.* **26** (2007) 420–432, [arXiv:astro-ph/0606564](https://arxiv.org/abs/astro-ph/0606564) [astro-ph]. for further information contact the authors of CORSIKA, see url at [147].
- [163] H.-J. Drescher and G. R. Farrar, “Air shower simulations in a hybrid approach using cascade equations,” *Phys. Rev. D* **67** (2003) 116001, [arXiv:astro-ph/0212018](https://arxiv.org/abs/astro-ph/0212018) [astro-ph]. downloads and manuals to the software can be found at <http://th.physik.uni-frankfurt.de/~drescher/SENECA/>.
- [164] “Apache - Xerces.” <http://xerces.apache.org/>.
- [165] “XML - SCHEMA.” <http://www.w3.org/standards/xml/schema>.
- [166] “CppUnit - C++ port of JUnit.” <http://sourceforge.net/projects/cppunit/>.
- [167] “Buildbot - The Continuous Integration Framework.” <http://buildbot.net/>.
- [168] “CMake.” <http://www.cmake.org>.
- [169] “Auger Package Environment.” <https://svn.auger.unam.mx/trac/projects/ape/>.

- [170] "Public Event Explorer." <http://auger.colostate.edu/ED/>.
- [171] **Pierre Auger** Collaboration, "The prototype muon module for the AMIGA project of the Pierre Auger Observatory (draft, 2015)." Available for reviewers at http://auger.fnal.gov/upgrade_review/.
- [172] "The Agreement for the Organization, Management and Funding of the Pierre Auger Observatory." http://www.auger.org/admin/FinanceBoard/auger_fb_agreement_AUG2008_revised.pdf.
- [173] "Pierre Auger Observatory Project Risk analysis." http://auger.fnal.gov/upgrade_review/.
- [174] "Visual Physics Analysis - VISPA." <http://vispa.physik.rwth-aachen.de/>.
- [175] "Upgrade Work Breakdown Structure (WBS)." http://auger.fnal.gov/upgrade_review/.
- [176] **Pierre Auger** Collaboration, J. Abraham *et al.*, "Properties and performance of the prototype instrument for the Pierre Auger Observatory," *Nucl. Instrum. Meth. A* **523** (2004) 50–95.
- [177] The Pierre Auger Collaboration, "The Pierre Auger Cosmic Ray Observatory," *submitted to Nucl. Instrum. Meth. A* (Feb., 2015), arXiv:1502.01323 [astro-ph.IM].
- [178] **Pierre Auger** Collaboration, X. Bertou *et al.*, "Calibration of the surface array of the Pierre Auger Observatory," *Nucl. Instrum. Meth. A* **568** (2006) 839–846.
- [179] **Pierre Auger** Collaboration, J. Abraham *et al.*, "The Fluorescence Detector of the Pierre Auger Observatory," *Nucl. Instrum. Meth. A* **620** (2010) 227–251, arXiv:0907.4282 [astro-ph.IM].
- [180] M. de Oliveira, V. de Souza, H. Reis, and R. Sato, "Manufacturing the Schmidt corrector lens for the Pierre Auger Observatory," *Nucl. Instrum. Meth. A* **522** (2004) 360–370.
- [181] **Pierre Auger** Collaboration, J. Baeuml, "Measurement of the Optical Properties of the Auger Fluorescence Telescopes," [233], p. 15. arXiv:1307.5059 [astro-ph.HE].
- [182] J. Brack, R. Cope, A. Dorofeev, B. Gookin, J. Harton, *et al.*, "Absolute Calibration of a Large-diameter Light Source," *JINST* **8** (2013) P05014, arXiv:1305.1329 [astro-ph.IM].
- [183] A. Rovero, P. Bauleo, J. Brack, J. Harton, and R. Knapik, "Multi-wavelength calibration procedure for the pierre Auger Observatory Fluorescence Detectors," *Astroparticle Physics* **31** no. 4, (2009) 305 – 311.
- [184] B. Gookin *et al.*, "Multi-Wavelength calibration, March 2014," *Pierre Auger Observatory technical note GAP2014-091* (2014) . Available for reviewers at http://auger.fnal.gov/upgrade_review/.
- [185] R. Rivest, "The MD5 Message-Digest Algorithm." <http://tools.ietf.org/html/rfc1321>.

- [186] **Pierre Auger** Collaboration, J. Abraham *et al.*, “Trigger and aperture of the surface detector array of the Pierre Auger Observatory,” *Nucl. Instrum. Meth. A* **613** (2010) 29–39, [arXiv:1111.6764 \[astro-ph.IM\]](https://arxiv.org/abs/1111.6764).
- [187] K. Kamata and J. Nishimura, “The Lateral and the Angular Structure Functions of Electron Showers,” *Proc. Theor. Phys. Supplement* **6** (1958) 93–155.
- [188] K. Greisen, “The extensive air showers,” *Progress in Cosmic Ray Physics* **3** (1956) 1. <https://archive.org/details/progessincosmic031401mbp>.
- [189] **Pierre Auger** Collaboration, R. Pesce, “Energy calibration of data recorded with the surface detectors of the Pierre Auger Observatory: an update,” [234], p. 13. [arXiv:1107.4809 \[astro-ph.HE\]](https://arxiv.org/abs/1107.4809).
- [190] J. Hersil, I. Escobar, D. Scott, G. Clark, and S. Olbert, “Observations of Extensive Air Showers near the Maximum of Their Longitudinal Development,” *Phys. Rev. Lett.* **6** (1961) 22–23.
- [191] **Pierre Auger** Collaboration, H. Dembinski, “The Cosmic Ray Spectrum above 4×10^{18} eV as measured with inclined showers recorded at the Pierre Auger Observatory,” [234], p. 5. [arXiv:1107.4809 \[astro-ph.HE\]](https://arxiv.org/abs/1107.4809).
- [192] **Pierre Auger** Collaboration, V. Verzi, “The Energy Scale of the Pierre Auger Observatory,” [233], p. 7. [arXiv:1307.5059 \[astro-ph.HE\]](https://arxiv.org/abs/1307.5059).
- [193] F. Arqueros, J. R. Hoerandel, and B. Keilhauer, “Air Fluorescence Relevant for Cosmic-Ray Detection - Summary of the 5th Fluorescence Workshop, El Escorial 2007,” *Nucl. Instrum. Meth. A* **597** (2008) 1–22, [arXiv:0807.3760 \[astro-ph\]](https://arxiv.org/abs/0807.3760).
- [194] **AIRFLY** Collaboration, M. Ave *et al.*, “Spectrally resolved pressure dependence measurements of air fluorescence emission with AIRFLY,” *Nucl. Instrum. Meth. A* **597** (2008) 41–45.
- [195] **AIRFLY** Collaboration, M. Ave *et al.*, “Precise measurement of the absolute fluorescence yield of the 337 nm band in atmospheric gases,” *Astropart. Phys.* **42** (2013) 90–102, [arXiv:1210.6734 \[astro-ph.IM\]](https://arxiv.org/abs/1210.6734).
- [196] M. Giller, G. Wieczorek, A. Kacperczyk, H. Stojek, and W. Tkaczyk, “Energy spectra of electrons in the extensive air showers of ultra-high energy,” *J. Phys. G* **30** no. 2, (2004) 97.
- [197] M. Roberts, “The role of atmospheric multiple scattering in the transmission of fluorescence light from extensive air showers,” *J. Phys. G* **31** no. 11, (2005) 1291.
- [198] J. Pekala, P. Homola, B. Wilczynska, and H. Wilczynski, “Atmospheric multiple scattering of fluorescence and Cherenkov light emitted by extensive air showers,” *Nucl. Instrum. Meth. A* **605** (2009) 388–398, [arXiv:0904.3230 \[astro-ph.HE\]](https://arxiv.org/abs/0904.3230).
- [199] M. Giller and A. Smialkowski, “An analytical approach to the multiply scattered light in the optical images of the extensive air showers of ultra-high energies,” *Astropart. Phys.* **36** (2012) 166–182, [arXiv:1201.4052 \[astro-ph.HE\]](https://arxiv.org/abs/1201.4052).

- [200] M. Unger, B. Dawson, R. Engel, F. Schussler, and R. Ulrich, “Reconstruction of Longitudinal Profiles of Ultra-High Energy Cosmic Ray Showers from Fluorescence and Cherenkov Light Measurements,” *Nucl. Instrum. Meth. A* **588** (2008) 433–441, [arXiv:0801.4309 \[astro-ph\]](https://arxiv.org/abs/0801.4309).
- [201] D. Gora, R. Engel, D. Heck, P. Homola, H. Klages, *et al.*, “Universal lateral distribution of energy deposit in air showers and its application to shower reconstruction,” *Astropart. Phys.* **24** (2006) 484–494, [arXiv:astro-ph/0505371 \[astro-ph\]](https://arxiv.org/abs/astro-ph/0505371).
- [202] B. Dawson, M. Giller, and G. Wieczorek, “Influence of the scattered Cherenkov light on the width of shower images as measured in the EAS fluorescence experiments,” *Proceedings of the 30th International Cosmic Ray Conference, Mexico-City, Mexico* **4** (2007) 401. <http://indico.nucleares.unam.mx/contributionDisplay.py?contribId=651&confId=4>.
- [203] T. Gaisser and A. Hillas, “Reliability of the method of constant intensity cuts for reconstructing the average development of vertical showers,” *Proceedings of the 15th International Cosmic Ray Conference, Plovdiv, Bulgaria* **8** (1977) 353.
- [204] **Pierre Auger** Collaboration, M. Tueros, “Estimate of the non-calorimetric energy of showers observed with the fluorescence and surface detectors of the Pierre Auger Observatory,” [233], p. 11. [arXiv:1307.5059 \[astro-ph.HE\]](https://arxiv.org/abs/1307.5059).
- [205] L. Prado, B. Dawson, S. Petrera, R. Shellard, M. do Amaral, R. Caruso, R. Sato, and J. Bellido, “Simulation of the fluorescence detector of the Pierre Auger Observatory,” *Nucl. Instrum. Meth.* **545** no. 3, (2005) 632 – 642.
- [206] **Pierre Auger** Collaboration, B. Dawson, “Hybrid Performance of the Pierre Auger Observatory,” *Proc. 30th International Cosmic Ray Conference (ICRC) 2007, Merida, Mexico* (2007) , [arXiv:0706.1105 \[astro-ph\]](https://arxiv.org/abs/0706.1105).
- [207] **Pierre Auger** Collaboration, H.-J. Mathes, “The HEAT Telescopes of the Pierre Auger Observatory. Status and First Data,” [235], p. 1. [arXiv:1107.4807 \[astro-ph.HE\]](https://arxiv.org/abs/1107.4807).
- [208] **Pierre Auger** Collaboration, F. Sanchez, “The AMIGA detector of the Pierre Auger Observatory: an overview,” [235], p. 5. [arXiv:1107.4807 \[astro-ph.HE\]](https://arxiv.org/abs/1107.4807).
- [209] M. Platino, M. Hampel, A. Almela, A. Krieger, D. Gorbena, *et al.*, “AMIGA at the Auger Observatory: The scintillator module testing system,” *JINST* **6** (2011) P06006.
- [210] **Pierre Auger** Collaboration, I. Mariş, “The AMIGA infill detector of the Pierre Auger Observatory: performance and first data,” [234], p. 9. [arXiv:1107.4809 \[astro-ph.HE\]](https://arxiv.org/abs/1107.4809).
- [211] **Pierre Auger** Collaboration, S. Maldera, “Measuring the accuracy of the AMIGA muon counters at the Pierre Auger Observatory,” [233], p. 4. [arXiv:1307.5059 \[astro-ph.HE\]](https://arxiv.org/abs/1307.5059).
- [212] **Pierre Auger** Collaboration, D. Ravignani, “Measurement of the energy spectrum of cosmic rays above 3×10^{17} eV using the AMIGA 750 m surface detector array of the Pierre Auger Observatory,” [233], p. 4. [arXiv:1307.5059 \[astro-ph.HE\]](https://arxiv.org/abs/1307.5059).

- [213] O. Wainberg *et al.*, “Digital Electronics for the Pierre Auger Observatory AMIGA Muon Counters,” *JINST* **9** (2014) T04003.
- [214] A. Supanitsky, A. Etchegoyen, G. Medina-Tanco, I. Allekotte, M. G. Berisso, *et al.*, “Underground Muon Counters as a Tool for Composition Analyses,” *Astropart. Phys.* **29** (2008) 461–470, [arXiv:0804.1068 \[astro-ph\]](https://arxiv.org/abs/0804.1068).
- [215] **Pierre Auger** Collaboration, B. Wundheiler, “The AMIGA muon counters of the Pierre Auger Observatory: performance and first data,” [235], p. 9. [arXiv:1107.4807 \[astro-ph.HE\]](https://arxiv.org/abs/1107.4807).
- [216] **LOFAR** Collaboration, S. Buitink *et al.*, “Shower X_{max} determination based on LOFAR radio measurements,” *Proc. 33rd International Cosmic Ray Conference (ICRC), Rio de Janeiro, Brazil* (2013).
- [217] H. Allan, “Radio emission from extensive air showers,” *Progress in Elementary Particles and Cosmic Ray Physics* **10** (1971) 171.
- [218] D. J. Fegan, “Detection of elusive Radio and Optical emission from Cosmic-ray showers in the 1960s,” *Nucl. Instrum. Meth. A* **662** (2012) S2–S11, [arXiv:1104.2403 \[astro-ph.IM\]](https://arxiv.org/abs/1104.2403).
- [219] **LOPES** Collaboration, H. Falcke *et al.*, “Detection and imaging of atmospheric radio flashes from cosmic ray air showers,” *Nature* **435** (2005) 313–316, [arXiv:astro-ph/0505383 \[astro-ph\]](https://arxiv.org/abs/astro-ph/0505383).
- [220] D. Ardouin, A. Bellettoile, D. Charrier, R. Dallier, L. Denis, *et al.*, “Radioelectric Field Features of Extensive Air Showers Observed with CODALEMA,” *Astropart. Phys.* **26** (2006) 341–350, [arXiv:astro-ph/0608550 \[astro-ph\]](https://arxiv.org/abs/astro-ph/0608550).
- [221] P. Schellart, A. Nelles, S. Buitink, A. Corstanje, J. Enriquez, *et al.*, “Detecting cosmic rays with the LOFAR radio telescope,” *Astron. Astrophys.* **560** (2013) A98, [arXiv:1311.1399 \[astro-ph.IM\]](https://arxiv.org/abs/1311.1399).
- [222] **Pierre Auger** Collaboration, B. Revenu, “Autonomous detection and analysis of radio emission from air showers at the Pierre Auger Observatory,” [235], p. 17. [arXiv:1107.4807 \[astro-ph.HE\]](https://arxiv.org/abs/1107.4807).
- [223] **Pierre Auger** Collaboration, J. Kelley, “AERA: the Auger Engineering Radio Array,” [235], p. 13. [arXiv:1107.4807 \[astro-ph.HE\]](https://arxiv.org/abs/1107.4807).
- [224] **Pierre Auger** Collaboration, P. Abreu *et al.*, “Results of a self-triggered prototype system for radio-detection of extensive air showers at the Pierre Auger Observatory,” *JINST* **7** (2012) P11023, [arXiv:1211.0572 \[astro-ph.HE\]](https://arxiv.org/abs/1211.0572).
- [225] **Pierre Auger** Collaboration, A. Aab *et al.*, “Probing the radio emission from air showers with polarization measurements,” *Phys. Rev. D* **89** (2014) 052002, [arXiv:1402.3677 \[astro-ph.HE\]](https://arxiv.org/abs/1402.3677).
- [226] **Pierre Auger** Collaboration, P. Abreu *et al.*, “Antennas for the Detection of Radio Emission Pulses from Cosmic-Rays,” *JINST* **7** (2012) P10011, [arXiv:1209.3840 \[astro-ph.IM\]](https://arxiv.org/abs/1209.3840).

- [227] P. Gorham, N. Lehtinen, G. Varner, J. Beatty, A. Connolly, *et al.*, “Observations of Microwave Continuum Emission from Air Shower Plasmas,” *Phys. Rev. D* **78** (2008) 032007, [arXiv:0705.2589 \[astro-ph\]](https://arxiv.org/abs/0705.2589).
- [228] **Pierre Auger** Collaboration, P. Allison, “Microwave detection of cosmic ray showers at the Pierre Auger Observatory,” [235], p. 25. [arXiv:1107.4807 \[astro-ph.HE\]](https://arxiv.org/abs/1107.4807).
- [229] **Pierre Auger** Collaboration, P. Facal San Luis, “Status of the program for microwave detection of cosmic rays at the Pierre Auger observatory,” *EPJ Web Conf.* **53** (2013) 08009.
- [230] J. Alvarez-Muñiz, E. Amaral Soares, A. Berlin, M. Bogdan, M. Boháčová, *et al.*, “The MIDAS telescope for microwave detection of ultra-high energy cosmic rays,” *Nucl. Instrum. Meth. A* **719** (2013) 70–80, [arXiv:1208.2734 \[astro-ph.IM\]](https://arxiv.org/abs/1208.2734).
- [231] J. Alvarez-Muñiz, A. Berlin, M. Bogdan, M. Boháčová, C. Bonifazi, *et al.*, “A Search for Microwave Emission From Ultra-High Energy Cosmic Rays,” *Phys. Rev. D* **86** (2012) 051104, [arXiv:1205.5785 \[astro-ph.HE\]](https://arxiv.org/abs/1205.5785).
- [232] **Pierre Auger** Collaboration, P. Abreu *et al.*, “The exposure of the hybrid detector of the Pierre Auger Observatory,” *Astropart. Phys.* **34** (2011) 368–381, [arXiv:1010.6162 \[astro-ph.HE\]](https://arxiv.org/abs/1010.6162).
- [233] **Pierre Auger** Collaboration, A. Aab *et al.*, “The Pierre Auger Observatory: Contributions to the 33rd International Cosmic Ray Conference (ICRC 2013),” *Proc. 33rd International Cosmic Ray Conference (ICRC) 2013, Rio de Janeiro, Brazil* (2013) , [arXiv:1307.5059 \[astro-ph.HE\]](https://arxiv.org/abs/1307.5059).
- [234] **Pierre Auger** Collaboration, P. Abreu *et al.*, “The Pierre Auger Observatory I: The Cosmic Ray Energy Spectrum and Related Measurements,” *Proc. 32nd International Cosmic Ray Conference (ICRC) 2011, Beijing, China* (2011) , [arXiv:1107.4809 \[astro-ph.HE\]](https://arxiv.org/abs/1107.4809).
- [235] **Pierre Auger** Collaboration, P. Abreu *et al.*, “The Pierre Auger Observatory V: Enhancements,” *Proc. 32nd International Cosmic Ray Conference (ICRC) 2011, Beijing, China* (2011) , [arXiv:1107.4807 \[astro-ph.HE\]](https://arxiv.org/abs/1107.4807).